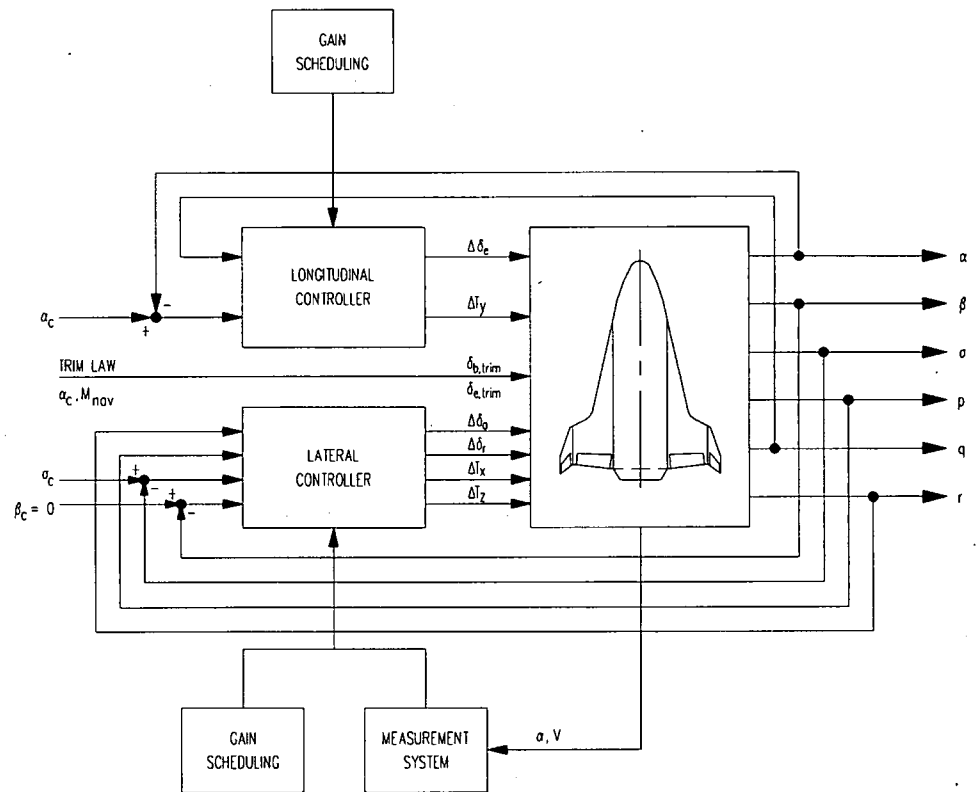


Linear Quadratic Regulator design for an unpowered, winged re-entry vehicle

February 1997

Ir. E. Mooij



Linear Quadratic Regulator design for an unpowered, winged re-entry vehicle

Ir. E. Mooij

Copyright © 1997, by Delft University of Technology, Faculty of Aerospace Engineering, Delft, The Netherlands.

All rights reserved. No part of this publication may be reproduced, stored in a retrieval system or transmitted in any form or by any means, electronic, mechanical, photocopying, recording or otherwise, without the prior written permission of the Delft University of Technology, Faculty of Aerospace Engineering, Delft, The Netherlands.

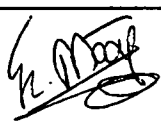
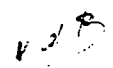


Publisher: Delft University of Technology
Faculty of Aerospace Engineering
P.O. Box 5058
2600 GB Delft
The Netherlands.
tel.: 015-2782058
fax: 015-2781822

Date February 1997

Report LR - 806

ISBN: 90-5623-040-9

Title	:	Linear Quadratic Regulator design for an unpowered, winged re-entry vehicle
Author(s)	:	E. Mooij
Abstract	:	<p>This report describes the design of an attitude controller for an unpowered, winged re-entry vehicle. The decoupling of the symmetric and asymmetric motion makes it possible to design two separate controllers, one for the pitch motion and one for the lateral motion. The design of the controller, a Linear Quadratic Regulator, is based on linearisation of the equations of motion and feedback of the attitude and angular rates. The gains appearing in the control laws are computed by defining a quadratic cost criterion and then solving the matrix Riccati equation. Results of the study include the step and ramp response of the two separate controllers and the flight along the nominal trajectory with the integrated controller. The deviations from the nominal trajectory are acceptable, so this controller can be used for a detailed sensitivity analysis.</p>
Keyword(s)	:	control-system design, linear state feedback, gain scheduling, Riccati equation, re-entry, HORUS-2B

Date	February 1997
Prepared	E. Mooij 
Verified	P.Ph. van den Broek 
Approved	P.Th.L.M. van Woerkom 
Authorized EB	P.G. Bakker 

CHANGE RECORD

Issue No.	Rev. No.	Date	Pages Changed/ Added/ Deleted	Topics Introduced
01	01	08-03-95	-	First version
	02	10-01-96	All	Comments processed
	03	02-04-96	All	Final draft
	04	14-06-96	All	Comments processed
	05	20-02-97	All	Comments processed

Table of Contents

Notations	v
Chapter 1 - Introduction	1
1.1. Background.	2
1.2. Attitude control of winged re-entry vehicles.	5
1.3. Attitude-control concepts.	8
1.4. Control-system design cycle.	13
Chapter 2 - The Motion of a Vehicle in a Planetary Atmosphere	17
2.1. The general form of the equations of motion.	17
2.2. Linearisation of the equations of motion.	19
2.3. The state-space form of the equations of motion.	24
Chapter 3 - Open-loop Behaviour of the Re-entry Vehicle	33
3.1. Introduction.	33
3.2. Nominal trajectory.	34
3.3. Eigenvalues and eigenmotion.	43
Chapter 4 - Design of the Controller	65
4.1. Introduction.	65
4.2. The matrix Riccati equation.	67
4.3. Longitudinal controller.	71
4.3.1. Reduced system for symmetric motion.	71
4.3.2. Root locus of the reduced system.	72
4.3.3. Selection of pitch controls.	75
4.3.4. Control laws.	76
4.3.5. Computation of the feedback gains.	77
4.4. Lateral controller.	80
4.4.1. Reduced system for asymmetric motion.	80
4.4.2. Root locus of the reduced system.	82
4.4.3. Selection of the controls.	84
4.4.4. Control laws.	84

4.4.5. Computation of the feedback gains.	88
Chapter 5 - Verification of the Controller	93
5.1. Introduction.	93
5.2. Root loci of the closed-loop systems.	94
5.2.1. Longitudinal controller.	94
5.2.2. Lateral controller.	94
5.3. Step response.	99
5.3.1. Introduction.	99
5.3.2. Longitudinal controller.	99
5.3.3. Lateral controller.	100
5.4. Ramp response.	103
5.4.1. Longitudinal controller.	103
5.4.2. Lateral controller.	104
5.5. Flight along nominal trajectory with integrated controller.	107
Chapter 6 - Conclusions and Recommendations	119
References	121
Appendix A - Definition of State Variables	127
Appendix B - Linear Stability Model of HORUS-2B	131
Appendix C - Selected Controller Gains	139

Notations

<i>Roman</i>		[unit]
a	element of state matrix	
a	speed of sound	m/s
\mathbf{A}	state or system matrix	
b	element of control matrix	-
b_{ref}	aerodynamic reference length	m
\mathbf{B}	control input matrix	
c_{ref}	aerodynamic reference length	m
\mathbf{C}	output matrix	
C_D	drag-force coefficient	-
C_l	roll-moment coefficient	-
C_L	lift-force coefficient	-
C_m	pitch-moment coefficient	-
C_n	yaw-moment coefficient	-
C_S	side-force coefficient	-
D	drag	N
\mathbf{D}	direct transmission matrix	
g_r	acceleration due to gravity in radial direction	m/s ²
g_δ	acceleration due to gravity in meridional direction	m/s ²
h	height	m
\mathbf{I}	identity matrix	
I	moment (product) of inertia	kg m ²
\mathbf{J}	cost criterion	
K	control gain	1/rad
\mathbf{K}	control-gain matrix	
L	lift	N
L'	roll moment	Nm
m	mass	kg
M	Mach number	-
M'	pitch moment	Nm

N'	yaw moment	Nm
p	roll rate	rad/s
P	period	s
\mathbf{P}	solution of matrix Lyapunov equation	
q	pitch rate	rad/s
q_{dyn}	dynamic pressure	N/m ²
\mathbf{Q}	control deviation weight matrix	
r	yaw rate	rad/s
R	modulus of position vector	m
\mathbf{R}	control effort weight matrix	
R_e	equatorial radius	m
S	side force	N
\mathbf{S}	square root of \mathbf{R}	
S_{ref}	aerodynamic reference area	m ²
t	time	s
T_1	half or doubling time	s
$\frac{T_1}{2}$		
T_x	roll-thruster moment	Nm
T_y	pitch-thruster moment	Nm
T_z	yaw-thruster moment	Nm
\mathbf{u}	control vector	
\mathbf{u}'	independent control vector	
V	modulus of velocity vector	m/s
V	Lyapunov function	
\mathbf{x}	state vector	
\mathbf{y}	output vector	
z	modulus of a complex number	-
X, Y, Z	axes	

Greek

α	angle of attack	rad
β	angle of sideslip	rad
γ	flight-path angle	rad
δ	geocentric latitude	rad
δ_a	aileron deflection angle	rad
δ_b	body-flap deflection angle	rad
δ_e	elevator deflection angle	rad
δ_r	rudder deflection angle	rad
δ_w	wing-flap deflection angle	rad
Δ	perturbation	-
ζ	damping ratio	-
θ	argument of complex number	rad
λ	eigenvalue	-

μ	gravitation parameter	m^3/s^2
$\boldsymbol{\mu}$	eigenvector	
ρ	(atmospheric) density	kg/m^3
σ	bank angle	rad
τ	geocentric longitude	rad
χ	heading	rad
ω_{cb}	rotational rate of the central body	rad/s
ω_n	eigenfrequency	rad/s
$\boldsymbol{\omega}$	rotation vector	rad/s

Indices

0	nominal state
<i>a</i>	aileron
<i>b</i>	body flap
<i>B</i>	body frame
<i>c</i>	commanded value
<i>cb</i>	central body
<i>e</i>	elevator
<i>f</i>	final, finite
<i>p</i>	in direction of roll rate
<i>q</i>	in direction of pitch rate
<i>r</i>	in direction of yaw rate
<i>r</i>	rudder
<i>r, R</i>	in direction of position vector
<i>V</i>	in direction of velocity
<i>w</i>	elevon
<i>x, y, z</i>	along X-, Y- and Z-axis
α	in direction of angle of attack
β	in direction of angle of sideslip
γ	in direction of flight-path angle
δ	in direction of latitude
σ	in direction of bank angle
χ	in direction of heading

Abbreviations

ACS	Aerodynamic Control System
c.o.m.	centre of mass
CPU	Central Processing Unit
d.o.f.	degree of freedom
FCS	Flight Control System
GNC	Guidance, Navigation and Control

LQG	Linear Quadratic Gaussian
LQR	Linear Quadratic Regulator
MIMO	Multiple Input, Multiple Output
MRAC	Model Reference Adaptive Control
PID	Proportional, Integral and Derivative
RCS	Reaction Control System
START	Simulation Tool for Atmospheric Re-entry Trajectories
STR	Self-Tuning Regulator

Chapter 1

Introduction

During all phases in the design and operations of space vehicles, computer simulation of the flight performance plays an important role. Models of the vehicle and the environment can be simple, to get a first impression of the feasibility of a vehicle design or a particular mission, or can be very detailed when, for instance, the influence of aeroelasticity on the performance of an attitude-control system has to be studied. Within the framework of an ongoing research at the Faculty of Aerospace Engineering, Delft University of Technology, the development of a flight-simulation tool has been initiated (Mooij, 1994) with which, amongst others, the guided and controlled ascent of air-breathing space planes subjected to disturbances and model uncertainties can be analysed.

The Simulation Tool for Atmospheric Re-entry Trajectories (START) has been selected to serve as a basis for further development. The original version of START did not include any guidance and control models, nor propulsion systems and the related variable mass properties. For a gradual development of START to a tool, capable of analysing the ascent missions that we mentioned before, several phases have been defined (Mooij, 1994). Current research focuses on the guided and controlled flight of unpowered, winged re-entry vehicles. A major step herein is the development of an attitude-control system.

In this report we describe the design of such an attitude-control system for a selected unpowered, winged re-entry vehicle. Before we come to a discussion of attitude-control systems in this chapter, we begin by giving some background information on re-entry missions and how to increase mission success by incorporating guidance, navigation and control (Section 1.1). In the succeeding Section 1.2, we will present the attitude control of winged re-entry vehicles. Section 1.3 introduces several attitude-control concepts and one will be selected to employ as our design (linear state feedback with gain scheduling). In Section 1.4, finally, the design process of the selected control system is detailed and an overview of the chapters of this report is given.

1.1. Background.

Two important aspects of the entry and descent of space vehicles are the tactical aspect of having control over the time and location of landing and the severe mechanical and thermal loading on the vehicle. For manned missions, for instance, the maximum deceleration is usually limited by an upper bound of 3 g to save the occupants from discomfort or worse. Also in case of unmanned (scientific) missions a too strong deceleration might be harmful to the on-board instruments. The thermal load, e.g., the maximum heat flux, the wall temperature in the stagnation point and the integrated heat load, define to a large extent the design and therefore also the mass of the thermal protection system, so obviously we want to have the most favourable load on the vehicle. However, first of all a winged re-entry vehicle like the American Space Shuttle is supposed to land on an air strip, so its trajectory should be targeted to the landing location right on from entry. And, in case of the parachute descent of the Apollo capsules, it was important that it would splash down in the ocean near the recovery ships.

During the process of mission analysis and mission design, an optimal trajectory is computed which usually satisfies trajectory constraints (e.g., a maximum allowable thermal load) and end conditions (e.g., the landing place in case of a re-entry mission). Once this so-called nominal trajectory has been defined it must be verified that the vehicle can actually fly this trajectory, or, in other words, whether the vehicle can execute the required manoeuvres without violating any constraints. Furthermore, it must be guaranteed that the vehicle will still be able to fulfil its mission when it encounters (unforeseen) disturbances which make it deviate from its nominal path. To ensure mission success, the space vehicle is equipped with a so-called Guidance, Navigation and Control system (GNC system).

The task of the guidance system is to generate steering commands, e.g., a commanded attitude or thrust level, taking a reference state, trajectory constraints and/or a final state into account. For this task, the system needs input from the outside world, for instance the current actual state. These data have to be provided by the navigation system, using sensor information and predefined theoretical models. The control system has to take care that the steering commands are carried out, such that, for example, the actual attitude equals the commanded attitude in a reasonably short time and that this attitude is dynamically stable (trim stability). To achieve this, the control system may drive aerodynamic control surfaces, reaction-control wheels and thrusters, etc.

The design of a GNC system is usually centred around a nominal mission that is free from disturbances. The environment is modelled at a certain level of complexity only and also the description of the vehicle is of course not infinitely accurate. An important question is whether the GNC system will be able to steer and control the vehicle in the presence of all kinds of uncertainties that it is bound to encounter during the actual mission. One way to assure this is to design a very robust system¹. But the next question that arises then is: how robust should

¹ Robustness is defined as the particular property that a control system must possess for it to operate properly in realistic situations (Shahian and Hassul, 1993). Mathematically, it means that the controller must not only work for the system that it has been designed for, but for a whole family of (similar) systems. If the controller is stable for a set of systems whose parameters deviate substantially from the nominal system, then the controller is said to have robust stability.

our system be? A too robust system might negatively influence the flying qualities and manoeuvrability and if the system is not robust enough, we can still end up with a severe control problem. It is therefore very important that already during the design process we study as many uncertainties as possible to see how our guidance and control system will deal with them. Usually what one does is, once the GNC system has been developed for the nominal mission, simulating a number of test cases with different error sources included, and with all dynamic, vehicle and environment models as accurate as possible.

In Mooij (TO BE PUBLISHED) such a sensitivity analysis of a GNC system is described. That analysis is centred around the HORUS-2B, an unpowered, winged re-entry vehicle that resembles the Space Shuttle (see also Fig. 1.1). Initially the HORUS was designed as an upper stage of the Ariane launcher. Later on, the concept was changed and it became the rocket-powered second stage of the German Sänger Two-Stage-To-Orbit space plane. A brief description of the mission will follow below.

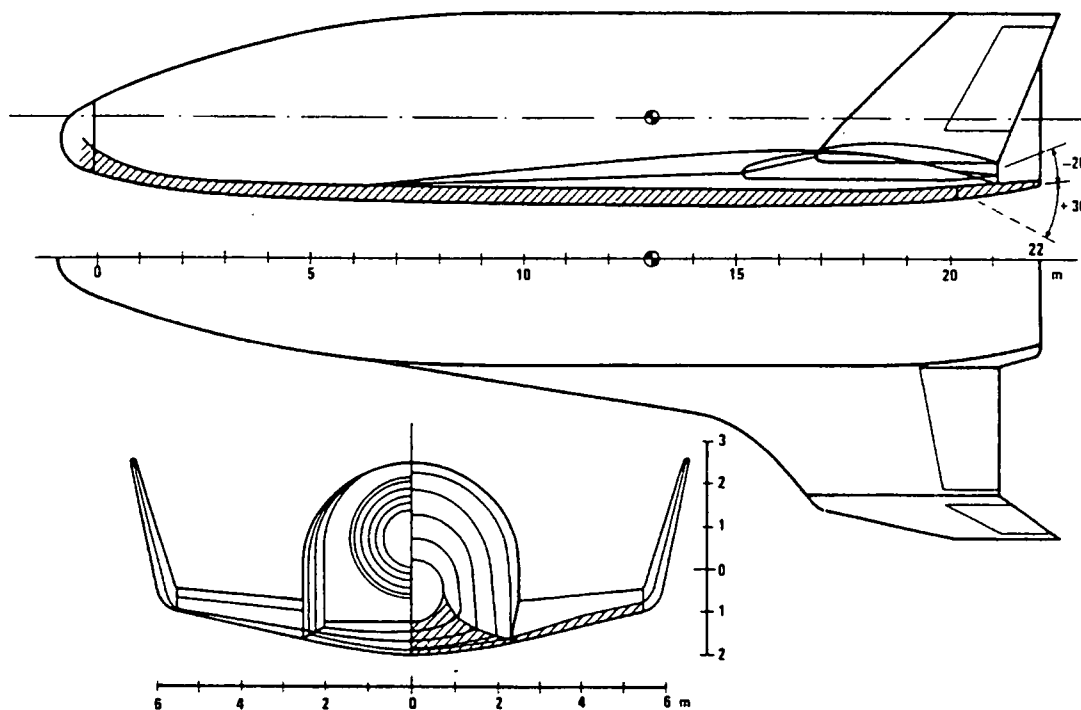


Fig. 1.1 - The HORUS-2B (MBB, 1988a).

After launch and orbital operations, it re-enters the atmosphere at an altitude of 120 km and the vehicle will begin its voyage back to its landing site, the European launch base in Kourou, French Guyana. The re-entry phase ends when HORUS is at a distance of about 80 km from the runway. It is said that the vehicle has reached the Terminal Area, which marks the beginning of the next mission phase in case of a winged re-entry vehicle. We will not study that phase, however.

The re-entry guidance system should track the prescribed trajectory as well as possible, while responding to disturbances and model errors by performing the appropriate manoeuvres. But the prescribed trajectory should not be followed at any cost because reaching the landing area without violating the constraints is the major mission objective. So another design goal is to limit the demands on the flight control system while being applicable to any reasonable reference trajectory. Since HORUS is basically an unpowered vehicle, only two steering variables are available, i.e., the angle of attack α and the bank angle σ (the angle of sideslip β is considered to be a disturbance, and will always be commanded to zero). For an efficient guidance, the nominal trajectory must provide sufficient margins for varying α and σ . This is also true for the path constraints, of course, and especially the thermal loads should remain well below the critical limits.

A fundamental functional separation in the HORUS guidance is the subdivision of the horizontal and vertical entry guidance, corresponding with the symmetric and asymmetric motion of the vehicle. The vertical flight path is controlled by adjusting the angle of attack and the absolute value of the bank angle, while the sign of the bank angle is provided by the horizontal guidance (MBB, 1988b).

To begin with the latter, this guidance controller steers the HORUS towards a targeting point at some 80 km from the runway. As a result from vertical guidance by means of the absolute bank angle, a lateral (or asymmetric) motion is introduced that needs to be compensated for, such that the average bank angle is zero and the vehicle will keep on heading towards the target. The reference parameters for the horizontal guidance logic are the actual heading of the vehicle and the heading of a direct trajectory towards the targeting point. The difference between the two is the so-called heading error, which has to be kept sufficiently small. The controller uses a predefined heading-error dead band to change the sign of the bank angle the moment the heading error exceeds the dead-band value. The corresponding manoeuvre is known as a bank reversal, and results in so-called S-turns as is also the case with the Space Shuttle.

The objectives of the vertical guidance are to:

- arrive at the Terminal-Area interface with a prescribed total energy and altitude (or velocity),
- meet the flight-path constraints during the flight.

To meet these objectives, the vertical guidance is divided into a separate energy and altitude control. The total energy, the sum of altitude-dependent potential and velocity-dependent kinetic energy, will be controlled such that only the final value at the Terminal-Area interface will be met with no direct effect on the constraints during the flight. The internal sharing of potential and kinetic energy, on the other hand, will affect the constraints through the altitude-velocity relation.

The decrease of total energy is due to the working of the atmosphere on the vehicle, in the form of the drag force. So to influence the difference between actual and reference energy, the dissipated energy due to drag can be changed. Since one of the control parameters to change the drag of the vehicle is the angle of attack, energy control is accomplished by varying this parameter. Altitude control is realised by variation of the vertical component of the lift force.

Whereas the angle of attack influences the lift force in absolute sense, by changing the bank angle this force can be rotated about the velocity vector, thus resulting in two components perpendicular to the trajectory, i.e., one vertical and one lateral. The vertical component defines the descent rate, so by changing the (absolute value of the) bank angle we can control the variation in altitude. Note that the lateral component of the lift results in a motion in the horizontal plane and thus a variation in heading. For this reason, bank reversals are required to keep the vehicle headed at the target without affecting the altitude control.

1.2. Attitude control of winged re-entry vehicles.

Until today, there has only been one winged re-entry vehicle that has actually returned from orbit to Earth: the American Space Shuttle. Its Russian counterpart, the Buran, only made one unmanned (atmospheric) test flight before the project was cancelled due to budget problems. Also in Europe budget cuts were the reason that Hermes, a smaller version of the Space Shuttle, did not leave the drawing board and was cancelled. But whether the vehicle has actually been built or not, also the many publications on space vehicles can usually teach us about applied subsystems, such as the attitude-control system. Unfortunately, we could not lay hands on any literature concerning either the Buran control system, or the proposed Hermes attitude controller.

Publicly-available documentation on the Space-Shuttle attitude controller was only sparsely available to us, and then in principle only for the ascent phase. McHenry *et al.* (1979) and Schleich (1982) give quite a detailed discussion on the Space-Shuttle ascent guidance, navigation and control. McDermott *et al.* (1982) do a linearised stability analysis for this control system, and Schletz (1982) discusses the use of quaternions in the GNC system. The attitude controller for the entry and descent phase is only marginally mentioned in those publications.

The Space Shuttle enters the atmosphere with a large angle of attack of about 40° , in order to minimise the heat load. Further down the trajectory, the angle of attack is reduced to meet with the cross- and downrange requirements. Range control throughout the entry is accomplished by control of the bank angle. The Flight Control System (FCS) must guarantee a safe and stable flight and thereby take into account wide variations in flight conditions and large model-data tolerances, next to the large attitude changes. To perform its tasks, the FCS can use a Reaction Control System (RCS) and aerodynamic control surfaces. Hamilton (1982) states five features of the Space Shuttle that present unique stability problems in combination with the large velocity range: i) the Shuttle is an unpowered vehicle, ii) the control of the aileron, rudder and the RCS jets is blended, iii) the gains of the FCS are scheduled, iv) the rigid-body stability margins are small, with strong bending modes within an octave of the cross-over frequency, and v) the control system is multi-rate digital.

Klinar *et al.* (1975) give a general overview of the Space Shuttle Flight Control System. However, this overview cannot give the final details of the FCS, since the first Space-Shuttle flight was in 1981 and the FCS design was continuously updated when new data became available. Since the general idea did not change, we will use this paper (and others) to give the reader a global impression of the FCS design. The system design goal was to maximise the

use of the aerodynamic control surfaces, of course within their power limitations, and to minimise the RCS propellant consumption while satisfying the handling qualities required for manual operation.

The longitudinal and lateral controllers of the Space Shuttle are described as follows. The longitudinal automatic and manual FCS designs are conventional pitch-rate feedback controllers, with outer loop closure accomplished by surface-position feedback or by the pilot. Actuators for both trim and control are the symmetric elevons, the body flap and for the low dynamic-pressure region the pitch jets. Also in case of the lateral automatic and manual FCS, the design exists of conventional rate-feedback controllers. Operations are depending on the angle of attack. For the higher angle-of-attack operation, the rudder is ineffective leaving only differential elevons (ailerons) and the RCS thrusters for control. The rudder is only activated below Mach numbers of 3.5. The yaw thrusters are used to control banking whereas the ailerons are used to damp sideslip. At lower angles of attack, there is a conventional aileron/rudder crossfeed for turn coordination.

A major concern during the design of the FCS was the flexible body interaction. As we can see in Fig. 1.2, which shows us the simplified entry FCS configuration in the all-aerodynamic phase, there are several bending filters included in the design. These filters were added because due to the high loads the Shuttle cannot be treated as a rigid body. The bending mode stabilisation was considered to be a problem that drove the design of the controller. What we can also see from this figure, is that the longitudinal and lateral motion are not completely decoupled, since the longitudinal controller has a feedback compensation of the yaw rate, which is a lateral-motion component. Note that the commanded attitude that is computed by the guidance logic, is translated into commanded angular rates which are fed to the attitude controller (attitude-rate control instead of attitude control).

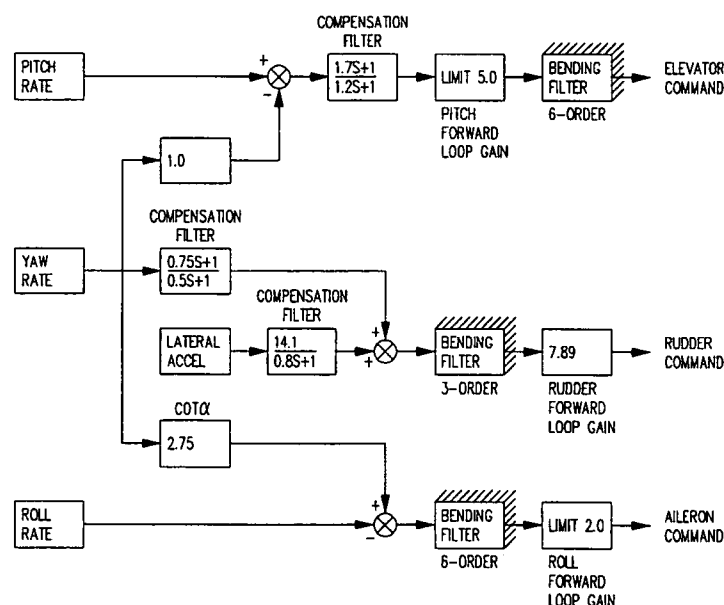


Fig. 1.2 - Entry FCS configuration for Mach = 3.5 (based on Eppler and Altenbach, 1983).



Hamilton (1982) discusses the flexible body stabilisation for the aerosurface control loops. In Fig. 1.3, we have included the simplified block diagram that Hamilton used for the discussion on the lateral FCS. We see that the basic idea is based on rate feedback, with several filters added to account for elasticity and to improve the response of the system. Furthermore, we find scheduled gains. The forward-loop gains are inversely proportional to the dynamic pressure, which raises the gains where aerosurface effectiveness is low. The aileron loop contains a yaw-rate feedback that is scheduled with the angle of attack. This gain is proportional to $COT \alpha$.

Analysis of the entry FCS has been described by a number of authors. Stone and Powell (1976) do an analysis of the entry guidance and control system to determine the sensitivity of the Shuttle to off-nominal stability and control aerodynamic parameters. Besides, they identified the boundary values for each of these parameters. The Space Shuttle entry flight control off-nominal design considerations are also the topic of a paper by Bayle (1984). He presents the sensitivity of the flight control stability margins to aerodynamics, discusses the flight control verification process and compares the predicted performance with the flight-test results of the first Space Shuttle flight, STS-1.

Nguyen *et al.* (1990) describe the testing methodology that was used for verification of the Shuttle FCS, using simulation (software: linear stability analysis and off-line non-linear simulation programs; hardware: MIL engineering and verification simulators) and flight tests (the first four orbiter missions). Epple and Altenbach (1983) describe the dynamic stability testing of the Space Shuttle Columbia FCS and flexible-body interaction. Input stimuli were applied to the Shuttle vehicle controllers to excite bending while the FCS is powered-up, and the measured responses from the operating FCS were compared with the predicted responses from the flex FCS flight model suitably modified to represent the ground-test configuration. Myers *et al.* (1982), finally, assess the FCS and the flying qualities of the Space Shuttle during approach and landing.

1.3. Attitude-control concepts.

A control-system design can be based on a number of underlying theories. The oldest and most widely used concept is the one of feedback, of either the output or state of a process. A technique which is being used more and more in industrial control systems is adaptive control. Modern, robust control techniques that are subject of many studies are based on H_∞ or μ -synthesis. Of course, there are many variations on the different concepts. Since we do not want to do an extensive survey of different control techniques, we shall limit ourselves to the three mentioned concepts that have known flight applications, and then only briefly.

Our selection criteria of a particular technique for the control of an unpowered, winged re-entry vehicle are quite simple and straightforward.

- We have a need for a control system in order to develop an analysis technique for testing guided and controlled flight of atmospheric space vehicles. This means, that we should be able to control the vehicle but that it does not have to be the best possible controller which guarantees mission success under all circumstances. In fact, it is no problem if the

sensitivity analysis will show the limitations of the controller. To put it in other words, not the performance of the controller is the study objective, but the analysis technique.

- The design should be as simple and transparent as possible, so that we can gain insight in the related flight dynamics.
- The controller has to be implemented in an existing flight-simulation software package, so its implementation should not be the cause of great difficulties.
- Preferably, but this does not have to be a necessity, we want to apply to HORUS a control technique that has not been applied before.
- Last but not least, for an actual flight application the algorithm should be easy to be embedded in an on-board computer. This is an aspect that we do not consider here, however.

Feedback control systems have found widespread use in, amongst others, aeronautical engineering (Bryson, 1985). Simple forms of feedback are (a combination of) Proportional, Integral and Derivative (PID) feedback of the output of the system or plant that has to be regulated. Classical control theory of linear systems was based on frequency response and root-locus techniques, see, for instance the books by Kuo (1987) and D'Souza (1988). A set of general performance requirements, that were not optimal in a mathematical sense but rather aimed at a reasonable performance, were commonly used.

Initially, the older concepts were not easy to apply to multi-variable plants. State feedback systems, however, are particularly suitable for systems with Multiple Inputs and Multiple Outputs, so-called MIMO systems. The parameters that define the control-system performance, the gains, can be obtained by pole placement or, alternatively, based on mathematically defined optimisation criteria. The Linear Quadratic cost criterion is well known in this respect, resulting in the so-called Linear Quadratic Regulator (LQR), see, for example, the books by Bryson and Ho (1975), Lewis (1986) and Gopal (1989). More recent trends in feedback design are given by Kokotovic (1984), who gives an overview dealing with non-linear feedback, i.e., adaptive and composite control, and with external linearisation. A recent application of the LQR using the method of extended linearisation is given by Wang and Sundarajan (1995), who describe a non-linear longitudinal flight controller for the F-8 aircraft.

An advantage of LQR is that it is a systematic method for designing MIMO systems. Furthermore, the implementation of the control laws in flight-simulation software is fairly simple, and the computational load for on-line simulation is low. The problems dealing with pole assignment linked with MIMO systems have been replaced by an optimisation problem, and pole selection is now changed to the selection of the optimisation parameters (weighting matrices). However, when not all the states of the controlled system are available, then most of the attractive properties of the LQR methodology are lost. In that case an estimator is introduced to estimate the unavailable states, see Shahian and Hassul (1993), which then results in a Linear Quadratic Gaussian (LQG) controller. However, the LQR seems to be a very appealing concept for our purposes, i.e., designing- and implementation-wise, so we keep this method in mind for selection.

When a process is dynamic, i.e., the system parameters vary strongly with time, or in case there are many disturbances, a controller with constant parameters is not likely to perform well

over the entire operational range. In that case we want in some way to adapt our controller parameters to the changing circumstances. Adaptive control, a special type of non-linear feedback control, found its way into use in the early fifties, as an autopilot for high performance aircraft (Åström and Wittenmark, 1989), later on followed by applications in the F-94, F-101 and X-15 research aircraft (Boskovich and Kaufmann, 1966). Throughout the succeeding years, several different adaptive techniques were developed, of which three are more common: Gain Scheduling, Self-Tuning Regulation and Model Reference Adaptive Control. These forms of adaptive control are discussed by many authors. We have already mentioned the book by Åström and Wittenmark, which gives an excellent treatment with many examples and applications. We will add here the survey of adaptive feedback control, given by Åström (1987). It focuses on the three mentioned concepts of adaptive control, but gives also a list with more than 350 references.

In case of gain scheduling, auxiliary variables, that relate well to the characteristics of the process dynamics, are used to change the controller parameters. However, since there is no feedback from the performance of the closed-loop system, which compensates for an incorrect schedule, Åström and Wittenmark (1989) do not regard this scheme as truly adaptive. With Self-Tuning Regulation, the system to be controlled is described by a model with (partially) unknown parameters. During operation, these parameters are estimated with a recursive estimation method. The estimated parameters are treated as the best 'guess' of the system and used to calculate new controller parameters.

The problem of self adjusting the parameters of a controller in order to stabilise the dynamic characteristics of a feedback control system when drift variations in the plant parameters occur, was the origin of Model Reference Adaptive Control or MRAC (Landau, 1974). With this technique, a reference model serves as the basis to generate the steering commands for the (unknown) plant. The parameters of the controller are adjusted in such a way that the difference between the model output and the plant output are minimised. The performance of the controller is in this way less sensitive to environmental changes, modelling errors and non-linearities within the system. A drawback might be, however, that a large control effort is required to make the plant follow the model (Messer *et al.*, 1994). Furthermore, the mathematical foundation of the original MRAC is quite large and may withstand a quick design and implementation.

A survey of model reference adaptive techniques, both in theory and applications, is given by Landau (1974). This survey includes over 250 references. A recent work on direct adaptive control algorithms, and especially a simplified form of Model Reference Adaptive Control, is given by Kaufman *et al.* (1994). This latter methodology seems to be promising with respect to ease of use and computational requirements, so in principle we will keep this method in mind. However, due to time constraints and lack of practical applications we will not apply this concept here, but keep it as a focus point for further research.

ACRI/LAN (1992) discusses guidance and adaptive-control techniques of moderate lift-to-drag vehicles, and applies them to the problem of atmospheric transfer. The attitude of the Apollo-like vehicle can be regulated by a pulsating reaction-control system. Three possible attitude-control concepts are discussed, i.e., gain scheduling, STR and MRAC, in order of mathematical complexity. Each of the controllers was based on a PID-type of control law and

gave satisfactory results, although the STR and MRAC increased the fuel consumption because the required extra signals generated oscillations in the angles of attack and sideslip.

The last of the three control concepts that we discuss here is robust control, or, to be more specific, application of H_∞ , i.e., the minimisation of the ∞ -norm² of some transfer function, and μ controller synthesis and analysis. These types of controller designs were developed for multi-variable feedback systems in the face of uncertainties (Doyle and Stein, 1981), since the performance of feedback systems is then ultimately limited. The name H_∞ refers to the space of stable and proper transfer functions. The objective in H_∞ control is to minimise the ∞ -norm of some transfer function, which will increase the robust stability margin of the system (Shahian and Hassul, 1993).

As is the case with LQG problems, also H_∞ uses a state estimator and feeds back the estimated states. The controller and estimator gains are computed from two Riccati equations. Differences can be found in the coefficients of the Riccati equations, the weights. In principle, transfer-function weights are used to shape the various measures of performance in the frequency domain. In H_∞ -control problems, they are also used to satisfy the so-called *rank* conditions, that are frequently violated in case of inappropriate weights. Proper selection of the weights depends primarily on the experience of the user, and his understanding of the physics of the problem and other engineering constraints. Because of this, H_∞ control is a complex method to apply.

The capturing of both the performance of feedback and uncertainty aspects has been presented by Doyle *et al.* (1982). It involves a generalisation of the ordinary Singular Value Decomposition, and it provides a reliable, non-conservative measure to determine whether both the performance and robustness requirements of a feedback loop are satisfied. This measure is called the Structured Singular Value, denoted by the symbol μ . Necessary and sufficient conditions to handle bounded structured uncertainty, that result from unmodelled system dynamics, are given by Doyle (1985). Since the theory is far too complicated to describe in a nutshell, we suffice by giving the above references and the book by Doyle *et al.* (1992), that gives an excellent introductory treatment of the robust performance problem.

Two applications of H_∞ -control and μ -synthesis are of interest. Doyle *et al.* (1987) apply μ -synthesis to the Space Shuttle lateral axis FCS during re-entry. Their conclusion was that the use of μ is a very promising and powerful tool, if only for analysis. The produced results were very encouraging, and they yielded important information about the performance and robustness of the controllers. The second application concerns attitude control of hypersonic space planes. Since the mid eighties there was an ever-growing interest in guidance and control of space planes. Because of the large flight regime and the uncertainties in the dynamics, the application of robust control to this class of vehicles has been studied by several authors. As an example

² The ∞ -norm of a transfer function $G(s)$ is defined by

$$\|G\|_\infty = \sup_{\omega} |G(j\omega)|$$

where s is the Laplace variable and ω the radial frequency (rad/s). Graphically, the ∞ -norm is simply the peak in the Bode magnitude plot of the transfer function.

we mention the work of Gregory *et al.* (1994). They applied the concepts of H_∞ and μ to a longitudinal model of a winged cone configuration at Mach 8. Their conclusion was that the addition of using μ provides robust performance, much more than H_∞ in itself. Although they restricted to linear analysis, the results are very promising to stimulate further research.

With respect to robust control, we found several references that give comparisons of different control techniques. Grocott *et al.* (1994) make a comparison between 5 different robust-control techniques for uncertain structural systems, i.e., Sensitivity Weighted Linear Quadratic Gaussian, Maximum Entropy, Multiple Model, H_∞ and μ -synthesis. The techniques were evaluated on computational requirements, the degree to which performance suffers from achieving robustness, and the maximum performance that can be experimentally achieved. For their low-order benchmark problem, they found that because of the (very conservative) guarantees of robustness (H_∞), a large performance penalty can result. Compensators based on μ -synthesis are much less conservative than H_∞ designs, but are computationally infeasible for large-order plants, because the order of the control system increases drastically.

Vincent *et al.* (1994) compared the Linear Quadratic Regulator with H_∞ , applied to a lateral-directional control-system design for a Mach = 0.9 flight condition. Both controller designs demonstrated excellent model-following performance, although each of the controllers had some individual strong points. The LQR control law was simpler than the H_∞ one, and could easily be implemented with in-line computer code. For the H_∞ design, some numerical points of concern were identified, i.e., a possible need for increased precision numerical representation (more memory required and a higher CPU load), and the fact that model-order reduction proved to be a delicate numerical problem.

In conclusion, we can state that H_∞ and μ -synthesis have promising features, although there are still practical problems with respect to performance and computational load. Furthermore, the mathematical foundation of both methods is complex and quite some experience is required to develop controllers. For this reason, we will not pursue these methods.

Summarised, we have introduced three different control techniques, in order of increasing complexity:

- 1) Output or state feedback, with the controller parameters (gains) obtained by
 - pole placement, or
 - optimal control theory (LQR).
- 2) Adaptive control, with three of the more common techniques given by
 - Gain scheduling,
 - Self-Tuning Regulation, and
 - Model Reference Adaptive Control.
- 3) Robust control, with two different schemes:
 - H_∞ -control, and
 - μ -synthesis.

Of these three techniques, for reasons of simplicity while still having a reasonable performance, we will select state feedback where we will compute the gains by means of the optimal control

theory. Furthermore, to cope with the large flight regime we will apply gain scheduling. In short, we will apply the Linear Quadratic Regulator with gain scheduling. Despite its old (but also proven) concept, and the introduction of many new control theories and techniques, the LQR is still widely in use, of which many examples can be found in literature (although they do not always focus on aircraft and space vehicles).

Gawronski (1994), for instance, proposes a linear quadratic design procedure for NASA's deep space network antennas, thereby dividing the antenna model into tracking and flexible subsystems and designing controllers for each of these parts separately. (Because of the separation the controller design showed a significant performance improvement.) Furthermore, Collins and Richter (1995) applied a Linear Quadratic Gaussian design as a possibility for the Hubble Space Telescope. The use of this control concept showed that it met all specifications, and that the precise attitude control required for Hubble was possible. Last but not least, we already mentioned the application to the F-8 aircraft. One of the disadvantages of linear state feedback control is its limited robustness in the presence of model uncertainties and non-linearities. Wang and Sundarajan (1995) used the extended linearisation approach together with the LQR, thus removing some of the difficulties of gain scheduling, namely, that the scheduling variable should vary slowly and also that the scheduling variable should capture the plant non-linearity. Their (preliminary) conclusion was that the non-linear controller performed much better than the conventional gain-scheduled controller.

The choice of this control scheme is based on the motivations given at the beginning of this section. Furthermore, to our knowledge this scheme has not been applied to a vehicle like HORUS, although the controller is based on similar control laws provided by MBB (1988b). However, they used pole placement to compute the gains instead of a quadratic cost criterion. Furthermore, the documentation of their controller was not complete (and not published in open literature), and there were no numerical values of the gains available. Last but not least, the design methodology for the LQR will be set up in a general way so that it can also be used for other vehicles and missions, and possibly also for a refinement of the controller design as to increase robustness and performance. In this respect we mention that the design methodology has been applied to a re-entry test vehicle with a triangular cross section, that is controlled only aerodynamically by three aerodynamic surfaces (Mooij *et al.*, 1995).

1.4. Control-system design cycle.

While studying the flight behaviour of conventional aircraft and designing autopilots for this class of vehicles, it is common practice, depending on the type of trajectory, to separate the longitudinal and lateral motion. This is usually allowed, because the two motions are decoupled, i.e., a symmetric manoeuvre only has a marginal effect on the asymmetric motion and vice versa. This decoupling implies a simplification of the autopilot design, and moreover, it gives an increased understanding of the natural aircraft motions.

For similar reasons, it would be useful to do the same for hypersonic vehicles. However, for air-breathing space planes the coupling between engine and aerodynamic effects results in violation of the separability conditions, although aerodynamic effects basically satisfy these

conditions (Sinai, 1990)³. Since the control-system design in this report is focused on an unpowered re-entry vehicle, one might expect that separation of the longitudinal and lateral motion is possible. But, HORUS will fly with a large angle of attack and bank angle, indicating a strong lateral motion, so the question: Is separation still possible? is worth asking.

The design cycle can be divided into a number of successive steps, which will be briefly described below. In Fig. 1.4, we have schematically depicted the design process. Once more, it should be noted that we do not aim at designing the optimal control system for this vehicle and mission. Therefore, some iteration loops which are indicated in Fig. 1.4 will not be executed, although they should be considered when starting from scratch and aiming at the best possible controller. In order to verify the controller and to set up a more general methodology of controller design, we take the following steps:

- 1) We will analyze the full six-degrees-of-freedom (6-d.o.f.) motion of the re-entry vehicle (both symmetric and asymmetric flight). The state of the vehicle is defined by three position variables (modulus of the position vector R , longitude τ and latitude δ), three variables for the velocity (groundspeed V , flight-path angle γ and heading χ), three angular rates (roll rate p , the pitch rate q and the yaw rate r) and three aerodynamic angles for the attitude (the angle of attack α , the angle of sideslip β and the bank angle σ). The corresponding flight-dynamics model consists of 12 first-order differential equations. The related equations are given in Section 2.1.
- 2) The 12 coupled differential equations are non-linear and time varying, which makes it impossible to design the linear state-feedback control system with classical control theory. To apply this theory, the equations of motion have to be linearised and to be made time invariant. To make this process as easy as possible, some assumptions will be made to simplify the starting equations. The linearisation is discussed in Section 2.2.
- 3) To study the open-loop behaviour of the vehicle flying its nominal trajectory, or in other words, the stability of steady flight, the linearised equations of motion have to be written in a special form, the so-called state-space form. This matrix equation will be presented in the final section (2.3) of Chapter 2. The nominal trajectory is divided into a number of discrete points, the so-called time points in which the vehicle is considered to be equilibrium. Per time point, a so-called Linear Time Invariant (LTI) system can be obtained. To address the time-varying character of the re-entry mission, each of the LTI systems will be combined in a series, that serves as the basis for the next step.
- 4) To study the open-loop behaviour of the vehicle it is sufficient to look at the eigenvalues of the system. More complete information about the characteristics modes is provided by

³ The performance of the propulsion system is depending on the angle of attack, in the form of pre-compression of the air with increasing angle of attack. This shows as an increment in the net installed thrust. In a similar manner, flying with a non-zero angle of sideslip will have its effect on the performance, but now in a negative sense. The in-coming airflow in the inlet of the propulsion system can decrease and shock waves can originate. Both phenomena decrease the available thrust. Since the thrust force is one of the major external forces in symmetric motion, the asymmetric angle of sideslip has established a coupling between the symmetric and asymmetric motion.

the corresponding eigenvectors. This so-called eigenmotion is studied in Chapter 3.

- 5) Chapter 4 describes the actual controller design. From the study of the eigenmotion around the nominal trajectory, it appeared that the symmetric and asymmetric motion are decoupled. For this reason, the controller is divided into two parts, i.e., a pitch controller (Section 4.3) and a lateral controller (Section 4.4). For each controller, the corresponding reduced system of equations of motion is discussed, as well as the eigenvalues of this system. Furthermore, the selected control laws and the computation of the feedback gains are presented. The underlying theory for gain computation, i.e., the application of optimal control theory, is given in Section 4.2.
- 6) The verification of the designed controller(s), consisting of three parts, is discussed in Chapter 5. For both the pitch and lateral controller, the response of the closed-loop system to both a step and a ramp input will be considered. Also, the flight along the nominal trajectory with the integrated controller is presented. *Nota bene*: at this place (before testing the controller in the non-linear flight environment), it would be possible to do a sensitivity analysis of the linear model. When the conclusion is that the linear model is not robust enough, a redesign has to be done. This sensitivity analysis is skipped in this report, because we are not doing an optimal design of an attitude controller.

Step 6 marks the end of the design process, as discussed in this report. Since we know from MBB (1988b), that a similarly developed controller gives a fair performance, not further improving the performance of the attitude controller seems a reasonable thing to do. However, the design of a controller is usually not that straightforward. After the feedback-gain computation and some response tests, one might have to go back one or two steps in the design process, as can be seen in Fig. 1.4. It is possible that the time points, which have been selected, are not sufficient to cover the whole trajectory. In that case, more time points need to be selected. On the other hand, it is quite well possible that for none of the time points the required behaviour can be achieved. Then, one has to reconsider the choice of the control laws.

When the two separately developed controllers prove to have done what they are supposed to do, they have to be integrated and cooperate so that the nominal mission for which the controllers were designed, can be simulated. At this stage, we can check whether the simplifying assumptions, which we made during the design process, were justified. Only after successfully completing this test, we can proceed with the next step: a sensitivity analysis, which should give us insight in the behaviour of the vehicle and the controller under other than the nominal conditions. Again, it is possible that we have to redesign the controller. The outcome of the analysis might even imply that a linear state-feedback controller with gain scheduling is not suitable at all. Whether that is the case, remains an open question within the framework of this research.

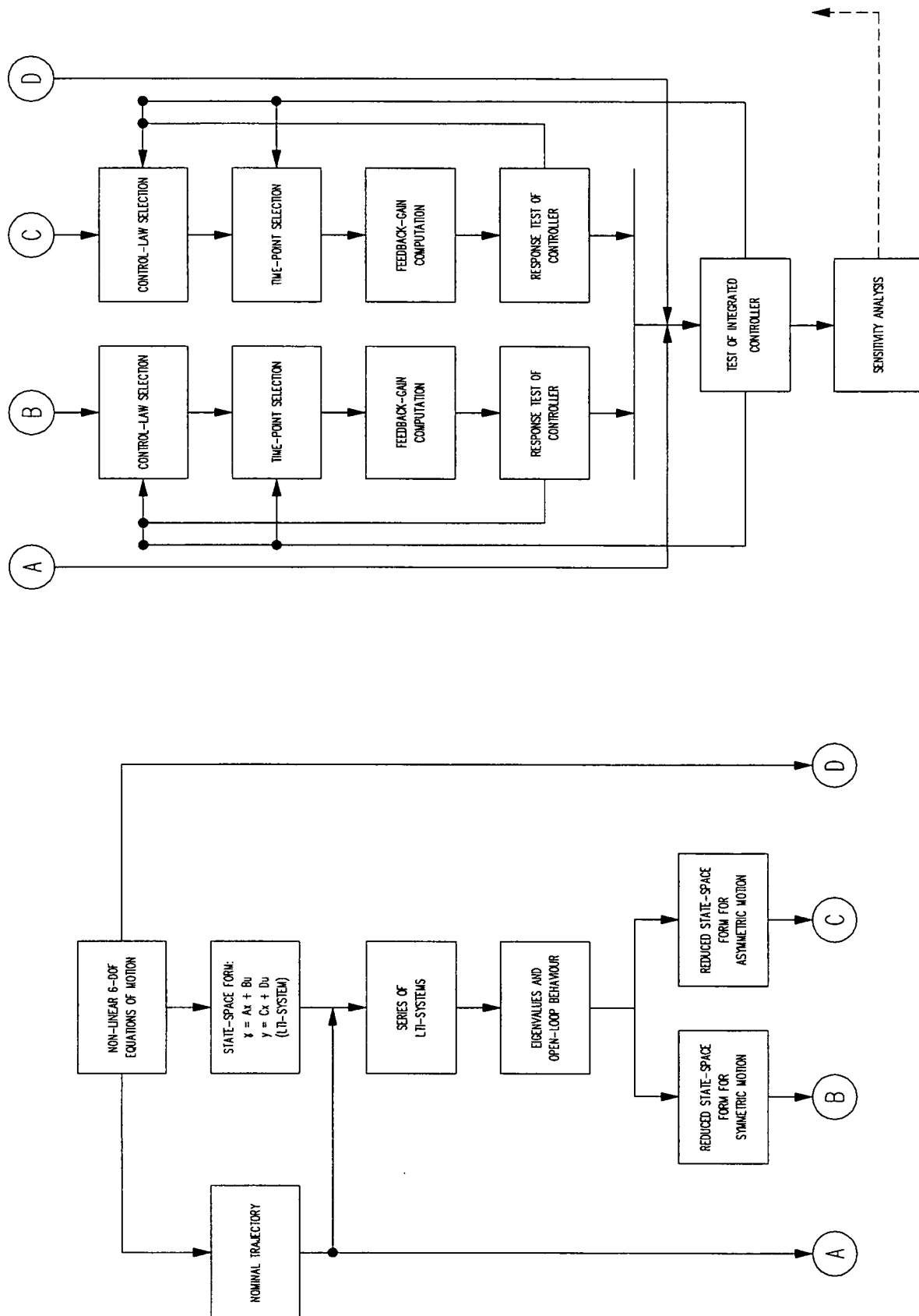


Fig. 1.4 - The design process of the linear state-feedback controller.

Chapter 2

The Motion of a Vehicle in a Planetary Atmosphere

To study the motion of a vehicle in a planetary atmosphere, it is necessary to derive a mathematical model of this motion. Starting with the Laws of Newton, the translational and rotational motion of a vehicle can be described by a system of 12 coupled, first-order differential equations. These (non-linear) differential equations can be numerically integrated to give us the variation of position, velocity, attitude and angular rate with time. The general form of these equations is introduced in Section 2.1. However, to design a state-feedback control system while applying classical control theory, it is necessary that the system of differential equations is linear in all its state variables. This process of linearisation is discussed in Section 2.2. The matrix form of this linearised system, also called the state-space form, is described in Section 2.3. This form enables us in the first place to study the characteristic motion (or open-loop behaviour), and in the second place to design our control system. These topics will be described in Chapters 3 and 4, respectively.

2.1. The general form of the equations of motion.

The control-system design is centred around an unpowered, winged re-entry vehicle. Detailed discussions on the equations of motion of such a vehicle can be found in Mooij (1994a). We will summarise these equations in this section. First, however, we will state the underlying assumptions.

- The Earth is represented as a sphere and is rotating with a constant rotational rate ω_{cb} ,
- The vehicle has a plane of mass symmetry ($X_B Y_B$ -plane), which means that $I_{xy} = I_{yz} = 0$.

In Appendix A, the definition of the state variables can be found.

The dynamic equations of translational motion:

$$\dot{V} = \frac{F_V}{m} + \omega_{cb}^2 R \cos \delta (\sin \gamma \cos \delta - \cos \gamma \sin \delta \cos \chi) \quad (2.1.1a)$$

$$\begin{aligned} V\dot{\gamma} = & \frac{F_\gamma}{m} + 2\omega_{cb} V \cos \delta \sin \chi + \frac{V^2}{R} \cos \gamma + \\ & + \omega_{cb}^2 R \cos \delta (\cos \delta \cos \gamma + \sin \gamma \sin \delta \cos \chi) \end{aligned} \quad (2.1.2a)$$

$$\begin{aligned} V \cos \gamma \dot{\chi} = & \frac{F_\chi}{m} + 2\omega_{cb} V (\sin \delta \cos \gamma - \cos \delta \sin \gamma \cos \chi) + \\ & + \frac{V^2}{R} \cos^2 \gamma \tan \delta \sin \chi + \omega_{cb}^2 R \cos \delta \sin \delta \sin \chi \end{aligned} \quad (2.1.3a)$$

with

$$F_V = -D - mg_\rho \sin \gamma - mg_\delta \cos \gamma \cos \chi \quad (2.1.1b)$$

$$F_\gamma = -S \sin \sigma + L \cos \sigma - mg_\rho \cos \gamma + mg_\delta \sin \gamma \cos \chi \quad (2.1.2b)$$

$$F_\chi = -S \cos \sigma - L \sin \sigma + mg_\delta \sin \chi \quad (2.1.3b)$$

The corresponding kinematic equations:

$$\dot{R} = V \sin \gamma \quad (2.1.4)$$

$$\dot{\tau} = \frac{V \sin \chi \cos \gamma}{R \cos \delta} \quad (2.1.5)$$

$$\dot{\delta} = \frac{V \cos \chi \cos \gamma}{R} \quad (2.1.6)$$

The dynamic equations of rotational motion:

$$\dot{p} = \frac{I_{zz}}{I^*} M_x + \frac{I_{xz}}{I^*} M_z + \frac{(I_{xx} - I_{yy} + I_{zz}) I_{xz}}{I^*} p q + \frac{(I_{yy} - I_{zz}) I_{zz} - I_{xz}^2}{I^*} q r \quad (2.1.7)$$

$$\dot{q} = \frac{M_y}{I_{yy}} + \frac{I_{xz}}{I_{yy}} (r^2 - p^2) + \frac{I_{zz} - I_{xx}}{I_{yy}} p r \quad (2.1.8)$$

$$\dot{r} = \frac{I_{xz}}{I^*} M_x + \frac{I_{xx}}{I^*} M_z + \frac{(I_{xx} - I_{yy})I_{xz} + I_{xz}^2}{I^*} pq + \frac{(-I_{xx} + I_{yy} - I_{zz})I_{xz}}{I^*} qr \quad (2.1.9)$$

with

$$I^* = I_{xx}I_{zz} - I_{xz}^2$$

The corresponding kinematic equations:

$$\begin{aligned} \dot{\alpha} \cos \beta = & -p \cos \alpha \sin \beta + q \cos \beta - r \sin \alpha \sin \beta + \\ & + \sin \sigma [\dot{\chi} \cos \gamma - \dot{\delta} \sin \chi \sin \gamma + (\dot{\tau} + \omega_{cb})(\cos \delta \cos \chi \sin \gamma - \sin \delta \cos \gamma)] + \\ & - \cos \sigma [\dot{\gamma} - \dot{\delta} \cos \chi - (\dot{\tau} + \omega_{cb}) \cos \delta \sin \chi] \end{aligned} \quad (2.1.10)$$

$$\begin{aligned} \dot{\beta} = & p \sin \alpha - r \cos \alpha + \\ & + \sin \sigma [\dot{\gamma} - \dot{\delta} \cos \chi - (\dot{\tau} + \omega_{cb}) \cos \delta \sin \chi] + \\ & + \cos \sigma [\dot{\chi} \cos \gamma - \dot{\delta} \sin \chi \sin \gamma + (\dot{\tau} + \omega_{cb})(\cos \delta \cos \chi \sin \gamma - \sin \delta \cos \gamma)] \end{aligned} \quad (2.1.11)$$

$$\begin{aligned} \dot{\sigma} = & -p \cos \alpha \cos \beta - q \sin \beta - r \sin \alpha \cos \beta + \\ & + \dot{\alpha} \sin \beta - \dot{\chi} \sin \gamma - \dot{\delta} \sin \chi \cos \gamma + (\dot{\tau} + \omega_{cb})(\cos \delta \cos \chi \cos \gamma + \sin \delta \sin \gamma) \end{aligned} \quad (2.1.12)$$

In these equations, $\dot{\gamma}$, $\dot{\chi}$, $\dot{\delta}$ and $\dot{\tau}$ are given by Eqs. (2.1.2) through (2.1.6). Note that the external moment components are expressed in the body-fixed reference frame.

2.2. Linearisation of the equations of motion.

The characteristic motion, or the open-loop behaviour, of a vehicle, is can be described by the eigenvalues and eigenvectors of the equations of motion. However, the eigenvalues and eigenvectors can only be obtained when the time derivatives of the states are given as a linear combination of the states. In other words: the equations of motion have to be linearised. As a result, the motion given by this linearised system should be regarded as an equilibrium trajectory, so that the characteristic motions are small deviations from this nominal path. To simplify the process of linearisation, we will make some assumptions:

- We will consider a non-rotating Earth ($\omega_{cb} = 0$ rad/s), which is allowed since the rotation of the vehicle is of a much higher frequency than the rotation of the Earth. As a result, the Coriolis and centripetal accelerations are zero as well,

- The gravity field of the Earth is assumed to be spherical ($g_\delta = 0 \text{ m/s}^2$). Nota bene: since there is only one component of the gravitational acceleration left, we will omit the subscript 'r'
- The vehicle is assumed to be rotationally symmetric (w.r.t. mass) around the X-axis of the body-fixed reference frame, which means that $I_{xz} = 0$.

With the above assumptions, we can neglect the smaller terms. The resulting equations of motion become:

$$\dot{V} = -\frac{D}{m} - g \sin \gamma \quad (2.2.1)$$

$$\dot{\gamma} = \left(\frac{V}{R} - \frac{g}{V} \right) \cos \gamma + \frac{(L \cos \sigma - S \sin \sigma)}{m V} \quad (2.2.2)$$

$$\dot{\chi} = \frac{V}{R} \cos \gamma \tan \delta \sin \chi - \frac{(L \sin \sigma + S \cos \sigma)}{m V \cos \gamma} \quad (2.2.3)$$

$$\dot{R} = V \sin \gamma \quad (2.2.4)$$

$$\dot{\tau} = \frac{V \cos \gamma \sin \chi}{R \cos \delta} \quad (2.2.5)$$

$$\dot{\delta} = \frac{V}{R} \cos \gamma \cos \chi \quad (2.2.6)$$

$$\dot{p} = \frac{M_x}{I_{xx}} + (I_{yy} - I_{zz}) q r \quad (2.2.7)$$

$$\dot{q} = \frac{M_y}{I_{yy}} + (I_{zz} - I_{xx}) p r \quad (2.2.8)$$

$$\dot{r} = \frac{M_z}{I_{zz}} + (I_{xx} - I_{yy}) p q \quad (2.2.9)$$

Since the kinematic attitude equations are very complex, we will introduce another simplification. We assume that the vehicle's attitude is only marginally influenced by an asymmetric translational motion, or in other words: we assume that the vehicle's trajectory is parallel to the equator ($\delta = 0^\circ$ and $\chi = 90^\circ$), and remains that way ($\dot{\delta} = 0 \text{ rad/s}$), see also MBB (1988b).

$$\dot{\alpha} = q - (p \cos \alpha + r \sin \alpha) \tan \beta - \frac{L - mg \cos \gamma \cos \sigma}{m V \cos \beta} \quad (2.2.10)$$

$$\dot{\beta} = p \sin \alpha - r \cos \alpha - \frac{S + mg \cos \gamma \sin \sigma}{mV} \quad (2.2.11)$$

$$\dot{\sigma} = -\frac{p \cos \alpha + r \sin \alpha}{\cos \beta} - \tan \beta \frac{L - mg \cos \gamma \cos \sigma}{mV} + \tan \gamma \frac{L \sin \sigma + S \cos \sigma}{mV} \quad (2.2.12)$$

As we can see, the equations for χ , τ and δ are not coupled to the rest of the equations, so a 9-d.o.f. linearised model for the state space formed by V , γ , R , p , q , r , α , β and σ can be derived.

The linearisation is performed as follows. We assume an equilibrium value of each of the state variables (index 0), and we will look at small deviations from this equilibrium state. Note that the vehicle is not powered (no fuel consumption), so the mass properties are constant. So:

$$\begin{aligned} V &= V_0 + \Delta V \\ \gamma &= \gamma_0 + \Delta \gamma \\ R &= R_0 + \Delta R \\ p &= p_0 + \Delta p \\ q &= q_0 + \Delta q \\ r &= r_0 + \Delta r \\ \alpha &= \alpha_0 + \Delta \alpha \\ \beta &= \beta_0 + \Delta \beta = \Delta \beta \\ \sigma &= \sigma_0 + \Delta \sigma \end{aligned} \quad (2.2.13)$$

The nominal position, velocity and corresponding control history follow from the nominal trajectory, which leaves us with three unknowns p_0 , q_0 and r_0 . However, since we want no perturbation of the nominal control (α_0 and σ_0) when we are flying the vehicle, we can compute the equilibrium angular rates from the condition

$$\dot{\alpha} = \dot{\beta} = \dot{\sigma} = 0$$

or, using Eqs. (2.2.10-12),

$$q_0 = \frac{L_0}{mV_0} - \frac{g_0}{V_0} \cos \gamma_0 \cos \sigma_0 \quad (2.2.14)$$

$$p_0 \sin \alpha_0 - r_0 \cos \alpha_0 = \frac{g_0}{V_0} \cos \gamma_0 \sin \sigma_0 \quad (2.2.15)$$

$$p_0 \cos \alpha_0 + r_0 \sin \alpha_0 = \frac{L_0}{mV_0} \tan \gamma_0 \sin \sigma_0 \quad (2.2.16)$$

Solving for p_0 , q_0 and r_0 gives us

$$p_0 = c_1 \sin \alpha_0 + c_2 \cos \alpha_0 \quad (2.2.17)$$

$$q_0 = \frac{L_0}{m V_0} - \frac{g_0}{V_0} \cos \gamma_0 \cos \sigma_0 \quad (2.2.18)$$

$$r_0 = -c_1 \cos \alpha_0 + c_2 \sin \alpha_0 \quad (2.2.19)$$

with

$$c_1 = \frac{g_0}{V_0} \cos \gamma_0 \sin \sigma_0$$

$$c_2 = \frac{L_0}{m V_0} \tan \gamma_0 \sin \sigma_0$$

Note that since $\beta_0 = 0$, also $S_0 = 0$.

Substituting expressions Eq. (2.2.13) in Eqs. (2.2.1-12), neglecting higher-order terms such as $\Delta V \Delta \gamma$, $p_0 \Delta \alpha^4$, etc., and subtracting the nominal state (i.e., $\dot{V}_0 = \dots$, etc.) results in the following 9 first-order differential equations:

$$\Delta \dot{V} = -\frac{\Delta D}{m} + 2 \frac{g_0}{R_0} \sin \gamma_0 \Delta R - g_0 \cos \gamma_0 \Delta \gamma \quad (2.2.20)$$

$$\begin{aligned} \Delta \dot{\gamma} = & \left(-\dot{\gamma}_0 + \frac{2 V_0}{R_0} \cos \gamma_0 \right) \frac{\Delta V}{V_0} + \left(\frac{2 g_0}{R_0} - \frac{V_0^2}{R_0^2} \right) \frac{\cos \gamma_0}{V_0} \Delta R - \left(\frac{V_0^2}{R_0} - g_0 \right) \frac{\sin \gamma_0}{V_0} \Delta \gamma + \\ & - \frac{L_0}{m V_0} \sin \sigma_0 \Delta \sigma + \frac{\cos \sigma_0}{m V_0} \Delta L - \frac{\sin \sigma_0}{m V_0} \Delta S \end{aligned} \quad (2.2.21)$$

$$\Delta \dot{R} = \sin \gamma_0 \Delta V + V_0 \cos \gamma_0 \Delta \gamma \quad (2.2.22)$$

$$\Delta \dot{p} = \frac{\Delta M_x}{I_{xx}} \quad (2.2.23)$$

⁴ The nominal rotational rates p_0 , q_0 and r_0 are small, and can therefore be treated as perturbations themselves.

$$\Delta \dot{q} = \frac{\Delta M_y}{I_{yy}} \quad (2.2.24)$$

$$\Delta \dot{r} = \frac{\Delta M_z}{I_{zz}} \quad (2.2.25)$$

$$\begin{aligned} \Delta \dot{\alpha} = & \Delta q - \frac{1}{m V_0} \Delta L - \frac{g_0}{V_0} \cos \gamma_0 \sin \sigma_0 \Delta \sigma + \left(\frac{L_0}{m V_0^2} - \frac{g_0}{V_0^2} \cos \gamma_0 \cos \sigma_0 \right) \Delta V + \\ & - \frac{g_0}{V_0} \sin \gamma_0 \cos \sigma_0 \Delta \gamma - \frac{2 g_0}{R_0 V_0} \cos \gamma_0 \cos \sigma_0 \Delta R \end{aligned} \quad (2.2.26)$$

$$\begin{aligned} \Delta \dot{\beta} = & \sin \alpha_0 \Delta p - \cos \alpha_0 \Delta r - \frac{\Delta S}{m V_0} - \frac{g_0}{V_0} \cos \gamma_0 \cos \sigma_0 \Delta \sigma + \frac{g_0}{V_0^2} \cos \gamma_0 \sin \sigma_0 \Delta V + \\ & + \frac{2 g_0}{R_0 V_0} \cos \gamma_0 \sin \sigma_0 \Delta R + \frac{g_0}{V_0} \sin \gamma_0 \sin \sigma_0 \Delta \gamma \end{aligned} \quad (2.2.27)$$

$$\begin{aligned} \Delta \dot{\sigma} = & -\cos \alpha_0 \Delta p - \sin \alpha_0 \Delta r - \left(\frac{L_0}{m V_0} - \frac{g_0}{V_0} \cos \gamma_0 \cos \sigma_0 \right) \Delta \beta + \frac{L_0}{m V_0} \sin \sigma_0 \Delta \gamma + \\ & + \frac{\tan \gamma_0}{m V_0} \left(\sin \sigma_0 \Delta L + \cos \sigma_0 L_0 \Delta \sigma + \cos \sigma_0 \Delta S - \frac{L_0}{V_0} \sin \sigma_0 \Delta V \right) \end{aligned} \quad (2.2.28)$$

In deriving the above equations, we have used the definition of the gravitational acceleration

$$g = \frac{\mu}{R^2}$$

which gives us

$$g_0 + \Delta g = \frac{\mu}{(R_0 + \Delta R)^2} = \frac{\mu}{R_0^2} \frac{1}{\left(1 + 2 \frac{\Delta R}{R_0}\right)} \approx \frac{\mu}{R_0^2} \left(1 - 2 \frac{\Delta R}{R_0}\right)$$

or

$$\Delta g = -2 g_0 \frac{\Delta R}{R_0}$$

Now that we have linearised the equations of motion, we can write them in matrix form, also called the state-space form. This will be described in the following section.

2.3. The state-space form of the equations of motion.

When equations of motion are written in state-space form, they have the following form in matrix notation:

$$\dot{\mathbf{x}} = \mathbf{A}\mathbf{x} + \mathbf{B}\mathbf{u} \quad (2.3.1a)$$

with \mathbf{x} an $n \times 1$ state vector, \mathbf{u} a $q \times 1$ control vector, and \mathbf{A} and \mathbf{B} the $n \times n$ state (or system) and $n \times q$ control coefficient matrices, respectively. Eq. (2.3.1a) is called the dynamics equation; to complete the description of the state of the vehicle we also need a so-called output equation:

$$\mathbf{y} = \mathbf{C}\mathbf{x} + \mathbf{D}\mathbf{u} \quad (2.3.1b)$$

In the above equation, \mathbf{y} is the $m \times 1$ output vector, and \mathbf{C} and \mathbf{D} are the $m \times n$ output and $m \times q$ direct transmission matrices, respectively. For the time being, we will restrict ourselves to the use of Eq. (2.3.1a).

To write Eqs. (2.2.20-28) in state-space form, we must distinguish between state variables and control variables. The choice of state variables is obvious, if we look at the original equations of motion with their state variables. We write

$$\mathbf{x} = (\Delta V, \Delta \gamma, \Delta R, \Delta p, \Delta q, \Delta r, \Delta \alpha, \Delta \beta, \Delta \sigma)^T$$

The selection of control variables is less clear. The principle of control is obvious: by changing the magnitude and direction of external forces (and therefore in principle also the external moments), the trajectory of the vehicle can be changed. As we mentioned in Chapter 1, the guidance system makes sure that the vehicle will follow its nominal trajectory by adjusting the angle of attack and bank angle, the control variables of the guidance system. These control variables determine the size and direction of the aerodynamic force vector, the only controllable external force acting on the unpowered vehicle. (The other external force is of gravitational origin; this force is depending on the position of the vehicle and cannot be controlled actively.)

The attitude controller has to guarantee that the commanded attitude is obtained (and maintained) with a certain accuracy in a finite time, which means that eventually there should be moment equilibrium. Note that the actual angle of attack and bank angle are given by the kinematic equations, which means that they have defined values depending on the rotation of the vehicle and thus the size and direction of the external moments. So whereas the forces acting on the centre of mass (c.o.m.) of the vehicle are the guidance control variables, the moments around the c.o.m. are the attitude control variables.

Inspecting the equations of motion, we find beside the three force components ΔD , ΔS and

ΔL , three moment components, i.e., ΔM_x , ΔM_y and ΔM_z . Part of the moment components is determined by the vehicle, depending on its actual attitude. However, the remaining part is given (and can be changed) by, for instance, aerodynamic control surfaces, reaction control thrusters and momentum wheels, depending on the vehicle configuration and sub-systems. So for the selection of the attitude-control effectors, we must have a closer look at the vehicle, the HORUS-2B. MBB (1988a) presents this vehicle as winged, without a major propulsion system, but with 5 aerodynamic control surfaces (two rudders, two wing flaps⁵ and a body flap) and a number of reaction control thrusters. The body flap is only used for trim, and does not have to be considered as a control. The two wing flaps, or elevons, can be deflected symmetrically (elevator function) and asymmetrically (aileron function). The rudders are outward movable only, and only one at a time.

It should be noted that by deflecting the control surfaces, an aerodynamic force is generated that gives a moment around the vehicle's c.o.m. depending on the moment arm, the distance to the c.o.m.. The deflection of a surface is in principle an analogous process, of course with a limited accuracy, which means that the generated moments are a continuous function of the deflection angle, as well as of flight and similarity parameters, such as the Mach number.

The reaction control system is only being used when the aerodynamic control surfaces are not sufficiently effective, e.g., in the upper layers of the atmosphere. The aerodynamic control surfaces are activated when their effectiveness is more than 10% of that of the corresponding thrusters and the thrusters are inhibited when their effectiveness is less than 10% of the corresponding aerodynamic surface⁶. Whereas the aerodynamic control moments are continuous functions, this is not the case with the reaction control moments. The principle of a thruster is that it is either ON or OFF. When it is on, it will generate a constant thrust force that will also result in a constant moment⁷. By switching the thrusters on and off repeatedly (so-called pulsing), the required moment can be approximated. Furthermore, in case there are more thrusters for generating moments about one particular axis, the magnitude of the moment can be varied by smartly combining the required thrusters. In this study, however, we will assume continuous reaction control moments, for reasons of simplicity. Besides, we will directly use the moments as control variables, instead of the thrust forces.

So, summarised we can write for the control vector u :

⁵ To be more in line with other literature, we will not use the term *wing flaps*, but *elevons* since this control surface combines the elevator and aileron function.

⁶ For the defined configuration of HORUS-2B, the maximal torque of the pitch thrusters is 10,400 Nm, the one of the roll thrusters is 1,600 Nm and the one of the yaw thrusters is 7,600 Nm. This results in activating the aerodynamic control surfaces at approximately 100 km and switching off the roll thrusters at about 75 km, while the yaw thrusters remain activated until the end of the descent.

⁷ The thrust force is in principle depending on the atmospheric conditions, which change significantly during the flight. Since we do not have extended thruster models at our disposal, we will assume constant thrust forces. However, it is known from the experience with the Space Shuttle that the operation of the reaction control thrusters can be significantly influenced by atmospheric conditions. Future models should take this effect into account so that the influence on attitude control can be studied.

$$\mathbf{u} = (\Delta\delta_e, \Delta\delta_a, \Delta\delta_r, \Delta T_x, \Delta T_y, \Delta T_z)^T$$

with

- δ_e = elevator deflection angle (rad)
- δ_a = aileron deflection angle (rad)
- δ_r = rudder deflection angle (rad)
- T_x = roll-thruster moment (Nm)
- T_y = pitch-thruster moment (Nm)
- T_z = yaw-thruster moment (Nm)

These definitions of \mathbf{x} and \mathbf{u} results in the following state-space matrix equation:

$$\begin{pmatrix} \Delta \dot{V} \\ \Delta \dot{\gamma} \\ \Delta \dot{R} \\ \Delta \dot{p} \\ \Delta \dot{q} \\ \Delta \dot{r} \\ \Delta \dot{\alpha} \\ \Delta \dot{\beta} \\ \Delta \dot{\sigma} \end{pmatrix} = \begin{bmatrix} a_{VV} & a_{V\gamma} & a_{VR} & a_{Vp} & a_{Vq} & a_{Vr} & a_{V\alpha} & a_{V\beta} & a_{V\sigma} \\ a_{\gamma V} & a_{\gamma\gamma} & a_{\gamma R} & a_{\gamma p} & a_{\gamma q} & a_{\gamma r} & a_{\gamma\alpha} & a_{\gamma\beta} & a_{\gamma\sigma} \\ a_{RV} & a_{R\gamma} & a_{RR} & a_{Rp} & a_{Rq} & a_{Rr} & a_{R\alpha} & a_{R\beta} & a_{R\sigma} \\ a_{pV} & a_{p\gamma} & a_{pR} & a_{pp} & a_{pq} & a_{pr} & a_{p\alpha} & a_{p\beta} & a_{p\sigma} \\ a_{qV} & a_{q\gamma} & a_{qR} & a_{qp} & a_{qq} & a_{qr} & a_{q\alpha} & a_{q\beta} & a_{q\sigma} \\ a_{rV} & a_{r\gamma} & a_{rR} & a_{rp} & a_{rq} & a_{rr} & a_{r\alpha} & a_{r\beta} & a_{r\sigma} \\ a_{\alpha V} & a_{\alpha\gamma} & a_{\alpha R} & a_{\alpha p} & a_{\alpha q} & a_{\alpha r} & a_{\alpha\alpha} & a_{\alpha\beta} & a_{\alpha\sigma} \\ a_{\beta V} & a_{\beta\gamma} & a_{\beta R} & a_{\beta p} & a_{\beta q} & a_{\beta r} & a_{\beta\alpha} & a_{\beta\beta} & a_{\beta\sigma} \\ a_{\sigma V} & a_{\sigma\gamma} & a_{\sigma R} & a_{\sigma p} & a_{\sigma q} & a_{\sigma r} & a_{\sigma\alpha} & a_{\sigma\beta} & a_{\sigma\sigma} \end{bmatrix} \begin{pmatrix} \Delta V \\ \Delta \gamma \\ \Delta R \\ \Delta p \\ \Delta q \\ \Delta r \\ \Delta \alpha \\ \Delta \beta \\ \Delta \sigma \end{pmatrix} + \begin{bmatrix} b_{Ve} & b_{Va} & b_{Vr} & b_{Vx} & b_{Vy} & b_{Vz} \\ b_{\gamma e} & b_{\gamma a} & b_{\gamma r} & b_{\gamma x} & b_{\gamma y} & b_{\gamma z} \\ b_{Re} & b_{Ra} & b_{Rr} & b_{Rx} & b_{Ry} & b_{Rz} \\ b_{pe} & b_{pa} & b_{pr} & b_{px} & b_{py} & b_{pz} \\ b_{qe} & b_{qa} & b_{qr} & b_{qx} & b_{qy} & b_{qz} \\ b_{re} & b_{ra} & b_{rr} & b_{rx} & b_{ry} & b_{rz} \\ b_{\alpha e} & b_{\alpha a} & b_{\alpha r} & b_{\alpha x} & b_{\alpha y} & b_{\alpha z} \\ b_{\beta e} & b_{\beta a} & b_{\beta r} & b_{\beta x} & b_{\beta y} & b_{\beta z} \\ b_{\sigma e} & b_{\sigma a} & b_{\sigma r} & b_{\sigma x} & b_{\sigma y} & b_{\sigma z} \end{bmatrix} \begin{pmatrix} \Delta\delta_e \\ \Delta\delta_a \\ \Delta\delta_r \\ \Delta T_x \\ \Delta T_y \\ \Delta T_z \end{pmatrix} \quad (2.3.2)$$

Before we derive the 135 matrix elements a_{ij} and b_{ij} , one more task remains to be done as we already indicated above: the evaluation of the force and moment variations in Eqs. (2.2.17-25), i.e., ΔD , ΔS , ΔL , ΔM_x , ΔM_y , ΔM_z , as a function of state and control variables. Starting with ΔD , we must first study the aerodynamic database of the HORUS-2B to find the dependency of drag D on flight parameters and deflection angles. We find:

$$D = f(M, \alpha, h, \delta_w, \delta_r, \delta_b)$$

with

- M = Mach number (-)
- α = angle of attack (rad)
- h = height (m)
- δ_w = elevon deflection angle (rad)
- δ_r = rudder deflection angle (rad)
- δ_b = body-flap deflection angle (rad)

Note that, as we mentioned before, the elevons perform the function of elevator and aileron, so for our derivations we need to replace δ_w by δ_e and δ_a .

ΔD can be written as

$$\Delta D = \frac{\partial D}{\partial M} \Delta M + \frac{\partial D}{\partial \alpha} \Delta \alpha + \frac{\partial D}{\partial h} \Delta h + \frac{\partial D}{\partial \delta_e} \Delta \delta_e + \frac{\partial D}{\partial \delta_a} \Delta \delta_a + \frac{\partial D}{\partial \delta_r} \Delta \delta_r + \frac{\partial D}{\partial \delta_b} \Delta \delta_b \quad (2.3.3)$$

To evaluate the partial derivatives, we write D as

$$D = C_D q_{dyn} S_{ref} \quad (2.3.4)$$

with

- C_D = drag coefficient = $f(M, \alpha, h, \delta_r, \delta_w, \delta_b)$
- $q_{dyn} = \frac{1}{2} \rho V^2$ = dynamic pressure (N/m²) = $f(h, V)$
- S_{ref} = reference area (m²)

The height dependency of the drag coefficient is only apparent for Mach numbers smaller than 1.5, and is small compared with the dependencies on Mach number and angle of attack. The body flap is only used for trim, so it has a nominal deflection angle only ($\Delta \delta_b = 0$). What remains are the contributions due to the elevators, ailerons and rudder. Since we are looking at corrective control only (the deflection angles are in principal in the order of a few degrees), and the contribution to the drag is small compared with the nominal drag, we will neglect these terms⁸. Eq. (2.3.3) simplifies to

$$\Delta D = \frac{\partial D}{\partial M} \Delta M + \frac{\partial D}{\partial \alpha} \Delta \alpha \quad (2.3.5)$$

Evaluating the first term on the right-hand side of Eq. (2.3.5) yields

⁸ Due to a similar reasoning the contribution of the elevons to the lift force, as compared to the nominal lift force, can be neglected as well.

$$\frac{\partial D}{\partial M} = \frac{\partial C_D}{\partial M} q_{dyn} S_{ref} + \frac{\partial q_{dyn}}{\partial M} C_D S_{ref} \quad (2.3.6)$$

Applying the definition of the Mach number,

$$M = \frac{V}{a} \quad (2.3.7)$$

with

a = speed of sound (m/s)

we obtain

$$\frac{\partial q_{dyn}}{\partial M} = \frac{1}{2} \frac{\partial (\rho M^2 a^2)}{\partial M} = \rho_0 a_0^2 M_0 = \frac{\rho_0 V_0^2}{M_0} = \frac{2 q_{dyn_0}}{M_0} \quad (2.3.8)$$

Furthermore,

$$\Delta M = \Delta \left(\frac{V}{a} \right) = \frac{1}{a_0} \Delta V = \frac{M_0}{V_0} \Delta V \quad (2.3.9)$$

In the above derivation, we have assumed that the variation of the speed of sound, which is a function of temperature (and thus altitude), is small and can be neglected with respect to other terms.

The second term on the right-hand side of Eq. (2.3.5) is easily derived as

$$\frac{\partial D}{\partial \alpha} = q_{dyn_0} S_{ref} \frac{\partial C_D}{\partial \alpha}$$

Summarising, we get for ΔD :

$$\Delta D = \left(\frac{M_0}{V_0} \frac{\partial C_D}{\partial M} + \frac{2 C_D}{V_0} \right) q_{dyn_0} S_{ref} \Delta V + \frac{\partial C_D}{\partial \alpha} q_{dyn_0} S_{ref} \Delta \alpha \quad (2.3.10)$$

The side force S is a function of M , α , β , δ_e , δ_a and δ_r . Again, we neglect the contribution due to the control surfaces, which results in

$$\Delta S = \frac{\partial S}{\partial M} \Delta M + \frac{\partial S}{\partial \alpha} \Delta \alpha + \frac{\partial S}{\partial \beta} \Delta \beta \quad (2.3.11)$$

Evaluating all the terms in a similar way as above, we get for ΔS :

$$\Delta S = \frac{\partial C_S}{\partial \beta} q_{dyn_0} S_{ref} \Delta \beta \quad (2.3.12)$$

Note that $C_S = 0$ for $\beta = \beta_0 = 0^\circ$, which is also true for the derivatives w.r.t. M and α evaluated at β_0 .

For ΔL we find

$$\Delta L = \left(\frac{M_0}{V_0} \frac{\partial C_L}{\partial M} + \frac{2 C_L}{V_0} \right) q_{dyn_0} S_{ref} \Delta V + \frac{\partial C_L}{\partial \alpha} q_{dyn_0} S_{ref} \Delta \alpha \quad (2.3.13)$$

The variation of the moments consist of an aerodynamic and a propulsive component, i.e.,

$$\Delta M_x = \Delta L' + \Delta T_x \quad (2.3.14a)$$

$$\Delta M_y = \Delta M' + \Delta T_y \quad (2.3.14b)$$

$$\Delta M_z = \Delta N' + \Delta T_z \quad (2.3.14c)$$

with

L' = aerodynamic roll moment (Nm)

M' = aerodynamic pitch moment (Nm)

N' = aerodynamic yaw moment (Nm)

Only the aerodynamic contributions have to be expanded to a state-variable and control-variable contribution, because the thruster moments are already control variables.

We will apply the same way of derivation as for the aerodynamic forces, with one difference. In this case, the contributions of the control surfaces cannot be neglected, because of their relative magnitude. Besides, if we did, it would reduce the means of control to reaction control only. After inspecting the aerodynamic database, we find that the ailerons contribute to both the roll and yaw moment, the elevators to the pitch moment and the rudder to the yaw moment. Furthermore, we found that there are no dynamic damping terms included in the definition of the moments as is usual the case, i.e.,

$$C_{l_p} = C_{m_q} = C_{n_r} = 0$$

In case of HORUS, it was mentioned that they had not been computed, but that does not mean that they are zero, as we know from a similar vehicle, the Space Shuttle (Trujillo, 1986). How-

ever, if we want to take the damping terms into account in the derivation, so that the model does not have to be expanded once these terms become available, or when we want to apply the model to another vehicle, we will see that in this case the related terms will vanish. In the previous section it was stated that the rotational rates are small, and can be treated in a similar manner as the variations ΔV , $\Delta\beta$, etc. This means that when we derive the small variation around a nominal damping term like

$$C_{l_p} \frac{\rho_0 b_{ref}}{2 V_0} q_{dyn_0} S_{ref} b_{ref}$$

the result is a second-order term and can be neglected. Therefore, the damping terms do not have to be included in our derivation. However, when the rotational rates p_0 , q_0 and r_0 are not small and can consequently not be neglected, the damping terms *will* appear in the model.

As a result, with the aerodynamic moments given by

$$L' = C_l q_{dyn} S_{ref} b_{ref}$$

$$M' = C_m q_{dyn} S_{ref} c_{ref}$$

$$N' = C_n q_{dyn} S_{ref} b_{ref}$$

we get

$$\Delta L' = \frac{\partial C_l}{\partial \beta} q_{dyn_0} S_{ref} b_{ref} \Delta\beta + \frac{\partial C_l}{\partial \delta_a} q_{dyn_0} S_{ref} b_{ref} \Delta\delta_a \quad (2.3.15)$$

$$\begin{aligned} \Delta M' = & \frac{M_0}{V_0} \frac{\partial C_m}{\partial M} q_{dyn_0} S_{ref} c_{ref} \Delta V + \frac{\partial C_m}{\partial \alpha} q_{dyn_0} S_{ref} c_{ref} \Delta\alpha + \\ & + \frac{\partial C_m}{\partial \delta_e} q_{dyn_0} S_{ref} c_{ref} \Delta\delta_e \end{aligned} \quad (2.3.16)$$

$$\Delta N' = \frac{\partial C_n}{\partial \beta} q_{dyn_0} S_{ref} b_{ref} \Delta\beta + \frac{\partial C_n}{\partial \delta_r} q_{dyn_0} S_{ref} b_{ref} \Delta\delta_r + \frac{\partial C_n}{\partial \delta_a} q_{dyn_0} S_{ref} b_{ref} \Delta\delta_a \quad (2.3.17)$$

Note that the nominal pitch coefficient $C_m = 0$ for trimmed flight. We will assume that trim is always guaranteed. This can be verified in the next chapter, when we introduce the nominal trajectory.

Finally, after substituting Eqs. (2.3.10), (2.3.12-13) and (2.3.15-17) in Eqs. (2.2.20-28) and rearranging terms, we find expressions for each of the coefficients a_{ij} and b_{ik} . These expressions are given in Appendix B. The obtained stability model, which has the desired form of Eq. (2.3.1),

$$\dot{\mathbf{x}} = \mathbf{Ax} + \mathbf{Bu}$$

or, fully written out:

$$\begin{pmatrix} \Delta \dot{V} \\ \Delta \dot{\gamma} \\ \Delta \dot{R} \\ \Delta \dot{p} \\ \Delta \dot{q} \\ \Delta \dot{r} \\ \Delta \dot{\alpha} \\ \Delta \dot{\beta} \\ \Delta \dot{\sigma} \end{pmatrix} = \begin{bmatrix} a_{VV} & a_{V\gamma} & a_{VR} & 0 & 0 & 0 & a_{V\alpha} & 0 & 0 \\ a_{\gamma V} & a_{\gamma\gamma} & a_{\gamma R} & 0 & 0 & 0 & a_{\gamma\alpha} & a_{\gamma\beta} & a_{\gamma\sigma} \\ a_{RV} & a_{R\gamma} & 0 & 0 & 0 & 0 & 0 & 0 & 0 \\ 0 & 0 & 0 & 0 & 0 & 0 & 0 & a_{p\beta} & 0 \\ a_{qV} & 0 & 0 & 0 & 0 & 0 & a_{q\alpha} & 0 & 0 \\ 0 & 0 & 0 & 0 & 0 & 0 & 0 & a_{r\beta} & 0 \\ a_{\alpha V} & a_{\alpha\gamma} & a_{\alpha R} & 0 & a_{\alpha q} & 0 & a_{\alpha\alpha} & 0 & a_{\alpha\sigma} \\ a_{\beta V} & a_{\beta\gamma} & a_{\beta R} & a_{\beta p} & 0 & a_{\beta r} & 0 & a_{\beta\beta} & a_{\beta\sigma} \\ a_{\sigma V} & a_{\sigma\gamma} & 0 & a_{\sigma p} & 0 & a_{\sigma r} & a_{\sigma\alpha} & a_{\sigma\beta} & a_{\sigma\sigma} \end{bmatrix} \begin{pmatrix} \Delta V \\ \Delta \gamma \\ \Delta R \\ \Delta p \\ \Delta q \\ \Delta r \\ \Delta \alpha \\ \Delta \beta \\ \Delta \sigma \end{pmatrix} + \begin{bmatrix} 0 & 0 & 0 & 0 & 0 & 0 \\ 0 & 0 & 0 & 0 & 0 & 0 \\ 0 & 0 & 0 & 0 & 0 & 0 \\ 0 & b_{pa} & 0 & b_{px} & 0 & 0 \\ b_{qe} & 0 & 0 & 0 & b_{qy} & 0 \\ 0 & b_{ra} & b_{rr} & 0 & 0 & b_{rz} \\ 0 & 0 & 0 & 0 & 0 & 0 \\ 0 & 0 & 0 & 0 & 0 & 0 \\ 0 & 0 & 0 & 0 & 0 & 0 \end{bmatrix} \begin{pmatrix} \Delta \delta_e \\ \Delta \delta_a \\ \Delta \delta_r \\ \Delta T_x \\ \Delta T_y \\ \Delta T_z \end{pmatrix} \quad (2.3.18)$$

can now be used to study the open-loop behaviour of the vehicle. This will be described in the next chapter.

Chapter 3

Open-loop Behaviour of the Re-entry Vehicle

3.1. Introduction.

The system of equations, Eq. (2.3.18), is a time-varying system. In order to apply classical control theory, we will discretise the nominal trajectory into a number of time intervals. During each of the intervals, the state of the vehicle and other system parameters are assumed to be constant. For each of the time points, the system can be investigated. By linearising the equations of motion and discretising the trajectory, the overall system has been divided into a sequence of Linear Time-Invariant systems (LTI systems).

The part

$$\dot{\mathbf{x}} = \mathbf{A}\mathbf{x} \quad (3.1.1)$$

is known as the homogeneous part of the state equation, with which we can study the free response (also called open-loop behaviour, characteristic motion or eigenmotion) of the system. The eigenvalues λ of state matrix \mathbf{A} and the corresponding eigenvectors $\boldsymbol{\mu}$ can be computed from the following equation:

$$\mathbf{A}\boldsymbol{\mu} = \lambda\boldsymbol{\mu} \quad (3.1.2)$$

This equation can be solved by

$$\mathbf{A}\boldsymbol{\mu} - \lambda\boldsymbol{\mu} = (\mathbf{A} - \lambda\mathbf{I})\boldsymbol{\mu} = 0 \quad (3.1.3)$$

The condition for a non-trivial solution is

$$|\mathbf{A} - \lambda\mathbf{I}| = 0 \quad (3.1.4)$$

Standard algorithms are available to calculate the eigenvalues and corresponding eigenvectors of a given matrix \mathbf{A} (Press *et al.*, 1990). The mathematical foundation of these algorithms is considered to be beyond the scope of this report.

With λ and μ , the eigenmotion $\mathbf{x}_\lambda(t)$ of the re-entry vehicle follows from (Kuo, 1987):

$$\mathbf{x}_\lambda(t) = e^{\lambda t} \mu \quad (3.1.5)$$

Since we are dealing with a linear system of 9 coupled equations, Eq. (3.1.5) gives only one solution. The general form is, because of the linearity of the system, written as

$$\mathbf{x}_\lambda(t) = \sum_{i=1}^9 c_i e^{\lambda_i t} \mu_i \quad (3.1.6)$$

The constants c_i can be computed from specified initial conditions $\mathbf{x}(0)$, for instance an initial perturbation in the nominal angle of attack.

The eigenmotion given by Eq. (3.1.6) will be discussed in Section 3.3. First, in the next Section 3.2, the nominal trajectory is introduced.

3.2. Nominal trajectory.

The design of the control system is centred around a nominal reference trajectory. Such a reference trajectory is usually the result of an optimisation process, taking mission requirements, performance criteria and trajectory constraints into account. Unfortunately, we neither have a reference trajectory nor an optimisation program at hand, so we must generate one ourselves. MBB (1988b) gives a nominal control history of α and σ as a function of time. With this control history as guidance output and applying ideal control, we can generate the corresponding re-entry trajectory using the Simulation Tool for Atmospheric Re-entry Trajectories START (Mooij, TO BE PUBLISHED).

The vehicle data which have been used for the simulation can be found in either MBB (1988a) or Mooij (1995). The mass of the vehicle is $m = 26,029$ kg, whereas the (principal) moments of inertia are

$$\tilde{I}_{xx} = 119,000 \text{ kg m}^2$$

$$\tilde{I}_{yy} = 769,000 \text{ kg m}^2$$

$$\tilde{I}_{zz} = 806,000 \text{ kg m}^2$$

The reference geometry is given by:

$$S_{ref} = 110.0 \text{ m}^2$$

$$\begin{aligned}c_{ref} &= 23.0 \text{ m} \\b_{ref} &= 12.0 \text{ m}\end{aligned}$$

The initial conditions for the simulation were:

$$\begin{aligned}V &= 7435.5 \text{ m/s} \\ \gamma &= -1.43^\circ \\ \chi &= 70.75^\circ \\ h &= 122 \text{ km} \\ \tau &= -106.58^\circ \\ \delta &= -22.3^\circ\end{aligned}$$

The vehicle is assumed to be heading towards a runway in Kourou (French Guyana).

The simulation has been executed for a trimmed condition (pitch equilibrium only), see also MBB (1988b). For the Mach range between 1 and 20^9 , trim is realised with the body flap as much as possible, and the rest with the elevons (elevator function). (For $0 < M \leq 1$, although this flight regime is not of interest here, the HORUS-2B is trimmed with the elevators, while having the body flap maximum up).

The nominal controls are shown in Fig. 3.1 and 3.2, for reasons of convenience at the end of this section. In Fig. 3.1, the nominal angle of attack is given as a function of flight time. As can be seen, HORUS enters the atmosphere with the high angle of attack of 40° . Because of this high angle, the maximum occurring heat flux can be kept sufficiently small. Further down the trajectory, the angle of attack is decreased in order to meet with the cross- and downrange requirements. The bank-angle profile is plotted in Fig. 3.2. The nominal history provided by MBB consists of absolute values only, guaranteeing a certain descent rate. The corresponding sign is determined by flying towards the targeting point near Kourou, while keeping the heading error within dead-band limits. Whenever the heading error exceeds the dead band, the sign of the bank angle is inverted. This manoeuvre, a so-called bank reversal, usually takes between 10 and 20 s. Since ideal control is applied, i.e., the actual attitude is equated to the commanded attitude, the reversals show as vertical lines. We see four reversals at $t \approx 724 \text{ s}$, $t \approx 1076 \text{ s}$, $t \approx 1184 \text{ s}$ and $t \approx 1240 \text{ s}$. The simulation is finished when the Terminal Area, 0.75° ($\approx 83 \text{ km}$) from the runway, has been reached. This is about 1250 s after re-entry.

Studying the coefficients of **A** and **B**, we find that we need the following parameters of the nominal trajectory as a function of time:

$$\alpha_0, \sigma_0, V_0, \gamma_0, R_0, q_{dyn0}, M_0, g_0, D_0, L_0$$

The control history provides α_0 and σ_0 ($\beta_0 = 0^\circ$), which we already discussed. The other relevant parameters are given in Figs. 3.3-10. For a detailed discussion of the trajectory we

⁹ The upper Mach boundary was in our case changed to a dynamic pressure boundary $q_{dyn} \geq 100 \text{ N/m}^2$, to prevent pitch instability and to be more in line with the body-flap activation of the Space Shuttle.

refer to Mooij (TO BE PUBLISHED). It should be noted that in the curves for the drag and the lift, the trim drag and lift are included. In Figs. 3.11 and 3.12, finally, the nominal body-flap and elevator deflection for trim stability are shown. We see that only at the end of the flight the body-flap deflection is saturated, and the elevons are required to provide the remaining trim moment. The deflections of the aerosurfaces take place with an infinite rate (zero time).

From coefficient $a_{\gamma V}$, we see that we need the value of $\dot{\gamma}_0$. This variable can be easily computed by substituting the related nominal values in Eq. (2.2.2),

$$\dot{\gamma}_0 = \left(\frac{V_0}{R_0} - \frac{g_0}{V_0} \right) \cos \gamma_0 + \frac{L_0 \cos \sigma_0}{m V_0} \quad (3.2.1)$$

Finally, we need the values of some aerodynamic coefficients and derivatives,

$$\frac{\partial C_D}{\partial M}, \frac{\partial C_D}{\partial \alpha}, \frac{\partial C_S}{\partial \beta}, \frac{\partial C_L}{\partial M}, \frac{\partial C_L}{\partial \alpha}, \frac{\partial C_I}{\partial \beta}, \frac{\partial C_n}{\partial \beta} \text{ with contributions of the base vehicle only}$$

$$\frac{\partial C_m}{\partial M}, \frac{\partial C_m}{\partial \alpha} \text{ with contributions of the base vehicle, the body flap and the elevons}$$

$$\frac{\partial C_I}{\partial \delta_a}, \frac{\partial C_m}{\partial \delta_e}, \frac{\partial C_n}{\partial \delta_a} \text{ with contributions of the elevons only}$$

$$\frac{\partial C_n}{\partial \delta_r} \text{ with contributions of the rudder only}$$

With M_0 , α_0 and the trimmed deflection angles of body flap and elevator at hand, these derivatives can be computed off-line. The aerodynamic properties are given in tabular form, for which linear interpolation is used to extract the information for a particular flight situation. A derivative is computed by simply taking the derivative of the connecting line, when the flight situation is located in between two tabular values. At a boundary tabular value, either the left or right derivative is used; in case the flight condition is located at a tabular value somewhere in the table, the connecting line of the two neighbouring values is used.

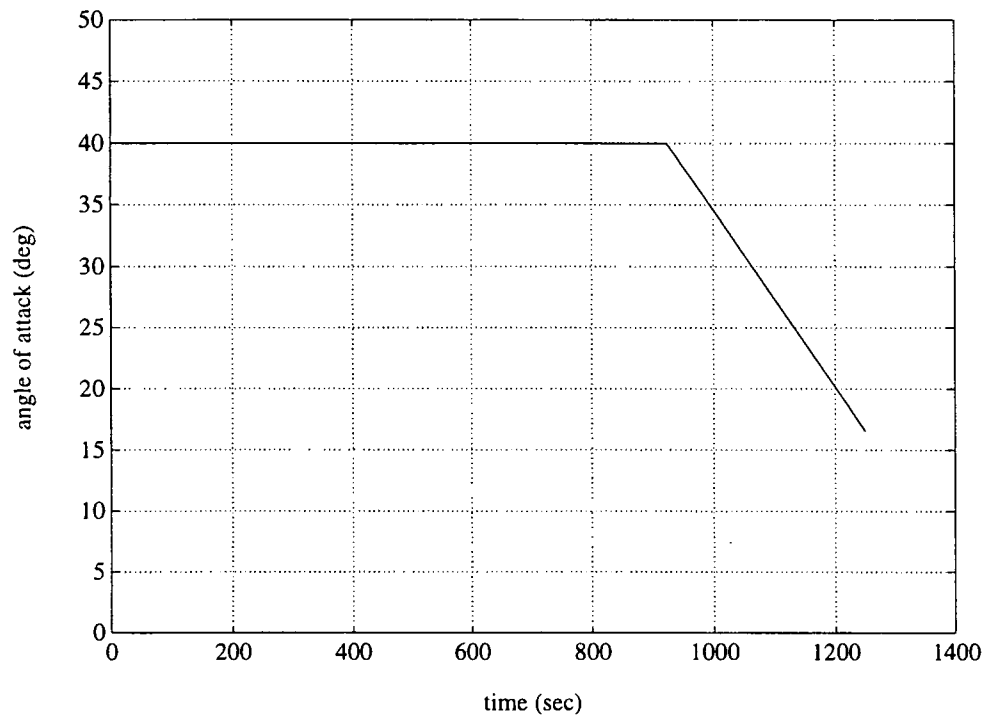


Fig. 3.1 - The nominal angle of attack as a function of flight time.

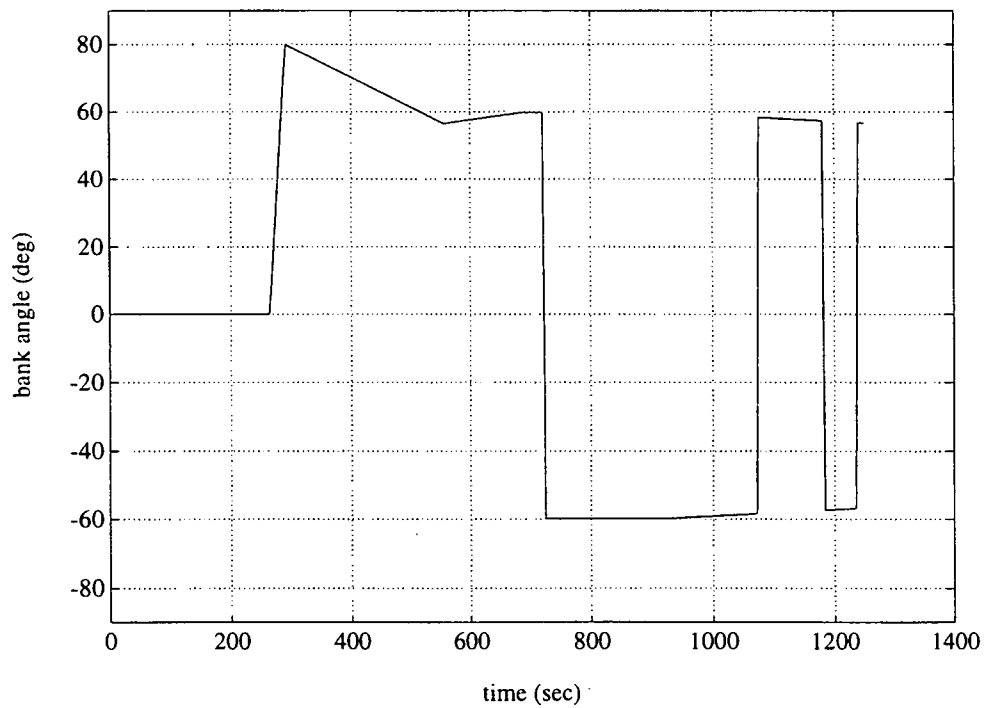


Fig. 3.2 - The nominal bank angle as a function of flight time.

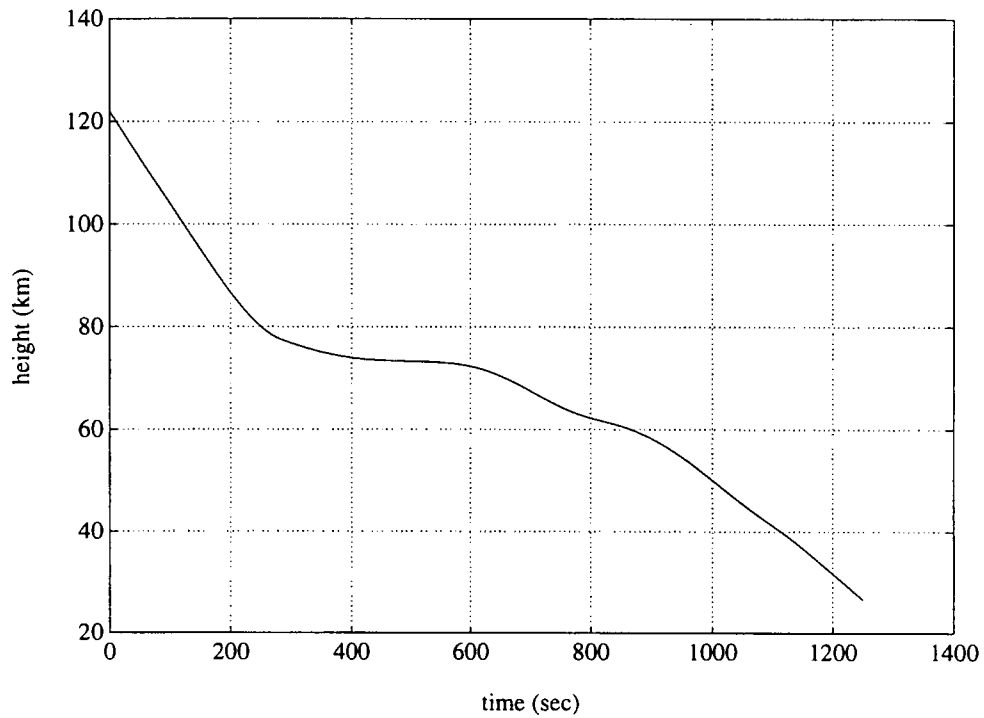


Fig. 3.3 - The nominal height as a function of flight time.

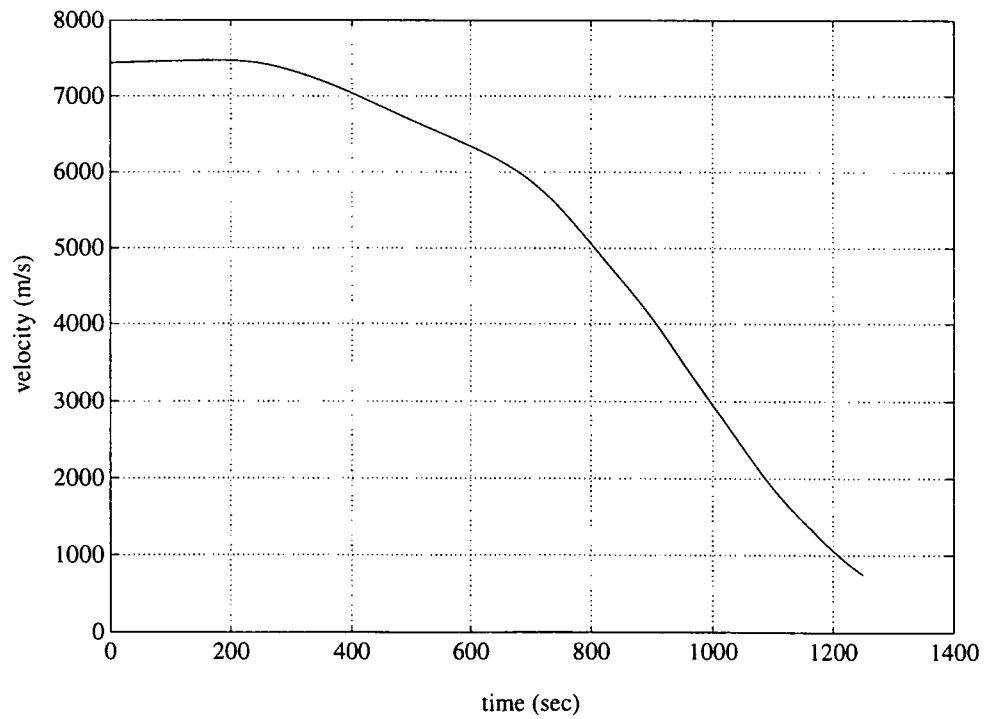


Fig. 3.4 - The nominal velocity as a function of flight time.

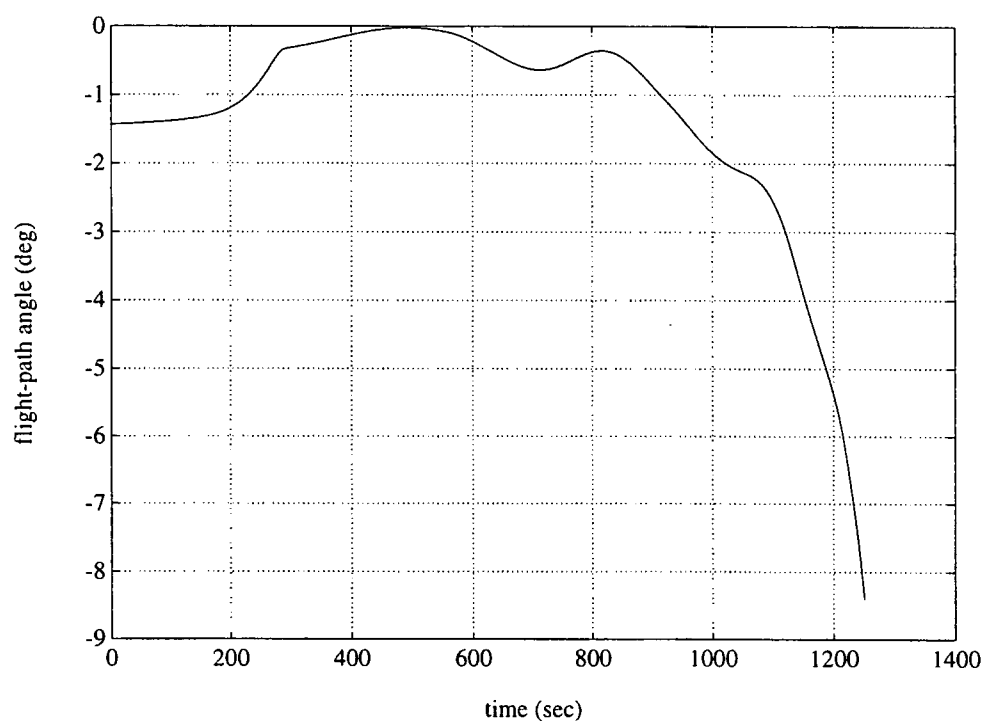


Fig. 3.5 - The nominal flight-path angle as a function of flight time.

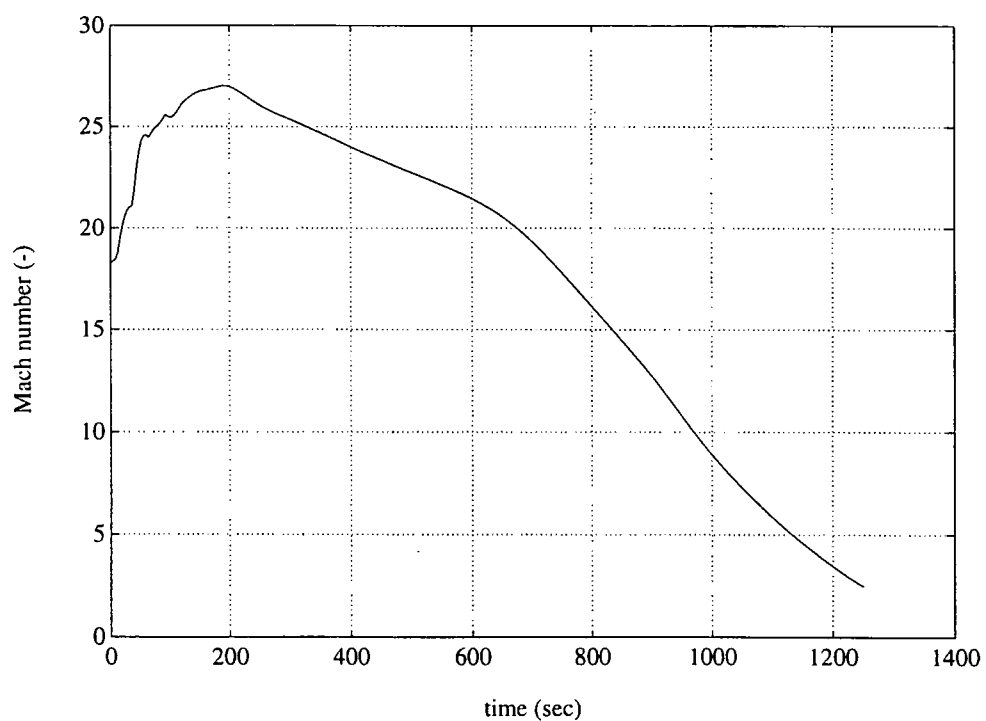


Fig. 3.6 - The nominal Mach number as a function of flight time.

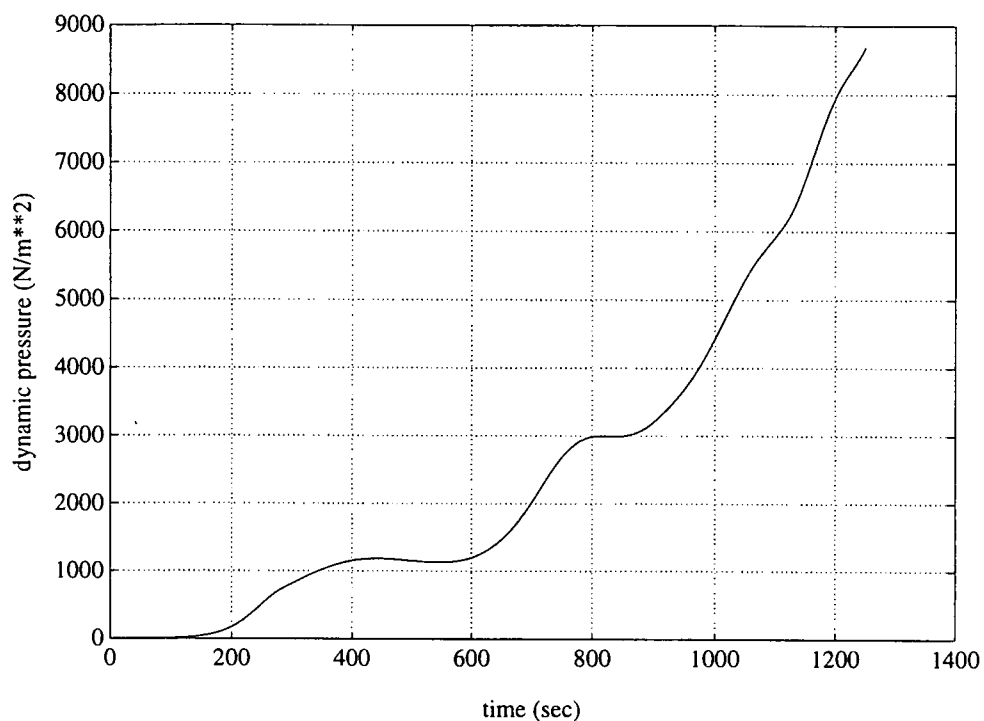


Fig. 3.7 - The nominal dynamic pressure as a function of flight time.

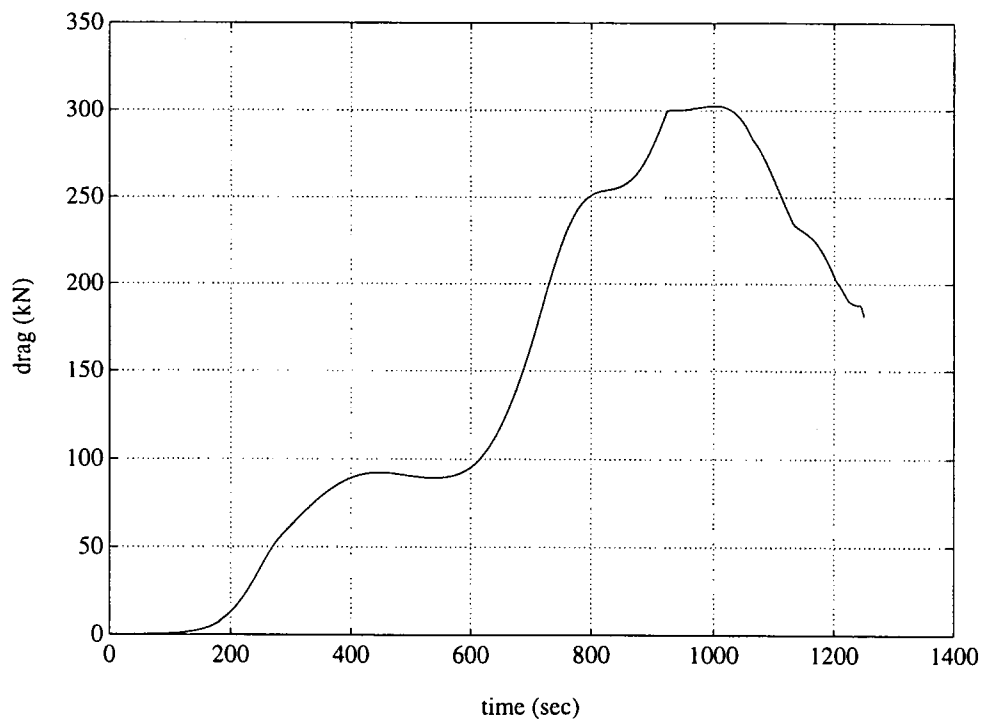


Fig. 3.8 - The nominal drag as a function of flight time (including trim drag).

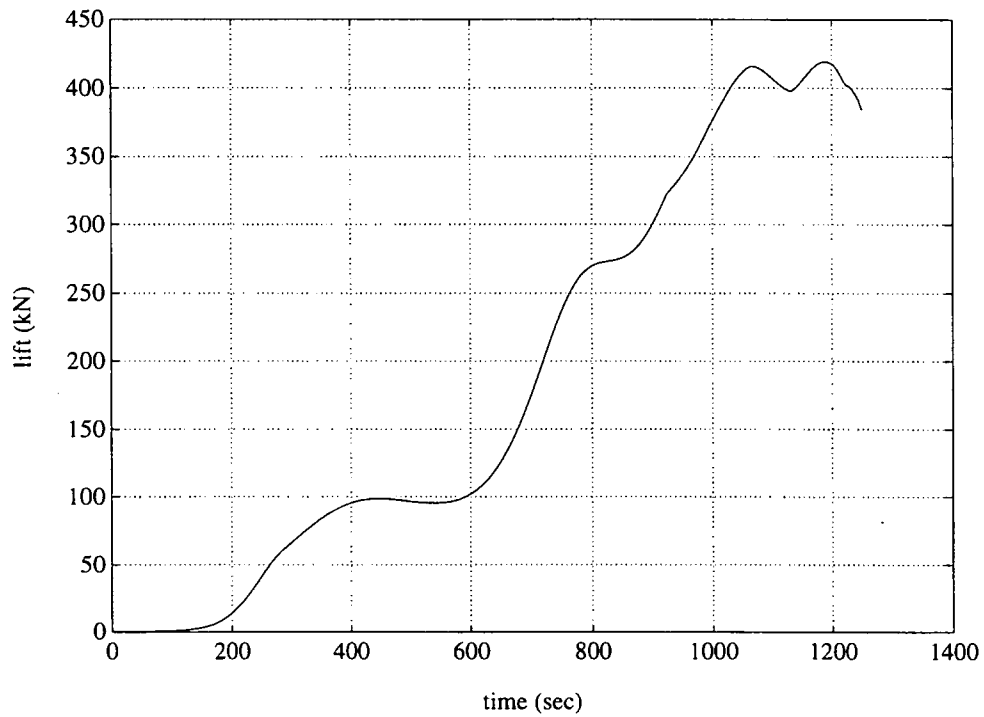


Fig. 3.9 - The nominal lift as a function of flight time (including trim lift).

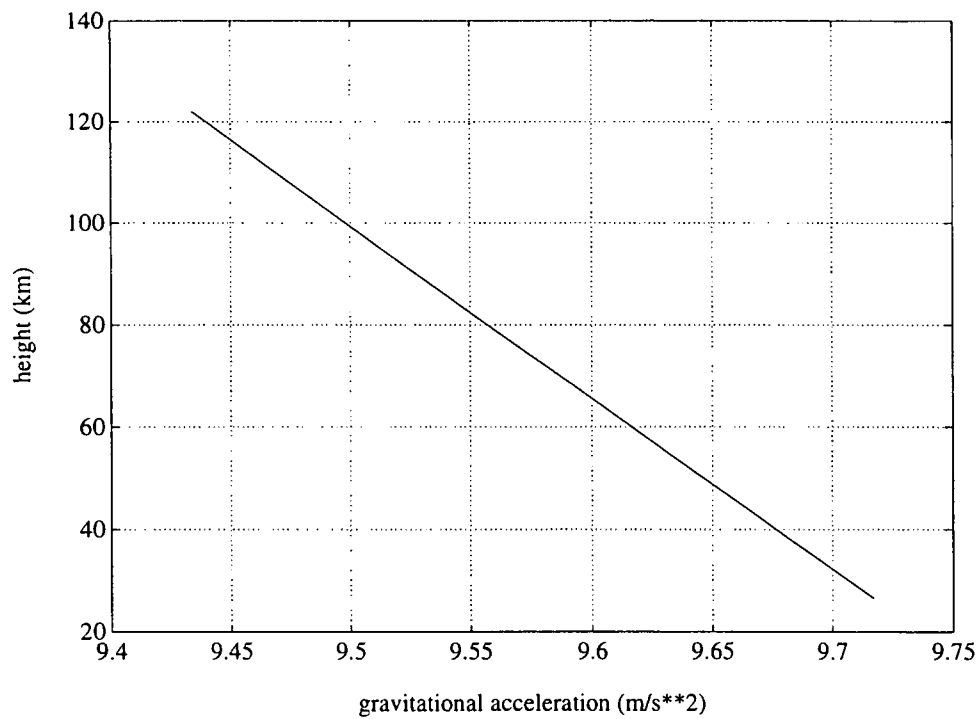


Fig. 3.10 - The nominal gravitational acceleration related to the height.

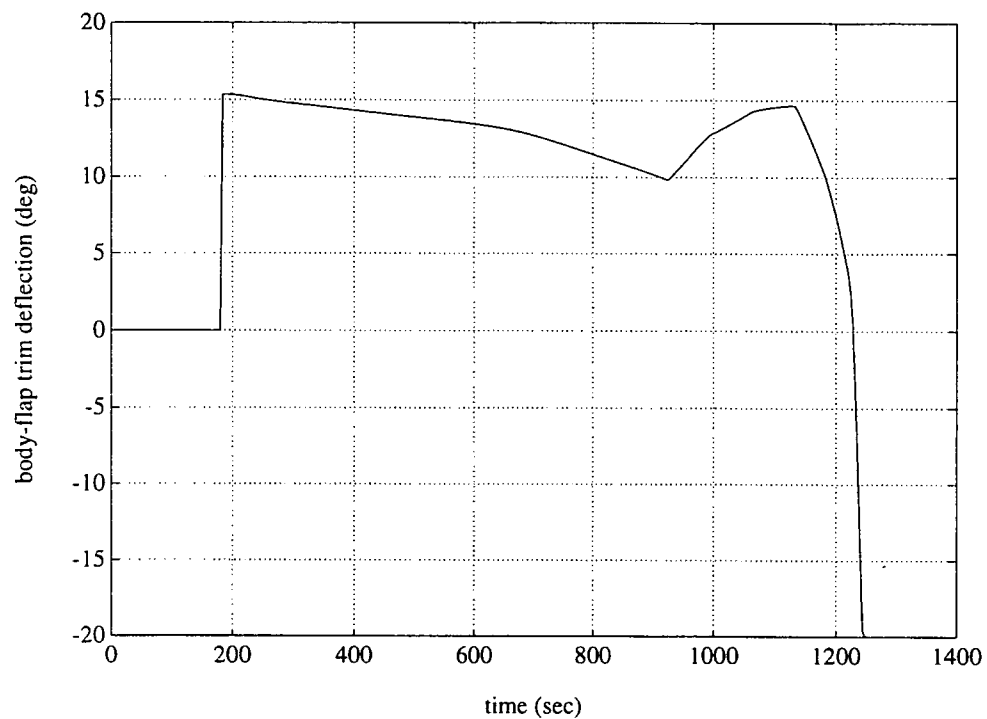


Fig. 3.11 - The nominal trimmed deflection of the body flap as a function of flight time.

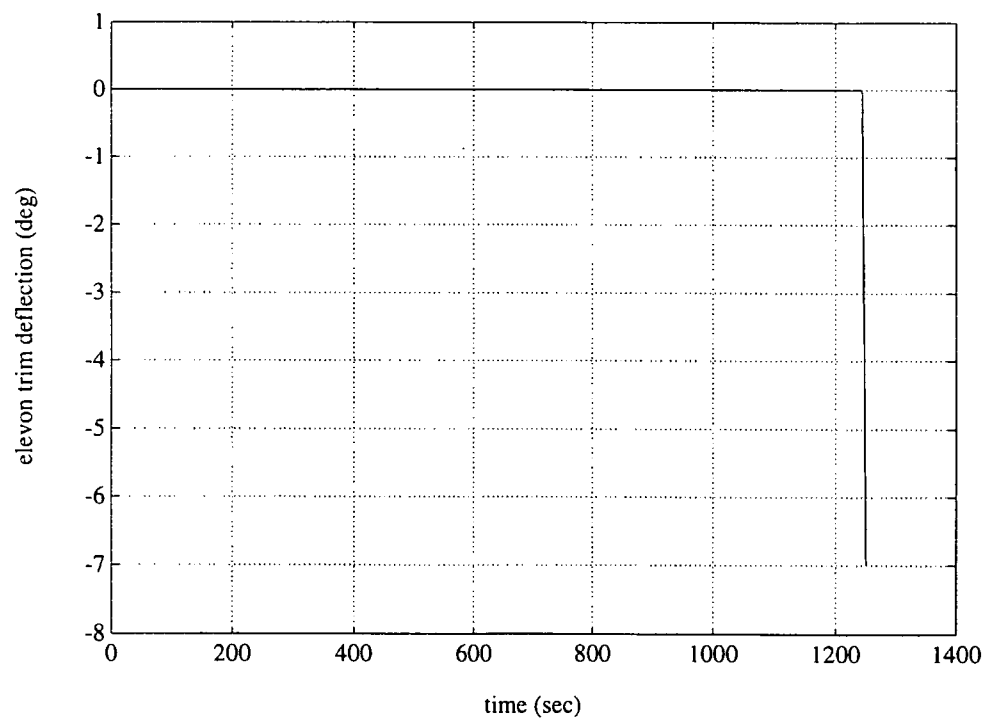


Fig. 3.12 - The nominal trimmed deflection of the elevators a function of flight time.

3.3. Eigenvalues and eigenmotion.

Before we start the discussion on the eigenvalues and eigenmotions of HORUS, we must note that it is not our intention to give a complete analysis of the open-loop behaviour of HORUS. We will restrict ourselves to a more general discussion, starting with a brief introduction on the relation between eigenvalues and eigenmotion. Then, we will introduce the characteristic motions which we find with subsonic, conventional aircraft. As we will see, the HORUS has similar motions in certain speed regimes. These characteristic motions will be discussed for a number of time points. To illustrate the eigenmotion, we will conclude this section by showing the results of a 6-dof open-loop re-entry simulation.

Having computed the eigenvalues and corresponding eigenvectors, how can we relate them to the actual motion of a vehicle? Based on the eigenvalues, we can see whether a component of the motion is (un)stable and (a)periodic, see also Fig. 3.13. An eigenvalue can be real or complex. Complex eigenvalues appear in (conjugated) pairs and indicate a periodic eigenmotion, whereas real eigenvalues imply an aperiodic eigenmotion. The sign of the real part of the eigenvalue shows whether the eigenmotion will be converging (negative real part) or diverging (positive real part). When the real part is zero, the oscillations have a constant amplitude. A more detailed discussion can, amongst others, be found in the books by Kuo (1987) and D'Souza (1988).

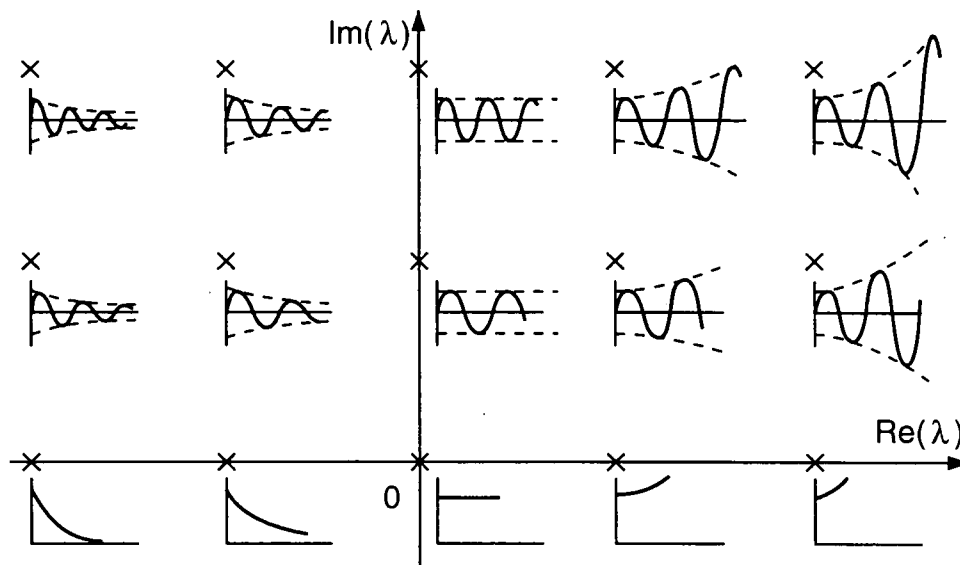


Fig. 3.13 - Impulse responses for various eigenvalue locations in the complex plane (based on D'Souza, 1988), where the conjugate eigenvalues are omitted.

To characterise the eigenmotion we compute some specific coefficients, i.e., the *period* P , when a pair of complex conjugate eigenvalues represents a periodic motion, defined as

$$P = \frac{2\pi}{\text{Im}(\lambda)} \quad (3.3.1)$$

An aperiodic motion does not have a period, which also follows from the fact that the imaginary part of the eigenvalue is zero.

Next, we define the *halving time* T_1 , indicating the time interval when the amplitude of the motion has become half its original value,

$$T_1 = \frac{\ln \frac{1}{2}}{Re(\lambda)} \quad (3.3.2)$$

However, when the real part of the eigenvalue is positive, the halving time becomes negative. In that case it is better to speak of the *doubling time* of the (diverging) eigenmotion:

$$T_2 = \frac{\ln 2}{Re(\lambda)}$$

The *damping ratio* ζ for periodic eigenmotion (complex eigenvalues) can be computed with

$$\zeta = -\frac{Re(\lambda)}{\sqrt{Re(\lambda)^2 + Im(\lambda)^2}} \quad (3.3.3)$$

In the case of damped eigenmotion, ζ is positive (a negative damping ratio is in principle an amplification ratio). For aperiodic motion, ζ is not defined.

Finally, the *natural frequency* ω_n for periodic eigenmotion is defined to be

$$\omega_n = \sqrt{Re(\lambda)^2 + Im(\lambda)^2} \quad (3.3.4)$$

The natural frequency is the theoretical frequency of the eigenmotion when the energy of the system is constant during that motion, which means that the amplitude is constant. Again, for aperiodic motion ω_n is not defined. It should be noted that the natural frequency is more a mathematical notion rather than a physical one.

Using the above definitions, we can write a relation between the period on the one hand, and the damping ratio and the natural frequency on the other:

$$P = \frac{2\pi}{\omega_n \sqrt{1 - \zeta^2}} \quad (3.3.5)$$

Sofar, we have only discussed the stability characteristics of the eigenmotion, but we do not know yet in which of the state variables we can trace this motion. Studying the eigenvectors

will help us to answer this question. Suppose we compute the modulus of each of the (complex) components of an eigenvector μ_i , then we can easily spot the components which are involved. Furthermore, computing the argument of the complex component, we get an impression of the phase difference between the related components.

In mathematical terms, see also Fig. 3.14, the modulus z of a complex number λ is defined to be

$$z = \sqrt{\operatorname{Re}(\lambda)^2 + \operatorname{Im}(\lambda)^2} \quad (3.3.6)$$

and the argument θ is

$$\theta = \arctan\left(\frac{\operatorname{Im}(\lambda)}{\operatorname{Re}(\lambda)}\right) \quad (3.3.7)$$

Note that the argument of a real number is always 0 or π ($\lambda < 0$).

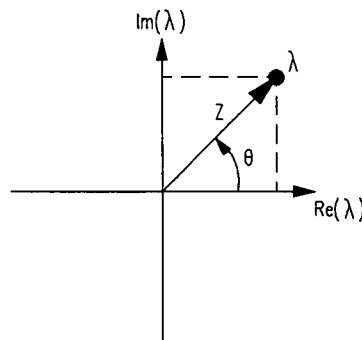


Fig. 3.14 - The modulus z and argument θ of a complex number.

Each component of the eigenvector can in principle be plotted as a time vector using z and θ , which will give us a visual aid to inspect the eigenmotion in the sense that the relative magnitude and phase difference of the related components can be distinguished, e.g., see Etkin (1972). Here, we will not do that but restrict to a numerical inspection of the more important components of the state vector.

Before we look at the eigenmotion of HORUS, we will briefly discuss the eigenmotion of conventional subsonic aircraft in steady flight, because we expect at least partly similar modes (a component of the eigenmotion) for HORUS. Etkin (1972) and Brandt and Van den Broek (1984) distinguish 5 different modes, two longitudinal and three lateral modes. The longitudinal modes are called the short-period and the phugoid mode, whereas the lateral modes are called the lateral oscillation (or Dutch roll), the rolling divergence and the spiral mode. Furthermore, the longitudinal and lateral modes are decoupled, which means that a symmetric motion (e.g., a disturbance) will not affect the asymmetric motion and vice versa.

The *short-period oscillation* is a fast, periodic aircraft motion, which is usually well damped. Because of the fast pitch rate, the aerodynamic forces acting on the vehicle are large. The flight path is nearly a straight line, and there is a negligible speed variation. The *phugoid* is a very slow oscillation which is poorly damped. The slowly oscillating speed results in small variations in the dynamic pressure and therefore the aerodynamic forces. Basically, the motion consists of translations in the aircraft plane of symmetry, while the rotation about the pitch axis is negligible. Since only the height and velocity are changing, the phugoid can be interpreted as a continuous exchange of potential and kinetic energy.

The *lateral oscillation* resembles the short-period oscillation, in that sense that it is usually a fast, well-damped aircraft motion (sometimes moderately damped). The large aerodynamic forces are in principal due to a rotation about the top axis (yaw). There is also a strong roll rate, but this does not influence the lateral oscillation that much. The flight path and the velocity almost have constant values. The *roll divergence* is a strongly damped, aperiodic eigenmotion, during which the aircraft rotates purely about the X-axis (roll). The roll divergence is aperiodic, because the roll angle does not have any influence on the external moments and thus the motion. The *spiral mode*, finally, is seen to consist mainly of yawing at nearly zero sideslip with some roll. The aerodynamic forces are very small, resulting in a large time constant. The spiral mode can be either a stable or unstable, aperiodic eigenmotion.

We will now have a look at the eigenmotion of HORUS. As we saw in Section 2.3, the system matrix \mathbf{A} is a 9x9 matrix, which means that there are 9 eigenvalues and corresponding eigenvectors. Inspecting \mathbf{A} will also tell us that there are some cross couplings between so-called symmetric (V, γ, R, q, α) and asymmetric variables (p, r, β, σ), indicating that the symmetric and asymmetric motion will not be completely decoupled. However, when these coupling terms are sufficiently small, decoupling will be possible. But this we will see later.

In Fig. 3.15 through 3.18, the 9 eigenvalues of HORUS along the nominal trajectory are plotted. The first two figures show the eigenvalues in the complex plane, whereas the latter two give the imaginary and real parts of the eigenvalues as a function of flight time. Since it is not easy to see which modes the curves represent, we will only draw some general conclusions from these figures.

Fig. 3.15 shows a mixture of complex and real eigenvalues, indicating that we can expect both periodic and aperiodic eigenmotions. The maximum imaginary parts of about 1.5 mean quite short periods. The real parts are between -1 and 1, which means that the modes can be either converging or diverging. Looking at Fig. 3.17, we see in principle two major periodic eigenmotions emerge, which are, as we will find out later, the lateral oscillation (the two outer curves) and the short-period oscillation (the two inner curves). The discontinuous jumps in the inner curves are due to the linearisation of the aerodynamic coefficients and the linear table interpolation: when we go from one table range to another, the aerodynamic derivatives sometimes change discontinuously. Fig. 3.18, finally, indicates that most of the time the eigenmotions are very lightly damped or undamped. Only towards the end of the flight strong divergencies and convergencies appear.

To study the eigenmotion of HORUS in more detail, we have selected several time points

for which we will compute the characteristic values (according to Eqs. (3.3.1) through (3.3.4)), and for which we will try to identify the modes by studying the eigenvectors. The selected time points are 1 ($t = 0$ s), 50 ($t = 196$ s), 100 ($t = 396$ s), 150 ($t = 596$ s), 200 ($t = 796$ s), 250 ($t = 996$ s), 300 ($t = 1196$ s) and 314 ($t = 1252$ s). The numerical results are presented in Table 3.1 through 3.8 at the end of this section.

In principle, we can trace the 5 motions which we discussed before for conventional aircraft. However, due to the larger speed regime and due to the distinct nature of the nominal trajectory (large bank angles as compared with the steady cruise flight of subsonic aircraft), we find some differences. Starting with time point 1, we find six eigenmodes. The first mode we have designated the short-period oscillation, because of the large-amplitude oscillations found in the angle of attack and pitch rate (note that the most important components of the eigenmotion have been printed bold).

Whereas in the aircraft case the height and velocity remained constant, it seems that here this is not the case, basically because of the much slower character of the re-entry short-period mode. However, it should be noted that despite the fact that the height component is the largest, only the relative difference is important. An amplitude of 0.0226 rad for the angle of attack means a 1-m amplitude for the height (or: $\Delta\alpha = 10^\circ$ gives $\Delta R \approx 6.7$ m). Besides, we do not have such a rapid oscillation here: the period is about 850 s, whereas for conventional aircraft this is in the order of seconds. Also the motion is hardly damped, because of the absence of aerodynamic forces in the upper layers of the atmosphere. If it had not been for the angle of attack, we might also call this a phugoid-kind of motion. However, we have reserved that name for the second mode¹⁰.

The dominating components of the phugoid mode are the height and velocity, with the angle of attack more or less constant. Furthermore, looking at the period, we find that this eigenmotion is indeed much slower than the short-period oscillation ($P = 5,183$ s). A difference with the aircraft phugoid is that this mode is unstable, although the doubling time is more than 17,000 s. The next mode, the lateral oscillation, compares well with its aircraft counterpart. Main components are the angle of sideslip and the bank angle, together with the corresponding angular rates. Initially, this mode is unstable, but as we will see later the oscillation changes into a damped one. The three remaining modes are all aperiodic. The first two have been given the common name *aperiodic roll mode* for obvious reasons: the bank angle is by far the largest component. Surprising is to see that in one mode the influence of the angle of sideslip is many orders larger¹¹. This means that the first aperiodic roll mode can be compared with the roll divergence of conventional aircraft. Both modes are stable. The last aperiodic mode has been given the name *height mode*. This mode represents a lightly damped aperiodic motion, which has also been found by Sachs (1993), while studying the stability and control problems in hypersonic flight.

¹⁰ As we already find out, at this altitude it is not altogether useful to compare the characteristic modes of re-entry vehicles with those of aircraft, because of the completely different flight regime. However, we will stick to it because it is our only comparison method.

¹¹ In principle, the eigenvalue of the second aperiodic roll mode is so small that for practical reasons it can be considered to be zero.

Now that we have established the basic modes of the eigenmotion, we can focus on the time history of these modes. The short period oscillation changes its nature and comes closer to the aircraft mode. Because at lower altitudes the aerodynamic forces are higher, the damping of this mode increases (although the damping remains low). The period decreases from $P \approx 850$ s at $t = 0$ s, down to $P \approx 40$ s at $t = 96$ s down to $P \approx 9$ s at $t = 996$ s. Then, at time point 300 the periodic mode breaks into two aperiodic modes, of which one is strongly damped ($T_1 = 1.4$ s) and the other one is strongly diverging ($T_2 = 1.9$ s). The half and doubling time decrease further for the last time point. Last but not least, the influence of the bank angle becomes stronger towards the end of the flight, a phenomenon which we will also see with the next mode, the phugoid (for the re-entry flight; not for conventional aircraft).

The phugoid damping ratio increases in time (apart from a small decrement at time point 150). It becomes a very well damped motion, with, for instance, a half time of 254 s at time point 200. The period of the phugoid decreases from over 5000 s ($t = 0$ s) to 430 s ($t = 1252$ s). One remark remains to be made and that is that at time point 100 the influence of the bank angle has changed a couple of orders of magnitude. This can be explained by the fact that initially the nominal trajectory is flown with zero bank angle, whereas later large bank angles are applied for lateral direction control. Because of this the influence of the bank angle in the phugoid becomes apparent, and a coupling (although small) exists between the symmetrical and asymmetrical motion).

As we mentioned before, the lateral oscillation is an unstable, periodic motion and this continues to be during the whole trajectory. But, some characteristics of the motion change. Towards time point 150, the negative damping coefficient gets smaller, which means that the motion becomes less unstable. From that point, the damping coefficient becomes more negative again. The period changes drastically during the first 100 s of flight (P changes from 373 s down to 19.3 s). It continues to decrease till time point 250 ($P = 4.2$ s), after which it varies only slightly. At $t = 396$ s, we see that the contribution of $\Delta\alpha$ has changed many orders of magnitude, indicating that due to a large bank angle a small coupling exists between the symmetrical and asymmetrical motion. Besides, the ratio between $\Delta\sigma$ and $\Delta\beta$ changes from 1.39 to 1.36 indicating a slightly weaker coupling between the bank angle and the angle of sideslip at higher bank angles. Δh becomes the major component, although when we see this in proportion to the attitude angles it does not seem that major (for time point 100, an amplitude of 17.3° in the bank angle corresponds with an amplitude of 1 m in the height). The relative difference between the height and the attitude angles, however, becomes larger towards the end of the flight.

The aperiodic roll modes changes into a single unstable periodic roll mode with a small coupling to the angle of attack (an amplitude of $\Delta\sigma = 10^\circ$ gives $\Delta\alpha = 0.33^\circ$) at time point 100. Besides, the height becomes the major component. Again, this begins at the moment the vehicle starts banking. It should be noted that a small oscillation in the bank angle will result in a large amplitude in the height ($\Delta\sigma = 0.1^\circ$ gives $\Delta h \approx 3,300$ m). However, at the next time point this mode changes again into two aperiodic modes, which are similar to the aperiodic height mode. For time points 200 and 250, a (very) stable periodic roll mode is back, while at time point 300 we have again two aperiodic modes. In this case, the stable mode is similar to

the height mode, whereas the unstable one shows a coupling between the bank angle and the angle of attack, with the angle of attack the larger one.

The height mode already entered the discussion when we were focusing on the several roll modes. We will briefly finalise the discussion on characteristic modes. Initially, the height mode is stable. For time point 50, it has become unstable with an amplification ratio which is as large as the prior damping ratio. When the banking begins (time point 100), the eigenvalue related to the height mode modes very small, and stays very small during the rest of the flight, being alternately positive and negative. For this reason, the height mode is not interesting to discuss any further, because for the short time of the flight this mode is practically indifferent. However, as we discussed before, for some time points the height mode consists of more than one aperiodic component. These additional modes have much larger eigenvalues and become the dominating modes for the height mode, although the damping and/or amplification remains very small.

The free response according to Eq. (3.1.6) is in itself not that interesting. It will confirm what we have already seen in the tables with numerical results. Basically, the graphs will show us both periodic and aperiodic motions, either diverging or converging. Due to the sometimes long periods, the curves will not give us real insight in the eigenmotion at one particular moment in time. Only when the motion is, for instance, reasonably damped (or unstable, for that matter) and has a sufficiently short period, the resulting eigencurve can be quite informative. As an example, the curves for the angle of sideslip and the bank angle (the major variables for the lateral oscillation) have been plotted as a function of time for time point 300, see also Fig. 3.19.

There is another more important reason for not looking into more detail at the curves representing the eigenmotion. The eigenvalues are computed for a certain point in time. When we compute the eigenmotion for a certain time interval (100 s in Fig. 3.19), we assume that the dynamics of the vehicle are not changing (given by a constant system matrix and therefore constant eigenvalues). For a subsonic aircraft in steady (cruise) flight this can be a reasonable approximation, but for a re-entry vehicle this is most of the time not the case.

However, we thought it to be illustrative of the eigenmotion to simulate the descent of the HORUS-2B in the so-called open-loop 6-d.o.f. mode, i.e., a free-fall re-entry including attitude dynamics but without attitude control. For the same initial conditions as given in Section 3.2¹², the results (plots of the angle of attack, the angle of sideslip, the bank angle and the height as a function of flight time) are shown in Figs. 3.20 through 3.23.

We see that right from the beginning the angle of attack is rapidly diverging, reaching a kind of stable oscillation after $t \approx 500$ s, however with an initial amplitude of $\pm 5^\circ$. After $t = 1,400$ s, the vehicle is in a state of severe unstable oscillations (with a pitch rate of a few hundred degrees per second). The angle of sideslip and the bank angle show only small oscillations, mainly induced by the angle-of-attack oscillations. Also these angles reach large values

¹² Next to initial conditions for position and velocity, we need initial values for the attitude and angular rotation of the vehicle. The nominal attitude angles at $t = 0$ are $\alpha = 40^\circ$, $\beta = 0^\circ$ and $\sigma = 0^\circ$, whereas the nominal pitch rate is $0.072663^\circ/\text{s}$ (the nominal roll and yaw rate are considered to be zero).

when $t > 1,400$ s. In Fig. 3.23, we see that the vehicle is in fact doing a damped skipping flight, because of the strong variation in the aerodynamic forces. Finally, after more than 1,600 s the vehicle crashes on the Earth's surface.

A second simulation, now with zero initial attitude and angular rates, shows even worse results (Figs. 3.24 through 3.26). Beside large-amplitude oscillations in all three attitude angles, very unstable oscillations are reached after only 500 s (not plotted). It might not come as a surprise that also this time the vehicle crashes, even further off from the target.

The conclusion from the above discussion is, that it is necessary to control the vehicle if we want it to have a stable flight and reach the landing area safely. In the next chapter, we discuss the design of an attitude control system which must be able to execute these tasks. As is the case for conventional aircraft, we can decouple the symmetric and asymmetric motion. By doing so, we will introduce a small error since there exist a small coupling, as mentioned in the above discussion. However, we expect that this coupling effect will not influence the performance of the controller.

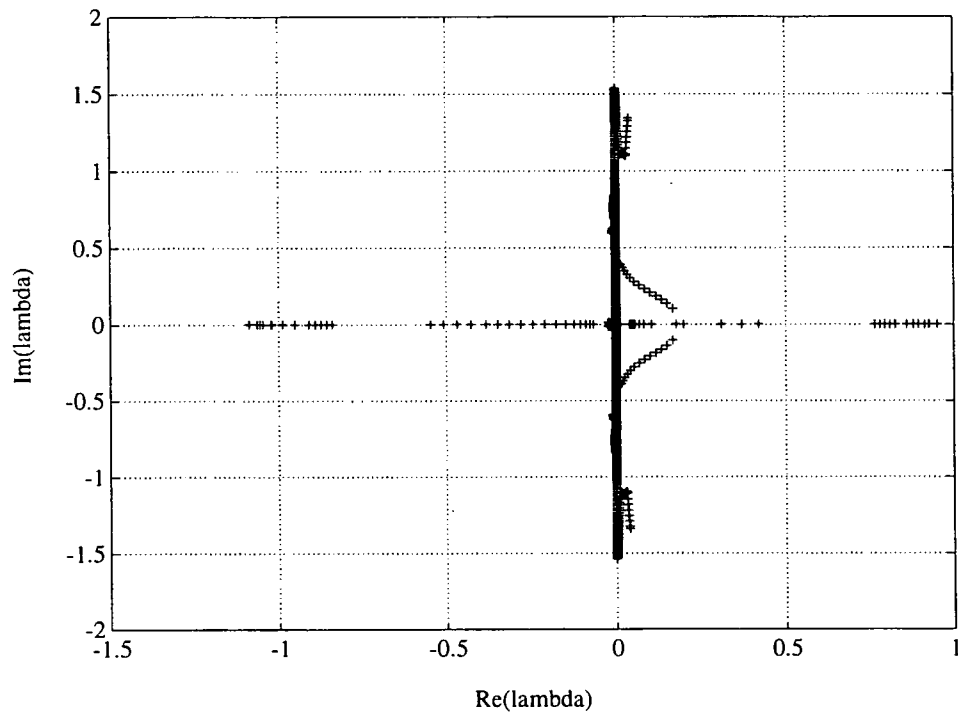


Fig. 3.15 - Variation of the eigenvalues along the nominal trajectory; the variation with time of both the real and imaginary parts can be more clearly seen in Figs. 3.17 and 3.18, respectively.

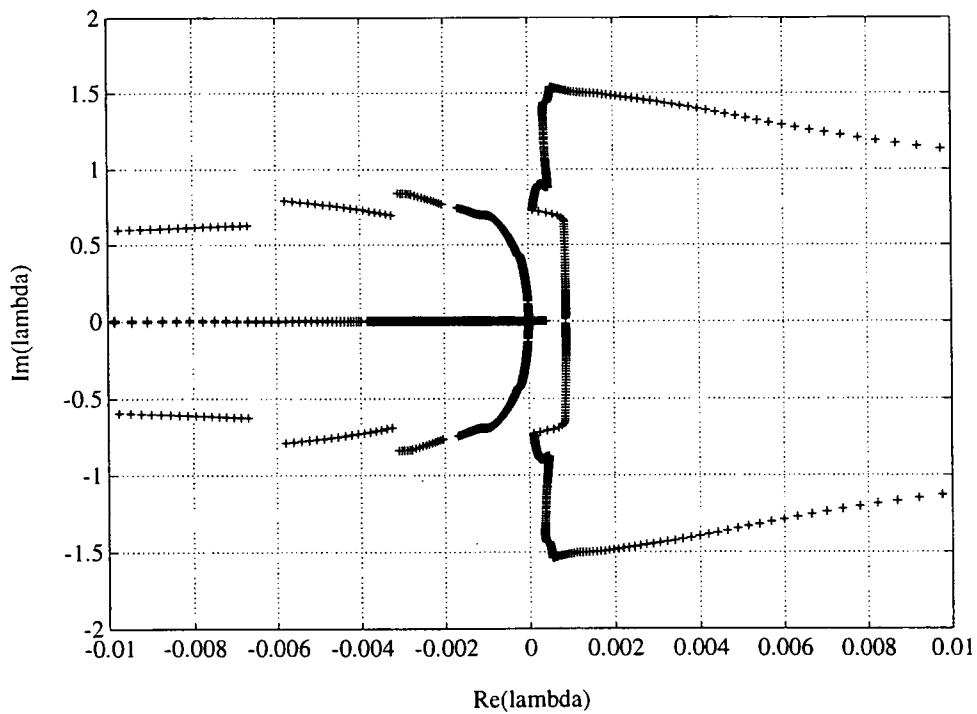


Fig. 3.16 - Detail of the eigenvalue plot centred around the origin.

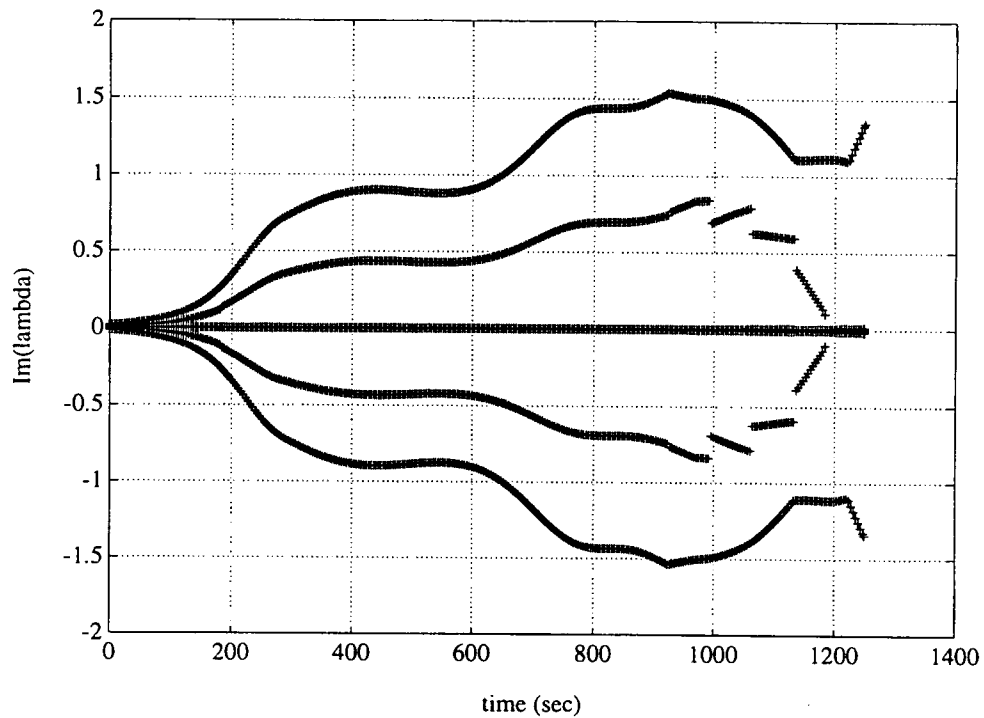


Fig. 3.17 - The imaginary parts of the eigenvalues as a function of flight time.

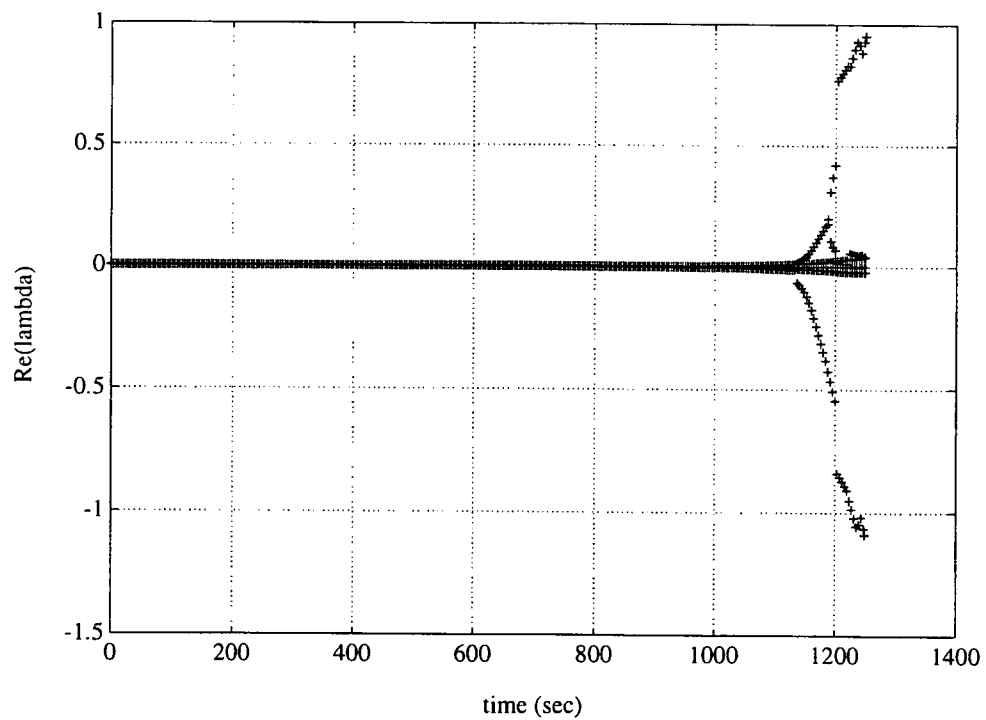


Fig. 3.18 - The real parts of the eigenvalues as a function of flight time.

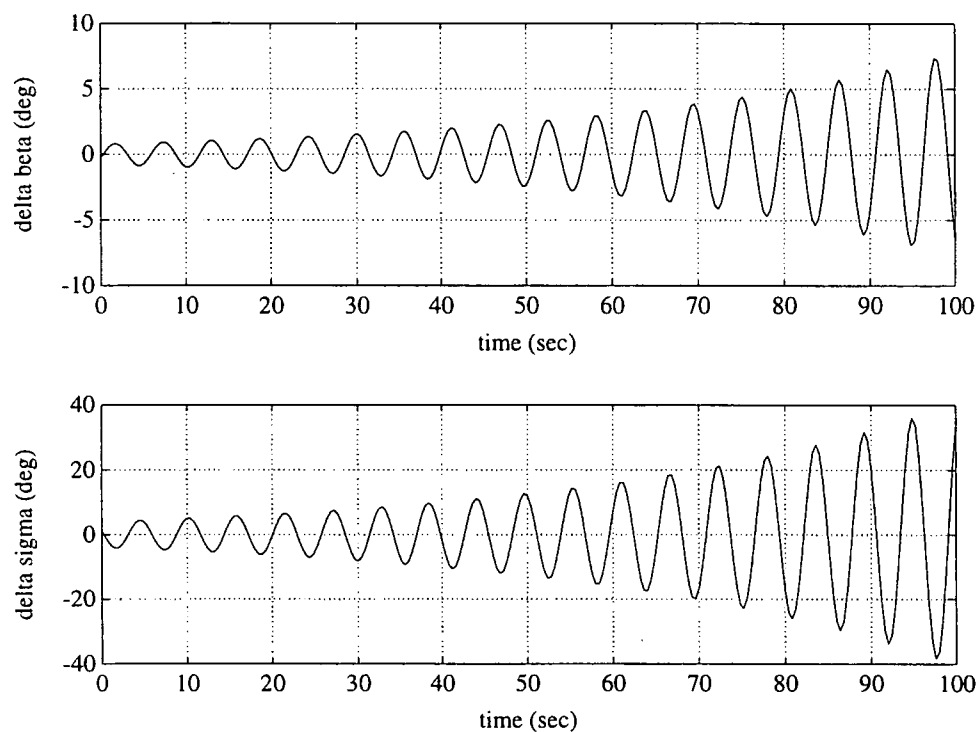


Fig. 3.19 - The variation of the angle of sideslip and the bank angle with time (unstable lateral oscillation) for $t = 1196$ (time point 300). The period of this mode is 5.6 s, whereas the doubling time is 30.3 s.

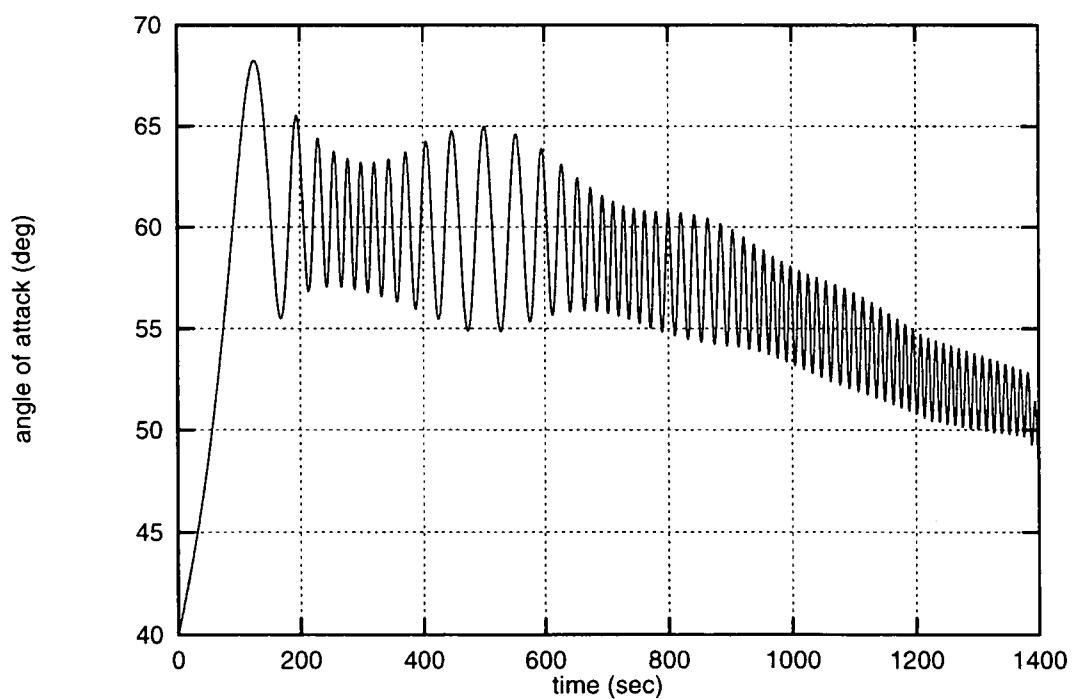


Fig. 3.20 - The angle of attack as a function of time (open-loop simulation).

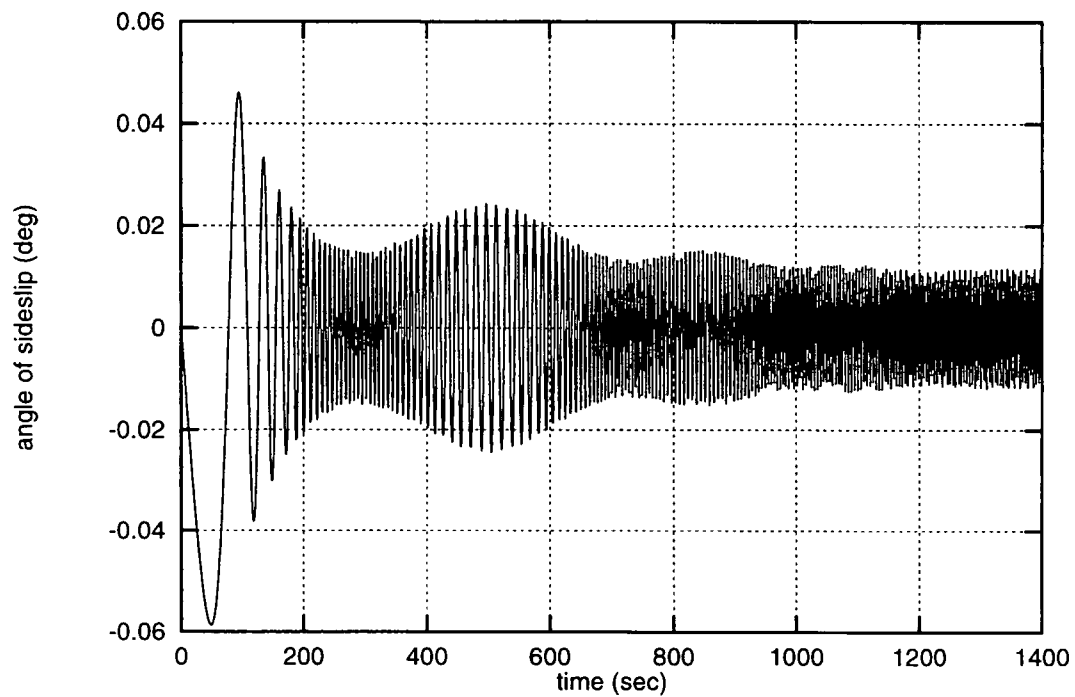


Fig. 3.21 - The angle of sideslip as a function of time (open-loop simulation).

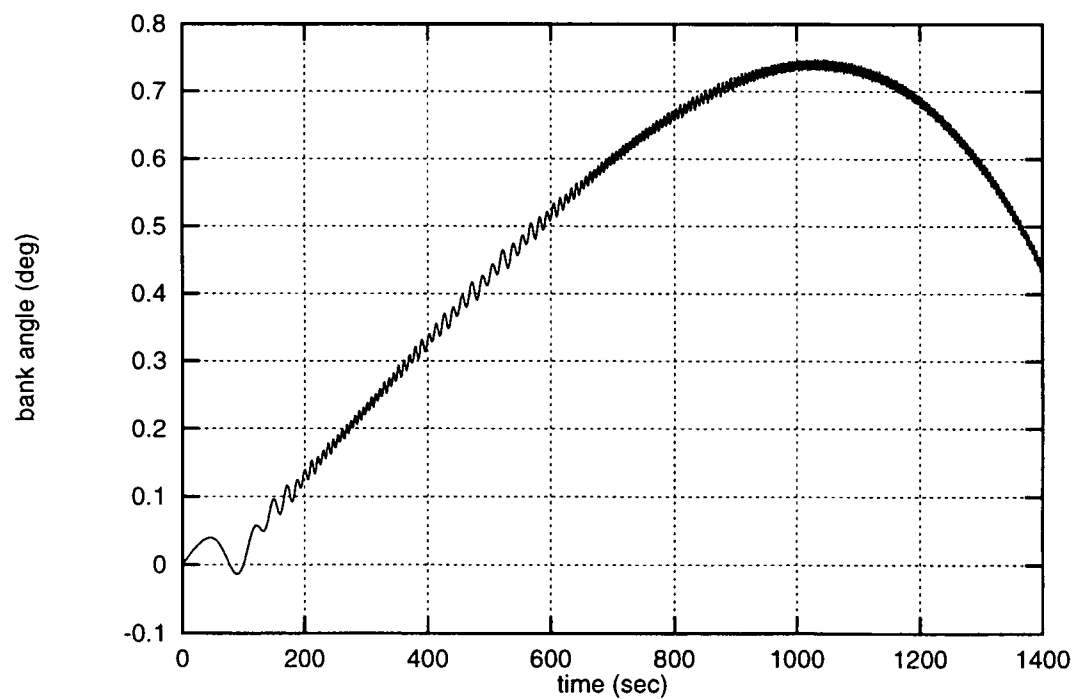


Fig. 3.22 - The bank angle as a function of time (open-loop simulation).

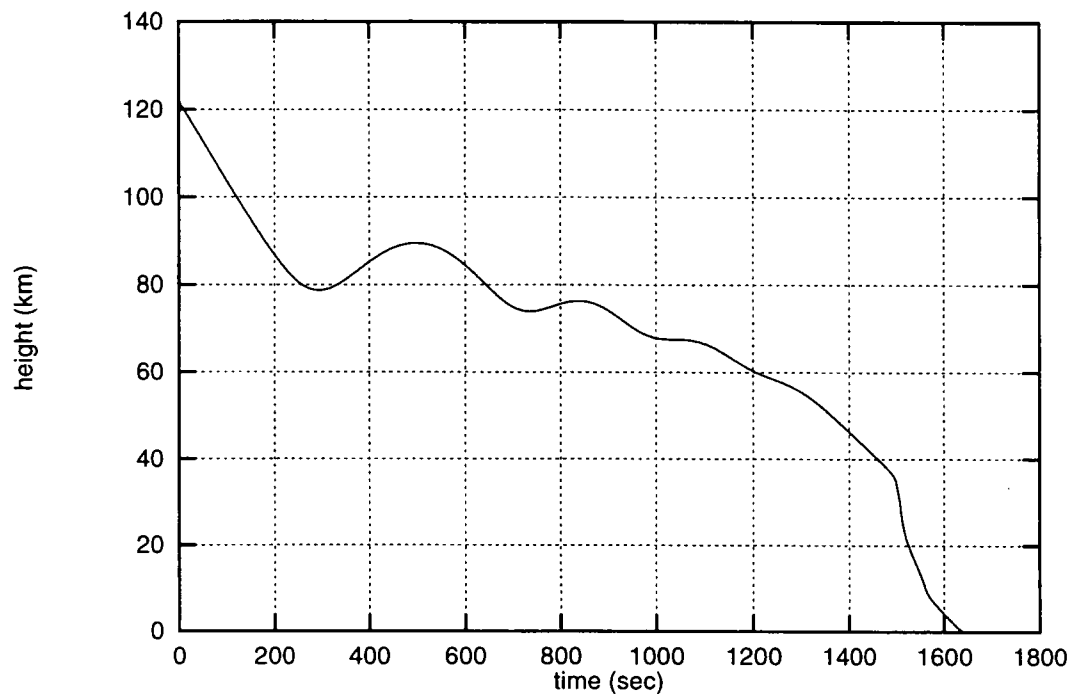


Fig. 3.23 - The height as a function of time (open-loop simulation).

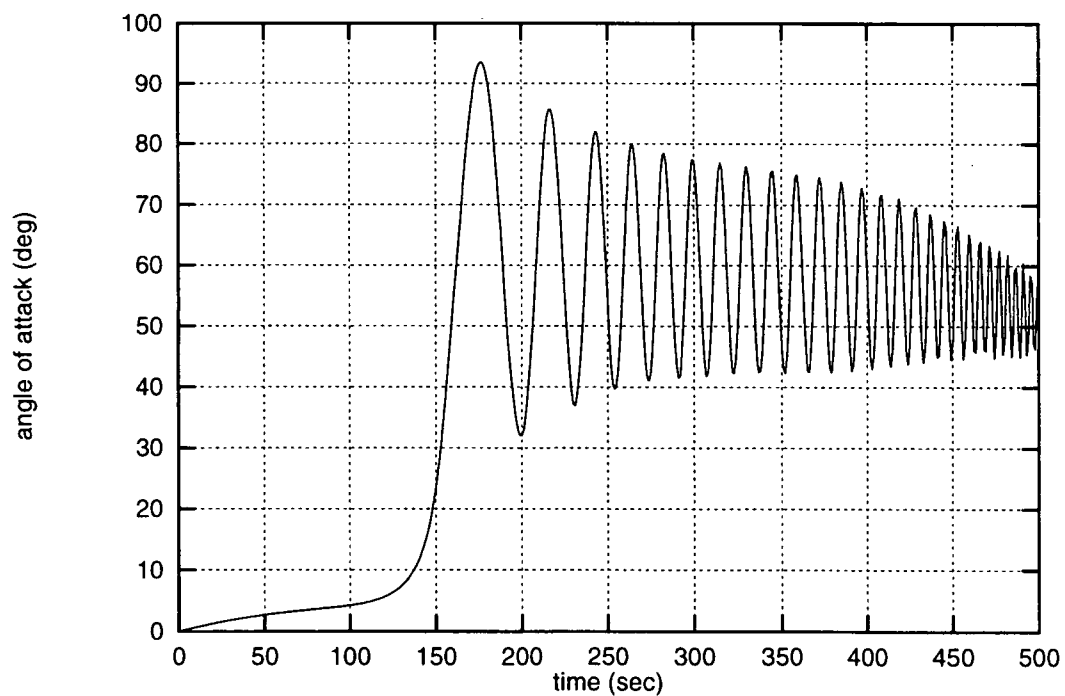


Fig. 3.24 - The angle of attack as a function of time (open-loop simulation, zero initial attitude).

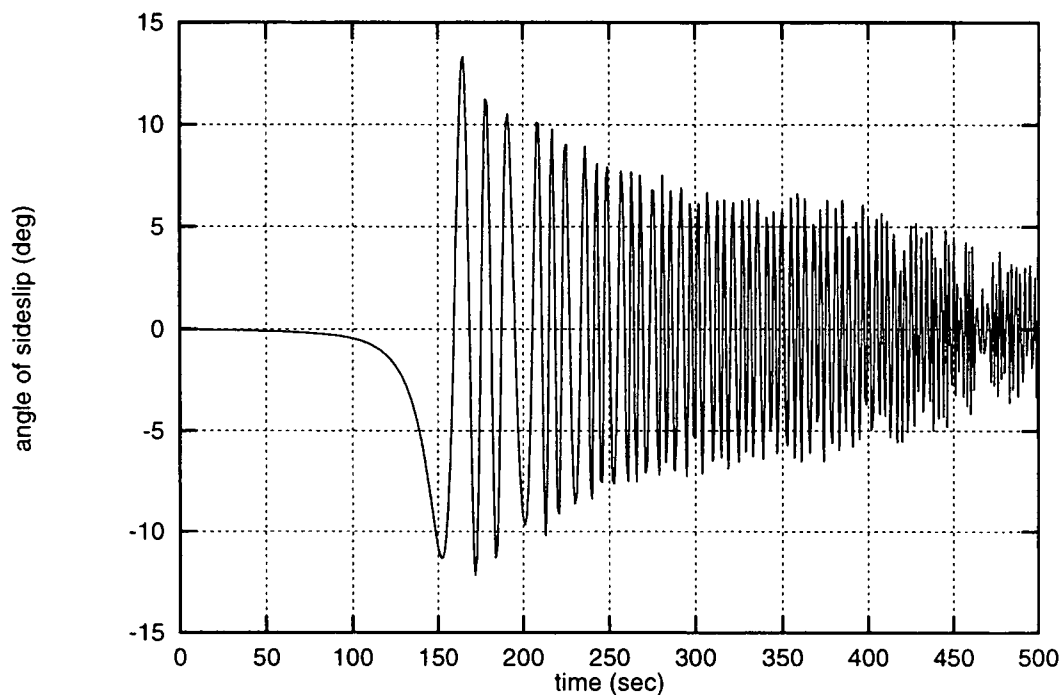


Fig. 3.25 - The angle of sideslip as a function of time (open-loop simulation, zero initial attitude).

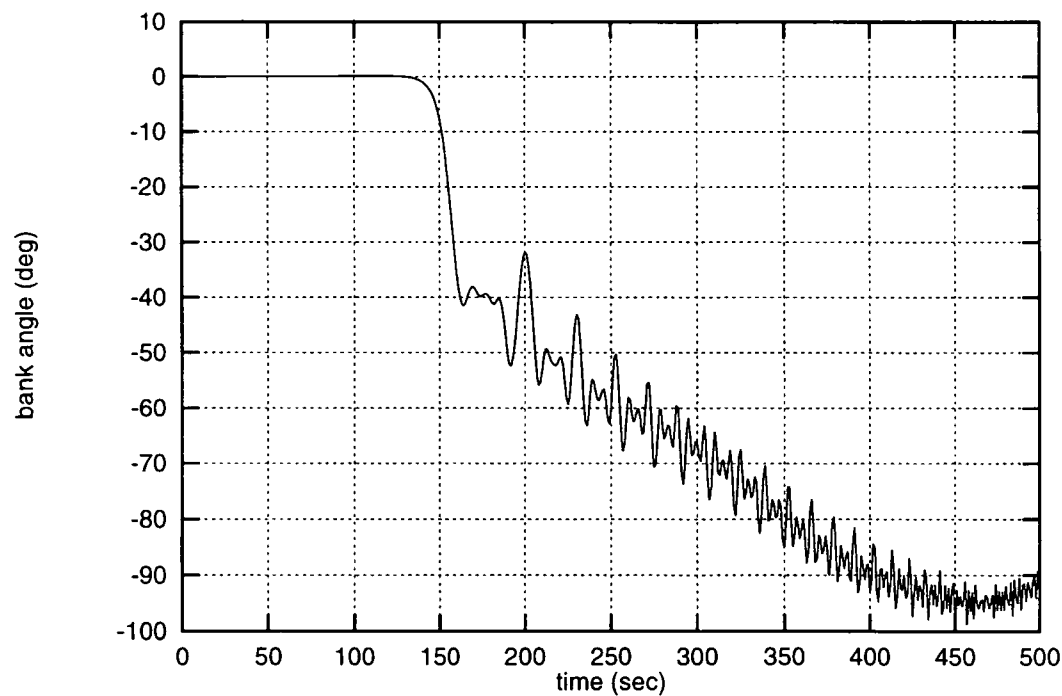


Fig. 3.26 - The bank angle as a function of time (open-loop simulation, zero initial attitude).

	short-period oscillation		phugoid		lateral oscillation		aperiodic roll mode		height mode
	z	θ (°)	z	θ (°)	z	θ (°)	z	θ (°)	
λ_i Re	-0.7302·10 ⁻⁷		0.4025·10 ⁻⁴		0.8677·10 ⁻³		-0.1735·10 ⁻²	-0.7925·10 ⁻¹⁸	-0.8402·10 ⁻⁴
λ_i Im	±0.7415·10 ⁻²		±0.1212·10 ⁻²		±0.0168		-	-	-
P (s)	847.3		5,183.0		373.8		∞	∞	∞
$T_{1/2}$ (s)	0.949·10 ⁷		-17,220.6		-798.9		399.4	0.875·10 ⁻¹⁸	8,250.0
ζ (-)	0.985·10 ⁻⁵		-0.033		-0.052		-	-	-
ω_n (rad/s)	0.742·10 ⁻²		0.121·10 ⁻²		0.017		-	-	-
μ_i	z	θ (°)	z	θ (°)	z	θ (°)	z	θ (°)	z
ΔV	0.0129	10.7	0.1271·10 ⁻²	288.9	0.1134·10 ⁻¹⁵	6.2	0.1678·10 ⁻¹⁶	0.2112·10 ⁻¹⁵	0.6573·10 ⁻³
$\Delta \gamma$	0.9637·10 ⁻⁶	331.7	0.1632·10 ⁻⁶	18.1	0.4382·10 ⁻²⁰	325.8	0.3441·10 ⁻²⁰	0.6882·10 ⁻²¹	0.1351·10 ⁻⁷
ΔR	1.0000	63.3	1.0000	287.7	0.2211·10 ⁻¹⁴	51.1	0.1475·10 ⁻¹³	0.3129·10 ⁻¹²	1.0000
$\Delta \rho$	0.8551·10 ⁻¹⁹	277.7	0.2260·10 ⁻²³	291.9	0.0206	287.8	0.2144·10 ⁻²	0.8153·10 ⁻³	0.1007·10 ⁻²²
Δq	0.1678·10 ⁻³	6.1	0.1804·10 ⁻⁹	300.2	0.3156·10 ⁻¹⁷	318.3	0.4950·10 ⁻¹⁹	0.4129·10 ⁻¹⁹	0.2798·10 ⁻⁹
Δr	0.9334·10 ⁻²⁰	291.6	0.7187·10 ⁻²⁴	0.4	0.1542·10 ⁻²	287.8	0.1606·10 ⁻³	0.9716·10 ⁻³	0.8683·10 ⁻²³
$\Delta \alpha$	0.0226	276.1	0.3150·10 ⁻⁷	281.9	0.3891·10 ⁻¹⁶	345.0	0.3712·10 ⁻¹⁶	0.1735·10 ⁻¹⁶	0.1527·10 ⁻⁷
$\Delta \beta$	0.1940·10 ⁻¹⁷	21.6	0.2444·10 ⁻²²	272.3	0.7277	20.8	0.7814·10 ⁻²	0.1235·10 ⁻¹⁵	0.2045·10 ⁻²²
$\Delta \sigma$	0.2609·10 ⁻¹⁷	11.3	0.5346·10 ⁻²¹	52.2	1.0000	11.7	1.0000	1.0000	0.9654·10 ⁻²⁰

Table 3.1 - Eigenvalues and corresponding characteristic values for time point 1 ($t = 0$ s).

Table 3.2 - Eigenvalues and corresponding characteristic values for time point 50 ($t = 96$ s).

	short-period oscillation		phugoid		lateral oscillation		periodic roll mode		spiral mode
	z	θ (°)	z	θ (°)	z	θ (°)	z	θ (°)	
λ_i Re	$-0.2032 \cdot 10^{-3}$		$-0.9924 \cdot 10^{-3}$		$0.2225 \cdot 10^{-3}$		$0.1022 \cdot 10^{-3}$		$-0.1053 \cdot 10^{-14}$
Im	± 0.4292		$\pm 0.1359 \cdot 10^{-2}$		± 0.8844		$\pm 0.5608 \cdot 10^{-3}$		-
P (s)	14.6		4,625.1		7.1		11,203.9		∞
$T_{1/2}$ (s)	3,410.4		698.4		-3,115.4		-6,784.2		$0.658 \cdot 10^{15}$
ζ (-)	$0.474 \cdot 10^{-3}$		0.590		$-0.252 \cdot 10^{-3}$		-0.179		-
ω_n (rad/s)	0.429		$0.168 \cdot 10^{-2}$		0.884		$0.570 \cdot 10^{-3}$		-
μ_i	z	θ (°)	z	θ (°)	z	θ (°)	z	θ (°)	z
ΔV	1.0000	270.6	$0.1666 \cdot 10^{-2}$	339.2	$0.8536 \cdot 10^{-2}$	270.1	$0.5610 \cdot 10^{-3}$	0.4	$0.6115 \cdot 10^{-5}$
$\Delta \gamma$	$0.2231 \cdot 10^{-4}$	88.5	$0.2385 \cdot 10^{-6}$	76.0	$0.1254 \cdot 10^{-3}$	0.3	$0.8066 \cdot 10^{-7}$	335.9	$0.2074 \cdot 10^{-11}$
ΔR	0.3721	358.5	1.0000	22.3	1.0000	270.3	1.0000	55.6	1.0000
$\Delta \rho$	$0.4047 \cdot 10^{-6}$	270.4	$0.5151 \cdot 10^{-9}$	56.3	0.3287	0.2	$0.3382 \cdot 10^{-9}$	29.0	$0.1072 \cdot 10^{-9}$
Δq	0.0166	270.7	$0.3228 \cdot 10^{-9}$	321.3	$0.1192 \cdot 10^{-3}$	270.2	$0.7965 \cdot 10^{-9}$	280.7	$0.7928 \cdot 10^{-9}$
Δr	$0.2939 \cdot 10^{-7}$	270.4	$0.3740 \cdot 10^{-10}$	56.3	0.0239	0.2	$0.2456 \cdot 10^{-10}$	29.0	$0.1274 \cdot 10^{-9}$
$\Delta \alpha$	0.0387	0.6	$0.5117 \cdot 10^{-7}$	339.2	$0.5723 \cdot 10^{-3}$	0.1	$0.1724 \cdot 10^{-7}$	0.4	$0.1878 \cdot 10^{-9}$
$\Delta \beta$	$0.1304 \cdot 10^{-6}$	0.4	$0.6505 \cdot 10^{-12}$	290.2	0.2182	270.2	$0.1447 \cdot 10^{-12}$	309.3	$0.2645 \cdot 10^{-23}$
$\Delta \sigma$	$0.7566 \cdot 10^{-6}$	348.9	$0.1853 \cdot 10^{-6}$	355.2	0.3020	270.2	$0.5266 \cdot 10^{-6}$	282.6	$0.5107 \cdot 10^{-6}$

Table 3.3 - Eigenvalues and corresponding characteristic values for time point 100 ($t = 396$ s).

	short-period oscillation		phugoid		lateral oscillation		spiral mode			
	z	θ (°)	z	θ (°)	z	θ (°)	z	θ (°)	z	θ (°)
λ_1										
Re										
Im										
P (s)										
$T_{1/2}$ (s)										
ζ (-)										
ω_n (rad/s)										
μ_j										
ΔV	1.0000	274.0	0.1815·10 ⁻²	82.2	0.9170·10 ⁻²	270.4	0.2713·10 ⁻³	0.1094·10 ⁻²	0.8003·10 ⁻⁵	
$\Delta \gamma$	0.4013·10 ⁻⁴	272.7	0.2974·10 ⁻⁶	1.2	0.1416·10 ⁻³	0.7	0.4491·10 ⁻⁷	0.8897·10 ⁻⁷	0.4561·10 ⁻¹¹	
ΔR	0.5933	2.7	1.0000	306.6	1.0000	270.6	1.0000	1.0000	1.0000	
Δp	0.4450·10 ⁻⁶	273.7	0.5502·10 ⁻⁹	344.9	0.3603	0.6	0.9548·10 ⁻¹⁰	0.9607·10 ⁻⁹	0.6063·10 ⁻¹⁰	
Δq	0.0166	274.1	0.4104·10 ⁻⁹	54.0	0.1268·10 ⁻³	270.5	0.6327·10 ⁻⁹	0.2328·10 ⁻⁸	0.1015·10 ⁻⁸	
Δr	0.3231·10 ⁻⁷	273.7	0.3995·10 ⁻¹⁰	344.9	0.0262	0.6	0.6933·10 ⁻¹¹	0.6976·10 ⁻¹⁰	0.7337·10 ⁻¹⁰	
$\Delta \alpha$	0.0380	4.0	0.5548·10 ⁻⁷	82.2	0.6003·10 ⁻³	0.5	0.8293·10 ⁻⁸	0.3343·10 ⁻⁷	0.2446·10 ⁻⁹	
$\Delta \beta$	0.1406·10 ⁻⁶	3.7	0.7542·10 ⁻¹²	39.8	0.2350	270.6	0.1982·10 ⁻¹³	0.3966·10 ⁻¹²	0.1012·10 ⁻²²	
$\Delta \sigma$	0.8149·10 ⁻⁶	347.6	0.1603·10 ⁻⁶	281.8	0.3253	270.6	0.3505·10 ⁻⁶	0.1455·10 ⁻⁵	0.6027·10 ⁻⁶	

Table 3.4 - Eigenvalues and corresponding characteristic values for time point 150 (t = 596 s).

	short-period oscillation		phugoid		lateral oscillation		roll divergence		spiral mode
	z	θ (°)	z	θ (°)	z	θ (°)	z	θ (°)	
λ_i Re	$-0.9485 \cdot 10^{-3}$		$-0.2730 \cdot 10^{-2}$		$0.3817 \cdot 10^{-3}$		$-0.6806 \cdot 10^{-4}$		$-0.8865 \cdot 10^{-15}$
Im	± 0.6923		$\pm 0.2006 \cdot 10^{-2}$		± 1.432		$\pm 0.1084 \cdot 10^{-2}$		-
P (s)	9.1		3,132.0		4.4		5,794.7		∞
$T_{1/2}$ (s)	730.8		253.9		-1,815.7		10,183.9		$0.782 \cdot 10^{15}$
ζ (-)	$0.137 \cdot 10^{-2}$		0.806		$-0.267 \cdot 10^{-3}$		0.063		-
ω_n (rad/s)	0.692		$0.339 \cdot 10^{-2}$		1.432		$0.109 \cdot 10^{-2}$		-
μ_i	z	θ (°)	z	θ (°)	z	θ (°)	z	θ (°)	z
ΔV	1.0000	276.0	0.0025	319.8	$0.1063 \cdot 10^{-1}$	270.1	$0.4720 \cdot 10^{-3}$	72.2	$0.4763 \cdot 10^{-5}$
$\Delta \gamma$	$0.4694 \cdot 10^{-4}$	275.1	$0.6628 \cdot 10^{-6}$	87.0	$0.2809 \cdot 10^{-3}$	0.5	$0.2126 \cdot 10^{-6}$	57.1	$0.6368 \cdot 10^{-11}$
ΔR	0.3553	5.2	1.0000	50.9	1.0000	270.5	1.0000	330.7	1.0000
Δp	$0.7156 \cdot 10^{-6}$	275.8	$0.1981 \cdot 10^{-8}$	288.2	0.5030	0.4	$0.2391 \cdot 10^{-9}$	323.5	$0.1658 \cdot 10^{-9}$
Δq	0.0163	276.3	$0.1057 \cdot 10^{-8}$	304.4	$0.1427 \cdot 10^{-3}$	270.3	$0.1008 \cdot 10^{-8}$	4.8	$0.7193 \cdot 10^{-9}$
Δr	$0.5546 \cdot 10^{-7}$	275.8	$0.1535 \cdot 10^{-9}$	288.2	0.0390	0.4	$0.1853 \cdot 10^{-10}$	323.5	$0.1947 \cdot 10^{-9}$
$\Delta \alpha$	0.0236	6.2	$0.7242 \cdot 10^{-7}$	319.8	$0.4260 \cdot 10^{-3}$	0.3	$0.1356 \cdot 10^{-7}$	72.2	$0.1368 \cdot 10^{-9}$
$\Delta \beta$	$0.1410 \cdot 10^{-6}$	5.8	$0.1911 \cdot 10^{-11}$	324.5	0.2050	270.4	$0.7395 \cdot 10^{-13}$	49.9	$0.2217 \cdot 10^{-23}$
$\Delta \sigma$	$0.9087 \cdot 10^{-6}$	328.9	$0.1993 \cdot 10^{-6}$	290.1	0.2867	270.4	$0.3978 \cdot 10^{-6}$	357.1	$0.2623 \cdot 10^{-6}$

Table 3.5 - Eigenvalues and corresponding characteristic values for time point 200 ($t = 796$ s).

λ_j	Re	short-period oscillation		phugoid		lateral oscillation		roll divergence		spiral mode
		z	θ (°)	z	θ (°)	z	θ (°)	z	θ (°)	
		-0.3245·10 ⁻²		-0.4386·10 ⁻²		0.1665·10 ⁻²		-0.1949·10 ⁻²		0.2946·10 ⁻¹⁴
	Im	±0.6936		±0.2865·10 ⁻²		±1.496		±0.4996·10 ⁻⁴		-
	P (s)	9.1		2192.8		4.2		12,577.2		∞
	T _½ (s)	213.6		158.0		-416.2		355.7		-0.235·10 ¹⁵
	ζ (-)	0.468·10 ⁻²		0.837		-0.111·10 ⁻²		1.000		-
	ω _n (rad/s)	0.694		0.524·10 ⁻²		1.500		0.195·10 ⁻²		-
H_I	ΔV	1.0000	283.5	0.2864·10 ⁻²	355.8	0.0138	271.5	0.8188·10 ⁻³	300.5	0.9978·10 ⁻⁵
	ΔY	0.1143·10 ⁻³	282.6	0.1725·10 ⁻⁵	325.9	0.5001·10 ⁻³	2.2	0.6430·10 ⁻⁶	300.1	0.1054·10 ⁻⁹
	ΔR	0.5387	13.0	1.0000	293.2	1.0000	272.2	1.0000	298.7	1.0000
	Δp	0.2483·10 ⁻⁵	283.1	0.8595·10 ⁻⁸	352.0	0.2990	2.2	0.2238·10 ⁻⁸	300.2	0.2914·10 ⁻⁹
	Δq	0.0127	284.2	0.5398·10 ⁻⁸	335.4	0.1345·10 ⁻³	271.7	0.3456·10 ⁻⁸	299.6	0.1101·10 ⁻⁸
	Δr	0.2959·10 ⁻⁶	283.1	0.1024·10 ⁻⁸	352.0	0.0356	2.2	0.2667·10 ⁻⁹	300.2	0.3884·10 ⁻⁹
	Δα	0.0183	13.8	0.1486·10 ⁻⁶	355.8	0.4180·10 ⁻³	1.7	0.4247·10 ⁻⁷	300.5	0.5174·10 ⁻⁹
	Δβ	0.3646·10 ⁻⁶	12.8	0.9533·10 ⁻¹¹	25.2	0.0947	272.2	0.9237·10 ⁻¹²	301.6	0.8725·10 ⁻²³
	Δσ	0.6543·10 ⁻⁵	306.0	0.6393·10 ⁻⁶	28.3	0.1776	272.2	0.3700·10 ⁻⁶	298.5	0.2211·10 ⁻⁶

Table 3.6 - Eigenvalues and corresponding characteristic values for time point 250 (t = 996 s).

λ_i	Re	former short-period oscillation		periodic pitch/roll mode		lateral oscillation		pitch/roll divergence		spiral mode	
		ΔV	$\Delta \gamma$	ΔR	Δp	Δq	Δr	$\Delta \alpha$	$\Delta \beta$	$\Delta \sigma$	
		-0.5078	0.3695	-0.0157		0.0229	0.0814	-0.2892·10 ⁻³	0.9450·10 ⁻¹⁴		
	Im	-	-	±0.7035·10 ⁻²		±1.113	-	-	-		
	P (s)	∞	∞	893.1		5.6	∞	∞	∞		
	T _½ (s)	1.4	-1.9	44.3		-30.3	-8.5	2,396.8	-0.734·10 ¹⁴		
	ζ (-)	-	-	0.912		-0.021	-	-	-		
	ω _n (rad/s)	-	-	0.017		1.113	-	-	-		
μ_I	ΔV	0.6721	0.5181	0.1758·10 ⁻²	9.3	0.0256	0.1215	0.3228·10 ⁻⁴	0.3896·10 ⁻⁵		
	$\Delta \gamma$	0.4118·10 ⁻³	0.2972·10 ⁻³	0.1598·10 ⁻⁴	14.0	0.1027·10 ⁻²	0.6490·10 ⁻⁴	0.2695·10 ⁻⁶	0.3286·10 ⁻⁹		
	ΔR	1.0000	1.0000	1.0000	349.9	1.0000	1.0000	1.0000	1.0000		
	Δp	0.2036·10 ⁻⁴	0.1595·10 ⁻⁴	0.4226·10 ⁻⁶	48.5	0.0808	0.3478·10 ⁻⁵	0.3717·10 ⁻⁸	0.5878·10 ⁻⁹		
	Δq	0.3447·10 ⁻²	0.1822·10 ⁻²	0.1025·10 ⁻⁶	278.8	0.7476·10 ⁻⁴	0.2963·10 ⁻⁴	0.6599·10 ⁻⁸	0.2753·10 ⁻⁸		
	Δr	0.3419·10 ⁻⁵	0.2680·10 ⁻⁵	0.7098·10 ⁻⁷	48.5	0.0136	0.5842·10 ⁻⁶	0.6244·10 ⁻⁹	0.1219·10 ⁻⁸		
	$\Delta \alpha$	0.7534·10 ⁻²	0.4372·10 ⁻²	0.3333·10 ⁻⁵	9.5	0.4170·10 ⁻³	0.2428·10 ⁻³	0.6126·10 ⁻⁷	0.7396·10 ⁻⁸		
	$\Delta \beta$	0.1604·10 ⁻⁵	0.9150·10 ⁻⁶	0.1125·10 ⁻⁸	72.7	0.0140	0.4397·10 ⁻⁷	0.1669·10 ⁻¹²	0.7179·10 ⁻²¹		
	$\Delta \sigma$	0.2726·10 ⁻⁴	0.7653·10 ⁻⁴	0.1671·10 ⁻⁴	48.9	0.0722	0.4241·10 ⁻⁴	0.3279·10 ⁻⁶	0.2092·10 ⁻⁶		

Table 3.7 - Eigenvalues and corresponding characteristic values for time point 300 (t = 1196 s).

λ_i	former short-period oscillation		periodic pitch/roll mode		lateral oscillation		pitch/roll divergence		spiral mode	
	Re	Im								
$P(s)$	-1.0884	-	0.9518	-0.0213	0.0392	0.0401	-0.1059·10 ⁻³	-0.9138·10 ⁻¹⁵	-	-
$T_{1/2}(s)$	0.6	∞	-0.7	32.6	430.4	±1.343	∞	∞	∞	∞
$\zeta(-)$	-	-	-	0.825	-0.029	-17.7	-	-	-	-
$\omega_n(\text{rad/s})$	-	-	-	0.026	1.343	-	-	-	-	-
μ_i	z		z		θ (°)		z		z	
ΔV	0.9895	0.8871	0.6586·10 ⁻²	52.8	0.0268	339.8	0.0419	0.3379·10 ⁻⁴	0.1613·10 ⁻⁴	0.1613·10 ⁻⁴
$\Delta \gamma$	0.1275·10 ⁻²	0.1111·10 ⁻²	0.3613·10 ⁻⁴	68.9	0.1815·10 ⁻²	72.9	0.4591·10 ⁻⁴	0.1498·10 ⁻⁶	0.3187·10 ⁻⁸	0.3187·10 ⁻⁸
ΔR	1.0000	1.0000	1.0000	35.0	1.0000	341.4	1.0000	1.0000	1.0000	1.0000
Δp	0.3547·10 ⁻⁴	0.3566·10 ⁻⁴	0.1380·10 ⁻⁵	305.5	0.1259	74.5	0.1785·10 ⁻⁵	0.3427·10 ⁻⁸	0.6985·10 ⁻⁹	0.6985·10 ⁻⁹
Δq	0.0266	0.0220	0.5895·10 ⁻⁶	343.9	0.3583·10 ⁻³	336.1	0.4785·10 ⁻⁵	0.8551·10 ⁻⁸	0.3164·10 ⁻⁸	0.3164·10 ⁻⁸
Δr	0.1701·10 ⁻⁵	0.1710·10 ⁻⁵	0.6617·10 ⁻⁷	305.5	0.6041·10 ⁻²	74.5	0.8561·10 ⁻⁷	0.1644·10 ⁻⁹	0.1977·10 ⁻⁸	0.1977·10 ⁻⁸
$\Delta \alpha$	0.0267	0.0210	0.7066·10 ⁻⁵	52.8	0.4624·10 ⁻³	71.3	0.4525·10 ⁻⁴	0.3632·10 ⁻⁷	0.1734·10 ⁻⁷	0.1734·10 ⁻⁷
$\Delta \beta$	0.5123·10 ⁻⁵	0.4504·10 ⁻⁵	0.4726·10 ⁻⁸	339.9	0.0225	346.2	0.9498·10 ⁻⁸	0.4817·10 ⁻¹³	0.1735·10 ⁻²²	0.1735·10 ⁻²²
$\Delta \sigma$	0.2715·10 ⁻³	0.2695·10 ⁻³	0.4661·10 ⁻⁴	298.7	0.0911	342.9	0.3464·10 ⁻⁴	0.3238·10 ⁻⁶	0.2104·10 ⁻⁶	0.2104·10 ⁻⁶

Table 3.8 - Eigenvalues and corresponding characteristic values for time point 314 ($t = 1252$ s)).

Chapter 4

Design of the Controller

4.1. Introduction.

The conclusion, which can be drawn from the results obtained in Section 3.3, is that when the HORUS-2B will be uncontrolled, it will end up in unstable oscillations after a small perturbation. For this reason, and because of the fact that we need to guide the vehicle along a specified (reference) trajectory, we must have an attitude control system. As we saw in the previous chapter, an oscillation in pitch will in principle not result in lateral oscillations. Also the opposite is true: lateral oscillations will not induce a pitch oscillation. In other words, the pitch and lateral motion are said to be decoupled.

To simplify the design of the controller, we will use this fact of decoupling by separating the controller into two parts: a longitudinal and a lateral controller. The longitudinal controller consists of an inner and an outer loop. The inner loop takes care of stability augmentation while the outer loop provides the corrective control, i.e., to make the actual attitude approach the commanded one in a finite time. The stability augmentation, or longitudinal trim, is executed by aerodynamic means only, i.e., in the first instance the body flap is used, and in case the maximum deflection has been reached, the elevators (symmetric deflection of the elevons), are used for additional control. For corrective longitudinal control, the elevators and pitch jets will be used. Lateral control consists of only the outer, corrective loop, because only small moments are required to maintain stability. This control is achieved by using the ailerons (asymmetric deflection of the elevons), the rudders, and the roll and yaw jets. The state of the vehicle is fed back into the two controllers. In order to react to the strongly varying dynamics, varying gains are used in both corrective control loops. In Fig. 4.1, the layout of the controller has been schematically depicted. In this respect, we mention that there are in principle three controllers discussed in this report: a longitudinal and a lateral controller, that are designed independently from each other, and an integrated controller, combining the longitudinal and lateral controllers.

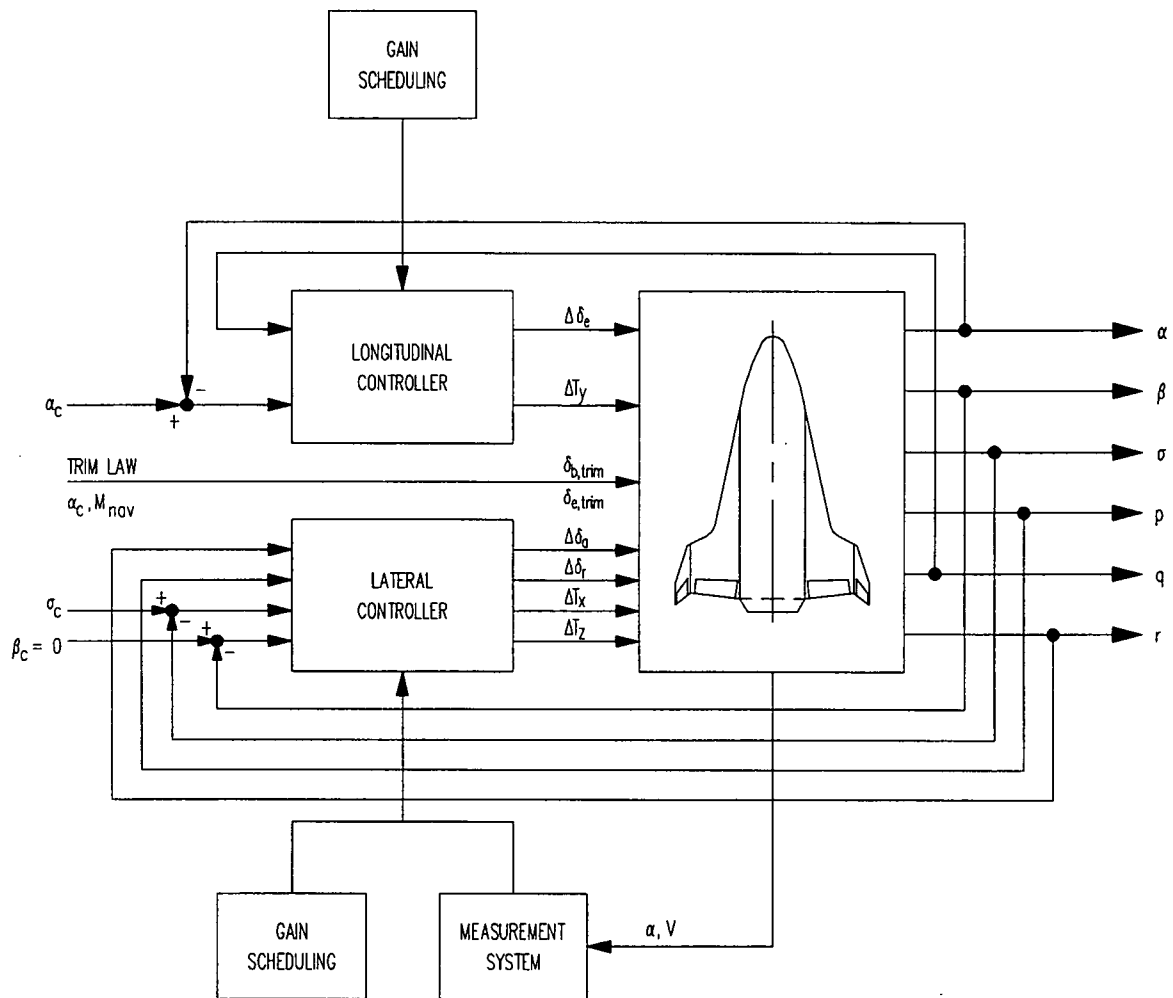


Fig. 4.1 - Schematic layout of the HORUS-2B attitude controller.

In this chapter, we will discuss the linear state-feedback controller with gain scheduling, the control laws of which are based on a design proposed by MBB (1988b). In Chapter 1, we motivated the choice for this type of controller, being easy to understand and implement, and not yet applied to a winged re-entry vehicle before. Whereas MBB derived the values for the gains by means of pole placement, in principle a technique that can easily be applied to Single-Input Single-Output systems, we will apply linear-quadratic optimal control theory, particularly suitable for Multiple-Input Multiple-Output systems.

The layout of the chapter is as follows. First, in Section 4.2, we give a synopsis of the derivation of the reduced matrix Riccati equation, which we will use in successive sections to compute the gains of the pitch and the lateral controller. Then, in Section 4.3, the design of the pitch corrective-controller will be discussed. The section begins with a description of the reduced state-space model, including the corresponding eigenvalues (the plot showing the eigenvalues is called the root locus). After introducing the state-feedback control law, the feedback gains for the longitudinal controller are computed. In Section 4.4, the design of the lateral corrective-controller is given, following the same line of thought as for the longitudinal controller.

4.2. The matrix Riccati equation.

Suppose, we have a state-space system given by

$$\dot{\mathbf{x}} = \mathbf{A}\mathbf{x} + \mathbf{B}\mathbf{u} \quad (4.2.1a)$$

$$\mathbf{y} = \mathbf{C}\mathbf{x} + \mathbf{D}\mathbf{u} \quad (4.2.1b)$$

In case of state-feedback, the control law is given by

$$\mathbf{u} = -\mathbf{K}\mathbf{x} \quad (4.2.2)$$

where \mathbf{K} is a time independent feedback or gain matrix. Eq. (4.2.2) substituted into Eq. (4.2.1a) yields

$$\dot{\mathbf{x}} = (\mathbf{A} - \mathbf{B}\mathbf{K})\mathbf{x} \quad (4.2.3)$$

The characteristic equation of Eq. (4.2.3), which gives us the eigenvalues and corresponding eigenmotion of the closed-loop system is given by

$$\det[\mathbf{A} - \mathbf{B}\mathbf{K} - \lambda \mathbf{I}] = 0 \quad (4.2.4)$$

As becomes obvious while studying the above equation, we can change the eigenvalues of the closed-loop system by varying the gain matrix \mathbf{K} . Whether the system will be controllable, however, is not only depending on the values of these gains. The system in itself should at least be controllable, and it is not necessarily true that this is always the case. *Controllability* is in this case defined as follows (Kuo, 1987):

Given a linear time-invariant system as described by Eqs. (4.2.1), the state $\mathbf{x}(t)$ is said to be controllable at $t = t_0$ if there exists a piece-wise continuous (and finite) input $\mathbf{u}(t)$ that will drive the state to any final state $\mathbf{x}(t_f)$ for a finite time $t_f \geq t_0$. If every state $\mathbf{x}(t_0)$ of the system is controllable in a finite time interval, the system is said to be completely state controllable or simply state controllable.

The condition of controllability depends on the coefficient matrices \mathbf{A} and \mathbf{B} .

To determine whether the system is unstable or not, it is also necessary that (at least the unstable) motions of the system are observable. *Observability* is defined by Kuo (1987) as:

Given a linear time-invariant system as described by Eqs. (4.2.1), the state $\mathbf{x}(t)$ is said to be observable if given any input $\mathbf{u}(t)$, there exist a finite time $t_f \geq t_0$ such that the knowledge of i) $\mathbf{u}(t)$ for $t_0 \leq t < t_f$ ii) the matrices \mathbf{A} , \mathbf{B} , \mathbf{C} and \mathbf{D} and iii) the output $\mathbf{y}(t)$ for $t_0 \leq t < t_f$ are sufficient to determine $\mathbf{x}(t_0)$. If every state of the system is observable for a finite time t_f , we say that the system is completely observable, or simply observable.

To check whether a system is controllable and observable, it is necessary and sufficient that the controllability matrix

$$\begin{bmatrix} B & AB & A^2B & \dots & A^{n-1}B \end{bmatrix} \quad (4.2.5)$$

and observability matrix

$$\begin{bmatrix} C^T & A^T C^T & (A^T)^2 C^T & \dots & (A^T)^{n-1} C^T \end{bmatrix} \quad (4.2.6)$$

have a rank n , i.e., the dimension of the state vector x . When not all of the eigenmotions are part of the observable and controllable state space, then only those eigenmotions that are part of it can be influenced by state feedback¹³.

The feedback matrix can be computed in a mathematically closed form. An indirect method is Quadratic Optimal Control, in which a mathematically defined cost criterion is minimised. A direct method is the so-called pole placement, in which K is solved on basis of the specified poles of the closed-loop system. In our study we will continue with the indirect method, where we will use the following quadratic cost criterion (Gopal, 1989):

$$J = \int_0^{\infty} (x^T Q x + u^T R u) dt \quad (4.2.7)$$

where the term $x^T Q x$ represents the control deviation and the term $u^T R u$ the control effort. Q is a real positive semi-definite matrix, whereas R is a real symmetric positive definite matrix, so any x , $u \neq 0$ cannot give a negative contribution to J . By varying Q and R more weight can be given to the control deviation, resulting in a faster response, or the control effort, giving smaller control signals. By varying each of the elements of Q and R , each of the corresponding elements of x and u can be addressed. Brandt and Van den Broek (1984) state that defining Q and R is usually done in an iterative manner, and that a good first choice is given by 'Bryson's Rule':

$$Q = \text{diag} \left\{ \frac{1}{\Delta x_{1\max}^2}, \frac{1}{\Delta x_{2\max}^2}, \dots, \frac{1}{\Delta x_{n\max}^2} \right\} \quad (4.2.8)$$

with $\Delta x_{i\max}$ the maximum allowable amplitude of the i -th element of the state vector, and

¹³ We assume that our system is fully observable. The output vector is equated to the state vector, which means that C is equal to the identity matrix.

$$R = \text{diag} \left\{ \frac{1}{u_{1\max}^2} \quad \frac{1}{u_{2\max}^2} \quad \dots \quad \frac{1}{u_{m\max}^2} \right\} \quad (4.2.9)$$

with $u_{j\max}$ the maximum allowable value of the j -th control.

Response tests must prove that these weighting matrices have been correctly selected. If not, the values of the diagonal elements should be adjusted. Frangos and Yavin (1992) propose a synthesis procedure that automatically varies the weighting matrices and computes the gains in an iterative manner, based on minimisation of the quadratic cost criterion J . Luo and Lan (1995), finally, describe a systematic method to determine the weighting matrices, so as to produce specified closed-loop eigenvalues. Implementation of either algorithm, however, is considered to be beyond the scope of the current study.

To find an expression for K , we substitute Eq. (4.2.2) into the cost criterion Eq. (4.2.7), yielding

$$J = \int_0^{\infty} \mathbf{x}^T (\mathbf{Q} + \mathbf{K}^T \mathbf{R} \mathbf{K}) \mathbf{x} dt \quad (4.2.10)$$

To solve the optimisation problem, we will use the stability analysis according to Lyapunov. The integrand of the above integral equation is considered to be the negative time derivative of the Lyapunov function $V(\mathbf{x})$:

$$V(\mathbf{x}) = \mathbf{x}^T \mathbf{P} \mathbf{x} \quad (4.2.11)$$

which attaches a mathematically formulated fictitious energy to the system as a function of the state vector (Gopal, 1989). This makes the minimisation of J to be a minimisation of the integrated fictitious power. \mathbf{P} is a positive definite matrix, so every deviation of the state from the equilibrium state is treated as a positive energy. Based on the above, we may write

$$\mathbf{x}^T (\mathbf{Q} + \mathbf{K}^T \mathbf{R} \mathbf{K}) \mathbf{x} = -\frac{d}{dt} (\mathbf{x}^T \mathbf{P} \mathbf{x}) \quad (4.2.12)$$

Differentiating results in

$$\begin{aligned} \mathbf{x}^T (\mathbf{Q} + \mathbf{K}^T \mathbf{R} \mathbf{K}) \mathbf{x} &= -\dot{\mathbf{x}}^T \mathbf{P} \mathbf{x} - \mathbf{x}^T \mathbf{P} \dot{\mathbf{x}} \\ &= -\mathbf{x}^T \left[(\mathbf{A} - \mathbf{B} \mathbf{K})^T \mathbf{P} + \mathbf{P} (\mathbf{A} - \mathbf{B} \mathbf{K}) \right] \mathbf{x} \end{aligned} \quad (4.2.13)$$

Since the above expression should be valid for all \mathbf{x} , the following expression holds:

$$(A - BK)^T P + P(A - BK) = -(Q + K^T R K) \quad (4.2.14)$$

or

$$\tilde{A}^T P + P \tilde{A} = -\tilde{Q} \quad (4.2.15)$$

with

$$\begin{aligned} \tilde{A} &= A - BK \\ \tilde{Q} &= Q + K^T R K \end{aligned}$$

Eq. (4.2.15) is called the *Lyapunov Equation*. Gopal (1989) states that the linear system

$$\dot{x} = \tilde{A}x$$

is globally asymptotically stable¹⁴ at the origin if and only if for any symmetric positive definite matrix \tilde{Q} , there exists a symmetric positive definite matrix P that satisfies the Lyapunov Equation. This gives us the possibility to check whether our system can be stabilised or not.

Continuing with Eqs. (4.2.10) and (4.2.12), the cost criterion can be written as:

$$J = -x^T P x \Big|_0^\infty = x(0)^T P x(0) \quad (4.2.16)$$

assuming that our system is asymptotically stable, or in mathematical terms

$$\lim_{t \rightarrow \infty} x(t) = 0$$

Minimising J is now the same as minimising the right-hand term of Eq. (4.2.16) by means of K . Because R is positive definite, we may decompose it as

$$R = S^T S \quad (4.2.17)$$

Substituting this into the Lyapunov Equation Eq. (4.2.14) yields

$$(A^T - K^T B^T)P + P(A - BK) + Q + K^T S^T S K = 0 \quad (4.2.18)$$

which can be further expanded to

¹⁴ Kuo (1987) defines asymptotic stability as follows: 'If the zero-input response $x(t)$, subject to the finite initial state $x(t_0)$, returns to the equilibrium state $x(t) = 0$ as t approaches infinity, the system is said to be stable; otherwise, the system is unstable. This type of stability is also known as the asymptotic stability.'

$$\mathbf{A}^T \mathbf{P} + \mathbf{P} \mathbf{A} - \mathbf{P} \mathbf{B} \mathbf{R}^{-1} \mathbf{B}^T \mathbf{P} + \mathbf{Q} + [\mathbf{S} \mathbf{K} - (\mathbf{S}^T)^{-1} \mathbf{B}^T \mathbf{P}]^T [\mathbf{S} \mathbf{K} - (\mathbf{S}^T)^{-1} \mathbf{B}^T \mathbf{P}] = \mathbf{0} \quad (4.2.19)$$

The last term on the left-hand side can be treated as a function of \mathbf{K} , so \mathbf{J} is minimised when

$$\mathbf{x}^T [\mathbf{S} \mathbf{K} - (\mathbf{S}^T)^{-1} \mathbf{B}^T \mathbf{P}]^T [\mathbf{S} \mathbf{K} - (\mathbf{S}^T)^{-1} \mathbf{B}^T \mathbf{P}] \mathbf{x} \quad (4.2.20)$$

is minimised w.r.t. \mathbf{K} . Since Eq. (4.2.20) is either zero or greater than zero, the minimum is found when Eq. (4.2.20) is zero, or

$$\mathbf{S} \mathbf{K} = (\mathbf{S}^T)^{-1} \mathbf{B}^T \mathbf{P} \quad (4.2.21)$$

so that the optimal feedback matrix \mathbf{K} can be expressed as a function of \mathbf{P} :

$$\mathbf{K} = \mathbf{S}^{-1} (\mathbf{S}^T)^{-1} \mathbf{B}^T \mathbf{P} = \mathbf{R}^{-1} \mathbf{B}^T \mathbf{P} \quad (4.2.22)$$

Substituting Eq. (4.2.22) into Eq. (4.2.19) gives us \mathbf{P} as a function of the system matrices \mathbf{A} and \mathbf{B} , and the weight matrices \mathbf{Q} and \mathbf{R} :

$$\mathbf{A}^T \mathbf{P} + \mathbf{P} \mathbf{A} - \mathbf{P} \mathbf{B} \mathbf{R}^{-1} \mathbf{B}^T \mathbf{P} + \mathbf{Q} = \mathbf{0} \quad (4.2.23)$$

Eq. (4.2.23) is also known as the *matrix Riccati equation*.

4.3. Longitudinal controller.

4.3.1. Reduced system for symmetric motion.

In order to decouple the pitch motion from the lateral motion, we put $\Delta\beta$ and $\Delta\sigma$ to zero. Furthermore, we will only consider rotational dynamics, so we neglect any contribution due to ΔV , $\Delta\gamma$ and ΔR . We can do this since the dynamics of the translational motion have much lower frequencies than the high-frequency rotational dynamics. As an approximation, the following system follows from Eqs. (2.2.17) through (2.2.25):

$$\Delta\dot{\mathbf{q}} = \frac{1}{I_{yy}} \left[\frac{\partial C_m}{\partial \alpha} q_{dyn} S_{ref} c_{ref} \Delta\alpha + \frac{\partial C_m}{\partial \delta_e} q_{dyn} S_{ref} c_{ref} \Delta\delta_e + \Delta T_y \right] \quad (4.3.1)$$

$$\Delta \dot{\alpha} = \Delta \dot{q} - \frac{1}{m V_0} \frac{\partial C_L}{\partial \alpha} q_{dyn} S_{ref} \Delta \alpha \quad (4.3.2)$$

In state-space form, the above system can be written as

$$\begin{pmatrix} \Delta \dot{q} \\ \Delta \dot{\alpha} \end{pmatrix} = \begin{bmatrix} 0 & \frac{1}{I_{yy}} \frac{\partial C_m}{\partial \alpha} q_{dyn} S_{ref} c_{ref} \\ 1 & -\frac{1}{m V_0} \frac{\partial C_L}{\partial \alpha} q_{dyn} S_{ref} \end{bmatrix} \begin{pmatrix} \Delta q \\ \Delta \alpha \end{pmatrix} + \begin{bmatrix} \frac{1}{I_{yy}} \frac{\partial C_m}{\partial \delta_e} q_{dyn} S_{ref} c_{ref} & \frac{1}{I_{yy}} \\ 0 & 0 \end{bmatrix} \begin{pmatrix} \Delta \delta_e \\ \Delta T_y \end{pmatrix} \quad (4.3.3)$$

so the matrices **A** and **B** are equal to

$$\mathbf{A} = \begin{bmatrix} 0 & \frac{1}{I_{yy}} \frac{\partial C_m}{\partial \alpha} q_{dyn} S_{ref} c_{ref} \\ 1 & -\frac{1}{m V_0} \frac{\partial C_L}{\partial \alpha} q_{dyn} S_{ref} \end{bmatrix} \quad (4.3.4)$$

$$\mathbf{B} = \begin{bmatrix} \frac{1}{I_{yy}} \frac{\partial C_m}{\partial \delta_e} q_{dyn} S_{ref} c_{ref} & \frac{1}{I_{yy}} \\ 0 & 0 \end{bmatrix} \quad (4.3.5)$$

4.3.2. Root locus of the reduced system.

Looking back at Chapter 3, where we computed the eigenvalues of the homogeneous part of the state equation, we will do the same here for the simplified equation, Eq. (4.3.3), flying along the same nominal trajectory as discussed in Section 3.2. The results are shown in Fig. 4.2 through 4.5. Comparing the results with the corresponding graphs in Section 3.3 shows a similar behaviour of the related eigenvalues, which indicates that the choice of decoupling the two types of motion was justified. Note that the eigenmotion shown in Fig. 4.2 corresponds with the short-period oscillation. Neglecting the translational motion has indeed not influenced this motion, so our assumption of frequency separation has been correct.

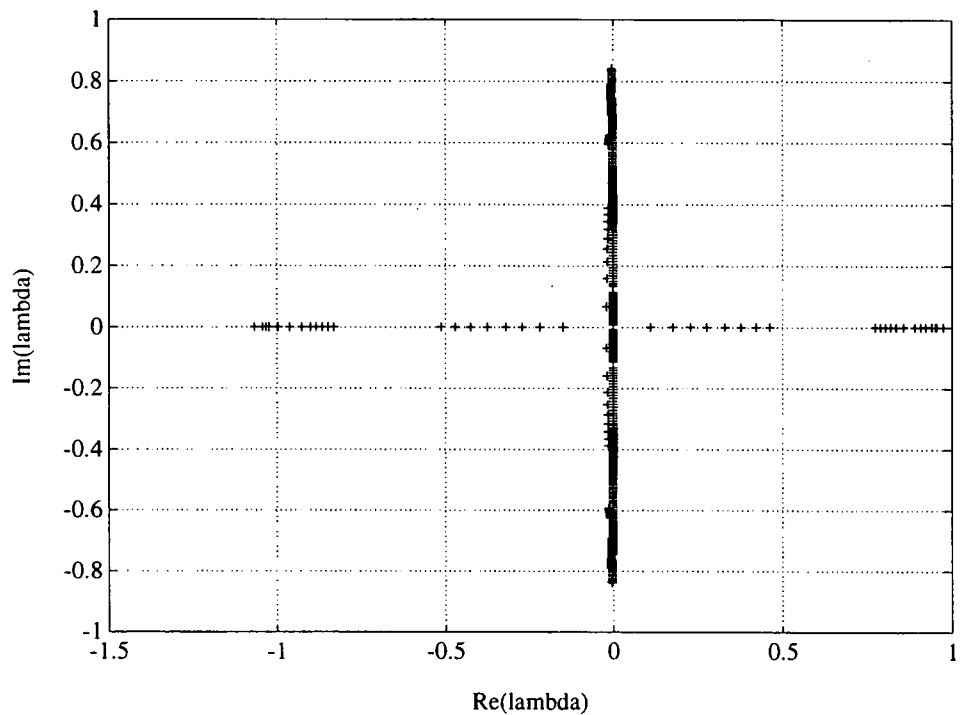


Fig. 4.2 - Variation of the eigenvalues of symmetric motion along the nominal trajectory.

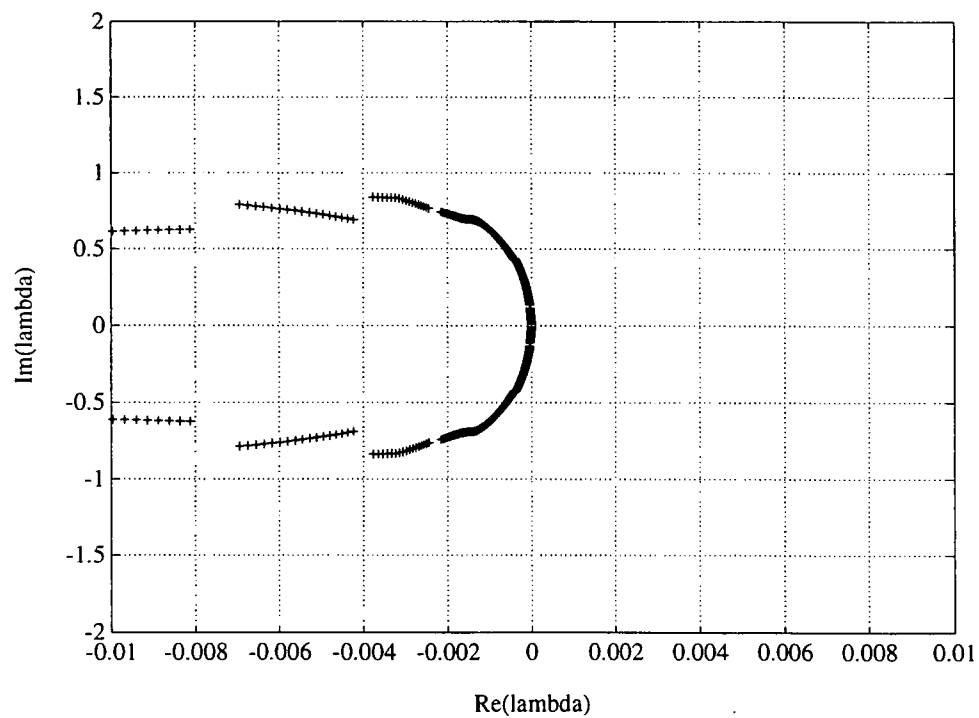


Fig. 4.3 - Detail of the eigenvalue plot centred around the origin for the symmetric motion.

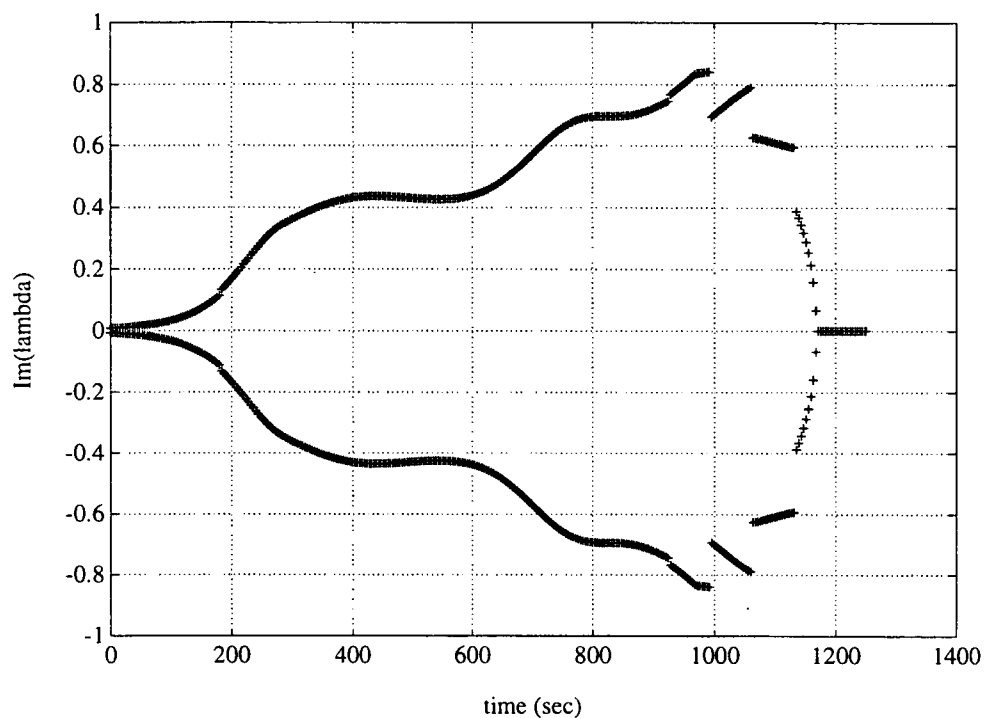


Fig. 4.4 - The imaginary parts of the eigenvalues as a function of flight time for the symmetric motion.

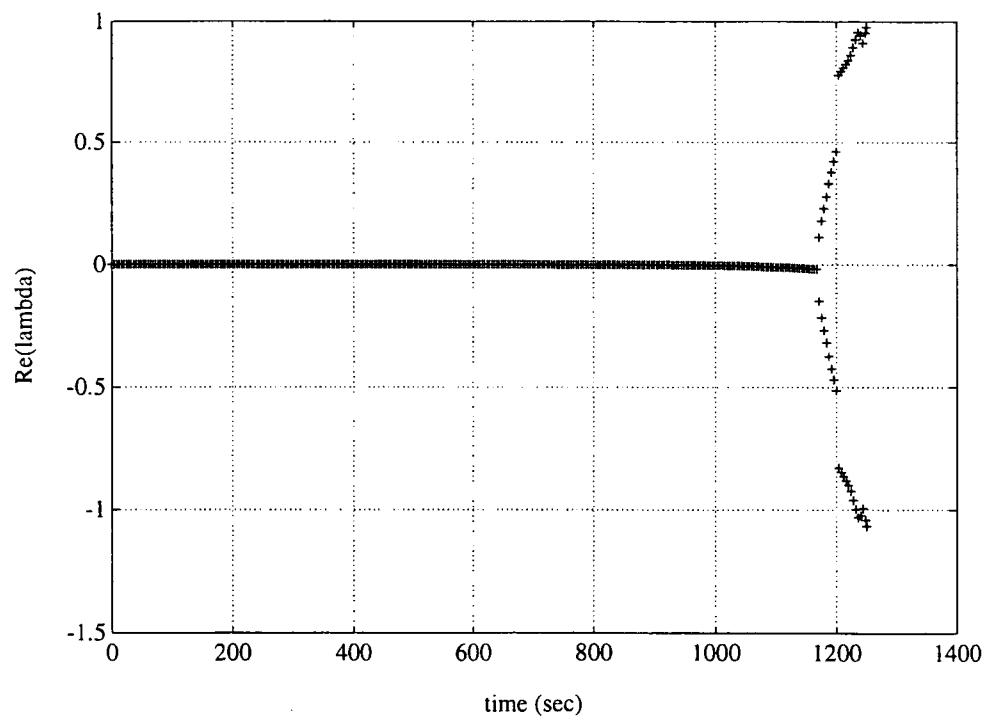


Fig. 4.5 - The real parts of the eigenvalues as a function of flight time for the symmetric motion.

4.3.3. Selection of pitch controls.

The aerodynamic control surfaces can only be efficiently used when the dynamic pressure is sufficiently high, otherwise large deflections will result in only small control moments. This means that for the upper layers of the atmosphere only the Reaction Control System will be used, whereas at low altitudes full control can be achieved with the control surfaces. The following criterion have been used by MBB (1988).

As long as

$$\left| \frac{\partial M}{\partial \delta_e} \delta_{e_{\max}} \right| < 0.1 T_{y_{\max}} \quad (4.3.6a)$$

then the aerodynamic gains (K_1 and K_2 , as we will see later) are put to zero. If

$$\left| \frac{\partial M}{\partial \delta_e} \delta_{e_{\max}} \right| > 0.9 T_{y_{\max}} \quad (4.3.6b)$$

then the reaction-control gains ($\tilde{K}_1 = \tilde{K}_2$) are equal to zero. When both actuators are operating then $|K_1| = |\tilde{K}_1|$ and $|K_2| = |\tilde{K}_2|$. The maximum elevator deflection angle and the maximum thrust of the pitch jet are

$$\delta_{e_{\max}} = 40^\circ$$

$$T_{y_{\max}} = 10,400 \text{ Nm}$$

The basic idea behind this is to select one of the two controls when its effectiveness is more than 10% of the other.

In case the above switch criterion is used, there are some points of interest. In the first place, the assumption that the contribution of the elevator to the pitch moment is linear over the full range of elevator deflection is (of course) not correct. This fact can be overlooked if the difference in the resulting pitch moment is not that large. In our case, for the larger part of the trajectory we compute the derivative for a nominal deflection of 0° . Because the maximum deflection is 40° , we found an overestimate of the maximum pitch control moment of more than 200 percent. Of course, this is only of importance when the control system actually commands such large deflections. In the second place, the absolute pitch moment for a deflection of -40° differs significantly from its positive counterpart (between -50 and +50%), see MBB (1988a).

To avoid any possible problems, we will just base the selection of the controls on a scheme used for the Space Shuttle (Cooke, 1982). In Fig. 4.7, this scheme is plotted. For pitch control, we see that the elevators are activated at a dynamic pressure of 100 N/m^2 ($\approx 2 \text{ psf}$). The pitch jets will start working at the entry interface (in principle a dynamic pressure of 0 N/m^2) and will

continue to do so until a dynamic pressure of 1000 N/m^2 ($\approx 20 \text{ psf}$) has been reached.

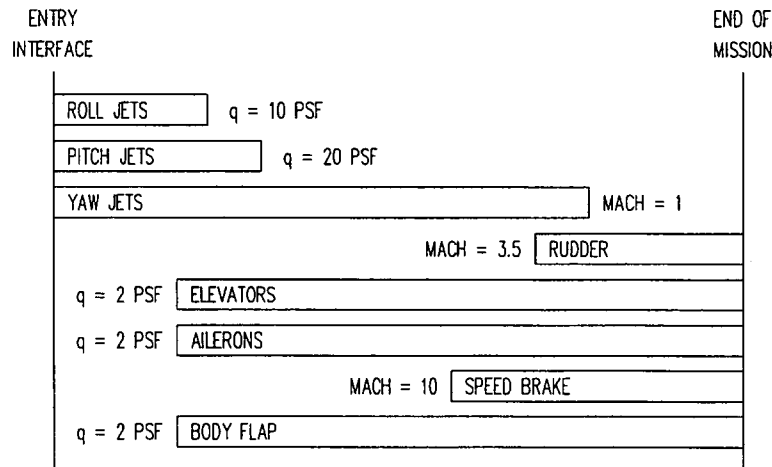


Fig. 4.7 - Entry control modes for the Space Shuttle (based on Cook (1982)).

Since we compute the gain matrix by solving the reduced matrix Riccati equation, we will not predefine that the gains for reaction and aerodynamic control are equal when both control modes are operational, as is the case with MBB. If one of the control modes is not active, then the corresponding gains are put to zero.

4.3.4. Control laws.

The state feedback law is chosen to be a simple P-law (MBB, 1988b), see also Fig. 4.6 for a schematic representation:

$$\frac{\Delta \delta_e}{\delta_{e_{\max}}} = -K_1 \Delta q - K_2 \Delta \alpha \quad (4.3.7)$$

$$\frac{\Delta T_y}{T_{y_{\max}}} = -\tilde{K}_1 \Delta q - \tilde{K}_2 \Delta \alpha \quad (4.3.8)$$

where

$$\Delta \alpha = \alpha - \alpha_0 \approx \alpha - \alpha_c$$

α_c = commanded angle of attack from the guidance system (rad)

Two assumptions were made: in the first place, the rate of change of the angle of attack is equal to the pitch rate, which seems logical when we look at our simplified system of equations, Eq. (4.3.2), and in the second place we approximate the nominal angle of attack with the commanded one. The latter seems logical too, since we want to fly a nominal profile.

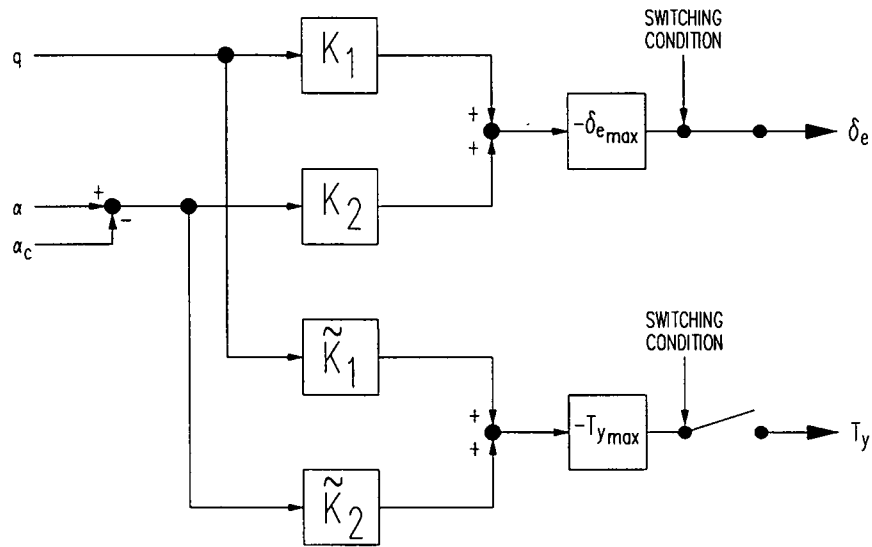


Fig. 4.6 - The longitudinal controller.

The above equations can be written in matrix form:

$$\begin{pmatrix} \Delta \delta_e \\ \Delta T_y \end{pmatrix} = - \begin{bmatrix} \delta_{e_{\max}} K_1 & \delta_{e_{\max}} K_2 \\ T_{y_{\max}} \tilde{K}_1 & T_{y_{\max}} \tilde{K}_2 \end{bmatrix} \begin{pmatrix} \Delta q \\ \Delta \alpha \end{pmatrix} \quad (4.3.9)$$

or, in symbolic notation,

$$\mathbf{u} = -\mathbf{K}\mathbf{x} \quad (4.3.10)$$

Substituting Eq. (4.3.10) into Eq. (4.2.1a) gives us

$$\dot{\mathbf{x}} = \mathbf{A}\mathbf{x} + \mathbf{B}\mathbf{u} = \mathbf{A}\mathbf{x} - \mathbf{B}\mathbf{K}\mathbf{x} = (\mathbf{A} - \mathbf{B}\mathbf{K})\mathbf{x} \quad (4.3.11)$$

which enables us to study the behaviour (i.e., eigenvalues) of the feedback system, once the gains have been selected. Or, as we mentioned before, we can influence the behaviour of the system by intelligently choosing the gains.

4.3.5. Computation of the feedback gains.

MBB computed the gains by pole placement, with as a starting point that the short period oscillation is well damped ($\zeta = 0.7$) and that a good tracking behaviour in pitch control is achieved. However, we will use an indirect method to find the proper gains of Eq. (4.3.9), with the following quadratic cost criterion:

$$J = \int_0^{\infty} (\mathbf{x}^T \mathbf{Q} \mathbf{x} + \mathbf{u}^T \mathbf{R} \mathbf{u}) dt \quad (4.3.12)$$

where the term $\mathbf{x}^T \mathbf{Q} \mathbf{x}$ represents the control deviation and the term $\mathbf{u}^T \mathbf{R} \mathbf{u}$ the control effort. The optimal gain matrix for this cost criterion is discussed in Section 4.2, Eq. (4.2.22),

$$\mathbf{K} = \mathbf{R}^{-1} \mathbf{B}^T \mathbf{P} \quad (4.3.13)$$

with the positive matrix \mathbf{P} following from the reduced matrix Riccati equation:

$$\mathbf{A}^T \mathbf{P} + \mathbf{P} \mathbf{A} - \mathbf{P} \mathbf{B} \mathbf{R}^{-1} \mathbf{B}^T \mathbf{P} + \mathbf{Q} = 0 \quad (4.3.14)$$

The matrices \mathbf{Q} and \mathbf{R} are in this case given by

$$\mathbf{Q} = \begin{bmatrix} \frac{1}{\Delta q_{\max}^2} & 0 \\ 0 & \frac{1}{\Delta \alpha_{\max}^2} \end{bmatrix} \quad (4.3.15)$$

$$\mathbf{R} = \begin{bmatrix} \frac{1}{\Delta \delta_{e_{\max}}^2} & 0 \\ 0 & \frac{1}{\Delta T_{y_{\max}}^2} \end{bmatrix} \quad (4.3.16)$$

Numerical values, which we will use, are:

$$\Delta q_{\max} = \infty \text{ (which means that the pitch rate is not used as a weighting factor)}$$

$$\Delta \alpha_{\max} = 2^\circ$$

$$\Delta \delta_{e_{\max}} = 40^\circ$$

$$\Delta T_{y_{\max}} = 10,400 \text{ Nm}$$

The value of $\Delta \alpha_{\max}$ has been chosen such, that, since the nominal angle of attack is close to the limit value, there is a small margin left. After calculating the gains, we will check in Chapter 5 what the damping factor and the tracking behaviour will be.

Basically, defining the weighting matrices is an iterative procedure, as we already mentioned in Section 4.2. An important aspect in this respect is, that we apply constant \mathbf{Q} and

R. However, it is quite well possible that in some flight phases we must change the weighting matrices so that the response of the vehicle will improve. As an example we refer to the paper by Hamilton (1982), who describes how the gains of the lateral aerosurface control loops had to be adjusted to give the correct performance. In this study, we will work with only one set of weighting matrices, but recognising the fact that this is not final. The references mentioned in Section 4.2 serve as a good basis, to improve the response of the controller if further study is going to be conducted.

The resulting gains can be found in Figs. 4.8 and 4.9. The three operational regimes, i.e., only reaction control, only aerodynamic control and the transition region where both reaction and aerodynamic control are used, can clearly be distinguished. Switching from one region to the other shows as discrete jumps in the gain values. The gains have been computed every four seconds (a total of 314 points). It is not necessary, however, to use all these gains since along some parts of the trajectory the gains do not vary that abruptly.

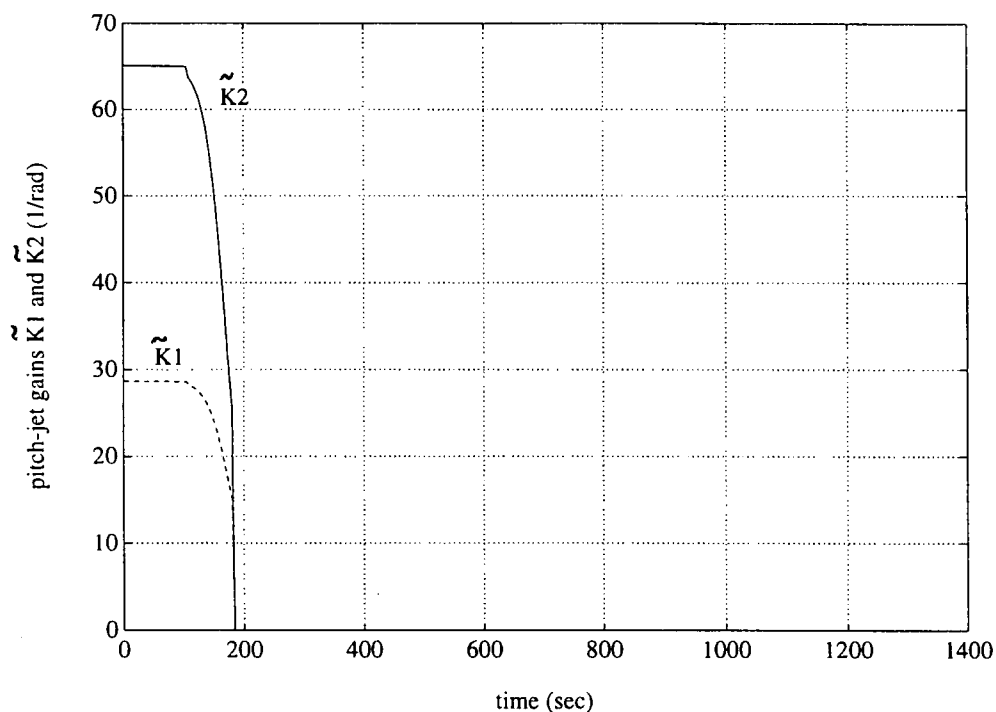


Fig. 4.8 - Pitch-jet gains \tilde{K}_1 and \tilde{K}_2 along the nominal trajectory.

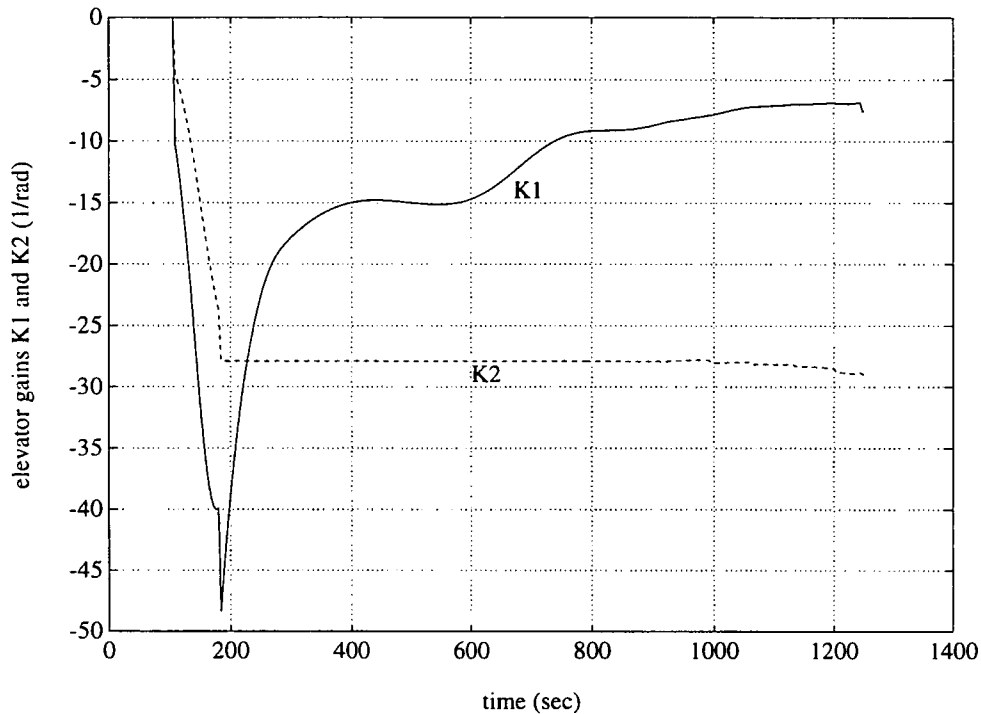


Fig. 4.9 - Elevator gains K_1 and K_2 along the nominal trajectory.

The gains, which have been selected to be used for flying along the trajectory, can be found in Tables C.1 and C.2 of Appendix C. They are given as a function of both the nominal flight time (for which they have been computed) and the dynamic pressure, which will be used to compute the gains for actual flight conditions. The actual implementation in the flight-dynamics software is as follows. The selected gains are stored in reference tables, as a function of the dynamic pressure. Taking the actual dynamic pressure, provided by the navigation system, as input, a scheduler extracts the appropriate gain from the table using simple linear interpolation.

4.4. Lateral controller.

4.4.1. Reduced system for asymmetric motion.

If we want to study the lateral rotational dynamics, i.e., the variation of β and σ with time, then it is possible to exclude the symmetric motion (α as a function of time) by putting $\Delta\alpha$ to zero and neglecting the translational motion. The result is

$$\Delta\dot{p} = \frac{1}{I_{xx}} \left(\frac{\partial C_l}{\partial \beta} \Delta\beta + \frac{\partial C_l}{\partial \delta_a} \Delta\delta_a \right) q_{dyn} S_{ref} b_{ref} + \Delta T_x \quad (4.4.1)$$

$$\Delta \dot{r} = \frac{1}{I_{zz}} \left(\frac{\partial C_n}{\partial \beta} \Delta \beta + \frac{\partial C_n}{\partial \delta_a} \Delta \delta_a + \frac{\partial C_n}{\partial \delta_r} \Delta \delta_r \right) q_{dyn} S_{ref} b_{ref} + \Delta T_z \quad (4.4.2)$$

$$\Delta \dot{\beta} = \sin \alpha_0 \Delta p - \cos \alpha_0 \Delta r - \frac{g_0}{V_0} \cos \gamma_0 \cos \sigma_0 \Delta \sigma \quad (4.4.3)$$

$$\Delta \dot{\sigma} = -\cos \alpha_0 \Delta p - \sin \alpha_0 \Delta r + \left(\frac{g_0}{V_0} \cos \gamma_0 \cos \sigma_0 - \frac{L_0}{m V_0} \right) \Delta \beta + \frac{\tan \gamma_0}{m V_0} \cos \sigma_0 L_0 \Delta \sigma \quad (4.4.4)$$

In state-space form, the above equations are written as

$$\begin{pmatrix} \Delta \dot{p} \\ \Delta \dot{r} \\ \Delta \dot{\beta} \\ \Delta \dot{\sigma} \end{pmatrix} = \mathbf{A} \begin{pmatrix} \Delta p \\ \Delta r \\ \Delta \beta \\ \Delta \sigma \end{pmatrix} + \mathbf{B} \begin{pmatrix} \Delta \delta_a \\ \Delta \delta_r \\ \Delta T_x \\ \Delta T_z \end{pmatrix} \quad (4.4.5)$$

with

$$\mathbf{A} = \begin{bmatrix} 0 & 0 & \frac{1}{I_{xx}} \frac{\partial C_l}{\partial \beta} q_{dyn} S_{ref} b_{ref} & 0 \\ 0 & 0 & \frac{1}{I_{zz}} \frac{\partial C_n}{\partial \beta} q_{dyn} S_{ref} b_{ref} & 0 \\ \sin \alpha_0 & -\cos \alpha_0 & 0 & -\frac{g_0}{V_0} \cos \gamma_0 \cos \sigma_0 \\ -\cos \alpha_0 & -\sin \alpha_0 & \frac{g_0}{V_0} \cos \gamma_0 \cos \sigma_0 - \frac{L_0}{m V_0} & \frac{\tan \gamma_0}{m V_0} \cos \sigma_0 L_0 \end{bmatrix} \quad (4.4.6)$$

$$\mathbf{B} = \begin{bmatrix} \frac{1}{I_{xx}} \frac{\partial C_l}{\partial \delta_a} q_{dyn} S_{ref} b_{ref} & 0 & \frac{1}{I_{xx}} & 0 \\ \frac{1}{I_{zz}} \frac{\partial C_n}{\partial \delta_a} q_{dyn} S_{ref} b_{ref} & \frac{1}{I_{zz}} \frac{\partial C_n}{\partial \delta_r} q_{dyn} S_{ref} b_{ref} & 0 & \frac{1}{I_{zz}} \\ 0 & 0 & 0 & 0 \\ 0 & 0 & 0 & 0 \end{bmatrix} \quad (4.4.7)$$

4.4.2. Root locus of the reduced system.

Since we have decoupled the equations, it would be interesting to see whether we recognise the time history of the eigenvalues, as we did in Section 4.3.2 for the longitudinal controller. The eigenvalues of the reduced system for lateral motion are plotted in Figs. 4.10 through 4.13. Comparing these root loci with the ones depicted in Figs. 3.15-3.18 shows a strong resemblance, which confirms the choice that we could decouple the symmetric and asymmetric motion. The differences between the corresponding eigenplots should be found in an absence of the symmetric motion and the neglected terms of the translational motion.

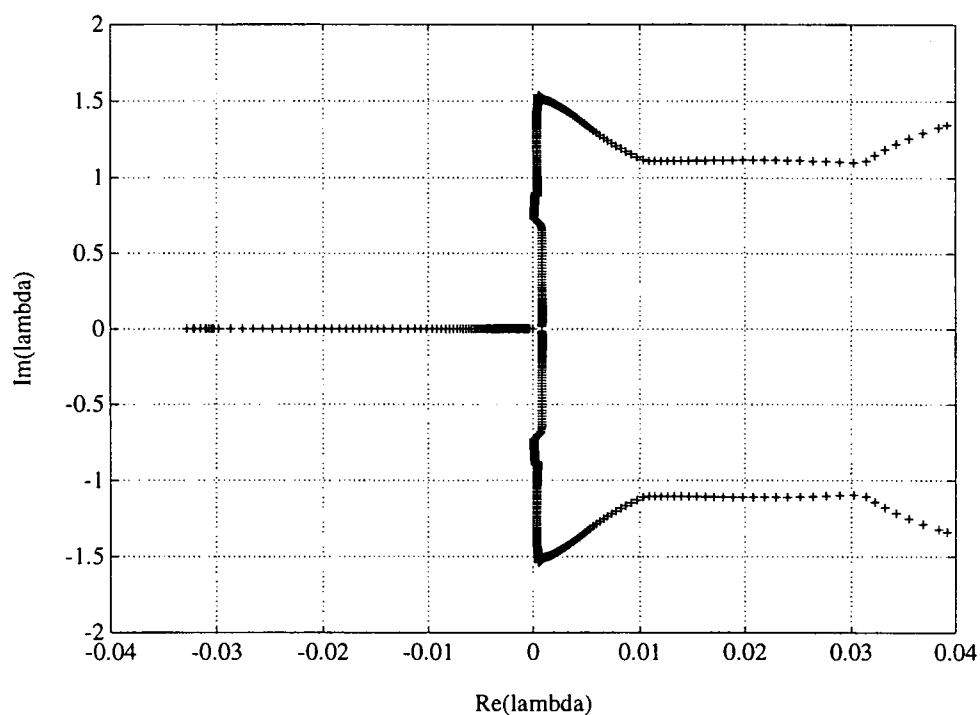


Fig. 4.10 - Variation of the eigenvalues of asymmetric motion along the nominal trajectory.

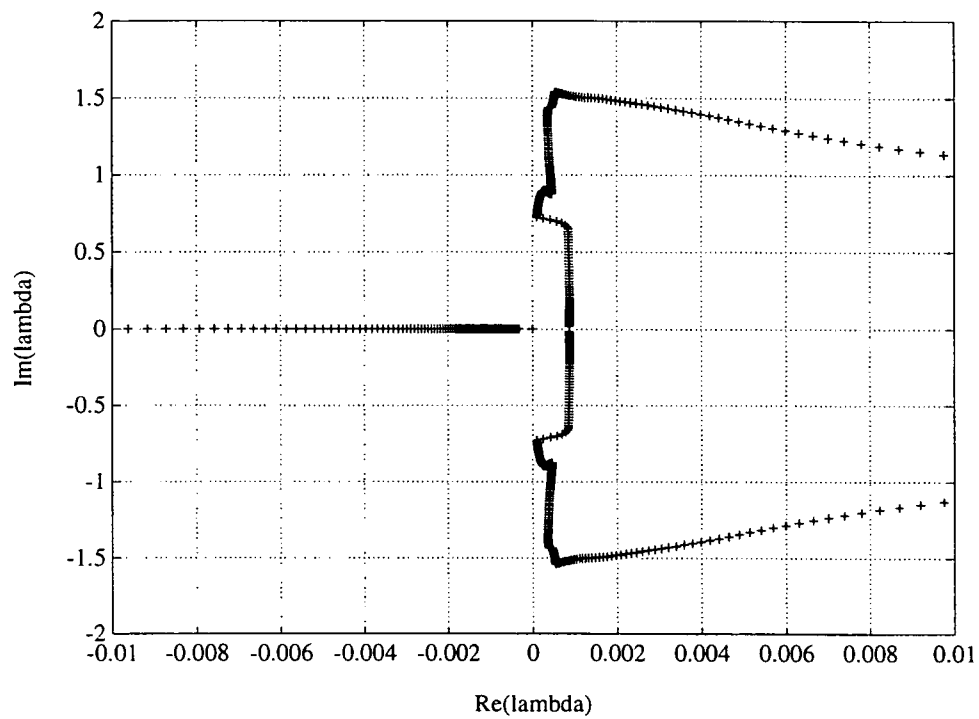


Fig. 4.11 - Detail of the eigenvalue plot centred around the origin for the asymmetric motion.

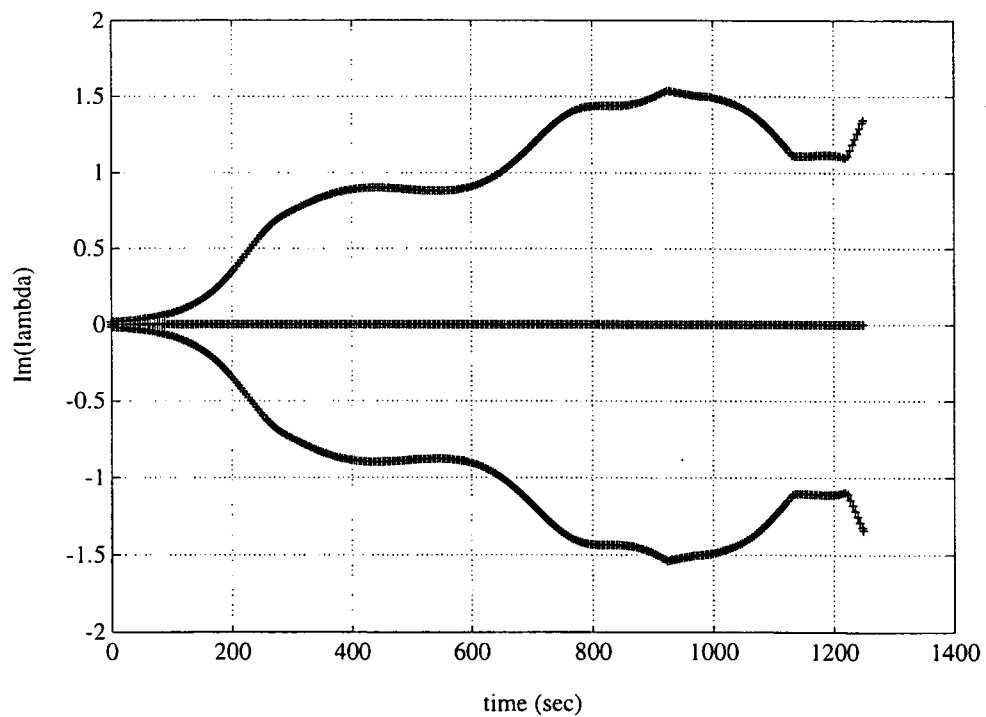


Fig. 4.12 - The imaginary parts of the eigenvalues as a function of flight time for the asymmetric motion.

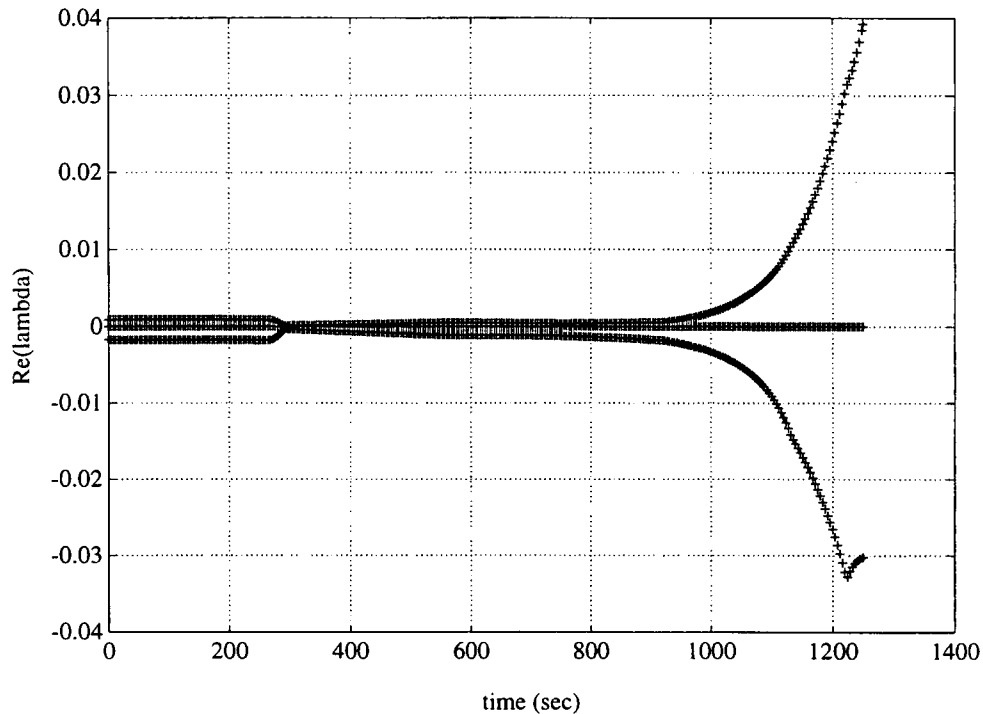


Fig. 4.13 - The real parts of the eigenvalues as a function of flight time for the asymmetric motion.

4.4.3. Selection of the controls.

For lateral control, HORUS is equipped with ailerons, rudders, and roll and yaw jets. To select the different control modes, we refer again to Fig. 4.7, the control modes for the Space Shuttle. In this figure, we find that the roll jets operate from the entry interface up to a dynamic pressure of about 500 N/m^2 (10 psf). The ailerons are activated at the same dynamic pressure as the elevators ($q_{dyn} = 100 \text{ N/m}^2$), since in both cases the elevons are concerned.

The yaw jets are working from the entry interface down to a Mach number of $M = 1$, which is also mentioned by MBB. However, different is the activation of the rudder ($M = 3.5$ in case of the Space Shuttle, and $q_{dyn} = 140 \text{ N/m}^2$ in case of HORUS). We will deviate from the Shuttle scheme to come closer to the original HORUS design. Although rudder control is quite weak, the rudder will be switched on at a dynamic pressure of $q_{dyn} = 150 \text{ N/m}^2$.

4.4.4. Control laws.

The control laws are chosen in the form of

$$\frac{\Delta T_x}{T_{x_{\max}}} = -\frac{\Delta \delta_a}{\delta_{a_{\max}}} = -[K_3 \dot{\sigma} + K_4 (\sigma - \sigma_c)] \cos \alpha - \left[K_5 \left(\dot{\beta} + \frac{g}{V} \sin \sigma \right) + K_6 \beta \right] \sin \alpha \quad (4.4.8)$$

$$\frac{\Delta T_z}{T_{z\max}} = -\frac{\Delta \delta_r}{\delta_{r\max}} = -[K_7 \dot{\sigma} + K_8 (\sigma - \sigma_c)] \sin \alpha - \left[K_9 \left(\dot{\beta} + \frac{g}{V} \sin \sigma \right) + K_{10} \beta \right] \cos \alpha \quad (4.4.9)$$

The lateral controller, which is represented by these equations, is schematically shown in Fig. 4.14.

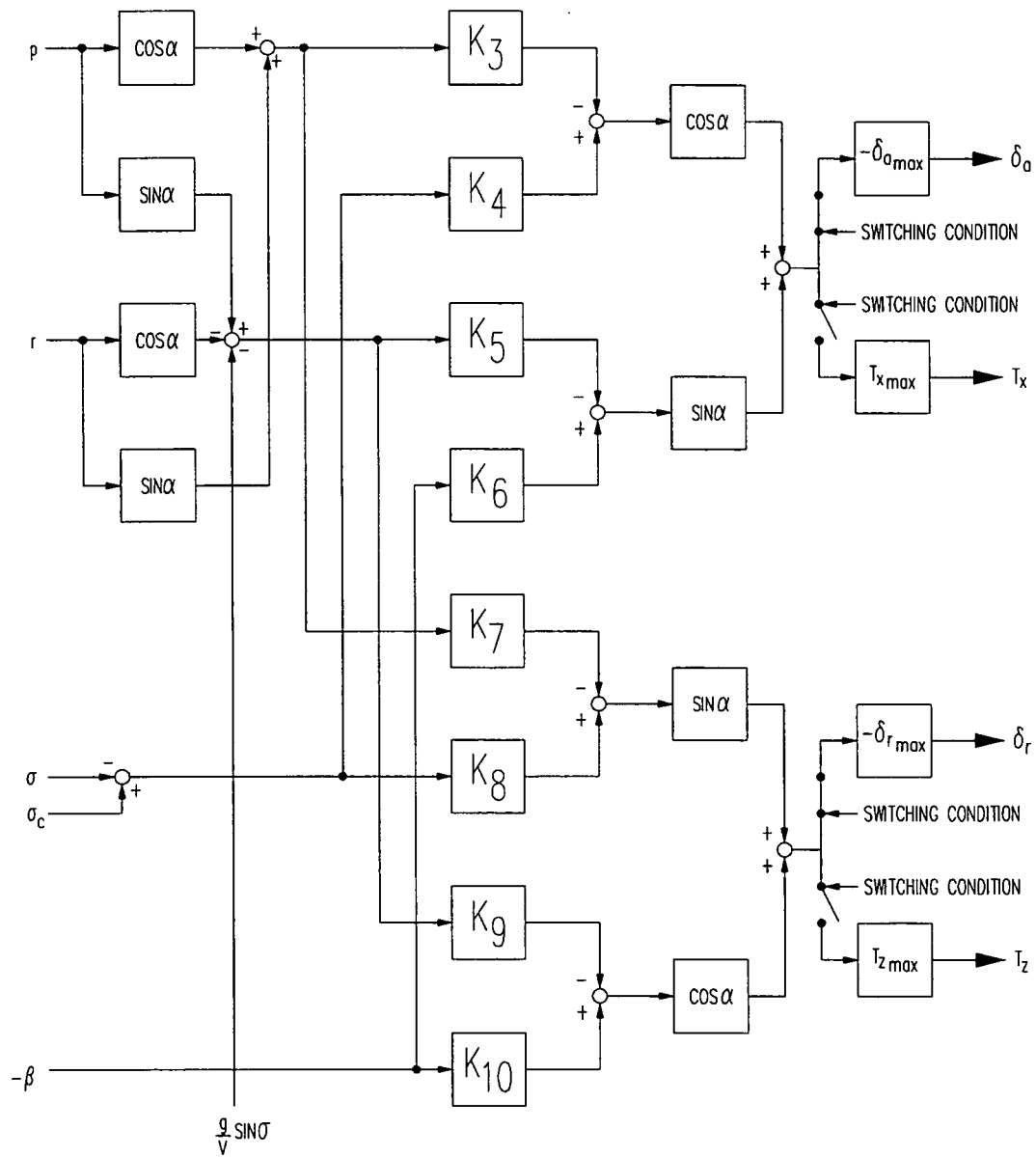


Fig. 4.14 - The lateral controller.

In order to determine the gains, we bring the control laws in the form

$$\mathbf{u} = -\mathbf{K}\mathbf{x} \quad (4.4.10)$$

In the on-coming derivation, we will assume that

$$\Delta\beta = \beta - \beta_0 = \beta - \beta_c = \beta$$

$$\Delta\sigma = \sigma - \sigma_0 \approx \sigma - \sigma_c$$

$$\Delta\rho = \rho - \rho_0 = \rho - \rho_c$$

$$\Delta r = r - r_0 = r - r_c$$

which will give a small error in the bank angle only. The commanded rotational rates are equal to the nominal ones, controlling the vehicle towards a zero rate of change of the angle of sideslip and the bank angle, see Section 2.2.

Starting with the first control law, by linearising and neglecting the smaller $\Delta\beta$ - and $\Delta\sigma$ -terms we can write the K_3 -term in Eq. (4.4.8) as:

$$K_3 \dot{\sigma} \cos\alpha = K_3 \left[-\cos^2\alpha_0 \Delta\rho - \sin\alpha_0 \cos\alpha_0 \Delta r \right] \quad (4.4.11)$$

Note that since $\Delta\alpha$ is assumed to be zero, α is equal to α_0 . The K_5 -term in Eq. (4.4.8) is approximated by

$$\begin{aligned} K_5 \left(\dot{\beta} + \frac{g}{V} \sin\sigma \right) \sin\alpha &= K_5 \left(\sin\alpha_0 \Delta\rho - \cos\alpha_0 \Delta r + \frac{g_0}{V_0} \sin(\sigma_0 + \Delta\sigma) \right) \sin\alpha_0 \\ &\approx K_5 \left(\sin^2\alpha_0 \Delta\rho - \cos\alpha_0 \sin\alpha_0 \Delta r + \frac{g_0}{V_0} \cos\sigma_0 \sin\alpha_0 \Delta\sigma \right) \end{aligned} \quad (4.4.12)$$

In the above equation, the constant term

$$\frac{g_0}{V_0} \sin\sigma_0 \sin\alpha_0$$

has been neglected, because otherwise we will not be able to bring the control laws in the form of Eq. (4.4.10). Neglecting this term will introduce a constant control error. Although the bank angle is large, the velocity is much larger, so the control error is not expected to be that large. Furthermore, it is assumed that the error can be kept small by the control system¹⁵. Compensation of this constant term can be interpreted as a part of the lateral trim.

Substituting the derived expressions for K_3 and K_5 into Eq. (4.4.8), the control law changes

¹⁵ In Chapter 5, Fig. 5.23, we will see that the control error is indeed sufficiently small.

into

$$\frac{\Delta T_x}{T_{x_{\max}}} = -\frac{\Delta \delta_a}{\delta_{a_{\max}}} = -K_3^* \Delta p - K_4^* \Delta r - K_5^* \Delta \beta - K_6^* \Delta \sigma \quad (4.4.13)$$

with

$$\begin{aligned} K_3^* &= -\cos^2 \alpha_0 K_3 + \sin^2 \alpha_0 K_5 \\ K_4^* &= -\sin \alpha_0 \cos \alpha_0 K_3 - \sin \alpha_0 \cos \alpha_0 K_5 \\ K_5^* &= \sin \alpha_0 K_6 \\ K_6^* &= \cos \alpha_0 K_4 + \frac{g_0}{V_0} \cos \sigma_0 \sin \alpha_0 K_5 \end{aligned} \quad (4.4.14)$$

In matrix notation this can be written as

$$K^* = HK \quad (4.4.15)$$

with

$$H = \begin{bmatrix} -\cos^2 \alpha_0 & 0 & \sin^2 \alpha_0 & 0 \\ -\sin \alpha_0 \cos \alpha_0 & 0 & -\sin \alpha_0 \cos \alpha_0 & 0 \\ 0 & 0 & 0 & \sin \alpha_0 \\ 0 & \cos \alpha_0 & \frac{g_0}{V_0} \cos \sigma_0 \sin \alpha_0 & 0 \end{bmatrix} \quad (4.4.16)$$

The gains K_i ($i=3,6$) can be computed from Eq. (4.4.15) with

$$K = H^{-1} K^* \quad (4.4.17)$$

For the second control law we can derive in a similar manner:

$$\frac{\Delta T_z}{T_{z_{\max}}} = -\frac{\Delta \delta_r}{\delta_{r_{\max}}} = -K_7^* \Delta p - K_8^* \Delta r - K_9^* \Delta \beta - K_{10}^* \Delta \sigma \quad (4.4.18)$$

with

$$\begin{pmatrix} K_7^* \\ K_8^* \\ K_9^* \\ K_{10}^* \end{pmatrix} = \begin{bmatrix} -\sin\alpha_0 \cos\alpha_0 & 0 & \sin\alpha_0 \cos\alpha_0 & 0 \\ -\sin^2\alpha_0 & 0 & -\cos^2\alpha_0 & 0 \\ 0 & 0 & 0 & \cos\alpha_0 \\ 0 & \sin\alpha_0 & \frac{g_0}{V_0} \cos\sigma_0 \cos\alpha_0 & 0 \end{bmatrix} \begin{pmatrix} K_7 \\ K_8 \\ K_9 \\ K_{10} \end{pmatrix} \quad (4.4.19)$$

Returning to Eq. (4.4.10), the matrix expression for the control laws, we can now write

$$\mathbf{u} = \begin{pmatrix} \Delta\delta_a \\ \Delta\delta_r \\ \Delta T_x \\ \Delta T_z \end{pmatrix} = - \begin{bmatrix} -\delta_{a_{\max}} K_3^* & -\delta_{a_{\max}} K_4^* & -\delta_{a_{\max}} K_5^* & -\delta_{a_{\max}} K_6^* \\ -\delta_{r_{\max}} K_7^* & -\delta_{r_{\max}} K_8^* & -\delta_{r_{\max}} K_9^* & -\delta_{r_{\max}} K_{10}^* \\ T_{x_{\max}} \tilde{K}_3^* & T_{x_{\max}} \tilde{K}_4^* & T_{x_{\max}} \tilde{K}_5^* & T_{x_{\max}} \tilde{K}_6^* \\ T_{z_{\max}} \tilde{K}_7^* & T_{z_{\max}} \tilde{K}_8^* & T_{z_{\max}} \tilde{K}_9^* & T_{z_{\max}} \tilde{K}_{10}^* \end{bmatrix} \begin{pmatrix} \Delta p \\ \Delta r \\ \Delta\beta \\ \Delta\sigma \end{pmatrix} = -\mathbf{K}^* \mathbf{x} \quad (4.4.20)$$

In the above equation, \tilde{K}_i ($i=3,10$) are the gains for reaction control. In the original design of MBB, each of the reaction-control gains is equal to its aerodynamic counterpart. As we discussed in Section 4.2, we will not determine the gains independently by pole placement but simultaneously by solving the Riccati equation. For this reason, we have defined the gains for reaction control to be different from the ones for aerodynamic control.

4.4.5. Computation of the feedback gains.

The idea behind computing the controller gains for control law Eq. (4.4.8) is, that the bank reversals must be performed with an angular bank velocity, demanded by the guidance system. This prescribed angular bank velocity is an increasing, piece-wise linear function of the dynamic pressure. MBB ensures this by choosing a damping factor of about 0.7-0.8 and such a natural frequency of the closed-loop system that the control error is limited to $|\sigma - \sigma_c| \approx 10^\circ$. For the second control law Eq. (4.4.9), the demands cannot be that stringent, since the yaw effectors are weak and it is therefore not possible to exert much influence on the dynamics of the lateral oscillation. As a result, the damping factor is chosen to be 0.3-0.4 to provide minimal damping. Based on these specifications, pole placement is used to find the values of the gains.

As was the case for the design of the longitudinal controller, we compute the gains by solving the reduced matrix Riccati equation. The weight matrices \mathbf{Q} and \mathbf{R} are in this case given by

$$Q = \begin{bmatrix} \frac{1}{\Delta p_{\max}^2} & 0 & 0 & 0 \\ 0 & \frac{1}{\Delta r_{\max}^2} & 0 & 0 \\ 0 & 0 & \frac{1}{\Delta \beta_{\max}^2} & 0 \\ 0 & 0 & 0 & \frac{1}{\Delta \sigma_{\max}^2} \end{bmatrix} \quad (4.4.21)$$

$$R = \begin{bmatrix} \frac{1}{\Delta \delta_{a_{\max}}^2} & 0 & 0 & 0 \\ 0 & \frac{1}{\Delta \delta_{r_{\max}}^2} & 0 & 0 \\ 0 & 0 & \frac{1}{\Delta T_{x_{\max}}^2} & 0 \\ 0 & 0 & 0 & \frac{1}{\Delta T_{z_{\max}}^2} \end{bmatrix} \quad (4.4.22)$$

Numerical values, which we will use, are:

$$\begin{aligned} \Delta p_{\max} &= \infty \\ \Delta r_{\max} &= \infty \\ \Delta \beta_{\max} &= 2^\circ \\ \Delta \sigma_{\max} &= 5^\circ \\ \Delta \delta_{a_{\max}} &= 40^\circ \\ \Delta \delta_{r_{\max}} &= 40^\circ \\ \Delta T_{x_{\max}} &= 1,600 \text{ Nm} \\ \Delta T_{z_{\max}} &= 7,600 \text{ Nm} \end{aligned}$$

The maximum nominal bank angle is 80° , so a maximum control error of 10° is thought to be too large (in fact, as specified by the guidance system, the maximum allowable bank angle is 87°). For this reason, we have decided on a maximum overshoot of 5° , so that the vertical lift component will never be completely zero.

The computed reaction-control gains can be found in Figs. 4.15 and 4.16, whereas the aerodynamic-control gains are plotted in Figs. 4.17 and 4.18. The selected gains for implementation in the actual controller can be found in Tables C.3 through C.10 of Appendix C. Again, they are given as a function of both the nominal flight time (for which they have been computed) and the dynamic pressure, which will be used to compute the gains for actual flight conditions. The three control regimes, reaction, aerodynamic and hybrid control, show again as discrete jumps in the curves for the gains.

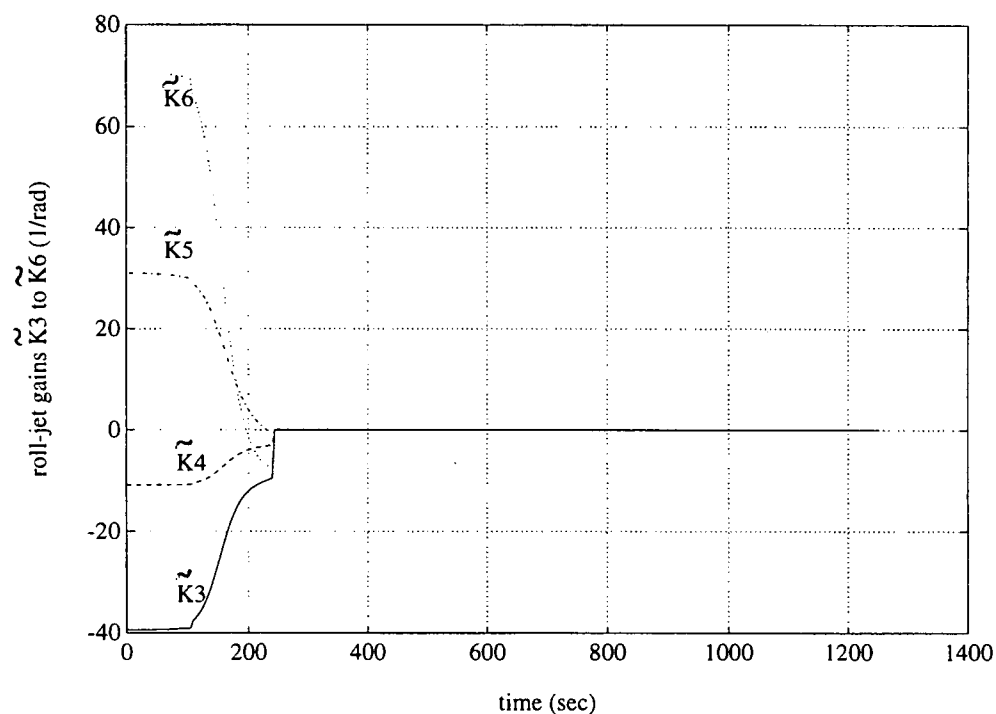


Fig. 4.15 - Roll-jet gains \tilde{K}_3 , \tilde{K}_4 , \tilde{K}_5 and \tilde{K}_6 along the nominal trajectory.

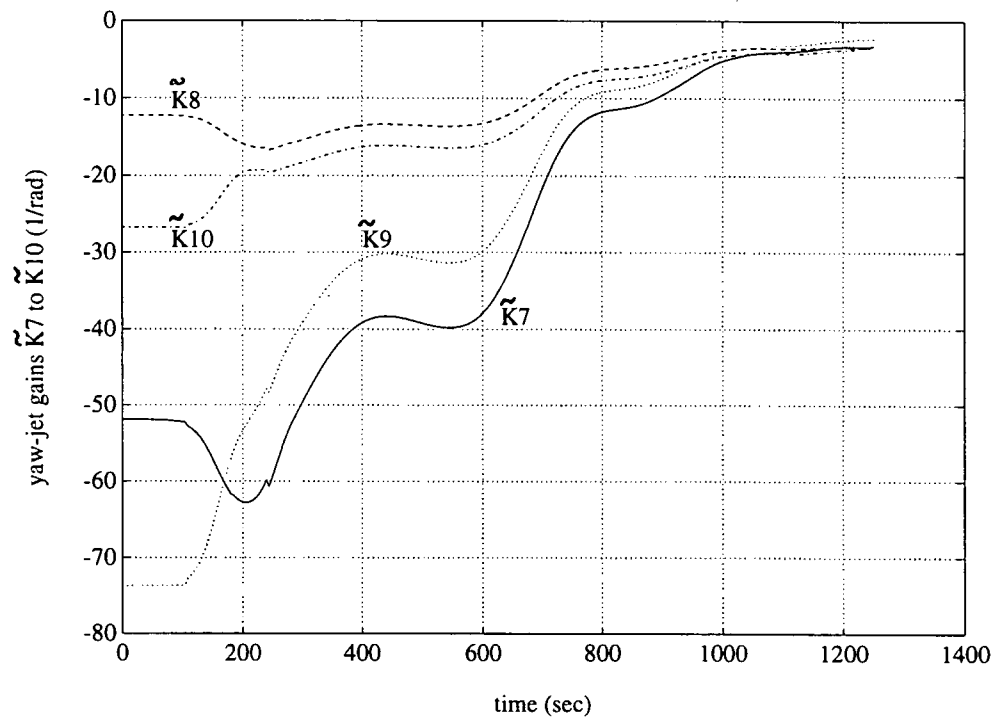


Fig. 4.16 - Yaw-jet gains \tilde{K}_7 , \tilde{K}_8 , \tilde{K}_9 and \tilde{K}_{10} along the nominal trajectory.

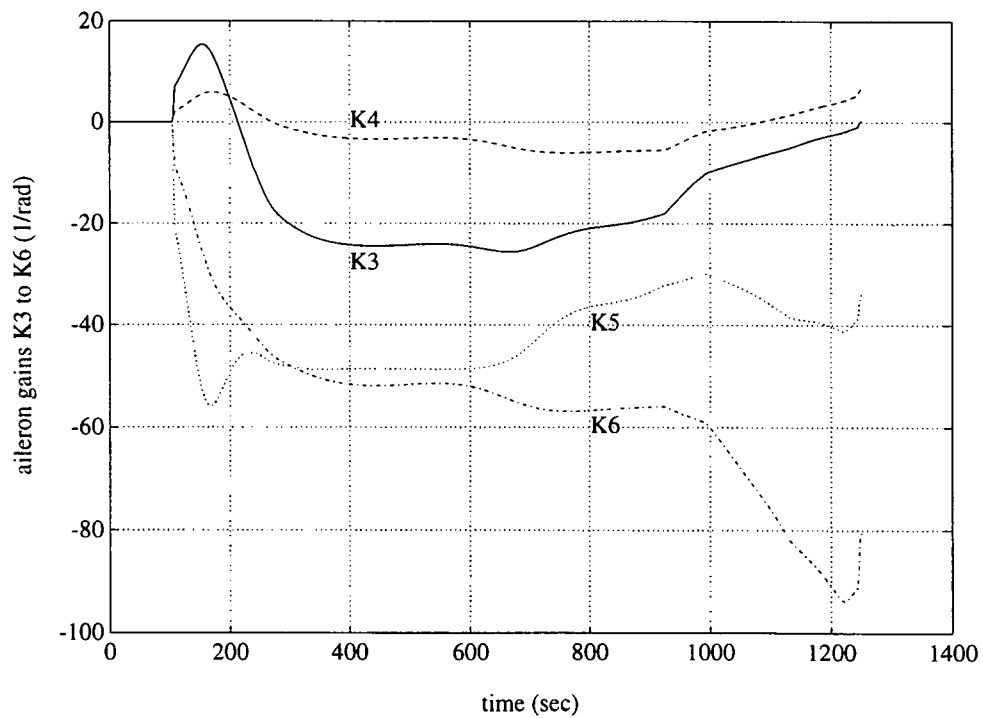


Fig. 4.17 - Aileron gains K_3 , K_4 , K_5 and K_6 along the nominal trajectory.

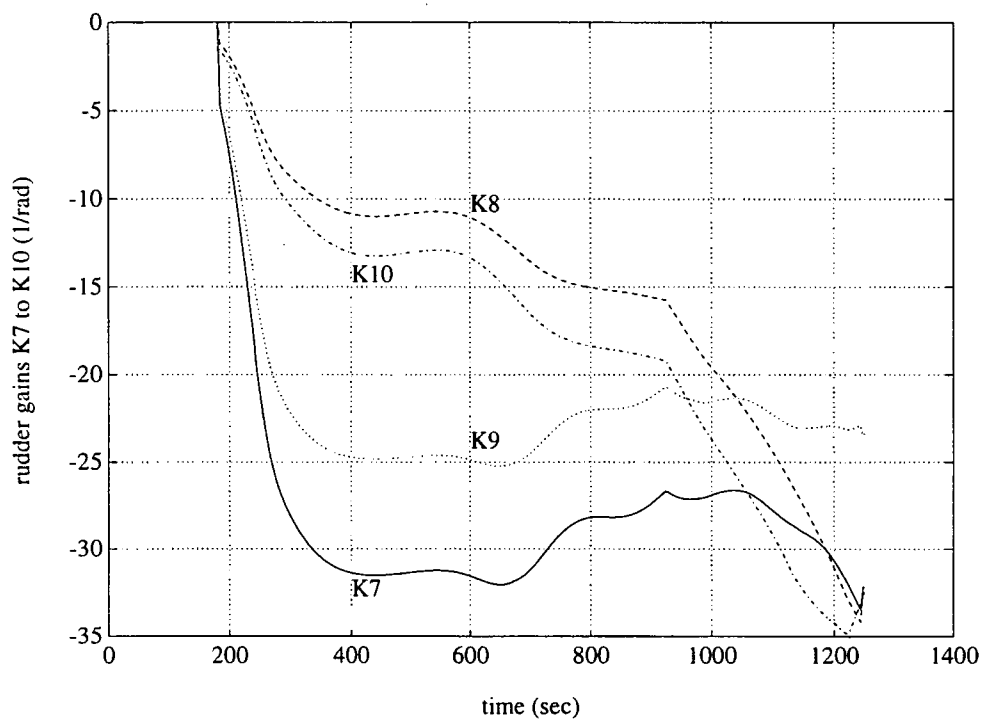


Fig. 4.18 - Rudder gains K_7 , K_8 , K_9 and K_{10} along the nominal trajectory.

Chapter 5

Verification of the Controller

5.1. Introduction.

The verification of an attitude controller is usually done in several steps, as we already discussed in the introduction, Chapter 1. A good starting point is to have a look at the location of the eigenvalues and the damping ratios of the closed-loop system. In that way we already get an impression whether (and where) we might run into trouble and whether our system needs a redesign. This we will do in the next section, Section 5.2. Since we designed two separate controllers for both the symmetric and asymmetric motion, we have to check two root loci. In Section 5.3, the response of the two controllers will be calculated. For our re-entry flight, two types of responses are of importance, i.e., the step response and the ramp response. Besides, we are interested in how the control system deals with deviations from the nominal state, for instance, an angle of sideslip which differs from zero.

The next step, of course only when the previous steps have given satisfying results, can be a sensitivity analysis of the linear closed-loop systems. This we will not do, since we want to develop an analysis technique based on a non-linear flight-dynamics model (Mooij, TO BE PUBLISHED). So in this case we will integrate the pitch and lateral controller, and verify whether we can fly the nominal trajectory in a full 6-dof guided and controlled simulation (Section 5.4). The final step will be a sensitivity analysis to see whether the control system can cope with all kinds of disturbances. We already mentioned that the study presented in this report, is part of a guidance and control analysis of a winged re-entry vehicle. In the report covering that study, the sensitivity analysis will be discussed.

5.2. Root loci of the closed-loop systems.

5.2.1. Longitudinal controller.

In Chapter 4, we discussed the computation of the feedback-gain matrix K . The closed loop system is in that case represented by

$$\dot{x} = (A - BK)x = A^*x \quad (5.2.1)$$

where the matrices A and B are given by the simplified expressions Eq. (4.3.4) and Eq. (4.3.5). The eigenvalues of the closed-loop system can be computed by determining the eigenvalues of the new system matrix A^* , analogous to Section 3.1. The result of that computation is shown in Figs. 5.1 through 5.3.

The conclusion which can be drawn from those figures is that all eigenvalues have negative real parts, indicating a damped system all along the trajectory. This is confirmed by Fig. 5.4, where the damping ratio is plotted as a function of flight time. We see that basically the damping ratio is about 0.7. The Reaction Control System (pitch jets) exhibit a somewhat better control effectiveness than the aerodynamic control surfaces when they are just activated. This is due to the relatively low dynamic pressure. Going to lower altitudes, the aerodynamic control surfaces are getting slightly more effective. Over all, the system is well damped which will usually give a fair response. These results increase our confidence in a well-behaving control system, but more attention will be given in Section 5.3.1. It should be noted that the discrete jumps in the damping ratio is due to the discrete jumps in the aerodynamic derivatives as a result of the linearisation process.

We conclude this brief discussion by pointing out that towards the end of the flight, the eigenvalues show a discrete jump, see, for instance, Fig. 5.2. This is due to the fact that at the end of the flight the body-flap has reached its maximum deflection and the elevators are suddenly activated to provide the additional trim moments. Because of the ideal control, the system dynamics change discretely resulting in a change of eigenvalues.

5.2.2. Lateral controller.

The eigenvalues of the closed-loop system for asymmetric motion, with the matrices A and B given by Eq. (4.4.6) and (4.4.7), are depicted in Figs. 5.5 through 5.7. Two series of complex conjugated eigenvalues can be distinguished. Both pairs of eigenvalues have negative real parts, so also the lateral system is stable. These real parts become larger (i.e., more negative) at lower altitudes, which means an even better damped system (although one should also consider the imaginary parts). In Fig. 5.7 the damping ratios as a function of time are plotted. In the early flight phase, the damping ratio for both asymmetric motions is about the same ($\zeta \approx 0.7$), but these values depart significantly from one another towards the end of the flight ($\zeta_1 \approx 0.82$ and $\zeta_2 \approx 0.68$). But, both motions are well damped.

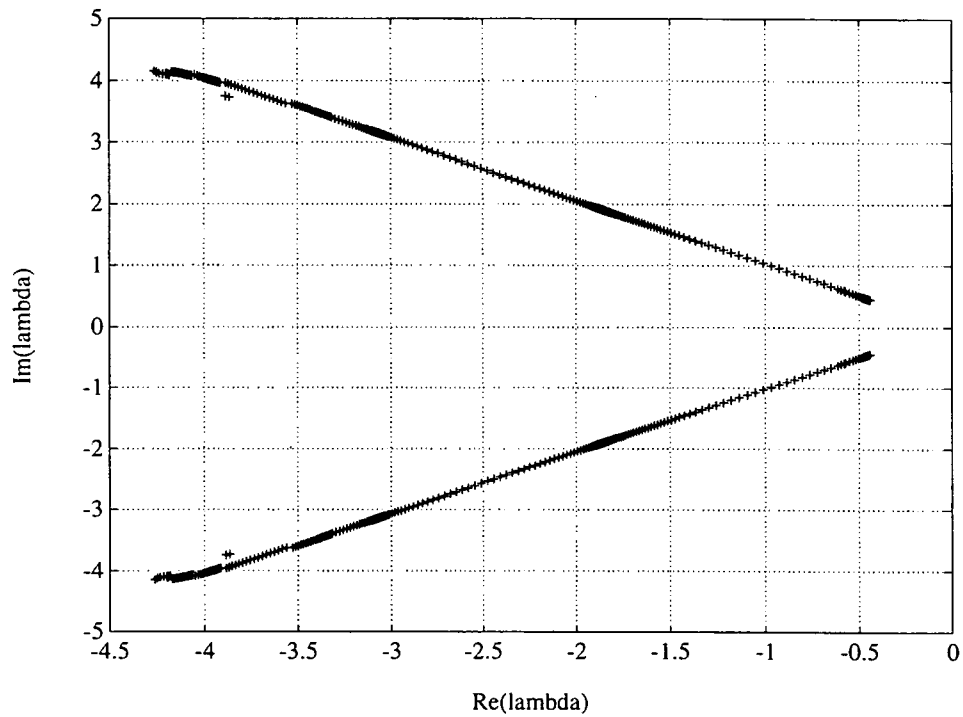


Fig. 5.1 - Variation of the eigenvalues of symmetric motion along the nominal trajectory for the closed-loop system. The smaller values of the eigenvalues appear at $t = t_0$, whereas they increase towards the end of the flight.

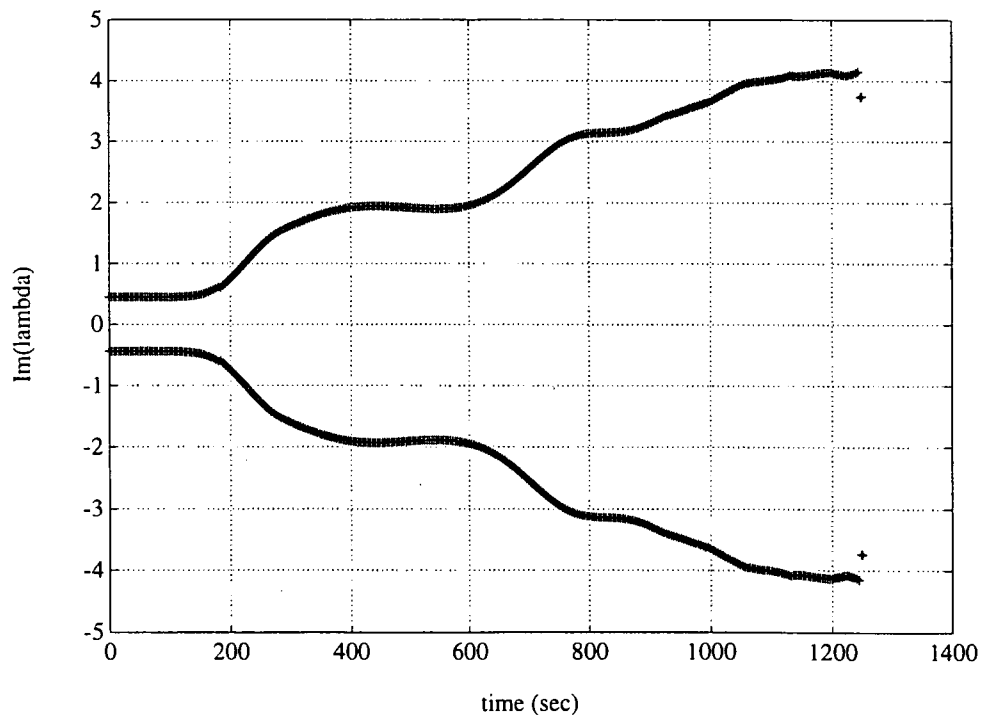


Fig. 5.2 - The imaginary part of the eigenvalues of symmetric motion as a function of flight time for the closed-loop system.

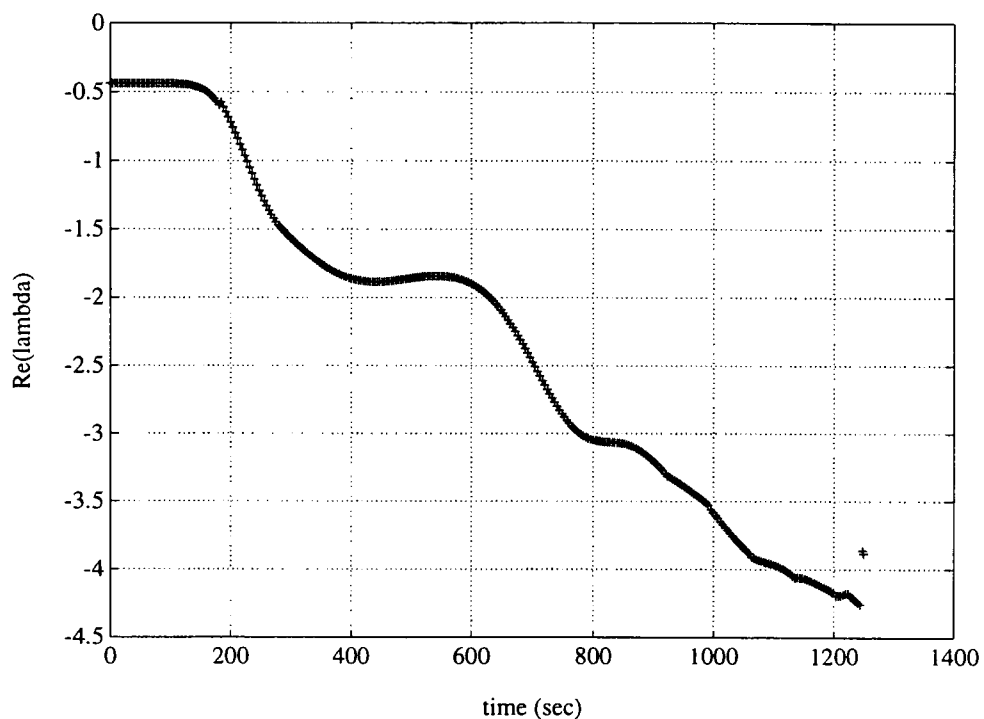


Fig. 5.3 - The real part of the eigenvalues of symmetric motion as a function of flight time for the closed-loop system.

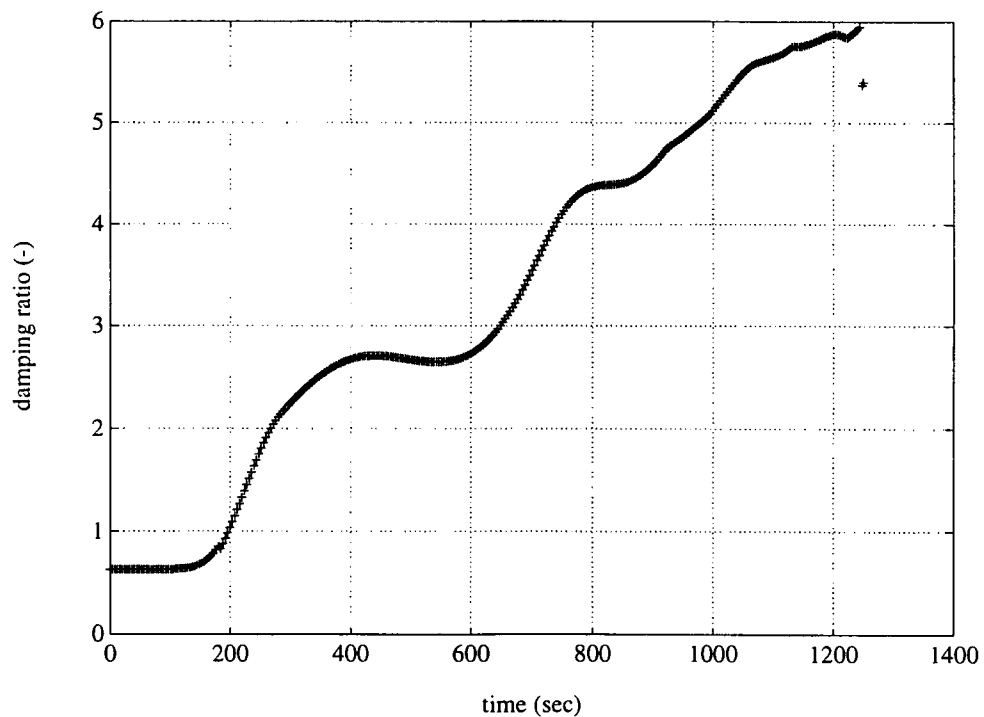


Fig. 5.4 - The damping ratio of the closed-loop system for symmetric motion.

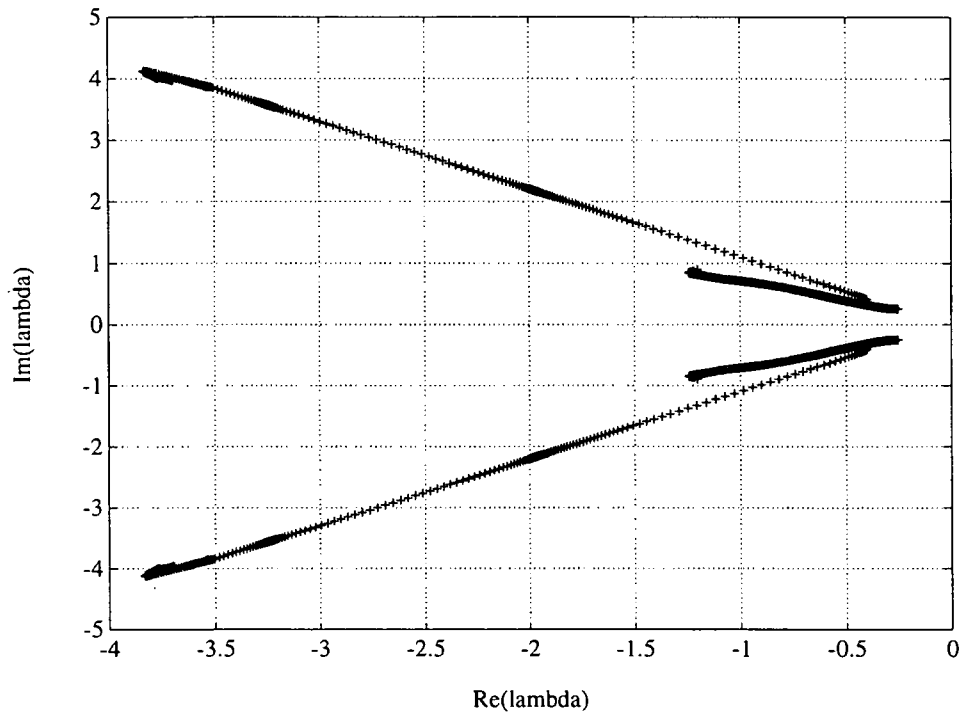


Fig. 5.5 - Variation of the eigenvalues of asymmetric motion along the nominal trajectory for the closed-loop system. The smaller values of the eigenvalues appear at $t = t_0$, whereas they increase towards the end of the flight

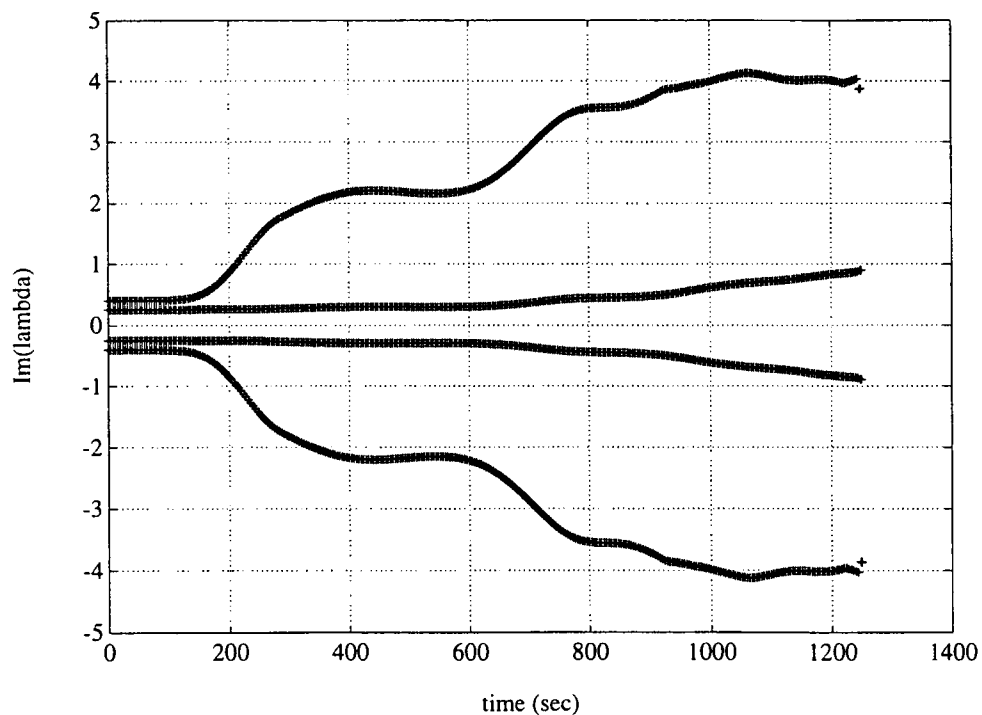


Fig. 5.6 - The imaginary part of the eigenvalues of asymmetric motion as a function of flight time for the closed-loop system.

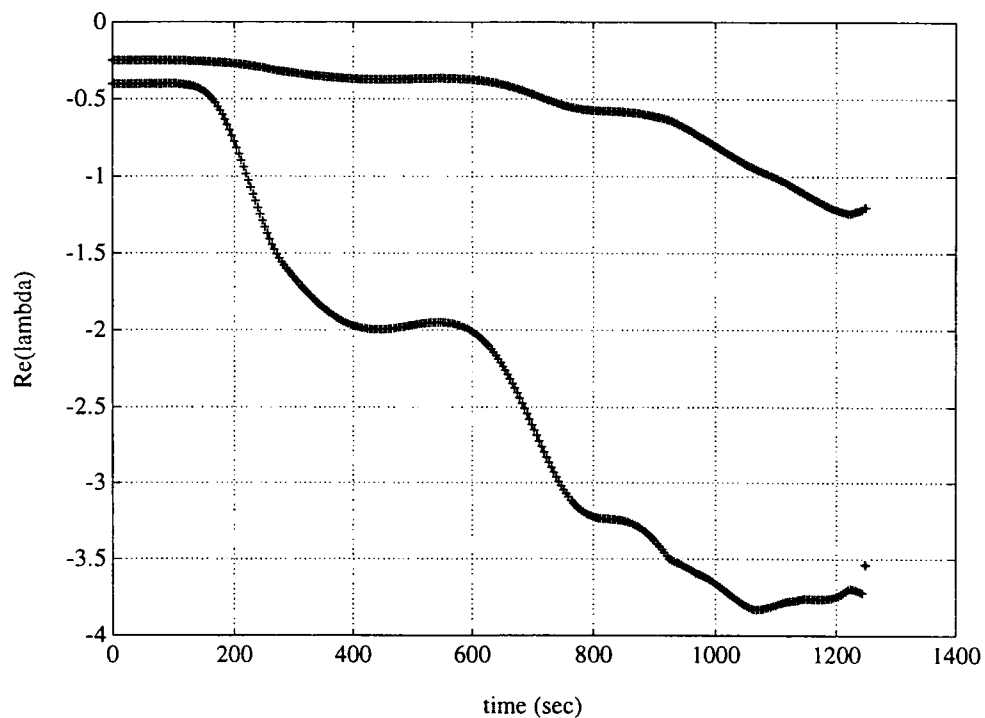


Fig. 5.7 - The real part of the eigenvalues of asymmetric motion as a function of flight time for the closed-loop system.

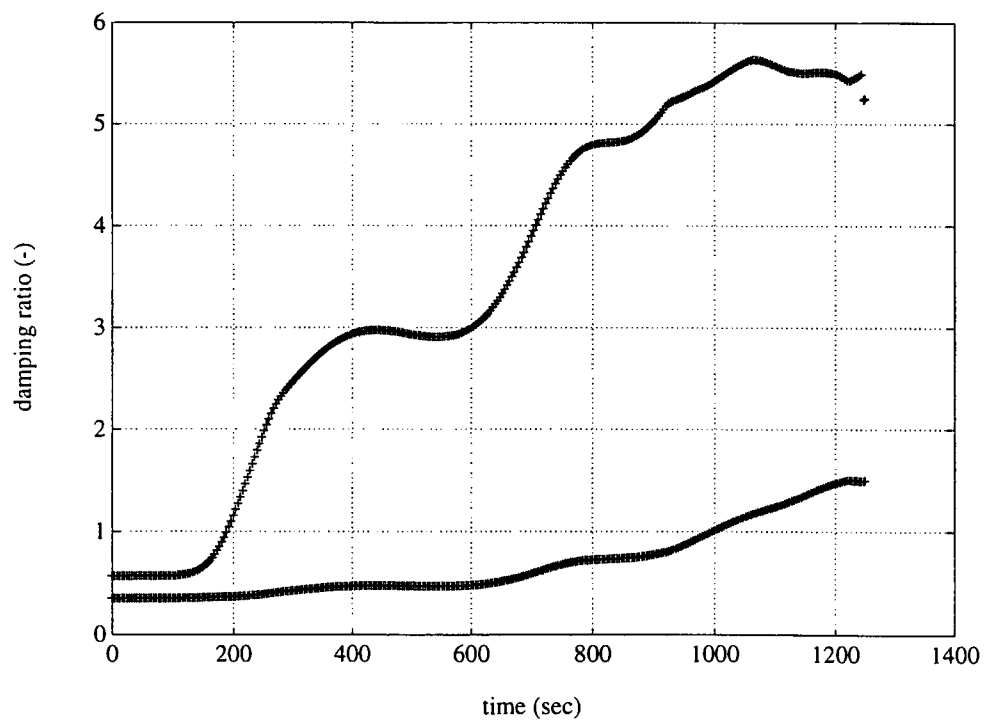


Fig. 5.8 - The damping ratios of the two complex conjugated sets of eigenvalues as a function of flight time (closed-loop system for asymmetric motion).

5.3. Step response.

5.3.1. Introduction.

In order to determine the response of the closed-loop system, we have to set up a new system of state equations. In principle, the closed-loop system is described by

$$\dot{\mathbf{x}} = (\mathbf{A} - \mathbf{BK})\mathbf{x} = \mathbf{A}^*\mathbf{x} \quad (5.3.1)$$

However, we want the system to be in the form

$$\dot{\mathbf{x}} = \mathbf{A}^*\mathbf{x} + \mathbf{B}^*\mathbf{u}^* \quad (5.3.2a)$$

$$\mathbf{y} = \mathbf{C}^*\mathbf{x} + \mathbf{D}^*\mathbf{u}^* \quad (5.3.2b)$$

When we define \mathbf{u}^* to be

$$\mathbf{u}^* = (0 \quad \Delta\alpha_c)^T \quad (5.3.3a)$$

for the longitudinal controller, and

$$\mathbf{u}^* = (0 \quad 0 \quad 0 \quad \Delta\sigma_c)^T \quad (5.3.3b)$$

for the lateral controller, then we can simulate a step function in the commanded angles and compute the response of the corresponding actual angles by defining \mathbf{B}^* to be

$$\mathbf{B}^* = -\mathbf{A}^* \quad (5.3.4)$$

\mathbf{C}^* and \mathbf{D}^* are the identity and zero matrix, respectively. In the remainder of this Section, we will compute the step response of both the pitch and lateral controller using standard libraries of the simulation tool Matlab (Mathworks Inc.).

5.3.2. Longitudinal controller.

To simulate the step response of the longitudinal controller, we have selected two time points, one for reaction control (pitch jets) and one for aerodynamic control (elevators). These time points are 13 ($t = 48$ s) and 250 ($t = 996$ s), respectively. In Fig. 5.9, the two response functions are plotted. It can be noticed that reaction control is much slower than aerodynamic control. However, in both cases the response is fairly quick and the overshoot is small, which indicates a reasonable good response.

The question is now: is this an acceptable response? We tried to find comparable data of

the Space Shuttle - a vehicle which can serve as a reference for HORUS - but did not succeed. The references we did find only discussed the flying qualities during the (piloted) approach and landing (Myers *et al.*, 1987 and McRuer *et al.*, 1992). Both references state, by paraphrasing an astronaut/pilot, that the importance of flying qualities in the Shuttle is inversely proportional to altitude. Following that reasoning, the response can be considered to be good, although it remains an unsatisfactory answer. A further study of the so-called MIL standards (particularly 'Flying qualities of piloted vehicles', MIL-STD-1797, USAF, March 1987) might be able to give a better answer. For the time being, we leave it at that.

5.3.3. Lateral controller.

Next, we will compute the step response of the lateral controller for two time points. In principle, there are two variables available on which we can put a step signal, i.e., the angle of sideslip and the bank angle. The angle of sideslip, however, is supposed to be kept zero throughout the flight and can better be treated as a disturbance rather than a control variable. For this reason, we will only put a step function on the bank angle and will furthermore check how the system will react to an initial value of the angle of sideslip which differs from zero. Since both attitude angles are coupled to each other, we will show the time histories of both of them while doing the related computations.

Beginning with the step response, in Figs. 5.10 and 5.11 we have plotted the results for time points 13 ($t = 48$ s) and 250 ($t = 996$ s). We see a similar kind of behaviour as we did with the longitudinal controller. When we have only reaction control, the response is much slower ($\Delta t \approx 20$ s) than which is the case with only aerodynamic control ($\Delta t \approx 7$ s). However, since the overshoot is small in both cases, the response time is much shorter when we consider the time needed to cross the 1° -level for the first time ($\Delta t \approx 9$ s and $\Delta t \approx 3.5$ s, respectively). The relative difference is still more or less the same, but the absolute response time is more than 50% smaller. Furthermore, the induced angle of sideslip is small in both cases, and they both go back to 0° . In the denser layers of the atmosphere the angle of sideslip gets larger, because of larger aerodynamic moments.

In case of time point 250, we see something strange happening. The induced β is initially positive, and after less than 1 second it changes sign. This sign reversal delays the response of the bank angle, which shows as an almost constant value during the first second. This phenomenon is related to the aerodynamic properties of the ailerons. They are such that aileron deflections initially result in conflicting rotations. Since the gains related to β and $\dot{\beta}$ are larger than the corresponding gains for σ and $\dot{\sigma}$, a rotation about the top axis (yaw) is dominating at first, but is damped quite well so that the rotation about the X-axis (roll) can become the larger one.

The response to an initial angle of sideslip of 1° gives similar results (Figs. 5.12 and 5.13). The response is faster when aerodynamic control is used. The induced bank angle is significant, for time point 250 the maximum bank angle even exceeds 1° . It shows that with a combination of a larger β and a large $\dot{\beta}$, a larger σ is induced.

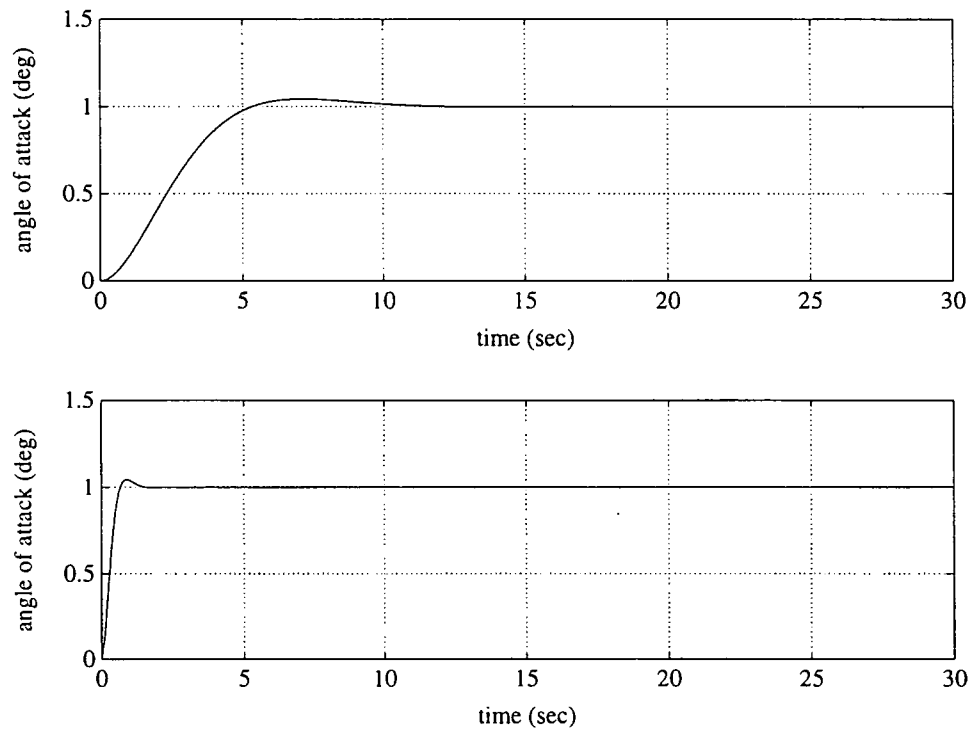


Fig. 5.9 - The step response of the angle of attack for time points 13 ($t = 48$ s), upper graph, and 250 ($t = 996$ s) in the lower graph.

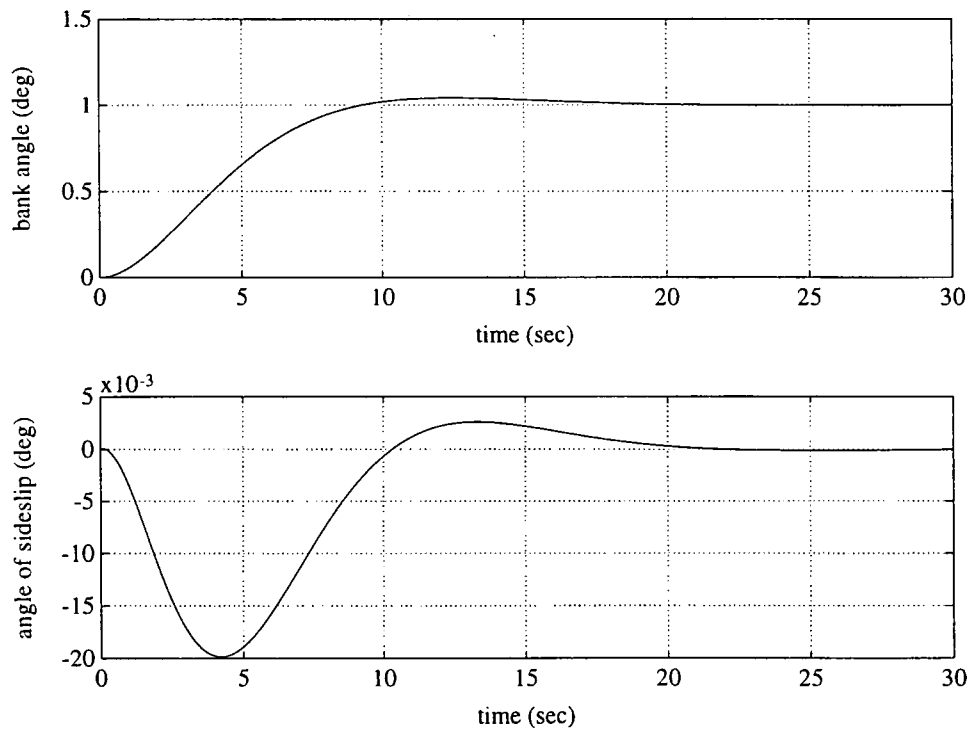


Fig. 5.10 - The step response of the bank angle for time point 13 ($t = 48$ s), upper graph, with the induced angle of sideslip in the lower graph.

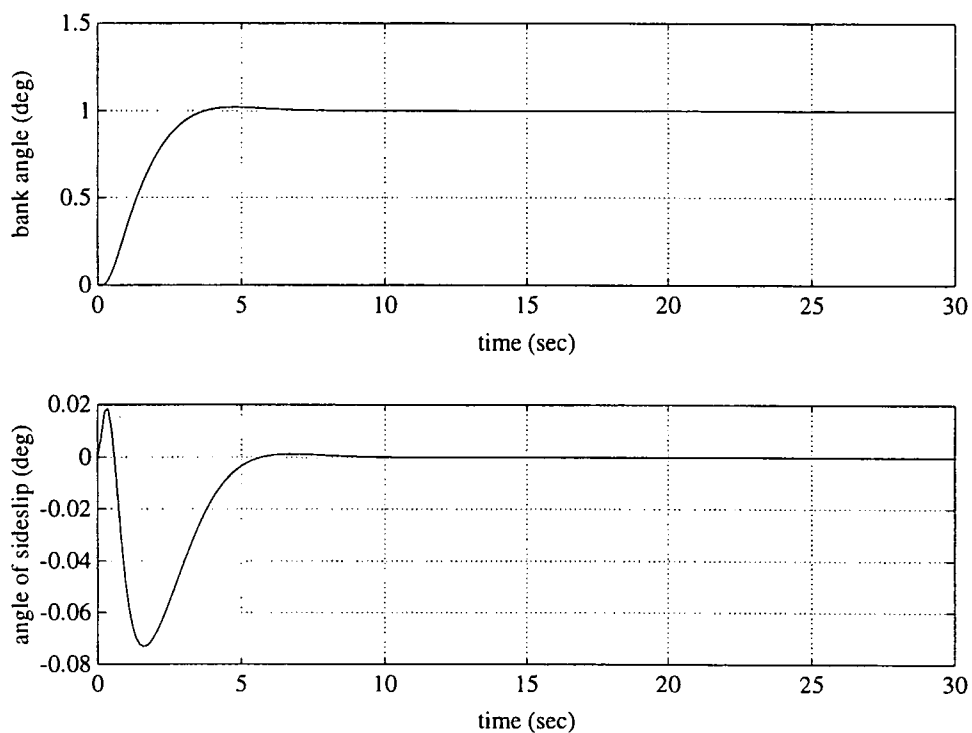


Fig. 5.11 - The step response of the bank angle for time point 250 ($t = 996$ s), upper graph, with the induced angle of sideslip in the lower graph.

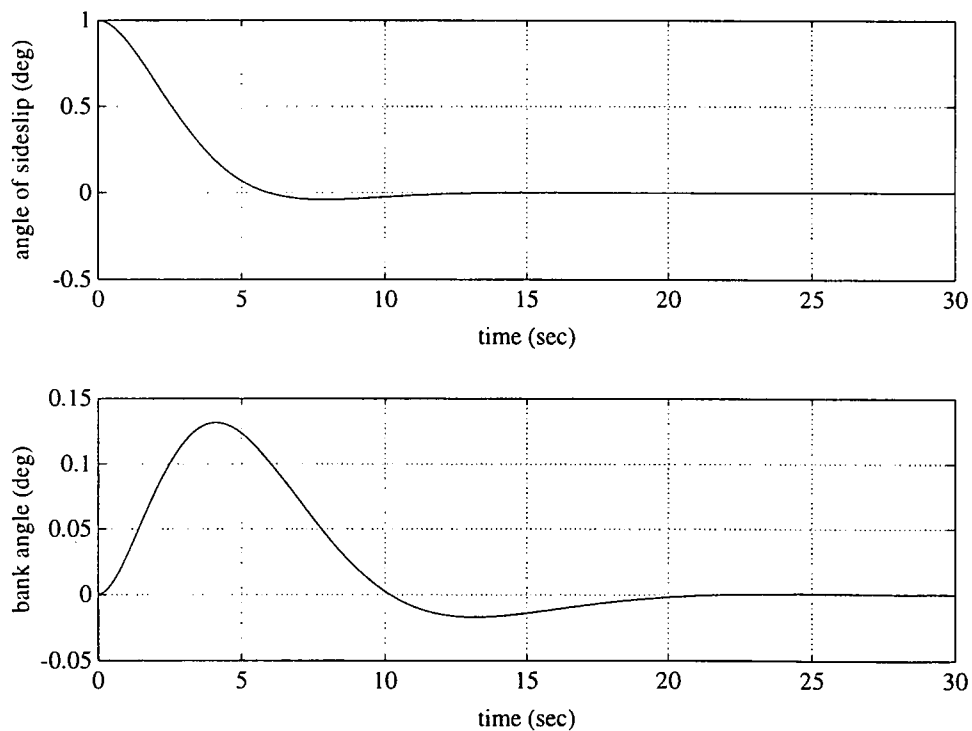


Fig. 5.12 - The response of the angle of sideslip to an initial condition of $\Delta\beta = 1^\circ$ for time point 13 ($t = 48$ s), upper graph, with the induced bank angle in the lower graph.

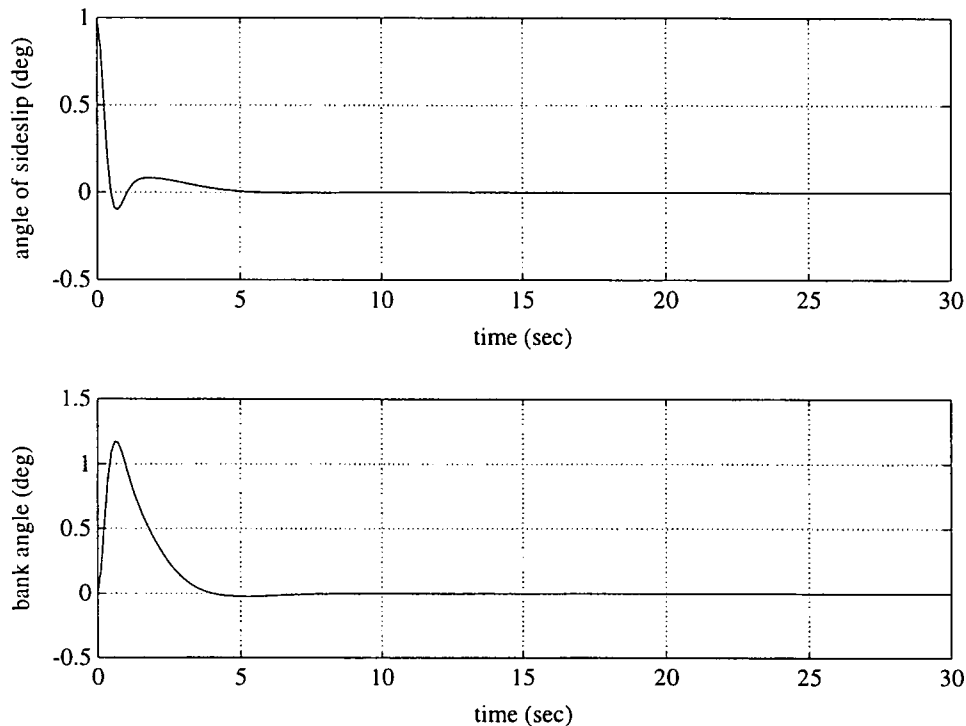


Fig. 5.13 - The response of the angle of sideslip to an initial condition of $\Delta\beta = 1^\circ$ for time point 250 ($t = 996$ s), upper graph, with the induced bank angle in the lower graph.

5.4. Ramp response.

5.4.1. Longitudinal controller.

The ramp response of a controller must indicate how well the controller responds to a linearly increasing or decreasing input signal,

$$u = u_0 + \frac{du}{dt}t \quad (5.4.1)$$

As we know from Section 3.2 (Fig. 3.1), the angle of attack starts decreasing linearly from $t \approx 924$ s. To see whether the longitudinal controller can handle this, we have examined the ramp response for time point 250 ($t = 996$ s). To be as complete as in Section 5.3.2, we have also looked at time point 13 (reaction control only).

The ramp function which we have defined is based on the following, prescribed notions:

- for the nominal trajectory, the initial angle of attack is $\alpha_1 = 40^\circ$ at $t_1 = 923.58$ s,
- the final angle of attack is $\alpha_2 = 11.5^\circ$ at $t_2 = 1,319.4$ s.

This means that the slope of the ramp is

$$\frac{d\alpha}{dt} = \frac{\alpha_2 - \alpha_1}{t_2 - t_1} = -0.072 \text{ } ^\circ/\text{s}$$

The results of simulating this ramp input are shown in Fig. 5.14. In the upper graph, the response with reaction control is shown. After an initial delay (about 2.5 s), the actual angle of attack follows the commanded angle of attack very well. The difference between the commanded and actual angle of attack is $\Delta\alpha \approx 0.15^\circ$, which is well below the design overshoot of 2° . The response with aerodynamic control is much better (lower graph), because of the higher dynamic pressure. The delay time is very short (about 0.15 s), with hardly any difference between the commanded and actual angle of attack. These results indicate that the longitudinal controller is not likely to encounter any problems with the nominal angle-of-attack profile.

5.4.2. Lateral controller.

In case of the lateral controller we are interested in the fact whether it can handle the bank reversals. However, the nominal trajectory assumes an infinite bank rate for these reversals so we do not have information at hand, what the commanded bank angle will be during the reversal. What we do know is how fast the first, pre-defined bank manoeuvre is performed (see also Fig. 3.2). The ramp function can therefore be defined as follows:

- for the nominal trajectory, the initial bank angle is $\sigma_1 = 0^\circ$ at $t_1 = 263.88 \text{ s}$,
- the final bank angle is $\sigma_2 = 80.0^\circ$ at $t_2 = 290.268 \text{ s}$.

The slope of the ramp function is then

$$\frac{d\sigma}{dt} = \frac{\sigma_2 - \sigma_1}{t_2 - t_1} = 3.031 \text{ } ^\circ/\text{s}$$

We have selected time point 67 ($t = 264 \text{ s}$), where the above mentioned manoeuvre starts, and time point 250 ($t = 996$), where a bank reversal could be executed (assuming a similar bank rate, although we can expect a higher one because of the increased dynamic pressure). The results are presented in Figs. 5.15 through 5.17. Again, the induced angle of sideslip is plotted as well.

In Fig. 5.15 we see that the ramp response is similar to the angle-of-attack response as discussed in Section 5.4.1. The delay time is about 3.7 s and the difference between the commanded and actual bank angle is 10° . The latter value is considered to be too large if we take a design overshoot of 5° into account. We have to verify later, when we are flying along the nominal trajectory, whether this is acceptable or not. One way to solve this problem is to increase the gains, and thus the response, for the initial part of the trajectory. For the time being we accept the results as they are. In the lower graph we see the induced angle of sideslip. The equilibrium value is over -1° , because of a continuous control action for the bank angle. This angle of sideslip should not be a problem to control once the command input for the bank angle has disappeared, considering our experience with the response to an initial value (Section 5.3.3).

However, to be on the safe side we will check this. We take the same ramp function for the bank angle as input signal, and in addition we simulate a constant bank angle after 27 s ($\sigma = 80^\circ$). The result of this simulation is shown in Fig. 5.16. We see a well-damped behaviour of the angle of sideslip as well as for the bank angle.

Fig. 5.17, finally, shows the ramp response for time point 250. A similar behaviour as before is found.

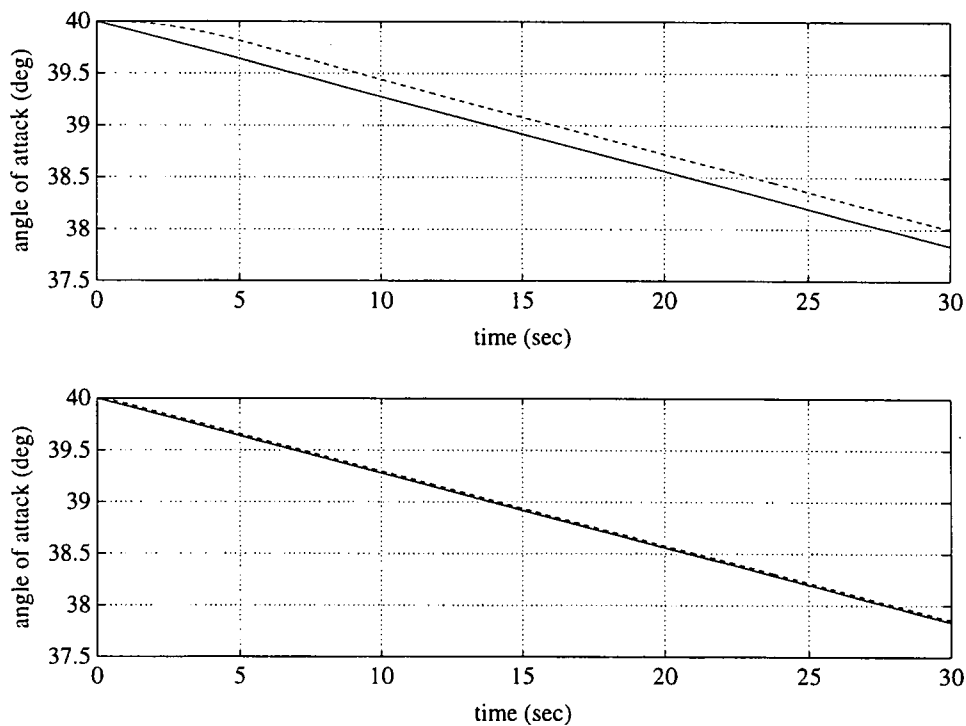


Fig. 5.14 - The ramp response of the angle of attack for time point 13 ($t = 48$ s), upper graph, and time point 250 ($t = 996$ s), lower graph. The nominal input signal is given by the solid line, and the response by the dashed line.

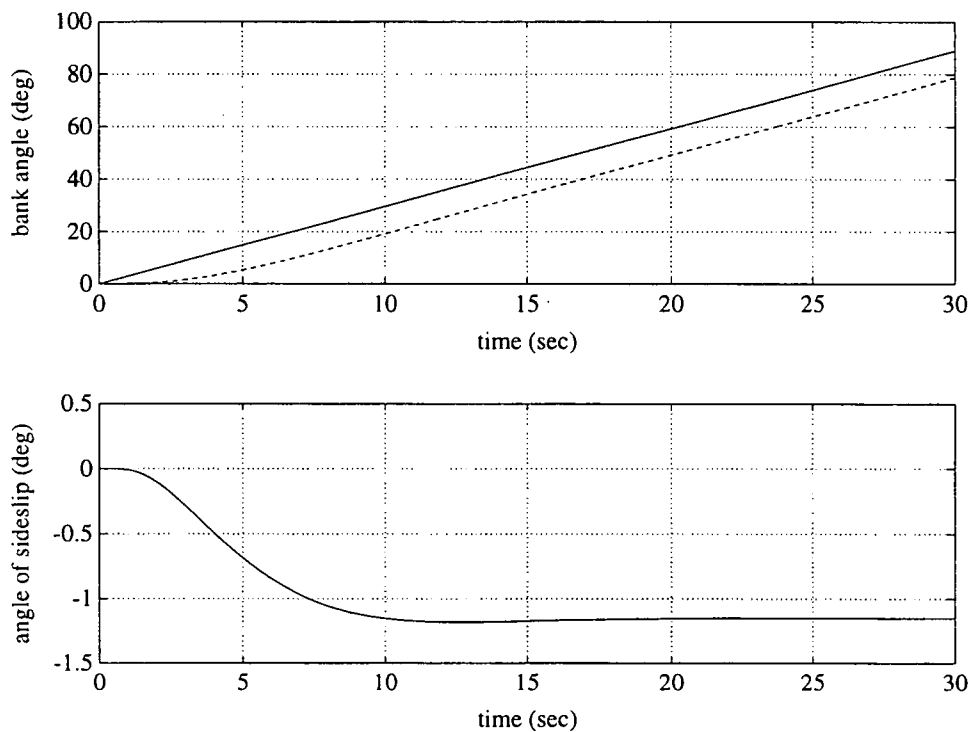


Fig. 5.15 - The ramp response of the bank angle for time point 67 ($t = 264$ s), upper graph, and the induced angle of sideslip, lower graph. In the upper graph, σ_c is given by the solid line, and the response (σ) by the dashed line.

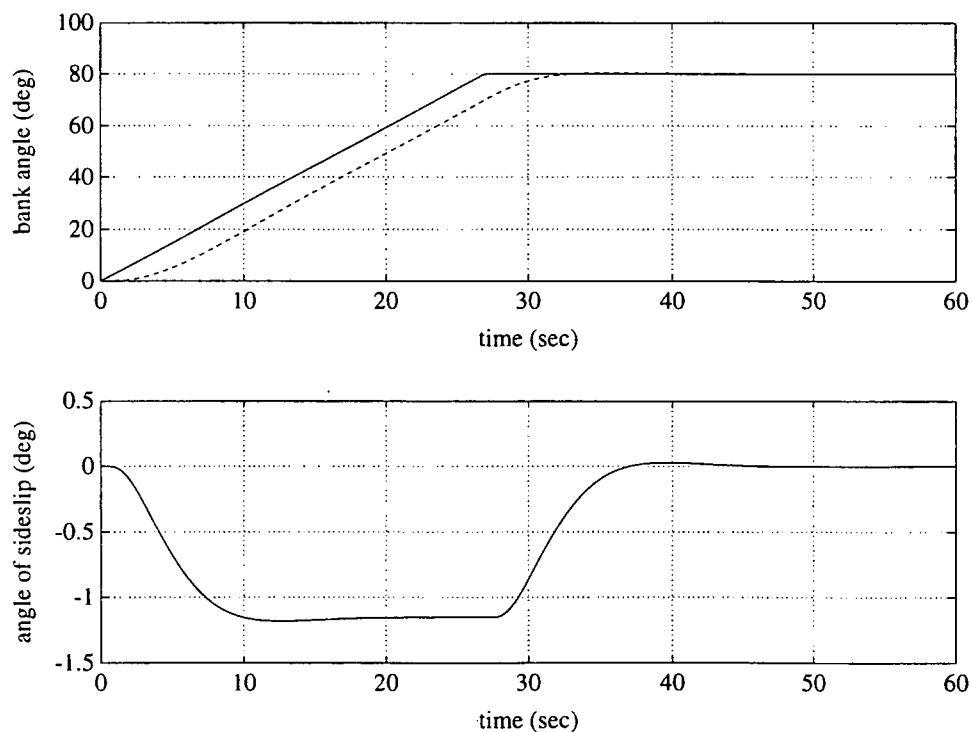


Fig. 5.16 - The ramp response of Fig. 5.15, combined with a constant bank angle after 27 s (time point 63).

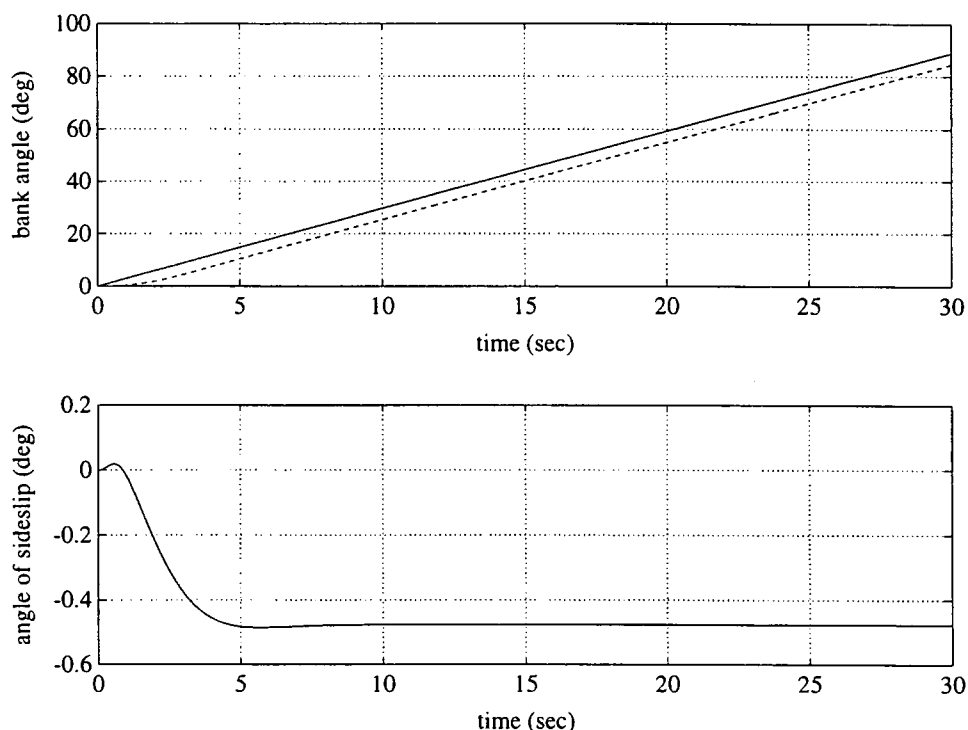


Fig. 5.17 - The ramp response of the bank angle for time point 250 ($t = 996$ s), upper graph, and the induced angle of sideslip, lower graph. In the upper graph, σ_c is given by the solid line, and the response (σ) by the dashed line.

5.5. Flight along nominal trajectory with integrated controller.

The outcome of the previous section is, that both the pitch and lateral controller show good tracking behaviour while simulating the step and ramp responses. However, we have to keep in mind that these response tests were done with simplified models. It is now the time to integrate the two controllers and simulate a 6-dof controlled re-entry flight, with all dynamics as introduced in Section 2.1 included. The initial conditions and the reference trajectory are the same as for the design of the controller.

However, before we start discussing the results of this simulation we must note that the integrated control system is also not a fully realistic model in that sense that we assume control surfaces to move instantaneously. In other words, when the attitude control system commands an aileron deflection, then the ailerons achieve that setting at that very instant. There are no delays due to hydraulic actuators. (On the other hand, the motion of the control surfaces is much faster than the fastest eigenmotion, and on this ground control-effector delays can be neglected.) Also the measurement system is assumed to be ideal, implying that the measured state is the same as the actual state. Last but not least, the applied guidance system is also a closed-loop system, as is the attitude control system. This means that any deviations from the reference trajectory will be compensated for by the guidance system, also those deviations resulting from attitude control and finite rigid-body motion. We must realise that our flight along the nominal trajectory will prove how well the attitude control system can execute the

commands generated by the guidance system.

In Fig. 5.18, the height as a function of flight time has been plotted, both for the controlled and the nominal trajectory. As we can see, the two curves match well, apart from two visible differences at $t \approx 750$ s and $t \approx 1,100$ s. The explanation for these two differences can be found in the time history of the bank angle (Fig. 5.22). As we already stated in Section 3.2, where we introduced the nominal trajectory, the nominal bank reversals are executed in zero time, assuming ideal control. Of course, in a realistic simulation the inertia of the vehicle will result in a finite time required for the reversals. The duration is, amongst others, depending on the control effectiveness (for aerodynamic control, this is basically determined by the dynamic pressure). The duration of a bank reversal can be in the order of 20 seconds. During that time, the bank angle has a smaller value than it should have, implying a larger vertical lift coefficient ($C_L \cdot \cos\sigma$). A larger vertical lift means that the descent rate gets smaller, or in other words, the vehicle flies at higher altitudes than it should. The height difference, however, is compensated for by the guidance system, since after the deviation the vehicle comes back to the nominal height.

In principle, a similar reasoning applies to the deviation from the nominal groundtrack (shown in Fig. 5.19). A bank reversal is initiated by an overshoot of the maximum allowable heading error. In case of ideal control, the heading error will decrease immediately after execution of a bank reversal. However, when a time delay due to the inertia of the vehicle has to be taken into account, it can easily be understood that the maximum allowable heading error will be exceeded before it starts decreasing again (see also Fig. 5.25). Far away from the target, this does not make much of a difference, but the closer the vehicle is to the target, the more rapidly it will deviate from its nominal groundtrack. For this reason, the two curves show more of a difference towards the end of the flight (when also the difference between the commanded and nominal bank angle is largest, see again Fig. 5.22).

Fig. 5.20 shows the first of the three attitude angles which are controlled by the attitude control system, i.e., the angle of attack. In this figure we see more of a difference between the controlled value and the nominal value. At the beginning of the trajectory we see a diverging angle of attack, caused by the fact that the trim law is not active. As we discussed earlier, trim is basically guaranteed by deflecting the body flap which is only activated when the dynamic pressure is higher than 100 N/m^2 . The moment the body flap is activated ($t \approx 194$ s), the angle of attack is stabilised at the nominal value. The diverging angle of attack is only partly compensated for by the pitch jets (Fig. 5.28) and later on by the elevators (Fig. 5.29), but apparently due to the design assumptions and simplifications, this offset is not properly controlled. On the other hand, it should be noted that the gain computation has been performed allowing a 2° overshoot of the angle of attack, so the offset is within range (see also the next figure, Fig. 5.21, where the difference between the commanded and the actual angle of attack is plotted). A revision of the trim law (trim with pitch jets, when the body flap is not active), a gain computation for the first 200 s with a smaller allowable overshoot can solve this problem. Another solution can be the following. When the body flap is set to a fixed deflection angle other than 0° , a pitch moment is generated that increases with the dynamic pressure. So when we put the body flap in the position that it will more or less acquire once the control of this control surface is activated, the oscillation in the angle of attack is greatly reduced.

Due to an angle of attack which is larger than the nominal one, the slightly higher lift results in an altitude error, which the guidance system wants to compensate by banking the vehicle. However, any altitude error will not be controlled in the upper layer of the atmosphere but only at lower altitudes¹⁶. This means, that the altitude error can grow, but of course only slowly due to the small lift force. When altitude control is activated by the guidance system, it is suddenly faced by an altitude error of some 250 m, which results in a suddenly commanded bank angle of almost 20° (see Fig. 5.22).

Returning to the time history of the angle of attack, we see that up to $t \approx 480$ s the controlled α is virtually equal to the nominal one. Then, we see noticeable differences. However, we should not panic before we have asked ourselves what the cause of these deviations is: the guidance controller or the attitude controller? Fig. 5.21 helps us in finding the answer. In this figure, the difference between the commanded and the actual angle of attack is plotted, which indicates how well the *attitude* controller performs. As we see, the differences are small at all times, from which we can conclude that the 'problem' is not related to the attitude controller but is a result of guiding the vehicle towards the target along the nominal trajectory.

In the same figure, three peaks in the right half of the graph need more explanation. During bank reversals, the guidance system keeps the commanded variation in the angle of attack at a constant value, which means that during the reversal no correction other than a change in the nominal value takes place. We already discussed above, that the bank angle is smaller than it should be during a reversal, resulting in a higher vertical lift. Any resulting errors can only be compensated after the reversal has been completed. This appears in an abrupt change in the commanded angle of attack, that can be found at $t \approx 730$ s, $t \approx 1,080$ s and $t \approx 1,200$ s.

Fig. 5.22 shows us the time history of the bank angle, that we have already partly explained during the course of this Section. We will restrict ourselves to some comments (nota bene: in Fig. 5.23, the difference between the commanded and the actual bank angle has been plotted, again indicating how well the attitude controller performs). The first difference between the actual and the nominal bank angle shows itself just before $t = 200$ s. We already explained that this is due to a sudden activation of the guidance system. However, we also find that we have a peak difference of over 15°, whereas the gains were calculated for an overshoot of 5°. This shows clearly the limitations of the attitude control system, that it cannot handle changes that are sudden and relatively large. The same is true for the second peak, when the first ramp function of the nominal bank angle is executed ($t \approx 270$ s). Since the altitude guidance is still compensating the altitude difference with the bank angle (although σ is getting smaller, so $\dot{\sigma} < 0$ °/s), the attitude control system is suddenly faced with a linearly increasing function of the bank angle ($\dot{\sigma} > 0$ °/s). However, before it can fulfil that demand, it has to change the sign of $\dot{\sigma}$, which introduces a certain time delay. Since the nominal bank angle is rapidly increasing it takes a while before the control system has made the difference between the commanded and actual bank angle equal to zero.

¹⁶ Altitude control has been divided into three regions. In the first region, no altitude control is performed because of the low dynamic pressure and therefore small aerodynamic forces. The second region is a transition region to the third one, in which full altitude control is being done. More information on the guidance system can be found in MBB (1988b) and Mooij (TO BE PUBLISHED).

The three remaining peaks are all related to the bank reversals. We can suffice by saying that the change in the commanded bank angle, generated by the guidance system based on a predicted bank rate, is too large for the attitude control system to achieve. As we know, the bank reversals are executed in a finite time, during which the vertical lift component is too large, resulting in a positive height error. For this reason, in order to compensate for this we see each time an overshoot of the bank angle. The oscillation, that shows at $t \approx 1080$ s, is probably induced because of a sudden change in the commanded (and therefore also the actual) angle of attack, right after finishing the bank reversal. Revising the guidance algorithm can solve this problem.

The last attitude angle to be discussed is the angle of sideslip (Fig. 5.24). We saw in the previous Sections, that there is a coupling between the angle of sideslip and the bank angle. Therefore, we might expect a deviation from the nominal 0° when we have a sudden change in the bank angle or when a bank reversal is being executed. Indeed, we see a number of peaks which damp out relatively quick at those moments. At $t \approx 1,000$ s, however, the angle of sideslip diverges slowly, without coming back to zero again. We think that this diversion is due to the simplifications made during the control-system design, for instance neglecting terms due the rotation of the local horizontal plane and the Earth's rotation.

Figs. 5.26 through 5.31, finally, show the control variables: the moments due to the roll, pitch and yaw jets, and the deflections of the ailerons, elevators and the rudders. A general remark, which has to be made before we give some brief comments on these Figures, is that these curves show the computed values. We have assumed that the exact reaction-control moments can be generated by the thrusters (for instance, by means of pulse modulation) and that the deflections of the control surfaces take place in zero time and are 100% accurate. Since these assumptions are very important for the performance of the attitude control system, we will study this in more detail in Mooij (TO BE PUBLISHED).

Most activity takes place when a bank reversal has to be initiated, or when a sudden change in the commanded attitude arises. The sudden change in bank angle for altitude control ($t \approx 200$ s) shows as sharp peaks in the roll moment and the aileron deflection, the latter only 5° away from the maximum allowable deflection. The yaw jets have to produce the maximum moment, amongst others to compensate for the induced angle of sideslip (the rudders are not yet active). Large control signals can be seen for the yaw jets and rudders when bank reversals are being executed. The peaks in the elevator deflection are also due to the bank reversals, although only indirectly. As we already said, during the bank reversal the commanded variation of the angle of attack is kept constant, which results in a sudden change in the commanded angle of attack right after completing the reversal.

It has to be noted that the strong oscillation in the aileron deflection must be studied in more detail. We already stated that the oscillation might be induced by the sudden change in commanded angle of attack. Furthermore, it is possible that the linearisation is another cause. The wing-flap deflection is the linear summation of the aileron and elevator deflection. However, for a negative deflection the aerodynamic forces and moments are not the same (in absolute sense) as for a positive deflection. Furthermore, the aerodynamics are such that for some flight conditions the commands for bank-angle control and angle-of-sideslip control are conflicting.

Last but not least, it is reasonable to expect that a real-life aileron cannot move so fast, therefore some kind of filtering might have to be included in the model.

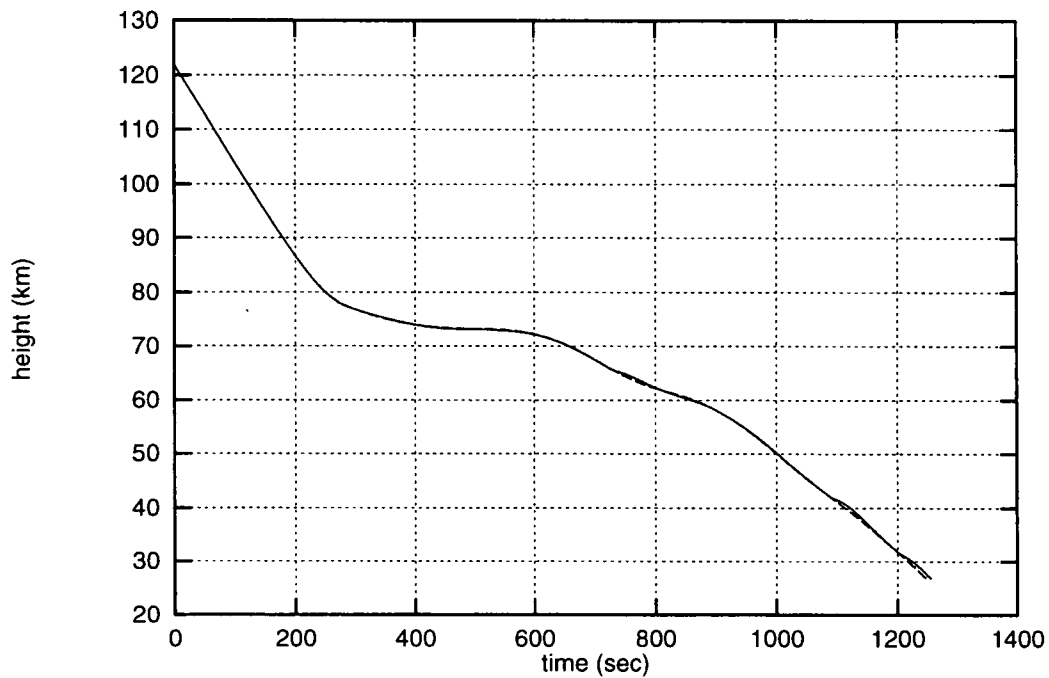


Fig. 5.18 - The height as a function of time for the controlled (solid line) and the nominal trajectory (dashed line).

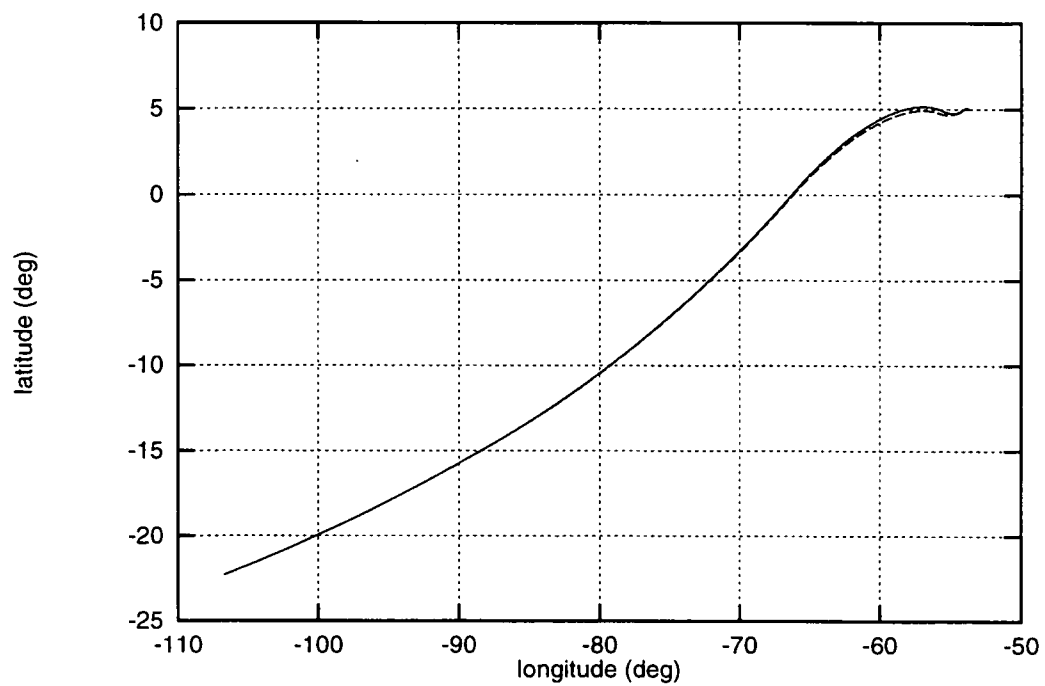


Fig. 5.19 - The groundtrack for both the controlled (solid line) and the nominal trajectory (dashed line).

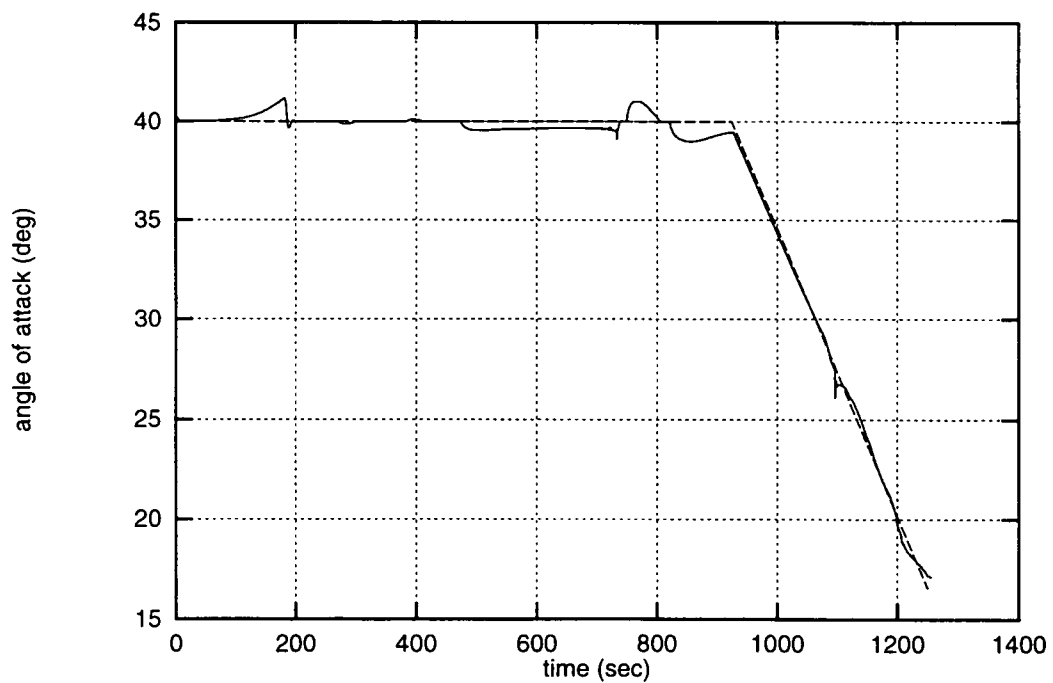


Fig. 5.20 - The angle of attack as a function of time for the controlled (solid line) and the nominal trajectory (dashed line).

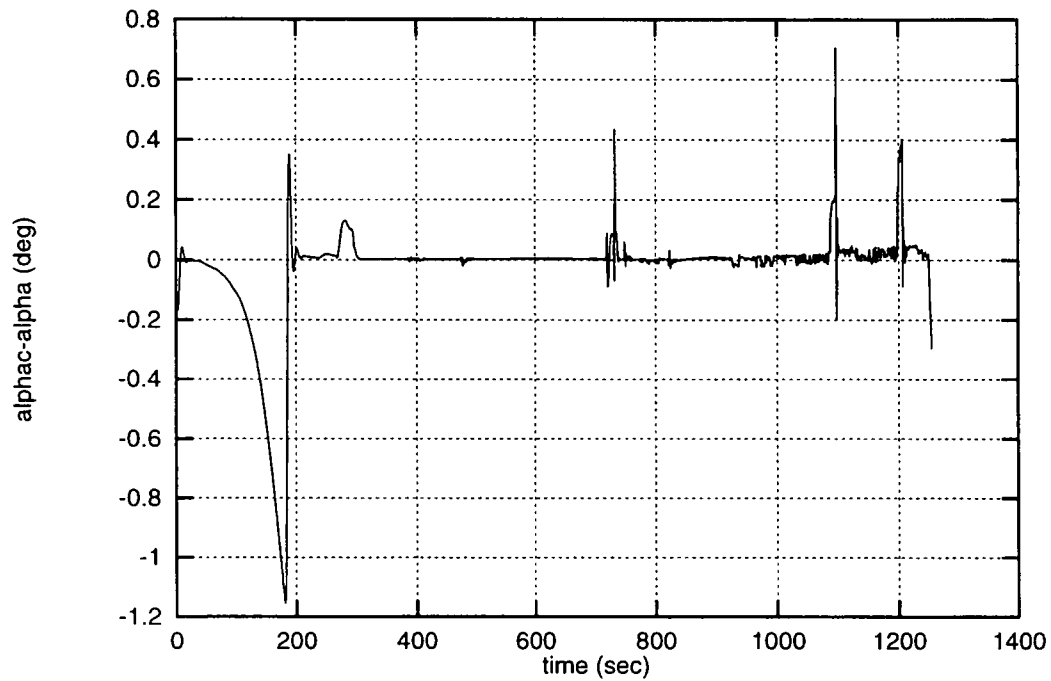


Fig. 5.21 - The difference between the commanded and the actual angle of attack, as a function of time.

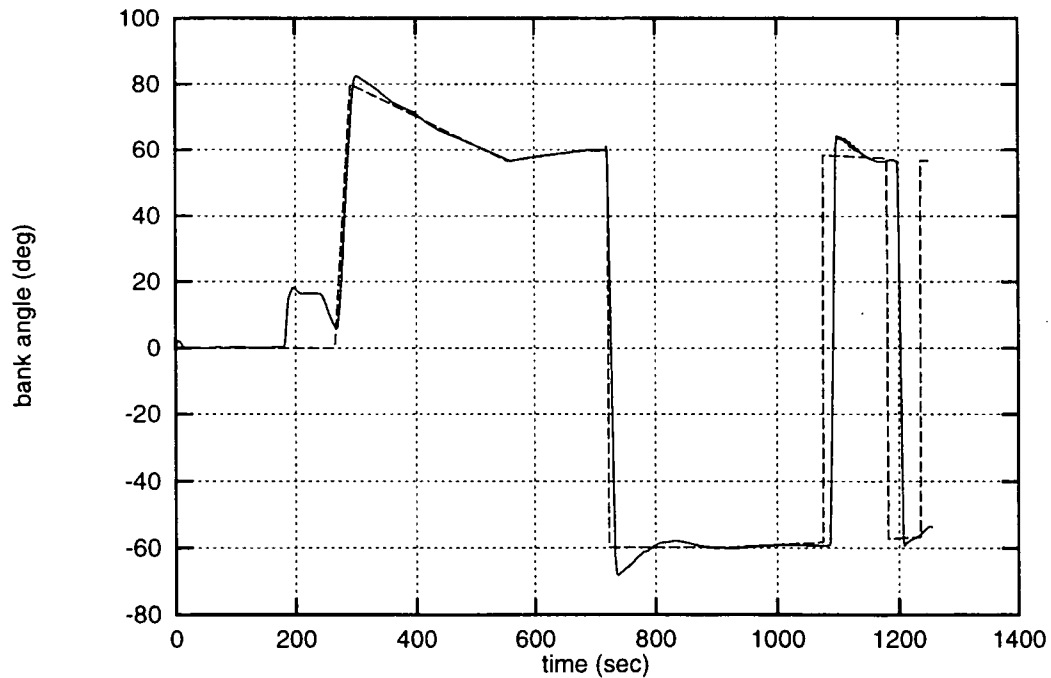


Fig. 5.22 - The bank angle as a function of time for the controlled (solid line) and the nominal trajectory (dashed line).

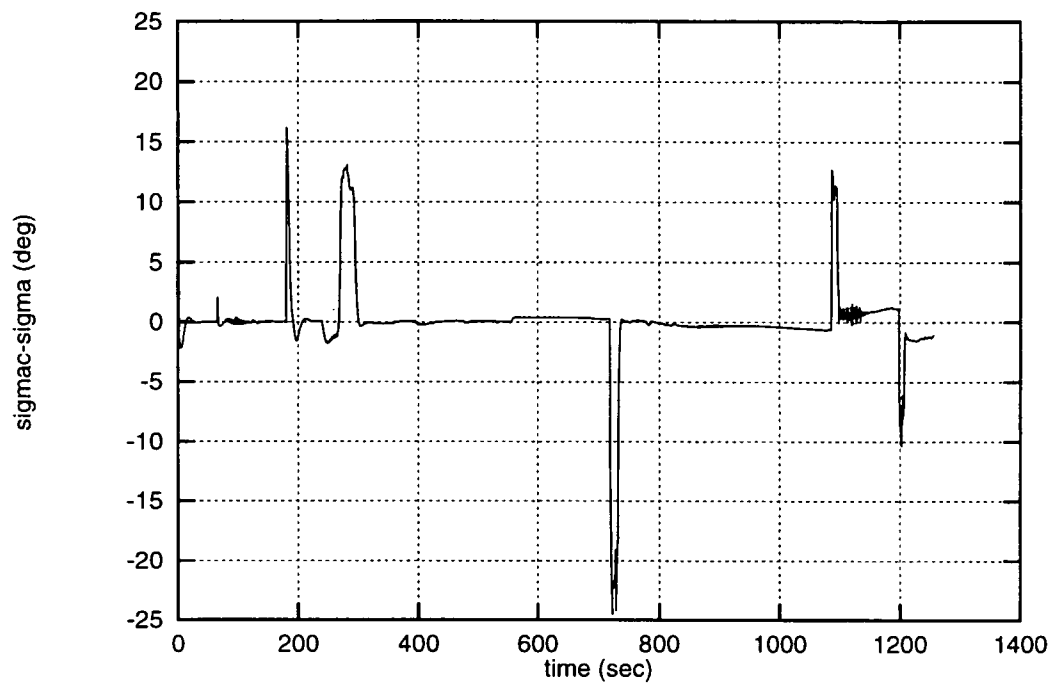


Fig. 5.23 - The difference between the commanded and the actual bank angle, as a function of time.

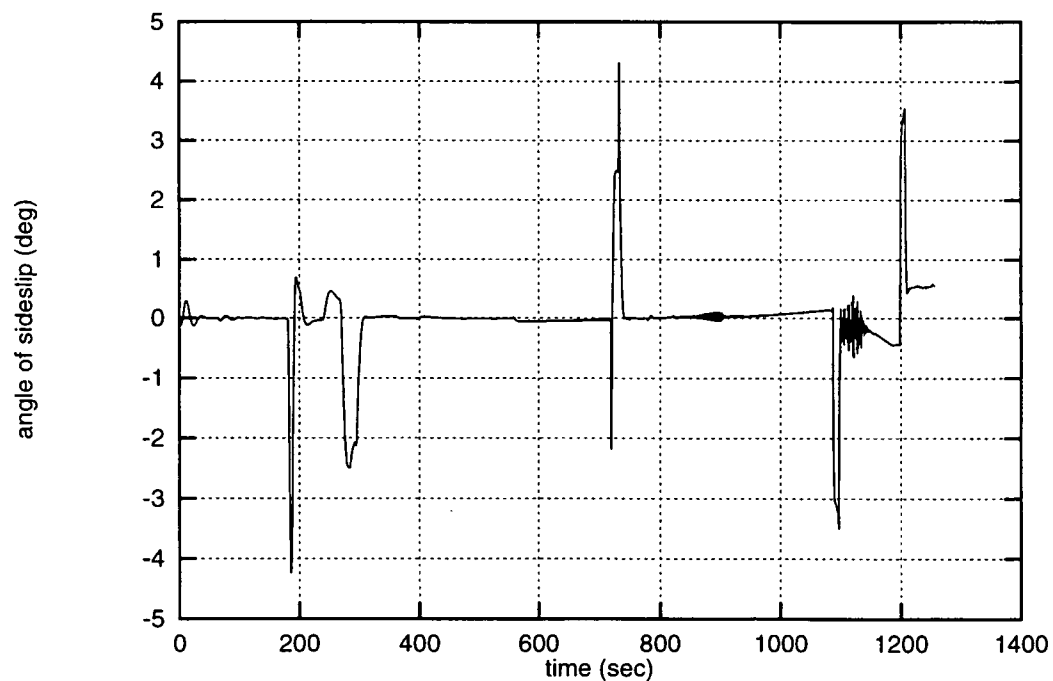


Fig. 5.24 - The angle of sideslip as a function of time for the controlled (solid line) and the nominal trajectory (dashed line).

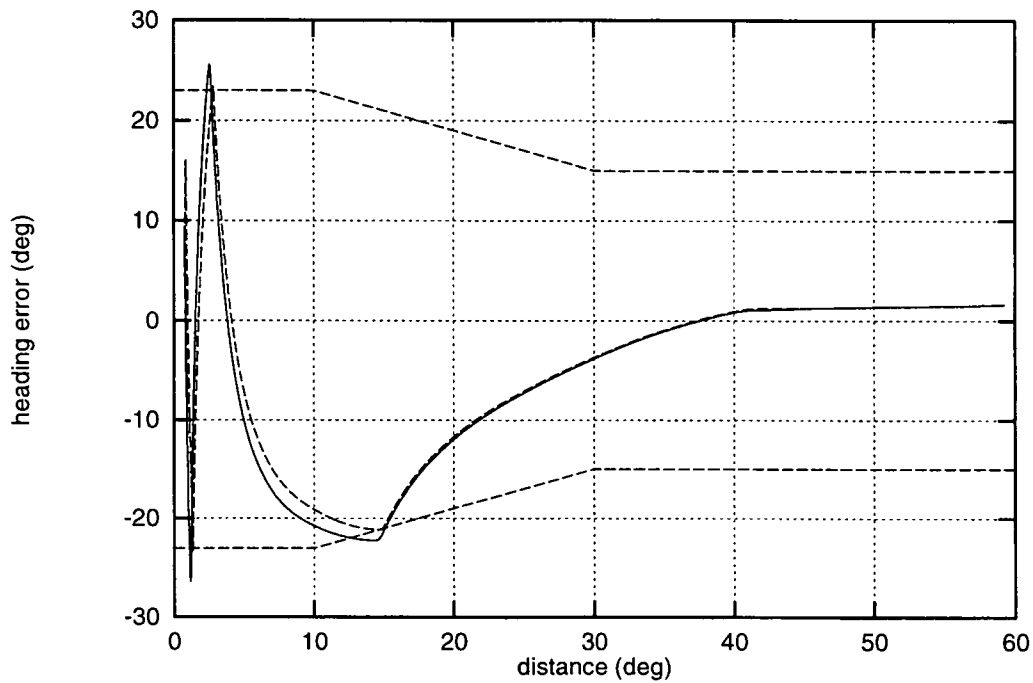


Fig. 5.25 - The heading error as a function of the distance to the target for the controlled (solid line) and the nominal trajectory (dashed line). The heading-error dead band is indicated by the two straight dashed lines.

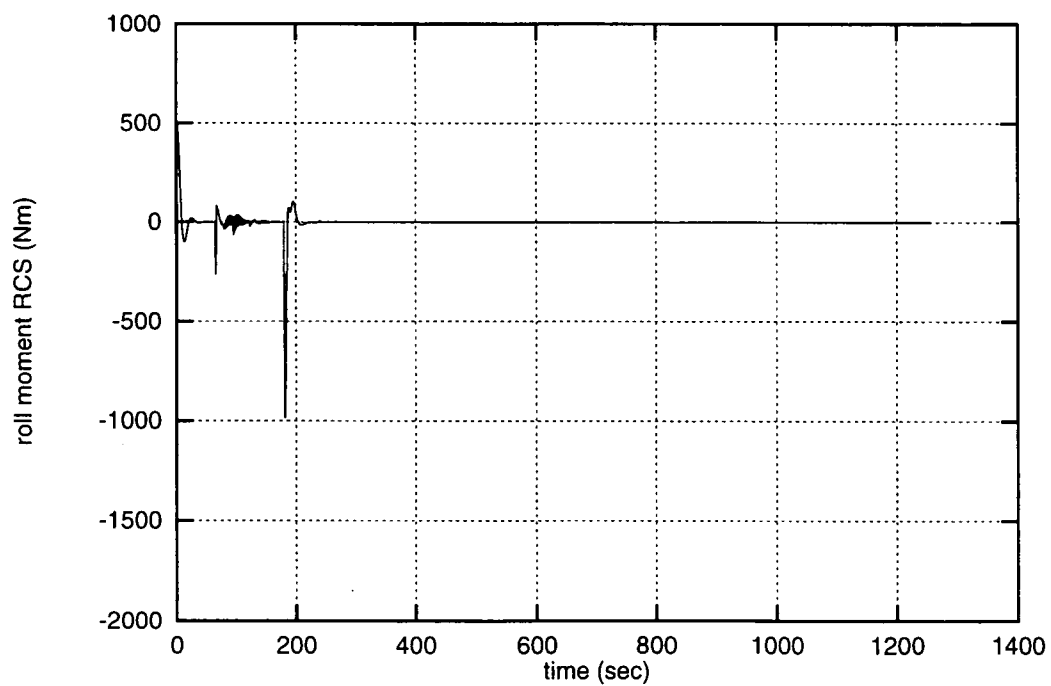


Fig. 5.26 - The roll moment due to reaction control as a function of time for the controlled trajectory.

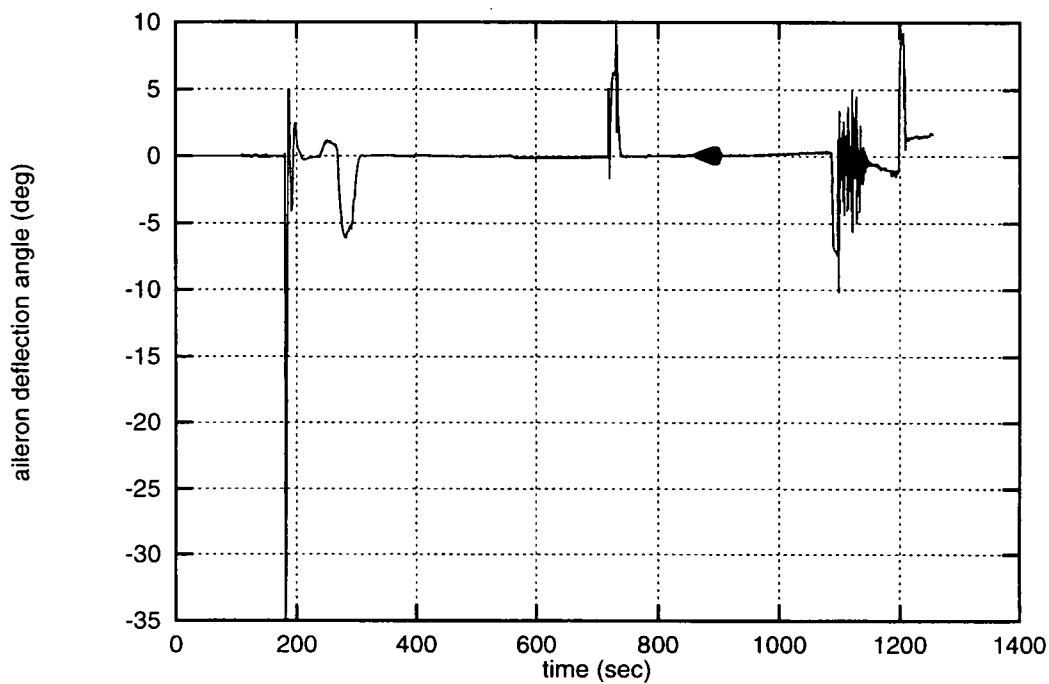


Fig. 5.27 - The control history of the aileron for the controlled trajectory.

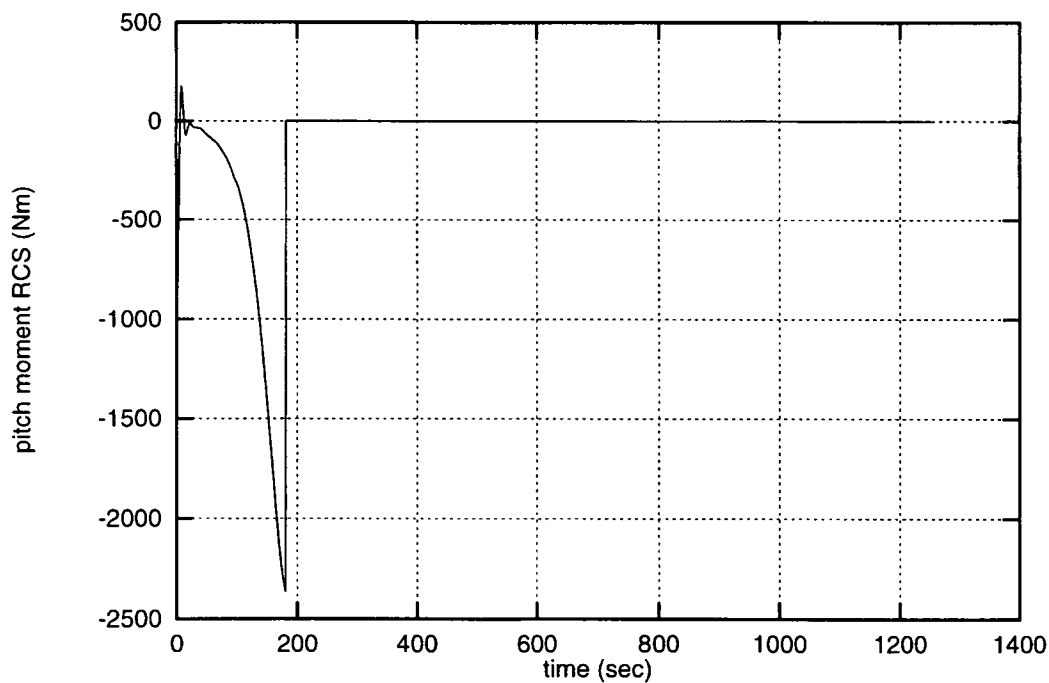


Fig. 5.28 - The pitch moment due to reaction control as a function of time for the controlled trajectory.

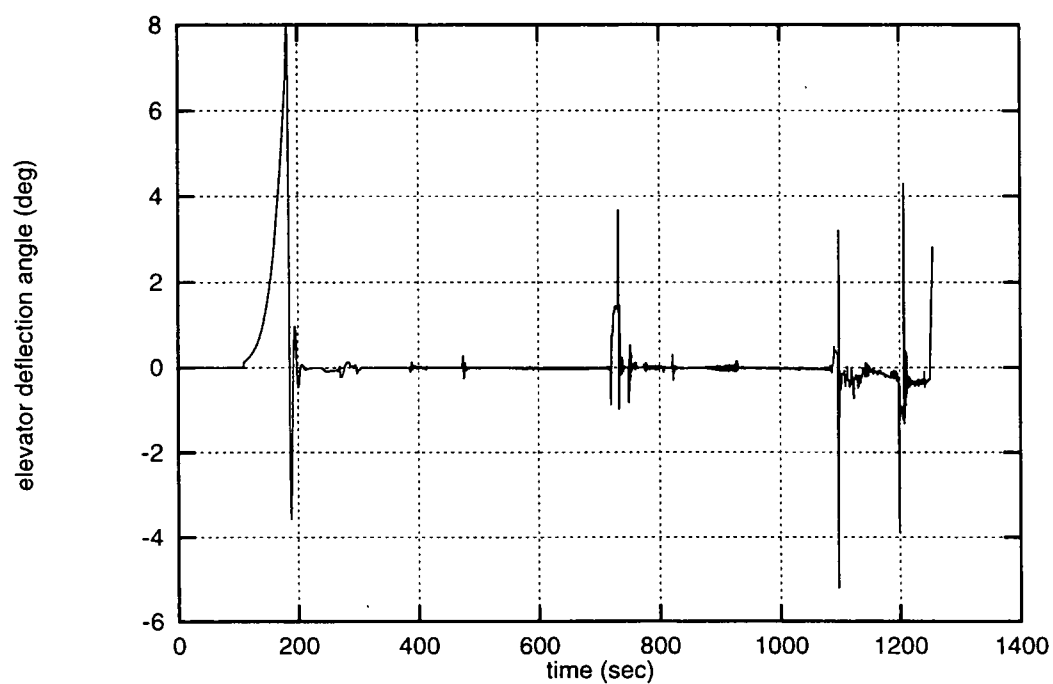


Fig. 5.29 - The control history of the elevator for the controlled trajectory.

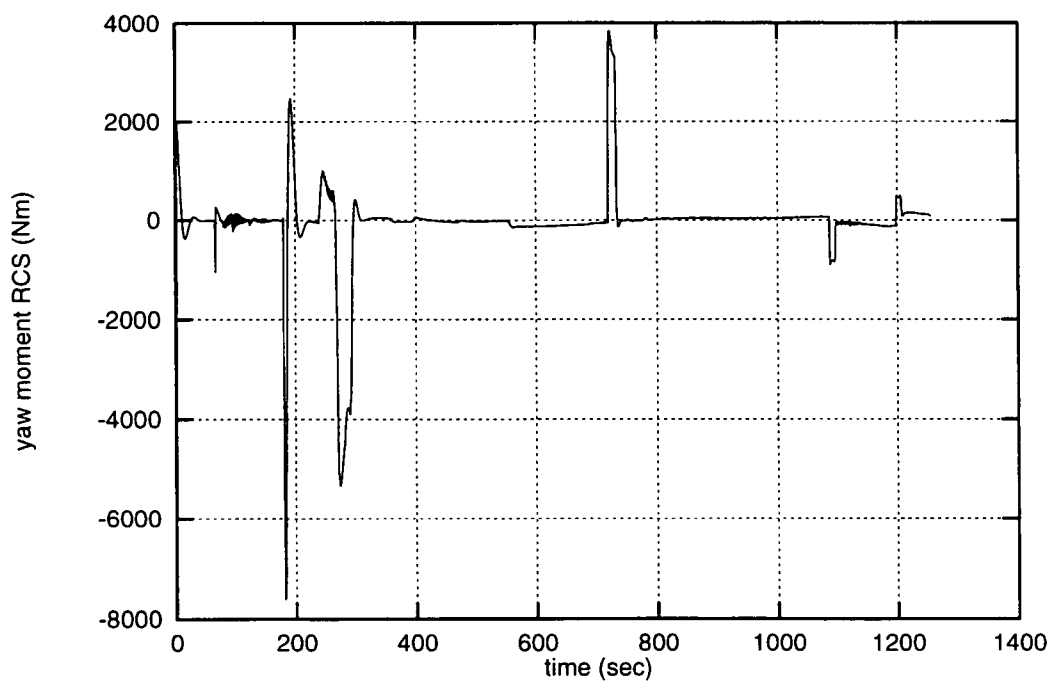


Fig. 5.30 - The yaw moment due to reaction control as a function of time for the controlled trajectory.

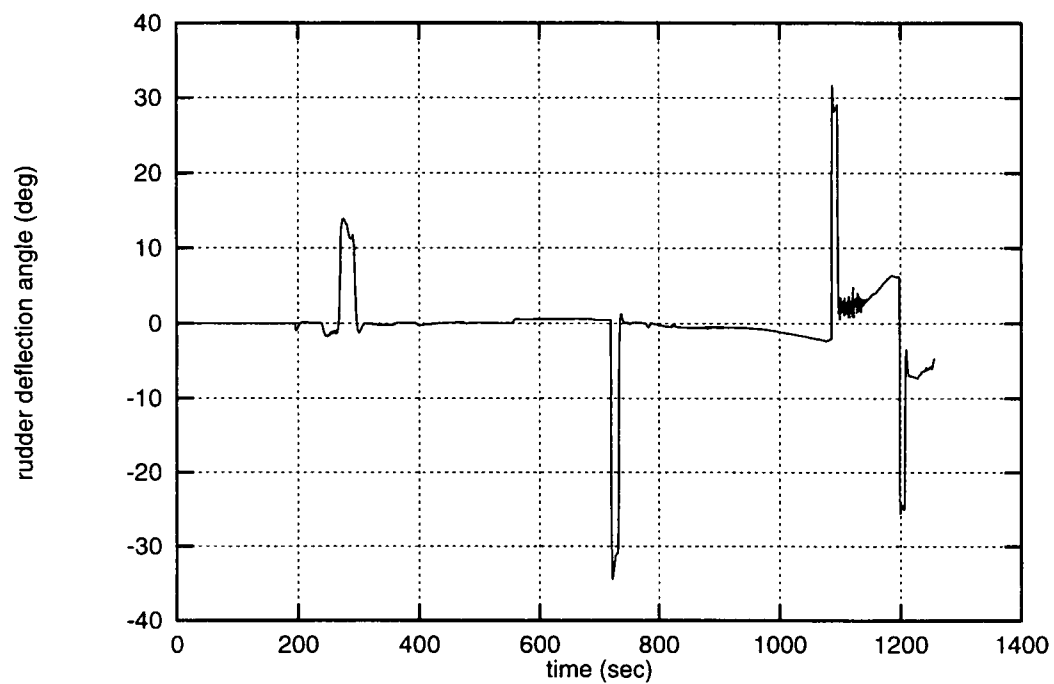


Fig. 5.31 - The control history of the rudder for the controlled trajectory.

Chapter 6

Conclusions and Recommendations

The HORUS-2B is an unpowered, winged re-entry vehicle, that has to be guided along a nominal trajectory in order to reach the target landing area. To enable a stable flight and to perform manoeuvres, an attitude controller must guarantee that the nominal control variables can be achieved and that perturbations will not force the vehicle too far away from its reference.

This report describes the design of a linear state feedback controller with gain scheduling. The design process has been divided into a number of successive steps. The starting point for the design is a system of 12 first-order differential equations, which enables the study of full 6-d.o.f. motion. After linearisation and introducing some simplifying assumptions, a state-space form of 9 state variables was left. Analysis of the eigenvalues and open-loop behaviour of this system showed that the vehicle exhibited diverging oscillations, but also that the eigenmotions could be decoupled into symmetric and asymmetric motions. For this reason, a pitch controller could be designed separately from a lateral controller. The gains which appeared in the control laws were solved simultaneously using the matrix Riccati equation.

The verification of the designed controllers has been divided into two steps. In the first step, the response of the closed-loop system to both a step and a ramp input for both the pitch and lateral controller has been considered. Both controllers showed a well-damped behaviour, which was sufficient for carrying out the second step. There, the two controllers were integrated and for the non-simplified equations of motion, the flight along the nominal trajectory was simulated. The results showed that HORUS can fly its nominal trajectory without major problems.

During the first 200 seconds of the trajectory, the angle of attack showed a moderately diverging behaviour, due to the absence of a trim law. A maximum deviation of about 1° was reached, which is within range of the overshoot boundary of 2° , and that can even be made smaller by revising the trim law. Other peak deviations of less than 1° arose due to the bank reversals, during which the commanded variation of the angle of attack was kept constant by the guidance system. After ending the reversal this resulted in sudden elevator deflections.

These deflections can be avoided by revising the guidance system.

The known coupling between the angle of sideslip and the bank angle was noticeable present during bank manoeuvres, when peak values in the angle of sideslip of about $\pm 4^\circ$ occurred. These deviations are well controlled. Some large differences between the commanded and actual bank angle were found, because the guidance system generated commanded bank angles by assuming a too large bank rate. A simple redefinition of the theoretical bank rate would solve this problem.

The only recommendation which can be made here is that a sensitivity analysis must give the final answer to whether the designed control system can fly the HORUS along a reference trajectory taking all kinds of perturbations into account. With this respect, one can think of, amongst others, atmospheric-density variations, uncertainties in the aerodynamic coefficients, mass deviations, the influence of wind, errors in the navigation system and delays in activating control surfaces. Such a sensitivity analysis, however, will be covered in another study (Mooij, TO BE PUBLISHED).

References

- 1) ACRI/LAN;
Guidance and control for moderate lift/drag reentry - Final report;
ESA Contract no. 9359/91/NL/JG (SC);
ACRI, Valbonne, 1992.
- 2) Åström, K.J.;
Adaptive feedback control;
Proceedings of the IEEE, Vol. 75, No. 2, February 1987, pp. 185-217.
- 3) Åström, K.J. and Wittenmark, B.;
Adaptive control;
Addison-Wesley Publishing Company, 1989.
- 4) Bayle, G.P.;
Space Shuttle entry flight control off-nominal design considerations;
Journal of Guidance, Navigation and Control, vol. 7, no. 1, pp. 9-14, Jan.-Feb. 1984.
- 5) Boskovich, B. and Kaufmann, R.E.;
Evolution of the Honeywell first-generation adaptive autopilot and its applications to F-94, F-101, X-15, and X-20 vehicles;
Journal of Aircraft, Vol. 3, no. 4, pp. 296-304, Jul.-Aug. 1966.
- 6) Brandt, A.P. and Van den Broek, P.Ph;
Vliegeigenschappen II (lecture notes in dutch);
D-34;
Delft University of Technology, Faculty of Aerospace Engineering, 1984.
- 7) Bryson Jr., A.E.;
New concepts in control theory, 1959-1984;
Journal of Guidance, Navigation and Control, vol. 8, no. 4, pp. 417-425, Jul.-Aug. 1985.
- 8) Bryson Jr., A.E. and Ho, Y.C.;
Applied optimal control;

John Wiley & Sons, 1975.

- 9) Collins, E.G. and Richter, S.;
Linear-Quadratic-Gaussian-based controller design for Hubble Space Telescope;
Journal of Guidance, Control and Dynamics, vol. 18, no. 2, pp. 208-213, Mar.-Apr. 1995.
- 10) Cooke, D.R.;
Space Shuttle stability and control test plan;
AIAA-82-1315;
From: AIAA 9th Atmospheric Flight Mechanics Conference, August 9-11, 1982, San Diego (CA).
- 11) Doyle, J.C.;
Structured uncertainty in control system design;
Proceedings of the 24th IEEE Conference on Decision and Control, Volume 1, 1985, pp. 260-265.
- 12) Doyle, J.C., Francis, B.A. and Tannenbaum, A.R.;
Feedback control theory;
Macmillan Publishing Company, New York, 1992.
- 13) Doyle, J., Lenz, K. and Packard, A.;
Design examples using μ -synthesis: Space Shuttle lateral axis FCS during re-entry;
NATO ASI Series, Vol. F34, 'Modelling, robustness and sensitivity reductions in control systems', pp. 128-154;
Springer Verlag, Berlin Heidelberg, 1987.
- 14) Doyle, J.C. and Stein, G.;
Multivariable feedback design: concepts for a classical/modern synthesis;
IEEE Transactions on Automatic Control, Volume AC-26, no. 1, pp. 4-16, February 1981.
- 15) Doyle, J.C., Wall, J.E. and Stein, G.;
Performance and robustness analysis for structured uncertainty;
Proceedings of the 21st IEEE Conference on Decision and Control, Volume 2, 1982, pp. 629-636.
- 16) D'Souza, A.F.;
Design of control systems;
Prentice Hall, Inc., Englewood Cliffs, New Jersey, 1988.
- 17) Epple, R.G.E. and Altenbach, R.E.;
Dynamic stability testing of the orbiter flight control system/flexible body interaction;
Journal of Guidance, Navigation and Control, vol. 6, no. 6, pp. 456-460, Nov.-Dec. 1983.
- 18) Etkin, B.;
Dynamics of atmospheric flight;

John Wiley and Sons, New York, 1972.

- 19) Frangos, C. and Yavin, Y.;
Design methodology for linear optimal control systems;
Journal of Guidance, Control and Dynamics, vol. 15, no. 5, pp. 1302-1304, Sep.-Oct. 1992.
- 20) Gawronski, W.;
Linear quadratic controller design for the deep space network antennas;
Journal of Guidance, Control and Dynamics, vol. 17, no. 4, pp. 655-660, Jul.-Aug. 1994.
- 21) Gockel, W.;
Angular control of a reentry vehicle in hypersonic flight regime;
AIAA-93-5090;
From: AIAA/DGLR Fifth International Aerospace Planes and Hypersonics technologies Conference, 30 November - 3 December 1993, Munich, Germany.
- 22) Gopal, M.;
Modern control system theory;
Wiley Eastern Ltd., New Delhi, Second Reprint, June 1989.
- 23) Gregory, I.M., Chowdhry, R.S., McMinn, J.D. and Shaughnessy, J.D.;
Hypersonic vehicle model and control law development using H_∞ and μ synthesis;
NASA Technical Memorandum 4562.
NASA, 1994.
- 24) Grocott, S.C.O., How, J.P. and Miller, D.W.;
A comparison of robust control techniques for uncertain structural systems;
AIAA-94-3571;
From: AIAA Guidance and Control Conference, 1994.
- 25) Hamilton, P.N.;
Flexible body stabilization for Space Shuttle aerosurface control loops;
AIAA-82-1532;
From: AIAA Guidance and Control Conference, San Diego, CA, August 9-11, 1982.
- 26) Kaufman, H., Bar-Kana, I. and Sobel, K.;
Direct adaptive control algorithms;
Springer-Verlag, New York, 1994.
- 27) Klinar, W.J., Saldana, R.L., Kubiak, E.T., Smith, Jr., E.E., Peters, W.H. and Stegall, H.W.;
Space Shuttle flight control system;
Volume 4, paper 6.2;
From: proceedings of the IFAC 6th World Congress, Boston/Cambridge, MS, August 24-30, 1975.
- 28) Kokotovic, P.V.;

Recent trends in feedback design: an overview;
Automatica, Vol. 21, No. 3, pp. 225-236.

- 29) Kuo, B.C.;
Automatic control systems;
Prentice Hall, Inc., Englewood Cliffs, New Jersey, 1987.
- 30) Lee, J.F.L. and Barrett, M.F.;
Nonlinear analysis of Shuttle entry RCS coupling with bending modes;
AIAA-82-1533;
From: AIAA Guidance and Control Conference, San Diego, CA, August 9-11, 1982.
- 31) Lewis, F.L.;
Optimal control;
John Wiley & Sons, 1986.
- 32) Luo, J. and Lan, C.E.;
Determination of weighting matrices of a Linear Quadratic Regulator;
Journal of Guidance, Navigation and Control, vol. 18, no. 6, pp. 1462-1463, Nov.-Dec. 1995.
- 33) MBB Space Communication and Propulsion Systems Division;
Study on re-entry guidance and control. Final report - Volume 2: Reference vehicle definition and orbital constraints. ESA report reference: ESA CR (P) 2652;
MBB, Munich, 1988a.
- 34) MBB Space Communication and Propulsion Systems Division;
Study on re-entry guidance and control. Final report - Volume 4: FCS and guidance concepts. ESA report reference: ESA CR (P) 2652;
MBB, Munich, 1988b.
- 35) McDermott, A.M. and Makowski, K.;
Space Shuttle linearized guidance, navigation and control stability analysis;
AIAA-82-1555;
From: AIAA Guidance and Control Conference, San Diego, CA, August 9-11, 1982.
- 36) McHenry, R.L., Brand, T.J., Long, A.D., Cockrell, B.F. and Thibodeau III, J.R.;
Space Shuttle ascent guidance, navigation, and control;
The Journal of the Astronautical Sciences, Vol. XXVII, No. 1, pp. 1-38, January-March, 1979.
- 37) McRuer, D.T., Myers, T.T. Hoh, R.H. and Johnston, D.E.;
Assessment of flying-quality criteria for air-breathing aerospacecraft;
NASA Contractor Report 4442;
NASA, Washington, D.C., 1992.

- 38) Messer, R.S., Haftka, R.T. and Cudney, H.H.;
Cost of Model Reference Adaptive Control: analysis, experiments, and optimization;
Journal of Guidance, Control and Dynamics, vol. 17, no. 5, pp. 975-982, Sep.-Oct. 1994.
- 39) Mooij, E.;
Flight simulation for advanced launchers;
Report LR-747;
Delft University of Technology, Faculty of Aerospace Engineering, 1994.
- 40) Mooij, E.;
The motion of a vehicle in a planetary atmosphere;
Report LR-768;
Delft University of Technology, Faculty of Aerospace Engineering, 1994.
- 41) Mooij, E.;
The HORUS-2B reference vehicle;
Memorandum M-692;
Delft University of Technology, Faculty of Aerospace Engineering, 1995.
- 42) Mooij, E.;
Guidance and control of an unpowered, winged re-entry vehicle;
Delft University of Technology, Faculty of Aerospace Engineering, TO BE PUBLISHED.
- 43) Mooij, E., Marée, A.G.M. and Sudmeijer, K.J.;
Aerodynamic controllability of a selected re-entry test vehicle;
IAF-95-V.4.04;
From: 46th International Astronautical Congress (October 2-6, 1995/Oslo, Norway).
- 44) Myers, T.T., Johnston, D.E. and McRuer, D.T.;
Space Shuttle flying qualities and criteria assessment;
NASA Contractor Report 4049;
NASA, Washington, D.C., 1987.
- 45) Nguyen, V.H., Hishimi, J.T., Payne, T.H. and Woosley, E.W.;
Space Shuttle descent flight verification by simulation: a challenge in implementing flight control system robustness;
AGARD-CP-489;
From: Space Vehicle Flight Mechanics Conference (paper 9);
Neuilly sur Seine, France, 1990.
- 46) Paradiso, J.A.;
Adaptable method of managing jets and aerosurfaces for aerospace vehicle control;
Journal of Guidance, Control and Dynamics, vol. 14, no. 1, pp. 44-50, Jan.-Feb. 1991.
- 47) Sachs, G.;
Stability and control problems in hypersonic flight;

- Paper 35;
From: Space Course Munich, 1993.
- 48) Schleich, W.T.;
The Space Shuttle ascent guidance and control;
AIAA-82-1497;
From: AIAA Guidance and Control Conference, San Diego, CA, August 9-11, 1982.
- 49) Schletz, B.;
Use of quaternions in Shuttle guidance, navigation, and control;
AIAA-82-1557;
From: AIAA Guidance and Control Conference, San Diego, CA, August 9-11, 1982.
- 50) Shahian, B. and Hassul, M.;
Control system design using MATLAB®;
Prentice Hall, Englewood Cliffs, New Jersey, 1993.
- 51) Sinai, M.;
Decentralized integrated control of hypersonic vehicles;
AIAA-90-5211;
From: AIAA Second International Aerospace Planes Conference (Orlando, FL, 29-31 October 1990).
- 52) Stone, H.W. and Powell, R.W.;
Space Shuttle orbiter entry guidance and control system sensitivity analysis;
AIAA CP-76-03, pp. 169-175;
From: AIAA 3rd Atmospheric Flight Mechanics Conference (Arlington, TX, June-7-9, 1976).
- 53) Trujillo, B.M.;
Determination of lift and drag characteristics of Space Shuttle Orbiter using maximum likelihood estimation technique;
AIAA-86-2225;
From: AIAA Atmospheric Flight Mechanics Conference (Williamsburg, Virginia, August 18-20, 1986).
- 54) Vincent, J.H., Emami-Naeini, A. and Khraishi, N.M.;
Case study comparison of Linear Quadratic Regulator and H_∞ control synthesis;
Journal of Guidance, Control and Dynamics, vol. 17, no. 5, pp. 958-965, Sep.-Oct. 1994.

Appendix A

Definition of State Variables

The position and velocity of the vehicle are expressed in spherical components w.r.t. the rotating frame with the origin in the centre of mass (c.o.m.) of the Earth (the so-called R -frame), see also Fig. A.1.

Position: distance R , longitude τ and latitude δ

Velocity: groundspeed V , flight-path angle γ and heading χ

The longitude is measured positively to the east ($0^\circ \leq \tau < 360^\circ$). The latitude is measured along the appropriate meridian starting at the equator, positive in north direction ($0^\circ \leq \delta \leq 90^\circ$) and negative to the south. The distance R , finally, is the distance from the CoM of the central body to the c.o.m. of the vehicle. The relative velocity V (i.e., the modulus of the velocity vector \mathbf{V}) is expressed with respect to the rotating planetocentric frame. γ is the angle between \mathbf{V} and the local horizontal plane; it ranges from -90° to $+90^\circ$ and is negative when \mathbf{V} is below the local horizon. χ defines the direction of the projection of \mathbf{V} in the local horizontal plane with respect to the local north and ranges from -180° to $+180^\circ$. When $\chi = +90^\circ$, the vehicle is moving parallel to the equator to the east.

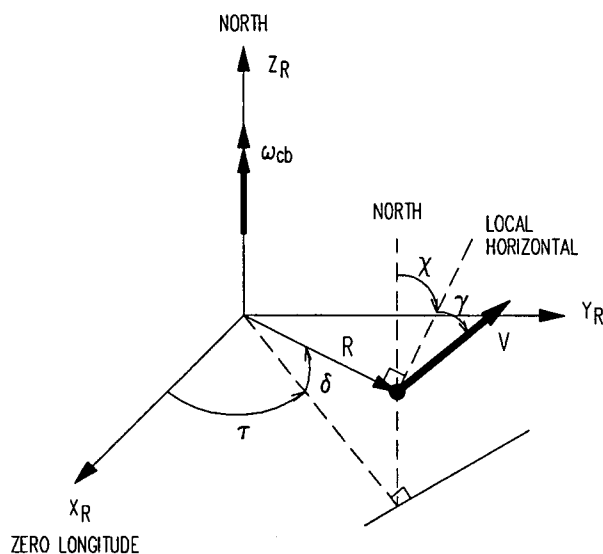


Fig. A.1 - Definition of the six spherical flight parameters, the position (R, τ, δ) and velocity (V, γ, χ) . Here, both τ, δ, γ and χ are positive. The indicated frame is the rotating planetocentric frame (index R), with its origin in the c.o.m. of the Earth and the Z_R -axis aligned with the Earth's rotation vector.

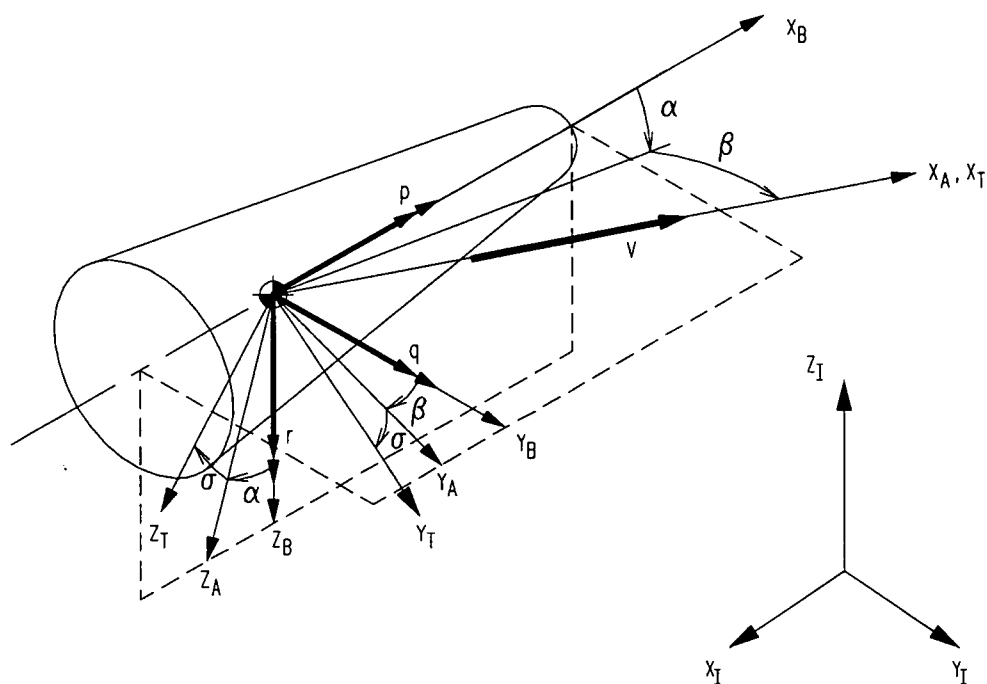


Fig. A.2 - Definition of the aerodynamic attitude angles α, β and σ , and the angular rates p, q and r . Here, all states are positive. The four related reference frames are the inertial frame (index I), the body frame (index B), the aerodynamic frame (index A) and the trajectory frame (index T). The I -frame has its origin in the c.o.m. of the Earth. The origin of the other frames is located in the c.o.m. of the vehicle. The B -frame is fixed to the body.

The attitude of a vehicle, or in more mathematical terms, the orientation of a body-fixed reference frame with respect to another, is expressed by the so-called aerodynamic angles, i.e., the angle of attack α ($-180^\circ \leq \alpha < 180^\circ$, for a 'nose-up' attitude $\alpha > 0^\circ$), the angle of sideslip β ($-180^\circ \leq \beta \leq 180^\circ$, β is positive for a 'nose-left' attitude) and the bank angle σ ($-180^\circ \leq \sigma < 180^\circ$, σ is positive for when banking to the right), see also Fig. A.2. Nota bene: in the equations of motion, these angles are related to the groundspeed, but since wind is not considered here, the groundspeed equals the airspeed.

The angular rate of the body is here defined as the rotation of the body frame with respect to the inertial frame, expressed in components along the body axes. The rotation vector ω is defined by the roll rate p , the pitch rate q and the yaw rate r (see again Fig. A.2).

Appendix B

Linear Stability Model of HORUS-2B

The local stability model is a linearised model giving the flight dynamics of a vehicle. It describes small deviations from an equilibrium state. In this appendix we will state the assumptions under which the local stability model has been derived, and we give the mathematical formulation of this model. To start with, the non-linear equations of motion are derived for an unpowered vehicle of constant mass, with a plane of mass symmetry ($X_B Y_B$ -plane). Aerodynamic control effectors are a body flap, two elevons and two rudders; furthermore, there are roll, pitch and yaw reaction-control jets.

The linearisation is done under the assumptions that:

- the Earth is not rotating,
- the gravity field is spherical,
- the vehicle is rotationally symmetric in mass,
- the asymmetric translational motion has no effect on the attitude kinematics, i.e., the trajectory is directed along the equator,
- the rotational rate of the vehicle is treated as a perturbation,
- pitch stability is guaranteed throughout the flight,
- the nominal angle of sideslip is zero, and
- higher-order terms are neglected.

The outcome, nine coupled, linear differential equations, can be written in matrix form:

$$\Delta \dot{\mathbf{x}} = \mathbf{A} \Delta \mathbf{x} + \mathbf{B} \Delta \mathbf{u} \tag{B.1}$$

with

$$\Delta \mathbf{x} = (\Delta V, \Delta \gamma, \Delta R, \Delta p, \Delta q, \Delta r, \Delta \alpha, \Delta \beta, \Delta \sigma)^T$$

$$\Delta \mathbf{u} = (\Delta \delta_e, \Delta \delta_a, \Delta \delta_r, \Delta T_x, \Delta T_y, \Delta T_z)^T$$

$$\mathbf{A} = \begin{bmatrix} a_{VV} & a_{V\gamma} & a_{VR} & a_{Vp} & a_{Vq} & a_{Vr} & a_{V\alpha} & a_{V\beta} & a_{V\sigma} \\ a_{\gamma V} & a_{\gamma\gamma} & a_{\gamma R} & a_{\gamma p} & a_{\gamma q} & a_{\gamma r} & a_{\gamma\alpha} & a_{\gamma\beta} & a_{\gamma\sigma} \\ a_{RV} & a_{R\gamma} & a_{RR} & a_{Rp} & a_{Rq} & a_{Rr} & a_{R\alpha} & a_{R\beta} & a_{R\sigma} \\ a_{pV} & a_{p\gamma} & a_{pR} & a_{pp} & a_{pq} & a_{pr} & a_{p\alpha} & a_{p\beta} & a_{p\sigma} \\ a_{qV} & a_{q\gamma} & a_{qR} & a_{qp} & a_{qq} & a_{qr} & a_{q\alpha} & a_{q\beta} & a_{q\sigma} \\ a_{rV} & a_{r\gamma} & a_{rR} & a_{rp} & a_{rq} & a_{rr} & a_{r\alpha} & a_{r\beta} & a_{r\sigma} \\ a_{\alpha V} & a_{\alpha\gamma} & a_{\alpha R} & a_{\alpha p} & a_{\alpha q} & a_{\alpha r} & a_{\alpha\alpha} & a_{\alpha\beta} & a_{\alpha\sigma} \\ a_{\beta V} & a_{\beta\gamma} & a_{\beta R} & a_{\beta p} & a_{\beta q} & a_{\beta r} & a_{\beta\alpha} & a_{\beta\beta} & a_{\beta\sigma} \\ a_{\sigma V} & a_{\sigma\gamma} & a_{\sigma R} & a_{\sigma p} & a_{\sigma q} & a_{\sigma r} & a_{\sigma\alpha} & a_{\sigma\beta} & a_{\sigma\sigma} \end{bmatrix}$$

$$\mathbf{B} = \begin{bmatrix} b_{Ve} & b_{Va} & b_{Vr} & b_{Vx} & b_{Vy} & b_{Vz} \\ b_{\gamma e} & b_{\gamma a} & b_{\gamma r} & b_{\gamma x} & b_{\gamma y} & b_{\gamma z} \\ b_{Re} & b_{Ra} & b_{Rr} & b_{Rx} & b_{Ry} & b_{Rz} \\ b_{pe} & b_{pa} & b_{pr} & b_{px} & b_{py} & b_{pz} \\ b_{qe} & b_{qa} & b_{qr} & b_{qx} & b_{qy} & b_{qz} \\ b_{re} & b_{ra} & b_{rr} & b_{rx} & b_{ry} & b_{rz} \\ b_{\alpha e} & b_{\alpha a} & b_{\alpha r} & b_{\alpha x} & b_{\alpha y} & b_{\alpha z} \\ b_{\beta e} & b_{\beta a} & b_{\beta r} & b_{\beta x} & b_{\beta y} & b_{\beta z} \\ b_{\sigma e} & b_{\sigma a} & b_{\sigma r} & b_{\sigma x} & b_{\sigma y} & b_{\sigma z} \end{bmatrix}$$

The used notations are:

- V = modulus of relative velocity vector (m/s)
- γ = flight-path angle (rad)
- R = modulus of position vector (m)
- p = roll rate (rad/s)
- q = pitch rate (rad/s)
- r = yaw rate (rad/s)
- α = angle of attack (rad)
- β = angle of sideslip (rad)
- σ = bank angle (rad)
- δ_e = elevator deflection angle (rad)
- δ_a = aileron deflection angle (rad)
- δ_r = rudder deflection angle (rad)

T_x = roll-thruster moment (Nm)
 T_y = pitch-thruster moment (Nm)
 T_z = yaw-thruster moment (Nm)

The elements of matrix **A** are given by:

$$a_{VV} = -\frac{1}{m V_0} \left(M_0 \frac{\partial C_D}{\partial M} q_{dyn_0} S_{ref} + 2 D_0 \right) \quad (B.2)$$

$$a_{V\gamma} = -g_0 \cos \gamma_0 \quad (B.3)$$

$$a_{VR} = 2 \frac{g_0}{R_0} \sin \gamma_0 \quad (B.4)$$

$$a_{V\alpha} = -\frac{1}{m} \frac{\partial C_D}{\partial \alpha} q_{dyn_0} S_{ref} \quad (B.5)$$

$$a_{Vp} = a_{Vq} = a_{Vr} = a_{V\beta} = a_{V\sigma} = 0 \quad (B.6)$$

$$a_{\gamma V} = \frac{1}{V_0} \left(-\dot{\gamma}_0 + \frac{2 V_0}{R_0} \cos \gamma_0 \right) + \frac{\cos \sigma_0}{m V_0^2} \left(M_0 \frac{\partial C_L}{\partial M} q_{dyn_0} S_{ref} + 2 L_0 \right) \quad (B.7)$$

$$a_{\gamma\gamma} = -\left(\frac{V_0}{R_0} - \frac{g_0}{V_0} \right) \sin \gamma_0 \quad (B.8)$$

$$a_{\gamma R} = \left(\frac{2 g_0}{V_0} - \frac{V_0}{R_0} \right) \frac{\cos \gamma_0}{R_0} \quad (B.9)$$

$$a_{\gamma\alpha} = \frac{\cos \sigma_0}{m V_0} \frac{\partial C_L}{\partial \alpha} q_{dyn_0} S_{ref} \quad (B.10)$$

$$a_{\gamma\beta} = -\frac{\sin \sigma_0}{m V_0} \frac{\partial C_S}{\partial \beta} q_{dyn_0} S_{ref} \quad (B.11)$$

$$a_{\gamma\sigma} = -\frac{L_0}{m V_0} \sin \sigma_0 \quad (B.12)$$

$$a_{\gamma p} = a_{\gamma q} = a_{\gamma r} = 0 \quad (B.13)$$

$$a_{RV} = \sin\gamma_0 \quad (B.14)$$

$$a_{RY} = V_0 \cos\gamma_0 \quad (B.15)$$

$$a_{RR} = a_{Rp} = a_{Rq} = a_{Rr} = a_{R\alpha} = a_{R\beta} = a_{R\sigma} = 0 \quad (B.16)$$

$$a_{p\beta} = \frac{1}{I_{xx}} \frac{\partial C_l}{\partial \beta} q_{dyn_0} S_{ref} b_{ref} \quad (B.17)$$

$$a_{pV} = a_{pY} = a_{pR} = a_{pp} = a_{pq} = a_{pr} = a_{p\alpha} = a_{p\sigma} = 0 \quad (B.18)$$

$$a_{qV} = \frac{M_0}{I_{yy} V_0} \frac{\partial C_m}{\partial M} q_{dyn_0} S_{ref} c_{ref} \quad (B.19)$$

$$a_{q\alpha} = \frac{1}{I_{yy}} \frac{\partial C_m}{\partial \alpha} q_{dyn_0} S_{ref} c_{ref} \quad (B.20)$$

$$a_{qY} = a_{qR} = a_{qp} = a_{qq} = a_{qr} = a_{q\beta} = a_{q\sigma} = 0 \quad (B.21)$$

$$a_{r\beta} = \frac{1}{I_{zz}} \frac{\partial C_n}{\partial \beta} q_{dyn_0} S_{ref} b_{ref} \quad (B.22)$$

$$a_{rV} = a_{rY} = a_{rR} = a_{rp} = a_{rq} = a_{rr} = a_{r\alpha} = a_{r\sigma} = 0 \quad (B.23)$$

$$a_{\alpha V} = -\frac{g_0}{V_0^2} \cos\gamma_0 \cos\sigma_0 - \frac{1}{m V_0^2} \left(M_0 \frac{\partial C_L}{\partial M} q_{dyn_0} S_{ref} + L_0 \right) \quad (B.25)$$

$$a_{\alpha Y} = -\frac{g_0}{V_0} \sin\gamma_0 \cos\sigma_0 \quad (B.26)$$

$$a_{\alpha R} = -\frac{2g_0}{R_0 V_0} \cos\gamma_0 \cos\sigma_0 \quad (B.27)$$

$$a_{\alpha q} = 1 \quad (B.28)$$

$$a_{\alpha\alpha} = -\frac{1}{m V_0} \frac{\partial C_L}{\partial \alpha} q_{dyn_0} S_{ref} \quad (B.29)$$

$$a_{\alpha\sigma} = -\frac{g_0}{V_0} \cos\gamma_0 \sin\sigma_0 \quad (\text{B.30})$$

$$a_{\alpha p} = a_{\alpha r} = a_{\alpha\beta} = 0 \quad (\text{B.31})$$

$$a_{\beta V} = \frac{g_0}{V_0^2} \cos\gamma_0 \sin\sigma_0 \quad (\text{B.32})$$

$$a_{\beta\gamma} = \frac{g_0}{V_0} \sin\gamma_0 \sin\sigma_0 \quad (\text{B.33})$$

$$a_{\beta R} = \frac{2g_0}{R_0 V_0} \cos\gamma_0 \sin\sigma_0 \quad (\text{B.34})$$

$$a_{\beta p} = \sin\alpha_0 \quad (\text{B.35})$$

$$a_{\beta r} = -\cos\alpha_0 \quad (\text{B.36})$$

$$a_{\beta\beta} = -\frac{1}{m V_0} \frac{\partial C_S}{\partial \beta} q_{dyn_0} S_{ref} \quad (\text{B.37})$$

$$a_{\beta\sigma} = -\frac{g_0}{V_0} \cos\gamma_0 \cos\sigma_0 \quad (\text{B.38})$$

$$a_{\beta q} = a_{\beta\alpha} = 0 \quad (\text{B.39})$$

$$a_{\sigma V} = \frac{\tan\gamma_0 \sin\sigma_0}{m V_0^2} \left(M_0 \frac{\partial C_L}{\partial M} q_{dyn_0} S_{ref} + L_0 \right) \quad (\text{B.40})$$

$$a_{\sigma\gamma} = \frac{L_0}{m V_0} \sin\sigma_0 \quad (\text{B.41})$$

$$a_{\sigma p} = -\cos\alpha_0 \quad (\text{B.42})$$

$$a_{\sigma r} = -\sin\alpha_0 \quad (\text{B.43})$$

$$a_{\sigma\alpha} = \frac{\tan\gamma_0 \sin\sigma_0}{m V_0} \frac{\partial C_L}{\partial \alpha} q_{dyn_0} S_{ref} \quad (\text{B.44})$$

$$a_{\sigma\beta} = \frac{\tan\gamma_0 \cos\sigma_0}{m V_0} \frac{\partial C_S}{\partial \beta} q_{dyn_0} S_{ref} - \frac{L_0}{m V_0} + \frac{g_0}{V_0} \cos\gamma_0 \cos\sigma_0 \quad (B.45)$$

$$a_{\sigma\sigma} = \tan\gamma_0 \cos\sigma_0 \frac{L_0}{m V_0} \quad (B.46)$$

$$a_{\sigma R} = a_{\sigma q} = 0 \quad (B.47)$$

The elements of matrix **B** are:

$$b_{Ve} = b_{Va} = b_{Vr} = b_{Vx} = b_{Vy} = b_{Vz} = 0 \quad (B.48)$$

$$b_{\gamma e} = b_{\gamma a} = b_{\gamma r} = b_{\gamma x} = b_{\gamma y} = b_{\gamma z} = 0 \quad (B.49)$$

$$b_{Re} = b_{Ra} = b_{Rr} = b_{Rx} = b_{Ry} = b_{Rz} = 0 \quad (B.50)$$

$$b_{pa} = \frac{1}{I_{xx}} \frac{\partial C_l}{\partial \delta_a} q_{dyn_0} S_{ref} b_{ref} \quad (B.51)$$

$$b_{px} = \frac{1}{I_{xx}} \quad (B.52)$$

$$b_{pe} = b_{pr} = b_{py} = b_{pz} = 0 \quad (B.53)$$

$$b_{qe} = \frac{1}{I_{yy}} \frac{\partial C_m}{\partial \delta_e} q_{dyn_0} S_{ref} c_{ref} \quad (B.54)$$

$$b_{qy} = \frac{1}{I_{yy}} \quad (B.55)$$

$$b_{qa} = b_{qr} = b_{qx} = b_{qz} = 0 \quad (B.56)$$

$$b_{ra} = \frac{1}{I_{zz}} \frac{\partial C_n}{\partial \delta_a} q_{dyn_0} S_{ref} b_{ref} \quad (B.57)$$

$$b_{rr} = \frac{1}{I_{zz}} \frac{\partial C_n}{\partial \delta_r} q_{dyn_0} S_{ref} b_{ref} \quad (B.58)$$

$$b_{rz} = \frac{1}{I_{zz}} \quad (B.59)$$

$$b_{re} = b_{rx} = b_{ry} = 0 \quad (B.60)$$

$$b_{\alpha e} = b_{\alpha a} = b_{\alpha r} = b_{\alpha x} = b_{\alpha y} = b_{\alpha z} = 0 \quad (B.61)$$

$$b_{\beta e} = b_{\beta a} = b_{\beta r} = b_{\beta x} = b_{\beta y} = b_{\beta z} = 0 \quad (B.62)$$

$$b_{\sigma e} = b_{\sigma a} = b_{\sigma r} = b_{\sigma x} = b_{\sigma y} = b_{\sigma z} = 0 \quad (B.63)$$

When we substitute the zero-coefficients in Eq. (B.1), the matrix equation gets the following structure:

$$\begin{pmatrix} \Delta \dot{V} \\ \Delta \dot{\gamma} \\ \Delta \dot{R} \\ \Delta \dot{p} \\ \Delta \dot{q} \\ \Delta \dot{r} \\ \Delta \dot{\alpha} \\ \Delta \dot{\beta} \\ \Delta \dot{\sigma} \end{pmatrix} = \begin{bmatrix} a_{VV} & a_{V\gamma} & a_{VR} & 0 & 0 & 0 & a_{V\alpha} & 0 & 0 \\ a_{\gamma V} & a_{\gamma\gamma} & a_{\gamma R} & 0 & 0 & 0 & a_{\gamma\alpha} & a_{\gamma\beta} & a_{\gamma\sigma} \\ a_{RV} & a_{R\gamma} & 0 & 0 & 0 & 0 & 0 & 0 & 0 \\ 0 & 0 & 0 & 0 & 0 & 0 & 0 & a_{p\beta} & 0 \\ a_{qV} & 0 & 0 & 0 & 0 & 0 & a_{q\alpha} & 0 & 0 \\ 0 & 0 & 0 & 0 & 0 & 0 & 0 & a_{r\beta} & 0 \\ a_{\alpha V} & a_{\alpha\gamma} & a_{\alpha R} & 0 & a_{\alpha q} & 0 & a_{\alpha\alpha} & 0 & a_{\alpha\sigma} \\ a_{\beta V} & a_{\beta\gamma} & a_{\beta R} & a_{\beta p} & 0 & a_{\beta r} & 0 & a_{\beta\beta} & a_{\beta\sigma} \\ a_{\sigma V} & a_{\sigma\gamma} & 0 & a_{\sigma p} & 0 & a_{\sigma r} & a_{\sigma\alpha} & a_{\sigma\beta} & a_{\sigma\sigma} \end{bmatrix} \begin{pmatrix} \Delta V \\ \Delta \gamma \\ \Delta R \\ \Delta p \\ \Delta q \\ \Delta r \\ \Delta \alpha \\ \Delta \beta \\ \Delta \sigma \end{pmatrix} + \begin{bmatrix} 0 & 0 & 0 & 0 & 0 & 0 \\ 0 & 0 & 0 & 0 & 0 & 0 \\ 0 & 0 & 0 & 0 & 0 & 0 \\ 0 & b_{pa} & 0 & b_{px} & 0 & 0 \\ b_{qe} & 0 & 0 & 0 & b_{qy} & 0 \\ 0 & b_{ra} & b_{rr} & 0 & 0 & b_{rz} \\ 0 & 0 & 0 & 0 & 0 & 0 \\ 0 & 0 & 0 & 0 & 0 & 0 \\ 0 & 0 & 0 & 0 & 0 & 0 \end{bmatrix} \begin{pmatrix} \Delta \delta_e \\ \Delta \delta_a \\ \Delta \delta_r \\ \Delta T_x \\ \Delta T_y \\ \Delta T_z \end{pmatrix} \quad (B.64)$$

Appendix C

Selected Controller Gains

In the attitude-controller design, the controller gains are computed every four seconds of the nominal trajectory. This results in 314 values for each of the 20 gains. To limit the number of data to be implemented in the flight-dynamics software, a selection of the controller gains has been made that is representative for the variation in gains. These gains are stored in the reference tables of the implemented attitude controller. They can be found in Tables C.1 through C.10, as a function of both flight time and dynamic pressure. Tables C.1 and C.2 give the gains for the pitch jets and elevators. Tables C.3 - C.6 present the gains for the roll and yaw jets, whereas Tables C.7 - C.10 show the gains for the ailerons and rudders.

t (sec)	q_{dyn} (N/m ²)	\tilde{K}_1 (1/rad)	t (sec)	q_{dyn} (N/m ²)	\tilde{K}_2 (1/rad)
0.0	0.4	65.1	0.0	0.4	28.6
104.0	9.0	65.0	132.0	22.2	28.0
108.0	10.2	64.7	152.0	41.8	26.8
116.0	13.3	64.4	164.0	60.3	25.3
124.0	17.3	64.0	168.0	68.1	24.7
132.0	22.3	63.4	172.0	77.0	23.9
140.0	28.7	62.3	176.0	86.9	23.0
148.0	37.0	60.8	180.0	98.0	22.0
156.0	47.2	58.5	184.0	110.3	0.0
164.0	60.3	55.2	1250.0	8681.2	0.0
172.0	77.0	50.6			
180.0	98.0	44.9			
184.0	110.3	0.0			
1250.0	8681.2	0.0			

Table C.1 - Selected pitch-jet gains \tilde{K}_1 and \tilde{K}_2 as a function of t and q_{dyn}

t (sec)	q_{dyn} (N/m ²)	K_1 (1/rad)	t (sec)	q_{dyn} (N/m ²)	K_2 (1/rad)
0.0	0.4	0.0	0.0	0.4	0.0
104.0	9.0	0.0	104.0	9.0	0.0
108.0	10.2	-5.3	108.0	10.2	-2.3
116.0	13.3	-6.8	128.0	19.6	-4.4
124.0	17.3	-8.8	148.0	37.0	-8.0
132.0	22.2	-11.2	164.0	60.3	-12.2
144.0	32.6	-16.0	176.0	86.9	-15.9
168.0	68.1	-28.8	180.0	98.0	-17.2
180.0	98.0	-35.1	184.0	110.3	-27.2
184.0	110.3	-67.6	924.0	3408.4	-27.2
188.0	123.9	-63.8	972.0	3971.1	-27.0
236.0	397.6	-35.6	992.0	4289.1	-27.0
240.0	428.8	-34.3	996.0	4357.7	-27.5
248.0	492.9	-32.0	1060.0	5457.1	-27.4
280.0	719.0	-26.5	1064.0	5512.8	-27.8
320.0	900.9	-23.6	1200.0	7947.7	-28.6
360.0	1054.3	-21.9	1204.0	8021.0	-29.2
400.0	1152.2	-20.9	1236.0	8463.4	-29.5
440.0	1183.7	-20.6	1240.0	8518.5	-29.5
480.0	1166.1	-20.8	1244.0	8574.5	-29.3
544.0	1129.9	-21.1	1250.0	8681.2	-29.8
612.0	1239.6	-20.2			
656.0	1520.0	-18.2			
728.0	2408.1	-14.4			
776.0	2901.3	-13.0			
876.0	3059.9	-12.5			
944.0	3614.3	-11.5			
1028.0	4927.6	-10.5			
1096.0	5880.4	-10.0			
1200.0	7947.7	-9.7			
1204.0	8021.0	-9.8			
1224.0	8306.4	-9.9			
1244.0	8574.5	-9.7			
1250.0	8681.2	-10.8			

Table C.2 - Selected elevator gains K_1 and K_2 as a function of t and q_{dyn} .

t (sec)	q_{dyn} (N/m ²)	\bar{K}_3 (1/rad)	t (sec)	q_{dyn} (N/m ²)	\bar{K}_4 (1/rad)
0.0	0.4	-41.2	0.0	0.4	-11.5
84.0	5.0	-41.0	104.0	9.0	-11.5
100.0	8.0	-40.8	136.0	25.3	-10.2
112.0	11.6	-38.9	148.0	37.0	-9.2
128.0	19.6	-35.9	160.0	53.4	-7.9
140.0	28.7	-32.0	172.0	77.0	-6.6
152.0	41.8	-27.0	188.0	123.9	-5.1
168.0	68.1	-20.1	204.0	192.4	-4.1
188.0	123.9	-13.9	224.0	310.4	-3.5
192.0	138.9	-13.1	240.0	428.8	-3.2
196.0	155.3	-12.4	244.0	460.7	0.0
200.0	173.2	-11.8	1250.0	8681.2	0.0
220.0	283.9	-9.9			
240.0	428.8	-8.6			
244.0	460.7	0.0			
1250.0	8681.2	0.0			

Table C.3 - Selected roll-jet gains \bar{K}_3 and \bar{K}_4 as a function of t and q_{dyn} .

t (sec)	q_{dyn} (N/m ²)	\tilde{K}_5 (1/rad)	t (sec)	q_{dyn} (N/m ²)	\tilde{K}_6 (1/rad)
0.0	0.4	41.2	0.0	0.4	11.4
80.0	4.4	40.6	72.0	3.4	11.0
104.0	9.0	39.9	104.0	9.0	10.2
108.0	10.2	37.4	156.0	47.2	3.9
152.0	41.8	17.3	184.0	110.3	0.3
160.0	53.4	12.0	212.0	235.2	-1.7
164.0	60.3	9.4	228.0	338.2	-2.4
176.0	86.9	2.9	240.0	428.8	-2.7
184.0	110.3	-0.4	244.0	460.7	0.0
188.0	123.9	-1.7	1250.0	8681.2	0.0
192.0	138.9	-2.8			
196.0	155.3	-3.8			
212.0	235.2	-6.3			
220.0	283.9	-6.9			
232.0	367.4	-7.4			
240.0	428.8	-7.5			
244.0	460.7	0.0			
1250.0	8681.2	0.0			

Table C.4 - Selected roll-jet gains \tilde{K}_5 and \tilde{K}_6 as a function of t and q_{dyn}

t (sec)	q_{dyn} (N/m ²)	\tilde{K}_7 (1/rad)	t (sec)	q_{dyn} (N/m ²)	\tilde{K}_8 (1/rad)
0.0	0.4	-49.3	0.0	0.4	-11.3
52.0	1.9	-49.4	116.0	13.3	-11.4
100.0	8.0	-49.8	144.0	32.6	-11.7
128.0	19.6	-51.4	164.0	60.3	-12.3
184.0	110.3	-58.2	200.0	173.2	-14.0
216.0	258.9	-60.8	248.0	492.9	-16.5
248.0	492.9	-57.2	352.0	1027.3	-13.9
300.0	812.5	-44.1	444.0	1183.6	-12.9
324.0	918.0	-40.0	544.0	1129.9	-13.2
400.0	1152.2	-32.4	600.0	1197.7	-12.8
440.0	1183.7	-31.5	636.0	1365.8	-11.8
544.0	1129.9	-33.0	720.0	2297.6	-7.7
572.0	1143.2	-32.6	760.0	2782.5	-6.3
600.0	1197.7	-31.1	800.0	2984.7	-5.7
720.0	2297.6	-13.6	900.0	3201.7	-5.0
740.0	2565.1	-11.5	1000.0	4427.1	-3.7
760.0	2782.5	-10.1	1100.0	5923.5	-3.5
780.0	2922.7	-9.2	1200.0	7947.7	-3.2
800.0	2984.7	-8.8	1250.0	8681.2	-2.7
860.0	3010.2	-8.2			
900.0	3201.7	-7.2			
1000.0	4427.1	-4.5			
1052.0	5338.0	-3.8			
1100.0	5923.5	-3.7			
1152.0	6808.5	-3.5			
1200.0	7947.7	-3.2			
1250.0	8681.2	-3.0			

Table C.5 - Selected yaw-jet gains \tilde{K}_7 and \tilde{K}_8 as a function of t and q_{dyn} .

t (sec)	q_{dyn} (N/m ²)	\tilde{K}_9 (1/rad)	t (sec)	q_{dyn} (N/m ²)	\tilde{K}_{10} (1/rad)
0.0	0.4	-49.3	0.0	0.4	-11.5
100.0	8.0	-49.2	136.0	25.3	-11.8
164.0	60.3	-47.0	164.0	60.3	-12.5
212.0	235.2	-49.0	184.0	110.3	-13.7
300.0	812.5	-35.5	252.0	525.1	-19.2
352.0	1027.3	-29.1	440.0	1183.7	-15.4
400.0	1152.2	-26.0	544.0	1129.9	-15.8
440.0	1183.7	-25.3	584.0	1160.0	-15.6
544.0	1129.9	-26.5	624.0	1295.2	-14.6
600.0	1197.7	-25.0	744.0	2613.8	-8.1
700.0	2020.2	-13.2	748.0	2660.1	-8.0
752.0	2703.8	-8.5	768.0	2848.6	-7.4
780.0	2922.7	-7.4	788.0	2955.9	-7.0
800.0	2984.7	-7.0	816.0	2994.8	-6.8
848.0	2993.8	-6.7	900.0	3201.7	-6.0
900.0	3201.7	-5.7	1000.0	4427.1	-4.5
948.0	3659.7	-4.7	1052.0	5338.0	-4.2
1000.0	4427.1	-3.7	1104.0	5967.7	-4.2
1048.0	5274.4	-3.2	1120.0	6166.2	-4.2
1100.0	5923.5	-3.0	1160.0	7013.1	-3.9
1148.0	6710.1	-2.8	1212.0	8147.7	-3.5
1200.0	7947.7	-2.4	1250.0	8681.2	-2.7
1250.0	8681.2	-2.1			

Table C.6 - Selected yaw-jet gains \tilde{K}_9 and \tilde{K}_{10} as a function of t and q_{dyn} .

t (sec)	q_{dyn} (N/m ²)	K_3 (1/rad)	t (sec)	q_{dyn} (N/m ²)	K_4 (1/rad)
0.0	0.4	0.0	0.0	0.4	0.0
104.0	9.0	0.0	104.0	9.0	0.0
108.0	10.2	7.5	108.0	10.2	2.3
148.0	37.0	17.3	168.0	68.1	8.0
156.0	47.2	17.8	184.0	110.3	8.4
164.0	60.3	17.4	200.0	173.2	8.0
268.0	646.2	-25.4	272.0	672.6	-0.2
308.0	848.4	-30.2	320.0	900.9	-2.9
328.0	934.7	-31.3	440.0	1183.7	-5.0
364.0	1067.0	-32.3	544.0	1129.9	-4.7
440.0	1183.7	-32.7	764.0	2817.2	-8.2
544.0	1129.9	-32.6	924.0	3408.4	-7.6
624.0	1295.2	-32.8	996.0	4357.7	-2.5
648.0	1452.7	-32.6	1244.0	8574.5	6.9
748.0	2660.1	-27.1	1250.0	8681.2	8.4
788.0	2955.9	-25.4			
828.0	2992.1	-24.7			
872.0	3044.2	-24.0			
924.0	3408.4	-22.1			
992.0	4289.1	-13.6			
1100.0	5923.5	-7.9			
1244.0	8574.5	-1.1			
1250.0	8681.2	0.3			

Table C.7 - Selected aileron gains K_3 and K_4 as a function of t and q_{dyn} .

t (sec)	q_{dyn} (N/m ²)	K_5 (1/rad)	t (sec)	q_{dyn} (N/m ²)	K_6 (1/rad)
0.0	0.4	0.0	0.0	0.4	0.0
104.0	9.0	0.0	104.0	9.0	0.0
108.0	10.2	-12.2	108.0	10.2	-3.1
168.0	68.1	-30.7	200.0	173.2	-11.2
188.0	123.9	-30.3	244.0	460.7	-20.1
276.0	696.8	-50.1	284.0	739.2	-27.6
316.0	883.6	-52.2	312.0	866.1	-30.1
352.0	1027.3	-52.6	364.0	1067.0	-33.1
440.0	1183.7	-52.2	400.0	1152.2	-34.1
544.0	1129.9	-52.4	440.0	1183.7	-34.5
600.0	1197.7	-52.2	544.0	1129.9	-33.9
632.0	1340.5	-51.4	600.0	1197.7	-34.6
660.0	1556.5	-49.9	752.0	2703.8	-40.0
756.0	2744.7	-40.0	800.0	2984.7	-39.9
776.0	2901.3	-38.7	924.0	3408.4	-39.1
800.0	2984.7	-37.8	960.0	3806.1	-40.1
860.0	3010.2	-36.6	996.0	4357.7	-40.6
920.0	3371.2	-33.7	1136.0	6441.0	-57.3
924.0	3408.4	-33.5	1212.0	8147.7	-57.2
992.0	4289.1	-32.2	1220.0	8254.6	-56.7
1140.0	6525.6	-40.2	1244.0	8574.5	-45.9
1220.0	8254.6	-40.0	1250.0	8681.2	-31.5
1244.0	8574.5	-35.5			
1250.0	8681.2	-28.2			

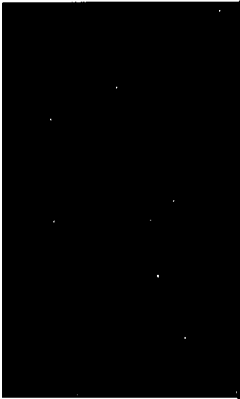
Table C.8 - Selected aileron gains K_5 and K_6 as a function of t and q_{dyn} .

t (sec)	q_{dyn} (N/m ²)	K_7 (1/rad)	t (sec)	q_{dyn} (N/m ²)	K_8 (1/rad)
0.0	0.4	0.0	0.0	0.4	0.0
180.0	98.0	0.0	180.0	98.0	0.0
184.0	110.3	-4.5	184.0	110.3	-1.0
272.0	672.6	-23.3	200.0	173.2	-1.7
304.0	830.5	-25.0	284.0	739.2	-8.1
384.0	1121.0	-25.9	356.0	1041.1	-10.0
600.0	1197.7	-25.9	400.0	1152.2	-10.5
632.0	1340.5	-25.6	440.0	1183.7	-10.6
660.0	1556.5	-25.0	544.0	1129.9	-10.4
752.0	2703.8	-21.6	600.0	1197.7	-10.7
780.0	2922.7	-21.1	700.0	2020.2	-12.5
800.0	2984.7	-21.0	748.0	2660.1	-13.3
852.0	2997.6	-21.1	800.0	2984.7	-13.8
924.0	3408.4	-20.2	924.0	3408.4	-14.6
996.0	4357.7	-23.7	996.0	4357.7	-19.2
1036.0	5070.6	-23.9	1228.0	8358.0	-31.4
1076.0	5663.0	-25.0	1244.0	8574.5	-31.2
1140.0	6525.6	-27.6	1250.0	8681.2	-27.7
1244.0	8574.5	-32.3			
1250.0	8681.2	-30.3			

Table C.9 - Selected rudder gains K_7 and K_8 as a function of t and q_{dyn} .

t (sec)	q_{dyn} (N/m ²)	K_g (1/rad)	t (sec)	q_{dyn} (N/m ²)	K_{10} (1/rad)
0.0	0.4	0.0	0.0	0.4	0.0
180.0	98.0	0.0	180.0	98.0	0.0
184.0	110.3	-3.6	184.0	110.3	-1.0
272.0	672.6	-18.7	200.0	173.2	-1.8
300.0	812.5	-20.0	236.0	397.6	-5.1
324.0	918.0	-20.5	272.0	672.6	-8.8
384.0	1121.0	-20.8	328.0	934.7	-11.2
600.0	1197.7	-20.8	400.0	1152.2	-12.5
632.0	1340.5	-20.6	440.0	1183.7	-12.7
664.0	1594.9	-20.0	544.0	1129.9	-12.4
760.0	2782.5	-17.1	600.0	1197.7	-12.7
804.0	2989.7	-16.8	712.0	2185.6	-15.3
848.0	2993.8	-16.9	744.0	2613.8	-15.9
924.0	3408.4	-16.1	800.0	2984.7	-16.5
996.0	4357.7	-19.3	924.0	3408.4	-17.5
1032.0	4999.5	-19.5	1000.0	4427.1	-23.3
1068.0	5565.6	-20.1	1152.0	6808.5	-32.1
1148.0	6710.1	-22.3	1180.0	7519.8	-32.9
1172.0	7322.7	-22.4	1220.0	8254.6	-33.3
1200.0	7947.7	-22.4	1244.0	8574.5	-30.2
1220.0	8254.6	-22.5	1250.0	8681.2	-27.6
1250.0	8681.2	-21.9			

Table C.10 - Selected rudder gains K_g and K_{10} as a function of t and q_{dyn}



Rapport 806



60141070649